



The
University
Of
Sheffield.

Conversion of magnesium bearing radioactive wastes into cementitious binders

Samuel Alexander Walling

A thesis submitted in partial fulfilment of the requirement for the degree
of Doctor of Philosophy

Department of Materials Science and Engineering

The University of Sheffield

June 2016

Abstract

The UK radioactive waste inventory contains sizeable portions of magnesium hydroxide rich Magnox sludges due to corrosion of historic wastes. These require disposal in suitable wasteforms, with one potential being solidification in a composite Portland cement matrix.

This thesis investigates magnesium hydroxide as a key component in the production of a cementitious binder, attempting to maximise waste loading and improve wasteform integrity through integral usage of these wastes.

Hydrated magnesium silicate cements were produced through reaction with amorphous silica, creating stable products comprising a poorly crystalline M-S-H gel. The formulations for this product were optimised, water contents reduced through the use of a polyphosphate dispersant, and the nature of the M-S-H binder investigated further. This was determined to be a lizardite-like structure, which is a stable mineral.

This system was modified through the addition of sodium aluminate, resulting in formulations with varying ratios of silicon to aluminium, each of which produced various zeolitic phases along with a magnesium aluminium hydrotalcite phase. This addition improved the setting characteristics of the binders, but did not produce any additional magnesium silicates binders.

Additionally to this, sodium carbonate activated slag cement binders blended with magnesium hydroxide were assessed. These were slower setting, low heat cements which formed stable mineral phases, largely unaffected by the addition of magnesium hydroxide. The chemistry of these binders was assessed over an 18 month period, remaining stable throughout.

Ultimately it was proved that magnesium hydroxide can be utilised to form cementitious binders, but only in the absence of competing calcium based binding systems.

Acknowledgements

This thesis owes a great deal to the support and encouragement of countless people, most notably my academic supervisors Prof. John Provis and Dr. Hajime Kinoshita, without whom none of this would have been possible. I would also like to especially thank Dr. Susan Bernal López for getting me back on track when I've been lost, and for proof reading a great deal of this thesis in various stages.

Thanks of course to my family and Laura Gardner for their (nearly) unending patience and help. Also thanks everyone within the Immobilisation Science Laboratory, especially Dr. Claire Corkhill, Dr. Oday Hussein, Dr. Martin Stennett and Prof. Neil Hyatt.

I would like to express my gratitude to my funding bodies, the Engineering and Physical Sciences Research Council for funding, *via* the Nuclear FiRST program, and to the Nuclear Decommissioning Authority for funding also. I am indebted to Dr. Nick Collier and Dr. Steve Palethorpe for industrial input, to Dr. Dinu Iuga for assistance undertaking high-field NMR experiments, and to Andrew Mould, Ben Palmer and Dr. Nik Reeves for ongoing technical assistance.

Publications

Journal publications

1. Walling, S.A., Provis, J.L. (2016) “Magnesium based cements – a journey of 150 years, and cements for the future?” – Submitted to *Chemical Reviews*
2. Walling, S.A., Provis, J.L. (2016) “A discussion of the papers “*Impact of hydrated magnesium carbonate additives on the carbonation of reactive MgO cements*” and “*Enhancing the carbonation of MgO cement porous blocks through improved curing conditions*”, by C. Unluer & A. Al-Tabbaa”, *Cement and Concrete Research*, **79**, 424-426.
3. Walling, S.A., Kinoshita, H., Bernal, S.A., Collier, N.C., Provis, J.L. (2015) “Structure and properties of binder gels formed in the system $\text{Mg}(\text{OH})_2\text{-SiO}_2\text{-H}_2\text{O}$ for immobilisation of Magnox sludge”, *Dalton Transactions*, **44**, 8126-8137.
4. Gardner, L.J., Bernal, S.A., Walling, S.A., Corkhill, C.L., Provis, J.L., Hyatt, N.C. (2015) “Characterisation of magnesium potassium phosphate cements blended with fly ash and ground granulated blast furnace slag”, *Cement and Concrete Research*, **74**, 78-87.
5. Walling, S.A., Bernal, S.A., Kinoshita, H., Collier, N.C., Provis, J.L. (2014) “Cementitious binders in the system $\text{Mg}(\text{OH})_2\text{-NaAlO}_2\text{-SiO}_2\text{-H}_2\text{O}$ ”, *Advances in Applied Ceramics*, **113**, 496-501.

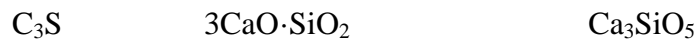
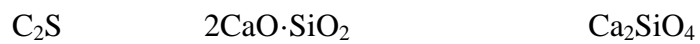
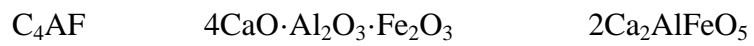
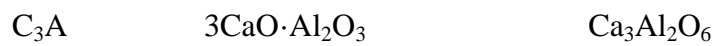
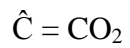
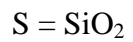
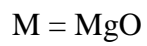
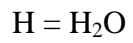
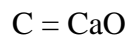
Conference publications

1. Walling, S.A., Bernal, S.A., Kinoshita, H., Provis, J.L. “Magnesium aluminium silicate hydrate (M-A-S-H) cements for Magnox sludge immobilisation”, Workshop on Waste Cementation, Sheffield, 17th September 2014. (*Extended abstract and poster presentation*)
2. Walling, S.A., Bernal, S.A., Collier, N.C., Kinoshita, H., Provis, J.L. “Sodium carbonate activated slag binders for the immobilisation of Magnox nuclear waste”, 34th Cement and Concrete Science Conference, Sheffield, UK, September 14-16th 2014. (*Extended abstract and poster presentation*)
3. Gardner L.J., Bernal S.A., Walling S.A., Corkhill C.L., Provis J.L., Hyatt N.C. “High-resolution multi-nuclear NMR characterisation of a novel GBFS/MKPC binder for nuclear waste encapsulation”, 34th Cement and Concrete Science Conference, Sheffield, 14-16th September 2014.
4. Walling, S.A., Bernal, S.A., Kinoshita, H., Collier, N.C., Provis, J.L. “Alternative binders in the systems $\text{Mg}(\text{OH})_2\text{-NaAlO}_2\text{-SiO}_2\text{-H}_2\text{O}$ ”, 33rd Cement and Concrete Science Conference, Portsmouth, 2-3rd September 2013 (*Extended abstract and presentation*)
5. Walling, S.A., Bryan, N.D., Kinoshita, H. “Magnesium silicate hydrate cement for Magnox sludge encapsulation” 32nd Cement and Concrete Science Conference, Belfast, 17-18th September 2012 (*Extended abstract & poster presentation*)

Other abstracts / posters

1. Walling, S.A., Bernal, S.A., Kinoshita, H., Provis, J.L. “Conversion of magnesium bearing radioactive wastes into cementitious binders”, Nuclear Decommissioning Authority PhD Research Seminar for NDA-Sponsored PhD Projects, 14th January 2015, Manchester. (*Abstract and poster presentation*)
2. Walling, S.A., Collier, N., Kinoshita, H. “Magnox sludge as a cementitious binder” – Nuclear Decommissioning Authority PhD Research Seminar for NDA-Sponsored PhD Projects, 29th January 2013, Manchester. (*Abstract*)

Cement Chemical Nomenclature



Contents

Abstract	i
Acknowledgements	ii
Publications	iii
Journal publications.....	iii
Conference publications	iv
Other abstracts / posters	v
1 Introduction	1
2 Literature Review	3
2.1 Nuclear power	3
2.2 Nuclear power in the UK.....	7
2.2.1 History.....	7
2.2.2 Today.....	10
2.3 Nuclear waste	15
2.3.1 Nuclear waste in the UK	16
2.4 Geological disposal	20
2.4.1 Geological disposal in the UK	20
2.5 Waste treatment	23
2.5.1 Vitrification.....	23
2.5.2 Cementation	24
2.5.3 Alternative ILW immobilisation technologies.....	29
2.6 Magnox sludges.....	31
2.6.1 Other sources of Magnox sludge.....	34
2.6.2 Magnox sludge encapsulation	35
2.6.3 Alternative processing techniques.....	36
2.6.4 Cement encapsulation of Magnox sludges.....	37
2.7 Summary	38
3 Review of magnesium cements	39
3.1 Introduction	39
3.1.1 Cements based on magnesia.....	39
3.1.2 Magnesia production	43
3.2 Magnesium carbonate and reactive magnesia cements	45
3.2.1 Reactive magnesia.....	46

3.2.2	Expansive MgO cements	47
3.2.3	Development of reactive magnesia cements.....	48
3.2.4	Carbonated magnesia blocks.....	54
3.2.5	Novacem	56
3.2.6	Limitations of carbon sequestration.....	58
3.2.7	Conclusions.....	60
3.3	Magnesium phosphate cements.....	61
3.3.1	Phosphate bonding of magnesia.....	61
3.3.2	Application as cements	62
3.3.3	Method of action.....	63
3.3.4	Struvite-K cements.....	67
3.3.5	Retardation of MPCs.....	71
3.3.6	MKPC expansion.....	74
3.3.7	Conclusions.....	75
3.4	Magnesium silicate hydrate (M-S-H) cements.....	76
3.4.1	M-S-H as a cementitious phase.....	77
3.4.2	Structure of M-S-H	80
3.4.3	Conclusions.....	85
3.5	Magnesium oxychloride (Sorel) cements.....	85
3.5.1	Phase composition	87
3.5.2	Chlorocarbonate: Relation to strength and durability	95
3.5.3	Influence of MgO calcination	96
3.5.4	Cost-effective production.....	97
3.5.5	Water resistance	100
3.5.6	Current uses for MOC.....	102
3.5.7	Conclusions.....	103
3.6	Magnesium oxysulfate cements	103
3.6.1	Phase composition	103
3.6.2	Hydrothermal production of magnesium oxysulfates.....	109
3.6.3	Current uses for MOS	110
3.6.4	Conclusions.....	110
3.7	Perspectives: What is the future of Mg-based cements?.....	110
3.8	Conclusions	112

4	Experimental	115
4.1	Analytical Methods	115
4.1.1	X-Ray Diffraction (XRD)	115
4.1.2	Fourier Transform Infra-Red Spectroscopy (FTIR).....	118
4.1.3	Nuclear Magnetic Resonance (NMR).....	120
4.1.4	Scanning Electron Microscopy (SEM) & Energy Dispersive X-Ray Spectroscopy (EDX).....	124
4.1.5	Thermal analysis (TGA, DTG and DTA) & coupled mass spectrometry (TG-MS)	127
4.1.6	Compressive strength	129
4.1.7	Mini-Slump	131
4.1.8	Isothermal calorimetry	133
4.1.9	Blaine	134
4.1.10	Particle Size Distribution (PSD)	135
4.1.11	Automatic Vicat	136
4.2	Materials	137
4.2.1	Chapter 5	137
4.2.2	Chapter 6	137
4.2.3	Chapter 7	137
4.2.4	Chapter 8	137
5	Magnesium silicate hydrate cementitious systems	139
5.1	Introduction	139
5.2	Preliminary experiments.....	140
5.2.1	MgO-SiO ₂ -H ₂ O	142
5.2.2	Mg(OH) ₂ -SiO ₂ -H ₂ O	150
5.3	In-depth study of structure and properties of the M-S-H binder	155
5.3.1	Formulation design	155
5.3.2	Results and discussion	156
5.4	Conclusions	180
5.4.1	Scientific findings	180
5.4.2	Industrial application.....	181
6	Aluminosilicate – Mg(OH)₂ binders	183
6.1	Introduction	183
6.2	Methodology	185

6.3	Results and Discussion.....	186
6.3.1	X-ray diffraction	186
6.3.2	Fourier transform infrared spectroscopy.....	192
6.3.3	Scanning electron microscopy	195
6.4	Conclusions	196
6.4.1	Scientific findings	196
6.4.2	Industrial application	196
7	Phase evolution in the Mg(OH)₂-NaAlO₂-SiO₂-H₂O system.....	197
7.1	Introduction	197
7.2	Methodology	198
7.3	Results and discussion.....	199
7.3.1	Early-age reaction processes.....	199
7.3.2	X-ray diffraction analysis of aged samples.....	204
7.3.3	Layered double hydroxide thermal identification.....	207
7.3.4	Solid-state NMR spectroscopy	210
7.4	Conclusions	218
7.4.1	Scientific findings	218
7.4.2	Industrial application	219
8	Sodium carbonate activated slag – Mg(OH)₂ binders	221
8.1	Foreword	221
8.2	Introduction	222
8.3	Experimental programme.....	224
8.3.1	Sample preparation	224
8.4	Results and discussion.....	225
8.4.1	Early age evolution of a Mg(OH) ₂ modified sodium carbonate activated slag cement.....	225
8.4.2	Long term structural evolution of a Mg(OH) ₂ modified sodium carbonate activated slag cement	231
8.5	Conclusions	266
8.5.1	Scientific findings	266
8.5.2	Industrial application	267
9	Conclusions.....	269
10	References.....	275
11	Appendix I – Supplementary data	311

11.1	Magnesium silicate hydrate cementitious systems supplementary data....	311
11.2	Sodium carbonate activated slag – Mg(OH) ₂ binders supplementary SEM images and EDX maps	314
11.2.1	Mg(OH) ₂ free binders	314
11.2.2	10 % Mg(OH) ₂ binders.....	316
11.2.3	30 % Mg(OH) ₂ binders.....	318
11.2.4	50 % Mg(OH) ₂ binders.....	321
12	Appendix II – CCR discussion publication	325

1 Introduction

The aim of this project was to produce a cementitious binder in which $\text{Mg}(\text{OH})_2$ might react to form a principal or additional binding phase, and to help stabilise the system. This entailed studying the current state of the art in magnesium cement technology, and applying this knowledge to the production and formation of a magnesium bearing binding phase.

The work presented in this thesis all follows this strand of thinking, attempting to utilise $\text{Mg}(\text{OH})_2$ as a constituent material for binder formation, with each chapter feeding information into the next, before concluding what has been learnt from this process and how to proceed further.

Chapter 2 begins by detailing the nuclear power technology, the history of this within the context of the UK, and the associated radioactive wastes that have accumulated. The nature and chemistry of Magnox sludges cement is also highlighted, along with known interactions in conventional cement systems

Chapter 3 comprises an extensive literature review of current and historical magnesium based cements and their application to current day engineering challenges. This consists of both technical and patent literature, focussing on magnesium cement chemistry, feasibility, environmental footprint, current usage and future prospects.

Chapter 4 details the experimental methods employed in this thesis, a summary of the theory behind these techniques, and the specific experimental setups used in each experimental chapter.

Chapter 5 comprises a study of $\text{Mg}(\text{OH})_2$ incorporation as part of a magnesium silicate hydrate (M-S-H) based cementitious system. Initial scoping studies analyse the ability to produce an M-S-H cement from a range of commercial MgO powders, before moving onto $\text{Mg}(\text{OH})_2$ -only systems. The mixing, structure and strength of these cements are studied with X-ray diffraction (XRD), Fourier Transform Infra-Red spectroscopy (FTIR) and thermal analysis. The study then moves to look in-depth at the gel structure of M-S-H, utilising conventional solid state, and high field

solid state Nuclear Magnetic Resonance (NMR) spectroscopy in reference to known magnesium silicate minerals.

Chapter 6 is a short trial, which attempts to improve the setting characteristics of the M-S-H cements *via* addition of reactive aluminium into the system. This is studied up to 90 days of curing using a range of analytical techniques to elucidate the binding phases formed, and whether $\text{Mg}(\text{OH})_2$ reacts within the system.

Chapter 7 expands the formulations studied in previous chapters, and extending the duration of analysis up to two years. Detailed phase analysis is undertaken, with specific emphases on determining whether an M-S-H or M-A-S-H type phase is formed.

Chapter 8 investigates the interaction of $\text{Mg}(\text{OH})_2$ within an alternative calcium based binder. Here $\text{Mg}(\text{OH})_2$ is blended into an alkali carbonate activated blast furnace slag cement system. $\text{Mg}(\text{OH})_2$ is added in excess with the aim to form stable magnesium phases within the activated system, and the resulting cementitious products analysed over an 18 month period.

Chapter 9 details the overall conclusions of this work, with recommendations for further work on these systems presented in Chapter 10.

2 Literature Review

2.1 Nuclear power

Nuclear power is the harnessing of energy from nuclear reactions for the production of usable heat, and often electricity. This energy can come from the fusion of light elements (e.g. ${}^2\text{H}+{}^2\text{H}$) or the ‘fission’ of heavier elements such as uranium or plutonium, which break up into smaller elemental components, releasing energy in the process. Although considerable research is bringing us closer to sustained fusion power, nuclear power is currently only produced *via* the fission process [1-2].

Fission is attractive due to the vast amounts of energy contained within atoms. This is a combination of various nuclear forces which hold the atoms together. Some of this energy can be released when heavier elements are broken down, and even a tiny fraction of this energy is enough for the basis of a nuclear power plant. Uranium is the element most commonly associated with nuclear fission, although other elements such as thorium and plutonium have been used as the basis for nuclear reactors to varying degrees of success. Uranium lies at the far end of the periodic table, where atoms are very large and unstable. Any element larger than lead is unstable, undergoing radioactive decay to bring them back to stability. Although radioactive, uranium (specifically the most common isotope ${}^{238}\text{U}$) has a long half-life of ~4.5 billion years (the less common ${}^{235}\text{U}$ has a half-life of ~704 million years), resulting in large deposits of this element still remaining within the Earth’s crust [1, 3].

Typically in a nuclear reactor the interaction of neutrons with ${}^{235}\text{U}$ is exploited to create useful energy. This isotope of uranium is especially vulnerable to capturing slow moving neutrons, forming ${}^{236}\text{U}$ which is even more unstable. This excites the nucleus, which undergoes deformation and splits into two unequal fragments, releasing neutrons and gamma rays in the process [4]. This creates fission fragments of unequal sizes, which can vary considerably. One such fission event is depicted in Figure 2.1, showing neutron capture and fission into ${}^{87}\text{Br}$ and ${}^{147}\text{La}$ (along with the start of their respective decay chains, ${}^{87}\text{Kr}$ and ${}^{147}\text{Ce}$ respectively), with ejection of two neutrons.

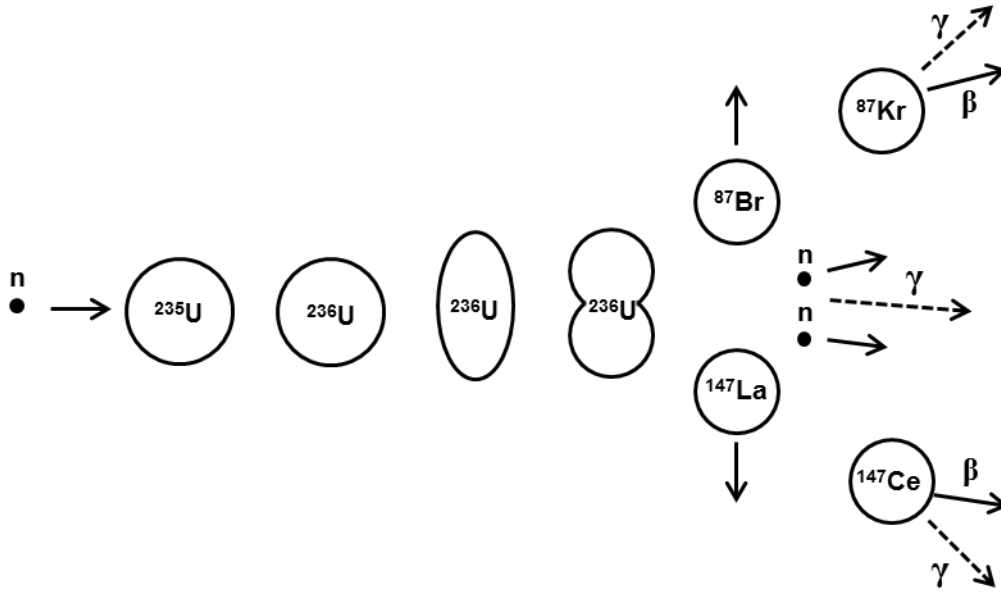
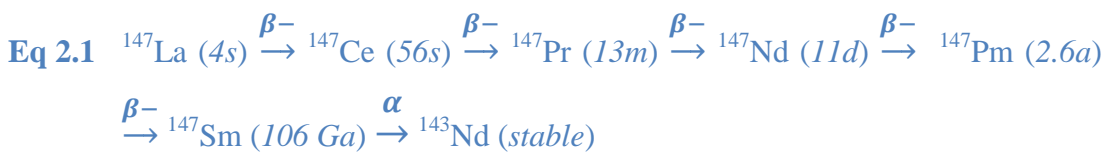


Figure 2.1 Illustration of ^{235}U fission, demonstrating typical decay products. Drawn and adapted from [4]

These fission fragments are neutron-rich compared to their stable forms, and undergo series of alpha, beta and gamma decays, releasing energy to bring them back down to stable isotopes. This is exemplified by the decay chain of ^{147}La in Eq 2.1 [5], a common fission product of ^{235}U , which decays *via* multiple steps, some of which occur minutes or seconds later.



The fragments undergo decay because they are energetically unstable. One of the principal reasons behind this is due to being neutron heavy. Figure 2.2 shows the line of stability for isotopes where $N = Z$ (with N the number of neutrons, and Z the number of protons), with the actual stable isotopes in red. Heavier elements require a higher proportion of neutrons to protons to remain stable, due to a combination of increased repulsive forces to attractive nuclear forces, and having a larger surface (amongst other factors) [2, 4].

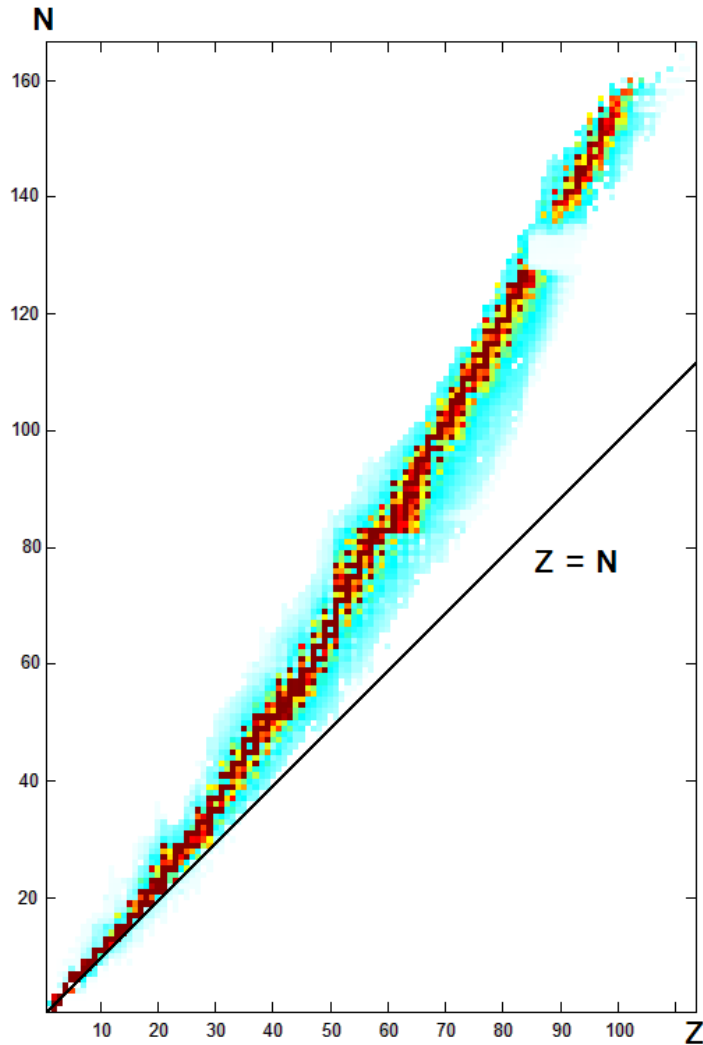


Figure 2.2 Line of stability for isotopes, plotting Z against N. Stable in red, unstable light blue

For example in ^{235}U $N/Z = 1.55$, while in ^{133}Cs (stable caesium) $N/Z = 1.42$, and in ^4He $N/Z = 1$. Fission fragments form with a higher proportion of neutrons than is stable, and radioactive decay brings them back towards stability. This fission product decay produces further radiative and kinetic energy (and therefore heat), contributing to the energy released from a fissile fuel (such as uranium), but also gives rise to nuclear waste due to the varied (and often long) half-lives of the fission products and in their decay chains.

This nuclear reaction process is harnessed within nuclear power plants. A nuclear reactor runs on the principle of maintaining sustained and controlled nuclear fission, with heat from this reaction being taken to heat water which drives turbines – generating electricity. Nuclear reactors control the nuclear reactions *via* a combination of control rods, burnable poisons and moderators, which can reduce the amount of neutrons available for reaction, and slow down those that remain so they are able to react. High-energy neutrons do not always interact with uranium, they require slowing down to give them a higher chance of interacting [1, 4]. Moderators typically consist of materials rich in light elements, such as water (H₂O or D₂O) or graphite. Helpfully, water can also act as a coolant – which is exploited by two of the most common types of reactors; PWR (pressurised water reactors) and BWR (boiling water reactors) types, while AGR and Magnox type reactors utilise graphite moderators with CO₂ gas coolant [1].

Typically, modern reactors use uranium as a fuel. Although quite plentiful in the Earth's crust, natural mined uranium consists of mainly ²³⁸U with 0.72% ²³⁵U, and it is the ²³⁵U which is crucial in most nuclear reactors. It has a much higher capture cross section for thermal neutrons (those which have been slowed due to elastic collisions with moderating materials) [4], making this the crucially “reactive” part of uranium. Some reactor types can use natural uranium, however most currently in operation require slight isotopic enrichment, increasing the ²³⁵U content to typically ~2-3%. This is a challenging process, as ²³⁵U and ²³⁸U are chemically identical, requiring separation and enrichment by exploitation of their slight difference in atomic weight. This is commonly achieved through gas centrifugation (historically through gaseous diffusion), in which uranium is reacted with fluorine to form UF₆, which sublimes to a gas at only slightly elevated temperatures. Fluorine is monoisotopic, so any difference in mass is due to the uranium isotopes. UF₆ is then spun in gas centrifuges to separate the isotopes very slightly, when repeated hundreds of times to slightly enrich the uranium in ²³⁵U [1, 6]. This resultant ‘enriched’ uranium can be defluorinated and turned into fuel, leaving behind waste ‘depleted’ uranium, which now has a lower ²³⁵U content than natural uranium.

Since nuclear power was first utilised it has become a mature technology worldwide, with 438 operable nuclear power plants with a capacity of 376 GW(e) at the end of 2014 [7], and a further 70 reactors under construction. However this includes ~50 Japanese reactors which were shut down following a severe nuclear accident at the Fukushima-Daiichi nuclear power plant, leaving the number of currently operational reactors <400 [8], though these reactors are slowly returning to operation. This accident has also affected the number of reactors under construction, with some projects mothballed, or suspended awaiting investment decisions or further regulatory approval. Many countries with established nuclear power programmes are in the process of deciding whether to permit the construction of new reactors, with current constructions primarily in China (29 units), Russia (10 units) and India (6 units) [9].

2.2 Nuclear power in the UK

2.2.1 History

The story of nuclear power in the UK began in the aftermath of the Second World War. During the war the UK was heavily involved with the US Manhattan Project to build an atomic bomb. Although this programme was a success, the UK and other contributing countries were frozen out of the accumulated knowledge and materials afterwards. This geopolitical situation led to the UK commencing its own independent military nuclear programme, which resulted in the rapid construction of the GLEEP (Graphite Low Energy Experimental Pile) and BEPO (British Experimental Pile 0) reactors in 1947/48 [10] at Harwell, Oxfordshire, followed by two larger scale pile reactors at Windscale, Cumbria (now Sellafield) in 1950/51. These reactors did not produce electricity, and were principally for increasing our understanding of reactors and ultimately the production of plutonium to be used in the atomic weapons programme. This was later supplemented by the construction of the Calder Hall nuclear power plant, containing four Magnox type reactors. Originally codenamed PIPPA (Pressurised Pile Producing Power and Plutonium) Calder Hall had dual military-civilian usage, producing both plutonium and electricity (generation began in 1956 [11]). Later reactors were based upon this Magnox design, but were primarily built for power production, rather than military applications.

Nuclear power has been operating commercially in the UK since 1965, with three different type of reactors having been in commercial operation: Magnox (schematic in Figure 2.3), Advanced Gas Reactor (AGR) and Pressurised Water Reactor (PWR) [12], all of which have generated varying quantities and types of nuclear waste. In 2014 nuclear fission provided 20% of the UK’s electricity generation from 9 power plants [13], down from a high of 29% in 1998 due to increased maintenance, repairs and the closure of ageing plants [14]. Alongside this the UK has developed a fully closed nuclear fuel cycle, being able to reprocess spent nuclear fuel and fabricate new fuel [15].

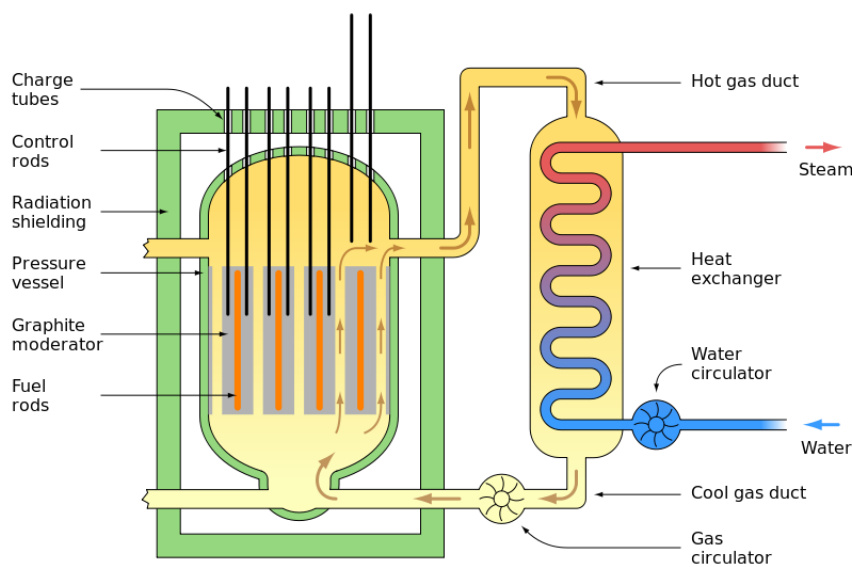


Figure 2.3 Schematic of a Magnox reactor [16]

Magnox reactors were the first civilian stations in the UK, using a magnesium alloy-clad natural uranium fuel. ‘Magnox’ refers to the name of the cladding “*Magnesium non-oxidising*”, and although usually thought of as being just an Mg-Al alloy, Magnox alloy refers to both Al80 and Zr55 alloys (cladding specifications in Table 2.1), though the former is more common (Zr55 has been used in the Bradwell plant [17]).

Table 2.1 Fuel element cladding types for Calder Hall reactors (wt.%) [18]

Alloy	Al	Be	Ca	Fe	Si	Zr	Mn	Zn	Mg
A12 (AL80)	0.7- 0.99	0.002- 0.015	<0.008	<0.006	<0.010	<0.02	<0.005	<0.015	Balance
ZA (ZR55)	<0.02	-	<0.008	<0.006	<0.010	0.45- 0.65	<0.005	<0.015	Balance

Fuel cladding is required to stop the fuel being oxidised by the reactor coolant, to assist in thermal transfer, and to help retain fission products within the fuel. The Magnox alloy also had the advantage of a low cross section for thermal neutrons, allowing natural uranium to be used instead of requiring enrichment [18]. This cladding is very different from that used in the majority of reactors worldwide, resulting in a unique situation for the UK. Typically BWR & PWRs use slightly enriched UO₂ fuel clad in a zirconium alloy (e.g. Zircaloy-4: 98.23% Zr, 1.45% Sn) [19].

Each Magnox plant that has been built is different, although the basic designs are the same. All have steel reactor pressure vessels (RPV) except Wylfa and Oldbury (the last two Magnox builds), which utilise prestressed concrete pressure vessels (later adapted into the AGR designs). Graphite bricks are used as moderators, with pressurised CO₂ as a coolant. The designs were refined between builds to increase power production, with later generations of Magnox and AGR reactors larger, with a higher gas temperature and thermal output than earlier reactors [20].

The Magnox design was initially chosen as it did not require enrichment of uranium, a technology unavailable to Britain at the time. 11 Magnox power stations were built in the UK, containing 26 Magnox reactors [21], the last closing at the end of December 2015 [22] having reached the end of its extended lifetime. Following their construction, a new second generation reactor type began to be built. These were of the AGR type, which operated at higher temperatures, with slightly enriched uranium fuel (~3% ²³⁵U) and subsequently could achieve higher efficiency than Magnox reactors [12]. The UK also operates a sole PWR reactor – Sizewell B, which

operates using water as both primary coolant and moderator, with fuel enriched to ~4% clad in a zirconium alloy [12].

2.2.2 Today

Nuclear reactors are eventually closed down as components age and new technologies become available. This has resulted in many currently operational, and many closed down, nuclear power plants across the UK. These are detailed in Tables 2.2 & 2.3, noting their unit reference power at time of construction, and scheduled end dates (assuming no further life extensions are permitted).

The development of nuclear power within the UK led to the building of a wide range of experimental and test reactors, most of which have been closed and either fully or partially decommissioned (Table 2.4). These have typically been materials testing reactors (MTR) designed to test components and materials in conditions similar to those inside a full-scale reactor, as well as a number of prototype reactors. Many of these prototypes never progressed beyond this stage. These included the Steam Generating Heavy Water Reactor (SGHWR) and the helium cooled high temperature DRAGON reactor. There was also the development of a fast breeder programme, resulting in the Dounreay Fast Reactor (DFR) and Prototype Fast Reactor (PFR), liquid metal cooled breeder reactors designed to safeguard the UK energy supply through closing the fuel cycle by using ^{239}Pu fuel and ‘breeding’ fuel from a ^{238}U or mixed oxide fuel (MOX) blanket.

The UK’s only operational PWR reactor, Sizewell B, is much closer to the type of reactor commonly used around the world. Most reactors worldwide are either PWR or BWR (Boiling Water Reactor) designs – i.e. water cooled, water moderated and using slightly enriched fuel. Pressurising the system enables higher temperatures, and therefore efficiencies to be achieved, although construction is more expensive due to an extra loop required for pressurisation [1]. BWRs are simpler to construct, but are mainly limited to the USA, Japan and Taiwan [7]. Canada runs a fleet of heavy water (D_2O) moderated and cooled reactors (CANDU), Russia uses a combination of graphite moderated water cooled reactors (RBMK) and PWRs (VVER-type), while the UK is unique in almost exclusively using gas cooled, graphite moderated reactors (Magnox & AGR). There also exist a scattering of

experimental reactors past and present, including liquid metal fast breeders, high temperature gas cooled and highly enriched reactors [1, 23].

Table 2.2 Active nuclear reactors (power producing) in the UK [24]

Location	Type	Reactors	Reference unit power (MWe) *	Commercial operation	Scheduled end date [25-27]
Dungeness (B)	AGR	2	520 x 2	1985, 1989	2028
Hartlepool (A)	AGR	2	595, 585	1989	2024
Heysham (A)	AGR	2	585, 575	1989	2024
Heysham (B)	AGR	2	610 x 2	1989	2030
Hinkley Point (B)	AGR	2	470, 475	1976, 1978	2023
Hunterston (B)	AGR	2	475, 485	1976, 1977	2023
Sizewell (B)	PWR	1	1198	1995	2035
Torness	AGR	2	590, 595	1988, 1989	2030

* Reference unit power defined by the IAEA as "...the maximum (electrical) power that could be maintained continuously throughout a prolonged period of operation under reference ambient conditions... after deducting the power taken by unit auxiliaries and the losses in the transformers that are considered integral parts of the unit" [29]

Table 2.3 Shut down nuclear reactors (power producing) in the UK [24]

Location	Type	Reactors	Reference unit power (MWe)	Commercial operation	Shut down
Berkeley	Magnox	2	138 x 2	1962	1988-89
Bradwell	Magnox	2	123 x 2	1962	2002
Calder Hall	Magnox	4	49 x 4	1956-59	2003
Chapelcross	Magnox	4	48 x 4	1959	2004
Dounreay (DFR)	Fast breeder	1	11	1962	1977
Dounreay	Fast	1	234	1976	1994

(PFR)	breeder				
Dungeness (A)	Magnox	2	225 x 2	1965	2006
Hinkley Point (A)	Magnox	2	235 x 2	1965	2000
Hunterston (A)	Magnox	2	150 x 2	1964	1989-90
Oldbury (A)	Magnox	2	217 x 2	1967-68	2011-12
Sizewell (A)	Magnox	2	210 x 2	1966	2006
Trawsfynydd	Magnox	2	195 x 2	1965	1991
Windscale	AGR	1	24	1963	1981
Winfrith	SGHWR*	1	92	1968	1990
Wylfa	Magnox	2	490 x 2	1971-2	2012-15

* Steam Generating Heavy Water Reactor

Table 2.4 Research reactors (non-power producing) in the UK [28] ***

Location / organisation	Name	Type	Reactors	Commission date	Shut down
	ZENITH I	CO ₂ -GCR	1	1959	1972
	ZENITH II	CO ₂ -GCR	1	1972	1975
	NERO (*)	Critical assembly	1	1960	1964
	NESTOR	Argonaut	1	1961	1995
Winfrith	DIMPLE	Pool	1	1962	1995
	ZEBRA	Fast reactor	1	1962	1982
	HECTOR	High temp MTR	1	1963	1976
	JUNO (*)	Critical assembly	1	1964	1973
	DRAGON	He-GCR	1	1964	1976
Harwell	GLEEP	Graphite pile GCR	1	1947	1990
	BEPO	Graphite pile GCR	1	1948	1968

	ZEPHYR	Zero power fast	1	1954	1963
	ZEUS	Zero power fast	1	1955	1957
	DIDO	D ₂ O - MTR	1	1956	1990
	LIDO	Pool	1	1956	1972
	PLUTO	D ₂ O - MTR	1	1957	1990
	HAZEL	HOMOG (L)	1	1957	1958
	DAPHNE	D ₂ O - MTR	1	1962	1967
Windscale	Windscale Piles	Pile GCR	2	1950-51	1957
	HERO	AGR	1	1962	1968
Dounreay	DMTR	D ₂ O - MTR	1	1958	1969
Rolls-Royce	NEPTUNE	Pool	1	1963	-
	HORACE	Critical assembly	1	1958	1976
	MERLIN	Pool	1	1959	1976
	HERALD	MTR	1	1960	1988
	VERA	Critical fast	1	1961	1971
AWE / MOD	JASON (<i>Vulcan</i>)	Argonaut	1	1962	1996
	DSMP1	PWR	1	1965	1984
	VIPER (<i>Vulcan</i>)	Fast burst - MTR	1	1967	2007
	STF	PWR	1	1987	-
ICI - Billingham	TRIGA	Pool type	1	1971	1996

	Scottish				
	University				
	Research	Argonaut	1	1963	1995
	Reactor				
	Queen Mary				
Universities	College	Argonaut	1	1964	1982
	reactor				
	Universities				
	Research	Argonaut	1	1964	1991
	Reactor				
	CONSORT	Pool	1	1965	2011
Nuclear	Berkeley				
electric	Zero Energy	Graphite	1	1966	1988

* NERO reactor modified to become JUNO

*** Excludes ZETA and JET fusion reactors

Alongside these nuclear reactors are a further 27 nuclear submarines, each containing a reactor, either retired (and in varying stages of defueling) or due to be retired by 2030 (excluding an additional 7 Astute class submarines, which are currently being built / commissioned). 11 of these submarines are laid up at Devonport, 7 at Rosyth, with 9 still in active service. All are powered by PWR reactors, which are due to be defueled and the RPVs removed to an interim ILW site before disposal in a national geological disposal facility (GDF) [30], as part of the submarine dismantling process.

The future of nuclear power in the UK is likely to change considerably. All the UK Magnox reactors have closed, with the fleet of AGR reactors increasingly ageing with tentative closure dates within the next 20 years. It is expected that new reactor designs will be built to replace these, based on international designs such as the EPR reactor (PWR), AP-1000 (PWR with passive safety systems) and ABWR (BWR).

Varying international consortia are in the process of licencing these designs for use in the UK, with several sites (Hinkley Point C, Sizewell C and Moorside) earmarked for future reactors [31]. There is the potential for this to be supplemented by CANDU or PRISM reactors depending on the final decision of Pu disposition. Magnox and AGR designs are now considered obsolete, and will no longer be built.

2.3 Nuclear waste

Nuclear waste is a wide term which can apply to any radioactive material produced by or as a consequence of nuclear reactions. This can be solid, liquid or gaseous in form.

As a consequence of nuclear fission, a wide array of fission products are produced, many of which are unstable, undergoing radioactive decay. These fission products have varying chemistries, half-lives and decay mechanisms, making nuclear waste very complicated to deal with. Spent nuclear fuel often contains the largest amount of these fission products, meaning it is both extremely radioactive and also releases heat, requiring cooling for years after removal from reactors. These typically contain most of the radioactivity found in the wastes.

Secondary wastes are typically more bulky, though contain less radioactivity. These can include operational wastes from power plants (ion exchange resins from reactors, contaminated oils and sludges), and liquid effluents. This also includes operational wastes from reprocessing facilities or enrichment plants, as well as lower activity wastes, such as contaminated clothing, gloves and laboratory wastes from handling.

Larger volume, less activated wastes can be produced through the decommissioning process due to contaminated soils, concrete and reactor components (graphite, activated steels).

The types and quantities of various wastes vary from country to country depending on the fleet of reactors which have been operated, the regulatory environment (i.e. how waste is categorised and segregated) and complications from the presence of legacy or defence wastes which might require alternative or entirely separate processing.

2.3.1 Nuclear waste in the UK

The historic use of indigenous reactor designs (Magnox and AGR) for the bulk of the nuclear generation capacity in the UK has contributed to a unique waste situation arising, primarily due to the alternative fuel cladding used and the historic drive towards nuclear fuel reprocessing. The decision to reprocess fuel (initially both for military purposes and for civilian energy security) was part of an initiative to close the fuel cycle, enabling unused uranium from spent fuel to be recycled into new fuels. This was due to be coupled with fast reactors (such as the DFR & PFR), which can utilise a greater portion of the uranium (and plutonium), and would have, in theory, allowed energy independence [1].

Reprocessing in the UK occurs *via* shearing the cladding from spent fuel, dissolving the fuel in nitric acid, then taking the resultant liquor through a solvent extraction process (PUREX: Plutonium Uranium Redox Extraction) to separate out the uranium, plutonium and fission products [3, 32]. The policy of reprocessing has led to a large number of buildings and facilities being built over the years to cool, store and process the fuels and associated secondary wastes arising from this process. Coupled with 60 years of nuclear activities in the UK, and this has created a complex and multifaceted nuclear waste issue for which there is no one solution.

As of 2013 a total of 4.3 million m³ of nuclear waste has been produced in the UK, which requires processing and suitable disposal. This is expected to rise to 4.5 million m³ total after currently operational power stations close, once reprocessing has finished and including continued production of defence wastes [33]. These are not uniform wastes, however, and currently radioactive wastes are designated as either High Level Waste (HLW), Intermediate Level Waste (ILW) or Low Level Waste (LLW), depending on the radioactive content and heat generated from the wastes.

HLW comes from spent nuclear fuel reprocessing, as a liquid waste, and is immobilised in borosilicate glasses *via* vitrification [34] into stainless steel canisters. Typically a glass wastefrom will consist of ~25wt.% calcined waste oxides to 75wt.% glass [35]. Glass is used as an immobilisation matrix due to its good chemical durability, the ability to incorporate a wide range of elements, and

wasteforms that occupy a smaller volume than those resulting from many other immobilisation techniques [3]. These wastes produce considerable heat due to their radioactivity [36]. This vitrification process is in contrast to many other nuclear operating countries, most of which do not operate reprocessing facilities, and are planning to directly dispose of spent nuclear fuel without further processing. This is likely to be the case for new nuclear plants which are due to be built in the UK, and for the currently operational Sizewell B spent fuel.

ILW is waste that has a higher than acceptable activity for waste to be categorised as LLW, but does not generate significant heat [34]. ILW includes fuel cladding, sludges, flocs, ion exchange resins, plutonium contaminated material and miscellaneous activated wastes [35, 37]. An estimated 290,000 m³ of ILW is due to be disposed of in a geological repository, corresponding to ~5% of the current radioactivity (although 7% of the volume, Figure 2.4) of UK higher activity waste, as noted in Figure 2.5. Much of the ILW in the UK is either immobilised, or due to be immobilised, within cementitious systems based on blended Portland cement (PC) matrices [3], although some power station ILW is packaged in containers without cementation [33].

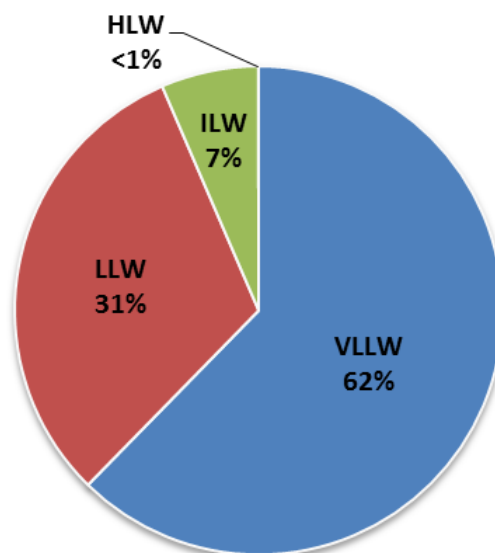


Figure 2.4 Volume of UK waste as of 2013 inventory (including future wastes) [33]

LLW consists of wastes not exceeding 4 GBq per tonne of alpha activity, or 12 GBq per tonne of beta/gamma activity [38]. This usually comprises metals, soils, building rubble and organic materials (such as paper towels and lab equipment) [35, 39], but

also reactor graphite and some ion exchange materials [36]. Much of this material is scheduled for disposal in the Low Level Waste Repository (LLWR), which consists of an engineered shallow disposal facility comprising half-sized ISO freight containers filled with compacted, grouted wastes (Figure 2.6). These containers are stacked on top of one another in concrete lined vaults, and backfilled with clay and other impermeable materials [33].

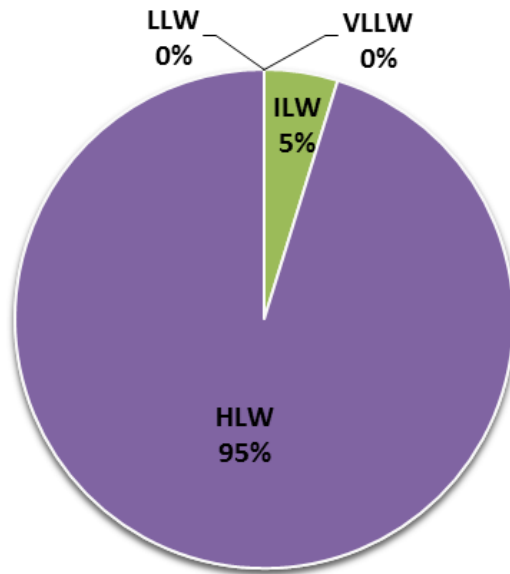


Figure 2.5 Radioactivity of UK waste as of 2013 inventory [35]

There is currently a drive towards reduction in the quantity of LLW to save space in the LLWR *via* a combination of waste prevention, reuse, recycling and volume reduction where possible. This involves a combination of sorting waste before it can become contaminated, decontaminating existing waste (i.e. removing surface contamination from metals or concrete), decay storage, compaction of wastes, and thermal treatment [40].



Figure 2.6 The LLWR near Drigg, Cumbria [34]

A sub-category of LLW is VLLW, which consists of material which is low enough activity that it can be sent to municipal landfill. This can be already low level waste, such as small scale wastes from hospitals or universities which can also be incinerated, or can also consist of larger volume LLW which has been treated to remove much radioactivity, such as metallic LLW and concretes [33, 40]. The bulk of the volume of the wastes produced in the UK (4.5 million m³) consist of VLLW and LLW (Figure 2.4), with HLW only comprising a very small volume of this (1100 m³). However HLW accounts of ~95% of the total radioactivity (78 million of 82 million TBq, Figure 2.5), compared to <0.001 TBq of VLLW (rising to 14 TBq in 2150 due to uranium decay products) [41].

Alongside current wastes, there also needs to be consideration of future waste arising from the continued operation and decommissioning of existing sites. This includes dismantling physical buildings on site, ongoing operational wastes and any contaminated land / groundwater which requires remediation or disposal. This might also include any future wastes from lifetime extensions given to AGR plants, future wastes from MOD submarines, ongoing defence wastes from AWE, and wastes from fuel manufacturing and healthcare. There will also be wastes associated with any future power reactors which might be built, along with the possibility of certain materials (currently non-waste) being reclassified as wastes in the future (e.g. the Pu stockpile, DU, Thorp Product Uranium (TPU) and Hex tails) [42-45].

2.4 Geological disposal

Due to the long-lived radioactive nature of many of these wastes, their safe management and disposal is of paramount importance. Most waste management systems involve radionuclide immobilisation in durable, chemically resistant, stable materials which can be easily stored over a long time [32]. Long-term waste management options investigated worldwide include above ground storage, deep borehole disposal, sea disposal, disposal in ice sheets and even disposal in outer space [46-48]. Many of these routes, however, are now banned under international laws regarding dumping at sea, in the Antarctic or in space [49].

The general consensus worldwide is that deep geological disposal in a multi-barrier system is the preferred option [3, 50]. The USA hosts the world's only currently operational geological disposal facility for higher activity wastes, at WIPP, in New Mexico, which is currently accepting defence wastes. Finland, France, Germany, China, Russia and South Korea are amongst the countries which have either submitted applications to begin building, are actively studying sites, or have begun construction of a geological repository. Many other countries have a policy of long-term storage of waste before making a decision on the disposal route [49].

2.4.1 Geological disposal in the UK

In the UK a Geological Disposal Facility (GDF) is to be the end state for higher activity wastes [36, 51], which will be designed to isolate waste from the biosphere, and to contain radionuclides within the waste packages.

Recently the Committee on Radioactive Waste Management (CoRWM), the independent advisory panel to the UK government, reiterated support for a geological repository, stating [52]:

“Within the present state of knowledge, CoRWM considers geological disposal to be the best available approach to the long-term management of all the material categorised as waste in CoRWM’s inventory when compared with the risks associated with other methods of management. The aim should be to progress to disposal as soon as practicable, consistent with developing and maintaining public and stakeholder confidence.”

This repository will be built between 200 – 1000 metres deep in a suitable geology, with wastes being placed into underground vaults and tunnels [36]. Both engineered and natural barriers are used as part of a multi-barrier system which include; the wasteform (e.g. glass), the waste container (e.g. copper or carbon steel), the backfill (e.g. cement or bentonite clay) and the geosphere (e.g. high strength rocks, evaporates, etc.) [50, 53], all of which help to create a defence in depth where the multiple barriers are highly unlikely to all fail. Figure 2.7 demonstrates a generic layout for a GDF in the UK, with further concepts for immobilisation in higher strength rock in Figure 2.8, showing how physical, geological and chemical properties help to retain waste within the GDF.

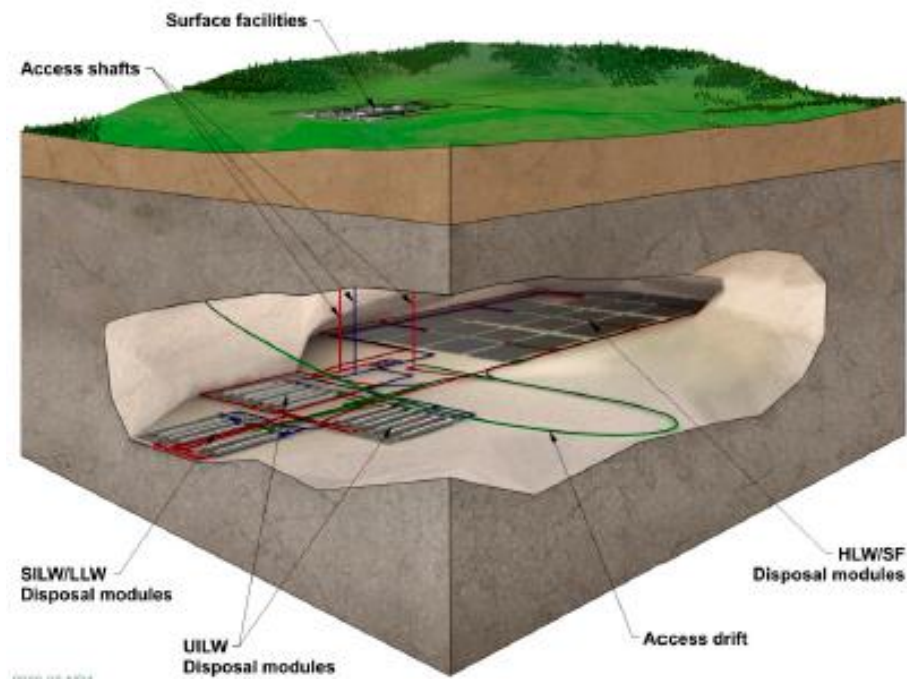


Figure 2.7 Layout of a generic GDF for all UK HAW [54]

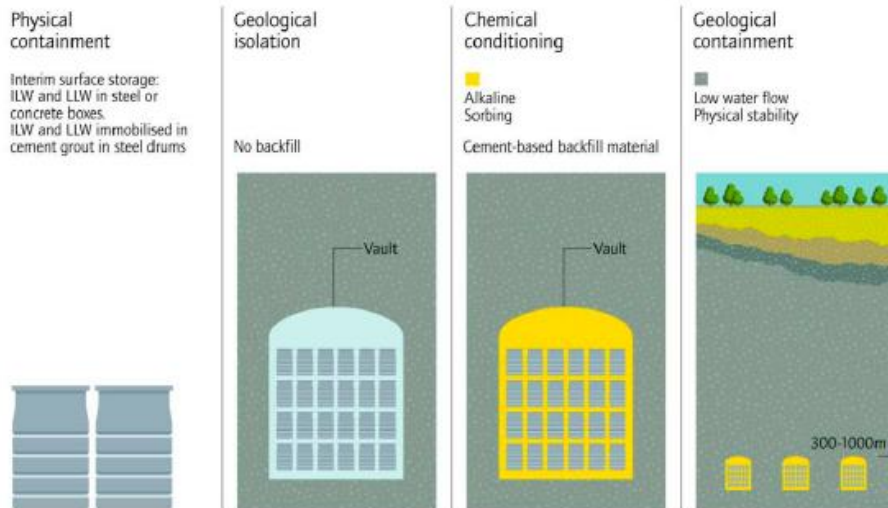


Figure 2.8 Concept for LLW & ILW in higher strength rock [55]

The UK concept is slightly different from many international concepts, as the waste inventory contains a large proportion of ILW waste immobilised in cementitious matrices. The high pH near-field condition caused by these packages within a saturated repository is likely to react with a clay backfill [56-57] (the standard backfill for repository designs [58]) and has necessitated the development of a cementitious backfill instead [59]. The UK design would potentially consist of a repository with two areas, one for ILW disposal in a cemented backfill, the other for HLW disposal in a more conventional clay backfill [60-61].

2.5 Waste treatment

2.5.1 Vitrification

In the UK, spent fuel from nuclear power plants (Magnox & AGR) is typically removed from reactors and cooled in ponds for ~180 days prior to transportation to Sellafield for processing, where it is further cooled before reprocessing. AGR fuel and light water reactor fuels (e.g. PWR/BWR fuel) from international customers are processed at the THERmal Oxide Reprocessing Plant (THORP), while Magnox fuel is sent to the Magnox reprocessing plant [62].

These plants de-can the fuels, shearing off the cladding (resulting in production of metallic swarf) and dissolving the fuel in nitric acid. This is then subject to a solvent extraction process (PUREX) to separate uranium, plutonium and the fission products. These fission products remain in a nitric liquor (called highly active liquor (HAL)), and are sent for vitrification [35, 62]. The decanning swarf from this process is diverted to cementation plants as ILW waste, or stored in silos.

The HAL streams contain ~99% of the radioactivity initially within the spent fuel. They are evaporated to reduce their volume, then calcined to produce a dry oxide powder. This is mixed with glass frit and heated to ~1200 °C, turning them into a glassy material. This is poured in a stainless steel canister, allowed to cool and harden, and transported to an engineered facility (Vitrified High Level Waste Store, Figure 2.9) until a geological repository is opened [62].



Figure 2.9 Vitrified high level waste store at Sellafield [33]

The rationale behind vitrification is a combination of volume reduction, physical immobilisation, chemical immobilisation and durability. Once produced, vitrified products are typically 1/3 the volume of the liquor, and immobilised within a solid matrix rather than remaining aqueous [35, 62]. The UK uses an alkali borosilicate glass matrix, which has long term durability (important for long-live radionuclides) and an ability to incorporate a wide range of elements within a glassy structure, without forming unwanted secondary crystalline phases [28, 58]. This chemically immobilises the radionuclides within the structure, rather than simply encasing them.

2.5.2 Cementation

Although there are many technologies available or in development for the safe immobilisation of ILW and LLW wastes, cementation within blended Portland cements is the current baseline route for much encapsulation in the UK [33]. As noted earlier, this includes a wide range of sludges, flocs, metallic swarf and ion exchange resins.

Blended Portland cement matrices have been chosen as the preferred medium of encapsulation for much ILW waste within the UK. As an encapsulation matrix Portland cement has many advantages [3, 63-64] including:

- Diffusion barrier due to sorption and reaction sites for radionuclides
- High pH environment which decreases radionuclide solubility
- Ability to convert dangerous / mobile wastes into a more solid form
- Providing radiation shielding
- Ambient temperature processing
- Low cost and flexible towards waste streams

The UK nuclear industry typically uses composite cements with partial replacement of PC with blast furnace slag (BFS) and pulverised fuel ash (PFA, also known internationally as fly ash) [65], especially for the production of wasteform monoliths (three different wasteforms are displayed in Figure 2.10). These composite cement systems offer a lower heat of hydration [63], reduced cracking [66-67] and reduced porosity whilst maintaining wasteform integrity.

The specifications for the performance of the cementitious grouts varies according to the wastes processed and from plant to plant. Open literature on the absolute requirements for each facility are sparse, however some literature exists. Table 2.5 key parameters for encapsulation grout at the Magnox Encapsulation Plant (MEP). This is typical of the requirement for a fluid grout which can penetrate complex wastes (such as Magnox swarf), a reduced heat output and a suitable curing time [68-69].

Table 2.5 Key process parameters for MEP encapsulation grout [68]

Operating condition	Control range
Matrix grout	
BFS/OPC ratio	2.33 to 9.00
Water/solids wt. ratio	0.31 to 0.37
Grout temperature	≤30°C
Grout fluidity	≥200mm Colflow
Curing time	≥10 hrs
Capping grout	
PFA/OPC ratio	2.33 to 4.00
Water/Solids wt. ratio	0.41 to 0.45
Grout temperature	≥40°C
Grout Fluidity	≥400mm Colflow
Curing time	≥12 hrs
Capping grout delivered to drum	≥30kg
Magnox Swarf Filling	
Waste loading	75 kg to 310 kg
Drum vibration	≥25Hz for first 70% of infill ≥10Hz for remaining 30%
Residual water level	<55mm in base of drum

Other than these, the produced wastes are required to conform to specifications for waste disposal, though much of the physical requirements are undertaken by the steel waste packages themselves rather than the cementitious wasteform [70-72], and the proposed engineered barriers within a final disposal facility [53, 60, 73]

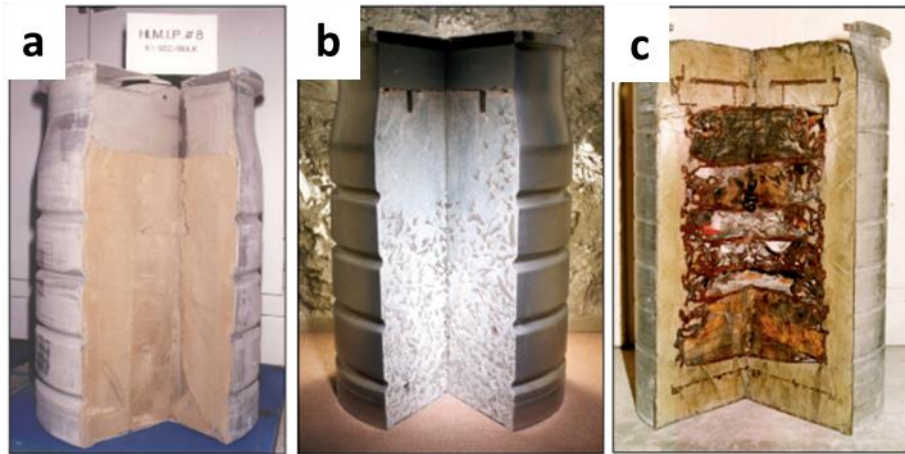


Figure 2.10 a) in-drum mixed wasteform, b) in-container grouted wasteform, c) annular grouted wasteform [53]

Waste packages themselves have tight specifications, with limits on radioactive dose rates, heat output, gas generation and a target of 500 years integrity of the waste container [70]. They must meet a minimum strength for transport [74] and further requirements such as fire resistance, mechanical properties, impact integrity, and other key characteristics, while being designed to immobilise radionuclide and toxic materials [71]. The cement system must also be tolerant of plant variability and variable waste streams to ensure a reliable wasteform [75]. There are, however, certain restrictions to ensure cement solidification, most notably that wastes should not contain oxidising agents, acids, organic materials, complexant or chelating agents, non-aqueous liquid phases and other materials detrimental to chemical containment [71].

There are various plants on sites throughout the UK for cementation of ILW, including but not limited to:

- Sellafield: [76]
 - MEP (Magnox Encapsulation Plant)
 - Magnox swarf
 - Possibility for future legacy pond and silo wastes
 - WEP (Waste Encapsulation Plant)
 - Thorp SS / zircaloy hulls & historic ILW

- WPEP (Waste Packaging and Encapsulation Plant [Figure 2.11])
 - EARP floc (ferric hydroxide / Al-Fe flocs)
- WTC (Waste Treatment Complex)
 - PCM supercompaction and grouting
- Dounreay:
 - PFR & MTR raffinate cementation [77]
- Trawsfynydd: [78]
 - MAC (Miscellaneous Activated Components) Plant
 - Solid activated waste
 - TILWSP (Transportable ILW Solidification Plant)
 - Resins, sludges, dessicants and other operational wastes

The WTC is unique in that cementation of plutonium contaminated material (PCM) allows these wastes to be reclassified as LLW and sent to the LLWR rather than remaining as part of the ILW inventory.



Figure 2.11 WPEP at Sellafield [34]

These plants produce cemented wasteforms as either 500 L drums or 3 m³ boxes, as shown in Figure 2.12, providing easier handling and stackable waste packages. The cementation process can be implemented *via* in-drum mixing, with cement mixed before pouring into a drum containing waste; *via* in-container mixing in which a sacrificial paddle is inserted into the drum along with cement and the waste, mixed and left in place; or *via* annular grouting of compacted materials [64, 68].

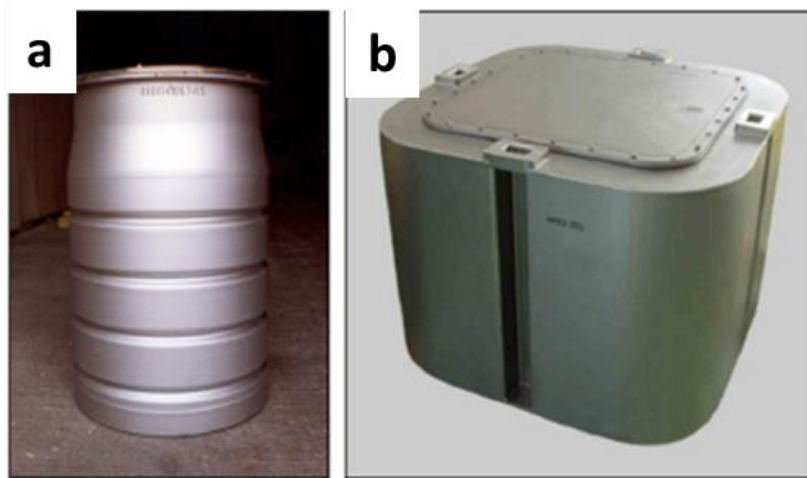


Figure 2.12 UK ILW packages: a) 500 litre drum and b) 3 m³ box [54]

Known issues with cementation include volume increase, problems with waste-cement interactions, and difficulty ensuring security of powder supply.

Volume increase is a particular issue, as ILW wastes and cement grout are often bulky. Unless wastes are incinerated or compacted beforehand, cementation potentially greatly increases the volume of the conditioned wastes, contributing to the cost and size of a final repository, and interim storage [79].

Waste-cement interactions are a problem for cementitious materials. Certain reactive metals such as uranium and aluminium are known to cause expansive cracking in wasteforms due to corrosion in the high-pH and free-water environment within the cement [63, 80]. Flocs, salts, oils and organics are known to cause formation of altered phases or to affect cement setting, potentially affecting durability or viability as a wasteform [81-84].

Security of powder supply is another major issue. Blended PC systems use large quantities of blast furnace slag and fly ash, which are industrial by-products. Much of the heavy industry in the UK has declined, and continues to decline, and coal combustion is being phased out, affecting the availability of these materials within the tight product specifications required. These materials and the Portland cement

itself need to be produced to tight guidelines so that future properties can be accurately predicted [68].

2.5.3 Alternative ILW immobilisation technologies

Although Portland cement blended systems are currently the preferred technology choice for ILW in the UK, around the world a wide range of immobilisation techniques and materials are used for nuclear wastes immobilisation, including: bitumen, organic polymers, phosphate ceramics, synthetic zeolites, glass and glass ceramics [74, 85]. For ILW wastes several technologies have been employed on an industrial scale, largely based around bitumen, cement or polymer matrices [64, 85].

Bitumen finds common usage in France and Belgium [74, 86], for low and intermediate level wastes [85, 87]. Bitumen has very low water permeability and can handle high waste loadings of liquids and sludges. However, due to concerns about flammability [53], potential interactions of organic degradation products with radionuclides, and swelling with certain hygroscopic wastes [88], bitumen is not used for routine encapsulation of wastes in the UK.

Polymer encapsulation is, however, used for certain wastes, with vinyl ester styrene and epoxy already used for some waste encapsulation and trials in UK (Figure 2.13). Polymer encapsulation can achieve high waste loadings, low permeability and a chemically inert environment. However, unlike cement it has no high pH barrier and modest radiation resistance, which could generate non-aqueous liquids, aiding migration of radionuclides [89].



Figure 2.13 Epoxy encapsulation trials of Pile fuel [90]

Alternative cement systems have been studied and find some usage for problematic waste streams such as reactive metals and volatiles. Magnesium phosphate cements/ceramics have been studied for metallic ILW encapsulation [69, 91] due to their lower internal pH and lower free water content, which reduces hydrogen generation. They have also been studied for other problematic waste streams, such as incinerator wastes [92], caesium containing resins [93], LLW with high lead content [94], Tc bearing wastes [95] and Pu wastes [96]. Some of these have benefitted from the addition of reducing salts, enhancing the retention of redox sensitive radionuclides.

Other cement systems for waste encapsulation include Alkali-Activated Slag Cements (AASC) [97-98], activated fly ash [99], and calcium aluminate / calcium sulphoaluminate systems [69, 100-101]. All of these offer some potential advantages over Portland cement systems in particular applications, such as reduced pH, precipitation of phases which can lock-up specific radionuclides, or a more chemically reducing environment.

Geopolymer based cements are another interesting addition to the suite of materials for ILW immobilisation. These are aluminosilicate binders produced from the reaction of a solid aluminosilicate source (such as metakaolin or low calcium fly ash) with an alkaline activator (such as sodium silicate/hydroxide). These can produce amorphous / poorly crystalline binders, which can also form zeolites throughout depending on the composition. These have been trialled for various wastestreams which are problematic for conventional Portland based cements, such as borated wastes and wastes high in calcium [102-103]. These can cause flash setting in Portland cements. Nitrate rich wastes (such as Hanford Tank wastes in the USA) have been simulated in geopolymer binders, with nitrates incorporated into nitrated sodalite zeolites [103]. Similar geopolymers have found some success immobilising wastes rich in Cs, which is typically highly mobile in conventional PC systems [100, 103-105].

2.6 Magnox sludges

As part of the nuclear fuel reprocessing process, spent nuclear fuel typically undergoes cooling for several years to allow short-lived fission products to decay. In the UK this is undertaken in engineered facilities on the Sellafield site once fuel has been received from domestic or international power plants.

During the 1950-60's the First Generation Magnox Storage Pond (FGMSP) was constructed for the storage and cooling of spent Magnox fuel before reprocessing. A long reprocessing shutdown in 1974 led to extended fuel retention times in the outdoor storage ponds, increasing fuel corrosion and slowing decanning due to poor visibility [62, 106]. This was caused by the reaction of the metallic magnesium cladding reacting with the water, as in Eq. 2.2, resulting in magnesium hydroxide and hydrogen formation. This $\text{Mg}(\text{OH})_2$ rich Sludge has since built up due to extended corrosion of the fuel cladding, along with fuel fragments, skips and debris blown into the exposed pond, shown in Figure 2.16.



Figure 2.16 First Generation Magnox Storage Pond [76]

In 2013 it was estimated there was 1487 m³ of pond sludge in the FGMSP [107], mainly constituting $\text{Mg}(\text{OH})_2$ sludge with some corroded uranium, hydrotalcite ($\text{Mg}_6\text{Al}_2(\text{CO}_3)(\text{OH})_{16}\cdot 4\text{H}_2\text{O}$) [108] and artinite ($\text{Mg}_2\text{CO}_3(\text{OH})_2\cdot 3\text{H}_2\text{O}$) [109]. Figure 2.17 shows images of the sludge *in-situ* in the pond.

Table 2.5 Key nuclides within Magnox fuel storage pond sludge [110]

Nuclide	Specific activity (TBq/m³)
Cl-36	1.04e-04
Co-60	9.54e-04
Se-79	1.72e-05
Sr-90	1.27e+01
Zr-93	8.00e-04
Tc-99	1.30e-02
I-129	1.00e-05
Cs-134	4.02e-05
Cs-137	3.53e+00
U-234	9.12e-04
U-235	2.60e-05
U-238	1.00e-03
Pu-238	3.35e-01
Pu-239	4.70e-01
Pu-240	5.90e-01
Pu-241	1.03e+01
Am-241	1.88e+00
Total α	3.39e+00
Total β/λ	2.65e+01

The sludge is highly radioactive (3.39 TBq/m³ total α , 26.5 TBq/m³ total β/λ) [107] with a large amount of mixed radionuclides, including significant quantities of ⁹⁰Sr, ¹³⁷Cs and ²⁴¹Pu [107], as noted in Table 2.5. This quantity of ²⁴¹Pu will result in a significant ingrowth of ²⁴¹Am and ²³⁷Np over time.



Figure 2.17 First generation Magnox storage pond sludge [111]

The precise characteristics of Magnox sludge are difficult to determine due to the highly heterogeneous nature of the material over various facilities, combined with the difficulty in analysing highly active samples. Gregson, et al. provide some of the best openly available information on this material. Their work analysed active sludges from various facilities. Selected SEM images of sludges are shown in Figure 2.18 from the fuel storage ponds, showing a characteristic platey morphology of $Mg(OH)_2$ interlocking platelets and colloids. The particle size of the sludges varied from sample to sample, typically 5-25 μm , but also containing smaller 1-2 μm clusters of platelets. The platelets exhibited a hexagonal morphology, typically 20-40nm in diameter each. Alongside this was various iron oxide particles, and also particles/clusters <50nm-5 μm of uranium oxide, along with hydrotalcite [108].

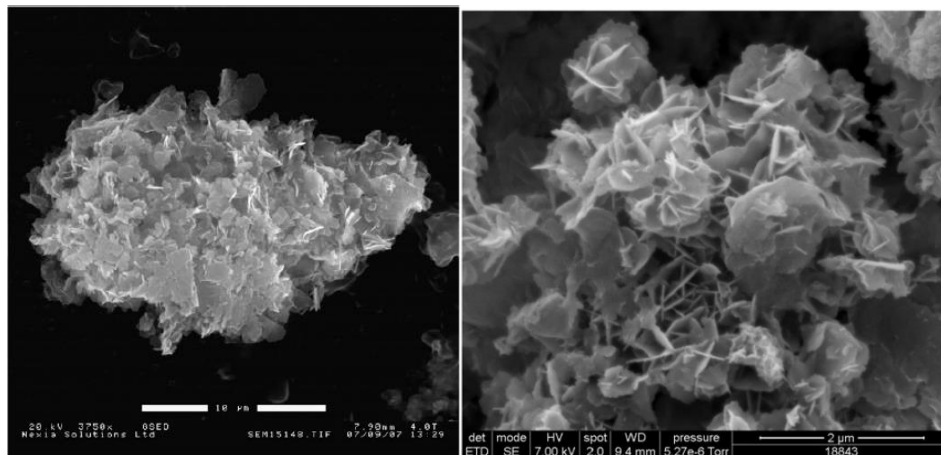


Figure 2.18 SEM images of Magnox sludges from [108]

Another source of Magnox sludges within the Sellafield site is the Magnox Swarf Storage Silos (MSSS). These consist of multiple silos constructed to hold decanned Magnox swarf and other miscellaneous beta-gamma wastes from the First Generation Magnox Storage Pond (FGMSP), Fuel Handling Plant (FHP) and various post-operative cleanout (POCO) operations [112]. They were constructed in the 1960's-1980's, with 6 wet silos by 1964, rising to 22 by 1983. By the early 1990's the use of these silos was phased out with the introduction of direct encapsulation of Magnox swarf in cementitious grout in the Magnox Encapsulation Plant (MEP) [112]. The last waste was received by this facility in 2000 [113].

The decommissioning of this facility involved removal of liquids, which are sent to SIXEP, then removal of silo waste for export to SDEP for immobilisation in 3m³ boxes [112, 114]. Mechanical retrieval machines are currently being emplaced on top of the silos, and encapsulation facilities (SDP/SDEP & BEP) are due to be available by 2027 and 2021 respectively [113, 115].

2.6.1 Other sources of Magnox sludge

Various other facilities involved in Magnox handling, reprocessing or effluent treatment past and present now contain significant quantities of highly active sludge. Some of these are legacy facilities which are currently undergoing hazard reduction operations and decommissioning. Identified waste streams containing large quantities of Magnox sludge are:

- Sludge settling tank – 26.5 m³ (100% sludge) [116]
- Decanner settling tank sludge – 35 m³ (100% sludge) [117]
- Settling pond sludge – 75 m³ (mostly sludge, 3% uranium) [118]
- Sludge from sand filters and transfers – 891 m³ (100% sludge)[119]
- Fuel handling plant sludges – 14 m³ (100% sludge) [120]

All these waste streams are active, some highly so, with a variety of fission products contributing to the activity. Figure 2.19 shows two pictures of the heterogeneous nature of the sludges.

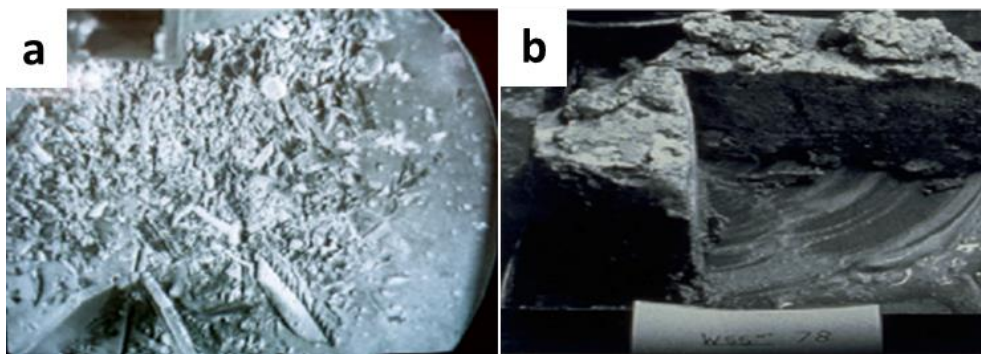


Figure 2.19 a) Partially corroded swarf & Mg(OH)₂ sludge, b) Magnox sludge [121]

Some further waste streams containing Magnox sludge also contain an assortment of other wastes including solid Magnox debris, fuel (U & UO₂), steel, pipework, swarf

bins and often other mixed beta/gamma waste. This has resulted in a challenging disposal situation, where wastes might need to be screened and sorted prior to encapsulation. In total there is ~2528 m³ of Magnox sludge wastes alone, plus a further ~9448 m³ of other wastes which contain 15-39 wt. % Magnox sludges. Many of these are defined as Magnox cladding & miscellaneous solid waste streams resulting from decladding operations in various facilities:

- Magnox cladding and miscellaneous solid waste [2D35] – 738 m³ [122]
 - 79% Magnox, 15% Mg(OH)₂, 5% fuel
- Magnox cladding and miscellaneous solid waste [2D24] – 1370 m³ [123]
 - 25% Magnox, 17% Mg(OH)₂, 44% water, 13% uranium
- Magnox cladding and miscellaneous solid waste [2D22] – 1040 m³ [124]
 - 21% Magnox, 25% Mg(OH)₂, 44% water, 8% fuel, 1% aggregate)
- Magnox cladding and miscellaneous solid waste [2D09] – 2850 m³ [125]
 - (38% Mg(OH)₂, 35% water, 13% MBGW, 8% Magnox and fuel furniture, 5% uranium, 1% aluminium, 1% aggregate)
- Magnox cladding and miscellaneous solid waste [2D08] – 3450 m³ [126]
 - (41% water, 39% Mg(OH)₂, 14% MBGW, 3% Magnox and fuel furniture, 3% uranium, 1% aggregate)

2.6.2 Magnox sludge encapsulation

Due to the quantities of Magnox sludge and the deteriorating facilities where the wastes are currently stored, hazard reduction and retrieval of sludges is a decommissioning priority. The FGMSP is a particular priority, with a target for clean-up of 2048 at the cost of £4-5 billion for overall retrieval into interim storage and decommissioning [106].

Immobilisation plans for Magnox sludge have yet to be finalised, though an interim sludge packaging plant (SPP1) has been constructed to interim store retrieved wastes [127-128]. This removes the sludges into a new, more stable building ready for disposal options. The FGMSP sludge is expected to be immobilised in 3m³ boxes [62] *via* cementation using the box encapsulation plant (BEP), although these plans are subject to ongoing review. It is proposed that sludges will be dewatered,

compacted into pucks and grouted using a PC matrix into the boxes for long-term storage [76].

2.6.3 Alternative processing techniques

Various advanced processing techniques have been assessed for Magnox sludge encapsulation, many being pilot-plant level technologies. Hot Isostatic Pressing (HIP) has been researched by the Australian Nuclear Science and Technology Organisation (ANSTO), using a sand-clinoptilolite and Magnox sludge blend for pressing [129] into canisters, where sludge was heated to remove water, enabling high waste loadings and a claimed ~60% waste volume reduction.

Vitrification of these wastes has been considered. This would enable volume reduction and immobilisation within a durable glassy wasteform. One such manifestation of this technique was using plasma arc technology, where de-watered sludge was fed (along with some additives) into a plasma reactor, turning the waste stream into a molten glass which is poured into a container to form a stable, vitreous solid [130]. This technology has been claimed to produce a packaged waste 64% smaller than the initial waste volume, with a final packaged product slightly less than one-fifth the size of a cemented product [130]. This technique is further outlined in a patent [131] where it is suggested that Al_2O_3 and/or SiO_2 may be added to Magnox sludge to enable a forsterite and/or cordierite mineral ($\text{MgO}\cdot 2\text{Al}_2\text{O}_3\cdot 5\text{SiO}_2$ / $2\text{MgO}\cdot \text{SiO}_2$) to be formed when molten. Vitrification of Magnox sludge has also been undertaken using a 35% waste loading with glass forming additives (Al_2O_3 , B_2O_3 , Na_2O & SiO_2), resulting in a volume reduction factor of 1.6 for the Magnox waste stream [132].

Another technique aimed to solidify the wastes within their disposal drums *via* direct heating, rather than processing and pouring into a drum. This in-drum mineralisation of Magnox sludge was patented [133], with the concept consisting of heating the sludge and drum at ~600 °C, then adding compounds (i.e. clay, phosphates or silica) to change the composition so that crystalline magnesium minerals are formed [133]. None of these techniques have, however, been scaled up to full plant size to process real Magnox sludges for final disposition. Many have been proven to produce durable solidified monoliths, but have not been continued beyond trial stages.

2.6.4 Cement encapsulation of Magnox sludges

The current policy of Magnox sludge disposal is that of cementitious encapsulation [62], within a suitable steel container (either 500 L drum or 3 m³ box) utilising a blended Portland cement matrix. Although this is the preferred option, little open literature exists on potential waste-cement interactions, the effect on hydration, and the long term stability of waste products resulting from this encapsulation.

One such study, by Hough and Palethorpe, studied the effect of simulant Magnox sludge incorporation in BFS:PC and PFA:PC mixes, alone and in combination with miscellaneous solid components likely to be in sludge holding facilities [134]. The study primarily focussed on the ability to mix the wastes, whether solid wasteforms can be produced, and the curing exotherms. All the samples formed solid monoliths, setting within 48 hours and not resulting in curing temperatures exceeding 100 °C. However, the authors noted that the high pH and water will likely cause corrosion of residual Magnox, uranium and aluminium metals within the wastes, which would ultimately decide the lifetime of the wasteform.

Work by Collier and Milestone looked at the interactions between Mg(OH)₂ sludges and a composite BFS:PC cement. They found little reaction between the sludge and cement, suggestive of encapsulation rather than immobilisation *via* chemical binding within hardened cement [65]. However, the authors cite literature suggesting that Mg can substitute for Ca in C-S-H [135] to form M-S-H, which would immobilise the waste. Shrivastava et al. [136] claimed Mg²⁺ ion exchange with C-S-H at room temperature, whereas other researchers require hydrothermal conditions for Mg to enter C-S-H crystals [137-139]. This is a contrast with the broader body of literature, which argues that Mg actually forms layers of hydrotalcite or other Mg phases alongside C-S-H, not substituting for Ca within the C-S-H structure [140-141]. This was supported by natural mineral studies by Mitsuda [142], showing that Mg cannot enter the tobermorite structure. Recent work by Lothenbach et al. confirmed this theory; having studied C-S-H and M-S-H in tandem, the authors noted that they form separate gels and do not undergo ion exchange between one another [143]. The chemistry and structure of magnesium silicate hydrate phases within cements will be reviewed in more detail in Chapter 3, and addressed throughout the thesis.

2.7 Summary

Nuclear power is widely used throughout the world, and its operation produces various nuclear wastes. In the UK, current and historic nuclear operations (both civilian and defence) have resulted in a large volume of different wastes, each with varying radioactivities, chemical compositions and disposal options. Much of the higher activity waste is vitrified into alkali borosilicate glasses, while intermediate level wastes are typically encapsulated in blended Portland cements. These wastes will be disposed of in an engineered deep geological facility, isolating them from the environment until most of the radioactivity has decayed away. Within these intermediate level wastes is a substantial quantity of Magnox sludges, derived from the corrosion of Magnox cladding over many years in various facilities. This has resulted in a $\text{Mg}(\text{OH})_2$ rich sludge forming at the bottom of pools, ponds and silos, which is rich in various radionuclides. Some of these facilities are currently being decommissioned, with interim storage of these sludges in new build engineered facilities. The sludges will likely be immobilised within conventional blended Portland cements, although alternative technologies exist which are being considered, such as vitrification, which offer significant volume reduction, although have a lower technological maturity than cementation. The process of cementation of these Magnox sludges does appear to be safely immobilising these wastes, although no reactions are observed between the $\text{Mg}(\text{OH})_2$ and the cementitious phases themselves.

3 Review of magnesium cements

This chapter comprises a literature review of existing and historical magnesium based cements, which was published as:

Walling, S.A. & Provis, J. L. (2016) “Magnesia based cements – a journey of 150 years, and cements for the future?”, *Chemical Reviews*, **116** (7), 4170-4204.

3.1 Introduction

3.1.1 Cements based on magnesia

The statement “*everything old is new again*” is certainly relevant to the current status of cements based on magnesia (MgO). The global construction materials industry, which was historically based on an extremely wide range of materials suitable for local conditions and specific applications, moved through the latter half of the 20th century to become almost a monoculture based on the use of PC, with other materials essentially sidelined. With the push for increasing environmental sustainability in the construction industry in the 21st century, we are now facing a situation where the global industry is rediscovering large-scale interest in materials which for decades held largely niche or curiosity value. This has led to the re-invention of a large quantity of information which was previously more widely understood. The key purpose of this review is to bring this information to light in the context of the modern use of magnesia-based cements, integrated with results generated more recently as these materials have come back into focus and utilization. In particular, this synthesis of information demonstrates the value of high-quality chemical and analytical data in designing and specifying these materials.

The dominant form of cement used worldwide is Portland cement (PC), with approximately 4 billion tonnes produced in 2014 [144]. Named in the 19th century due to its apparent visual resemblance to limestone quarried from the Isle of Portland, UK, this cement consists primarily of hydraulic calcium silicate phases, which are produced in a kiln at elevated temperature to produce ‘clinker’, which is then cooled and interground with gypsum. The resulting powder is a hydraulic

cement that will hydrate when combined with water, forming a cohesive, strong and dimensionally stable monolith. Hydrated PC has a high internal pH, generally around 12-13, which holds embedded mild steel reinforcing in a passive state, offering some degree of protection from the corrosive action of aggressive agents such as chlorides [145]. In typical usage, PC is blended with sand to form a mortar, or with fine and coarse aggregate to form a concrete, and can also be blended with a variety of ‘supplementary cementitious materials’ including coal fly ash, blast furnace slag, and other finely divided silicate and aluminosilicate powders, to enhance technical properties, cost and/or environmental credentials. There is an ongoing search for alternatives to PC due to its large CO₂ emissions footprint [146], which comprises around 8% of global anthropogenic Greenhouse gas emissions at present [147]. One class of materials that has been identified as a potential low-CO₂ alternative to PC, and has actually been used in industrial practice for more than 150 years, is the broad group of magnesia-based cements which form the subject of this review.

In recent decades, the major motivation for the development and uptake of magnesia-based cements has been driven from an environmental standpoint. The lower temperatures required for production of MgO compared to the conversion of CaCO₃ to PC, and the energy savings associated with this reduced temperature, have led many to envision magnesia-based cements as being central to the future of eco-friendly cement production. Equally, the ability of MgO to absorb CO₂ from the atmosphere to form a range of carbonates and hydroxy-carbonates lends itself well to the discussion of ‘carbon neutral’ cements, which could potentially absorb close to as much CO₂ during their service life as was emitted during their manufacture. These two interconnected aspects have led to an explosion in interest, both academic and commercial, in the area of magnesia-based cements in recent years.

In the past, magnesia-based cements were seen as a way to utilize abundant local resources, or used for perceived commercial advantages over PC such as desirable aesthetic or mechanical properties. Much impetus has come from workers in locations close to, or companies involved with, magnesium-rich brines such as the Great Salt Lake (Utah, USA), the Chinese salt lakes (Qinghai, Xinjiang and Tibet) and the Dead Sea (Israel/Jordan). However, this geological concentration of magnesium within certain brines and geological formations, which has attracted entrepreneurs and scientists, may prove to be the Achilles heel of magnesium

cements in a global sense. Calcination of magnesite (MgCO_3) is the principal route by which magnesia is obtained for use as a raw material in these cements, but reserves of magnesite are geographically limited, with large scale deposits limited to a handful of countries. In Europe, magnesite is sufficiently scarce and in-demand that it is listed on the 2014 EU ‘Critical Raw Materials’ list [148], even without large-scale production of magnesia-based cements in that region at present. China, North Korea and Russia account for >65% of global declared reserves [149], with China being the largest magnesite producer. Magnesia production can also occur close to saline lakes (themselves geographically limited), or *via* precipitation as $\text{Mg}(\text{OH})_2$ from seawater, although the latter option is considered energy intensive unless the brine is already highly concentrated, e.g. in a desalination operation.

Magnesia-based cements, by definition, use MgO as a building block rather than the CaO which comprises more than 60% of the elemental composition of PC. Due to the substantially different chemistry of MgO compared to CaO, one cannot simply change the feedstock for conventional Ca based cements to produce a directly-corresponding material using the same infrastructure. Comparison of the respective (MgO,CaO)- Al_2O_3 - SiO_2 ternary phase diagrams (Figure 3.1) shows vast differences in chemistry and phase formation. Specifically, there are no magnesium silicate phases formed at high temperature which possess hydraulic properties akin to those which are formed in the calcium-rich region of the CaO- SiO_2 - Al_2O_3 system: tricalcium silicate, dicalcium silicate and tricalcium aluminate (shaded regions in Figure 3.1b) are key hydraulic phases in PC, but have no magnesian analogues in Figure 3.1a.

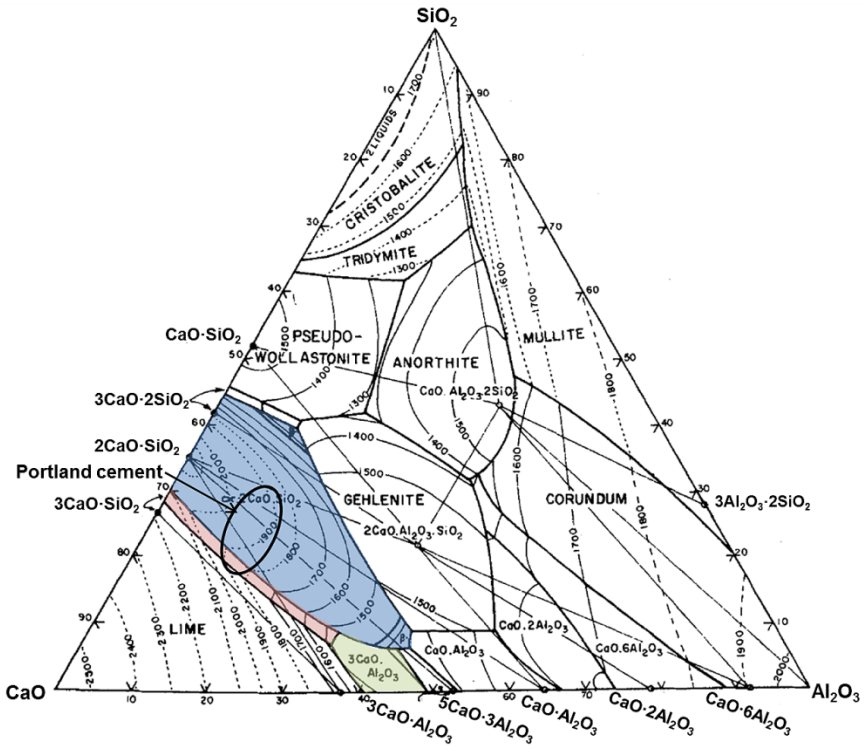
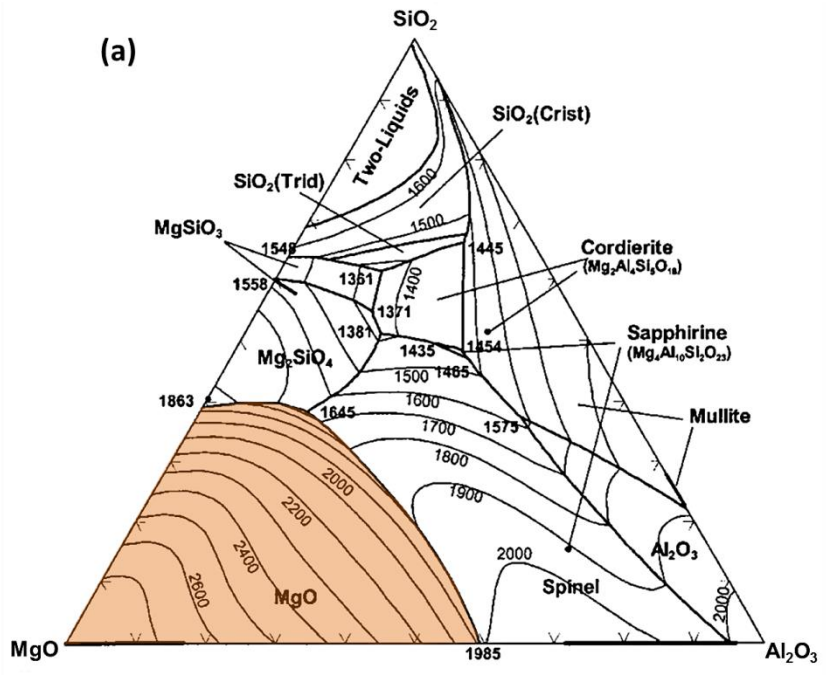


Figure 3.1 Ternary phase diagrams, in units of weight percent, for the systems (a) MgO-SiO₂-Al₂O₃ and (b) CaO-SiO₂-Al₂O₃, adapted from [150-151]

This therefore precludes the direct replacement of CaO in PC manufacture with MgO, and therefore different approaches are required for the development and utilization of magnesium based cements. Some of the possible approaches which have been demonstrated include the combination of carbonates or other oxysalts with MgO to form a solid cohesive mineral gel or mass (a ‘binder’ in cement terminology), and also the production of acid-base cements *via* the reaction between magnesia and acid phosphates. This review will discuss each of these subclasses of magnesium based cements in turn, with a particular focus on understanding the links between the chemistry and applications of each available class of materials.

3.1.2 Magnesia production

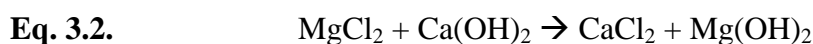
Commercially produced magnesium oxide (commonly referred to as magnesia, or periclase) is not mined directly, as periclase itself is relatively rare in nature and its hydration product brucite (Mg(OH)₂) only occurs in a limited number of commercially viable geological formations. MgO is instead generally obtained either by a dry route from mined magnesite (MgCO₃), or from by a wet route solution *via* magnesium bearing brines and seawater (wet route). The bulk of magnesia production worldwide is achieved *via* calcination of magnesite deposits due to the higher energy requirements for production *via* the wet route. [152-153]

The dry route for magnesia production typically requires the crushing of magnesite before calcination *via* Eq. 3.1. Higher grade magnesia requires careful selection of MgCO₃-bearing rocks, or pre-treatment due to Fe₂O₃ and SiO₂ impurities which can adversely affect refractory usage of MgO [154].



The wet route is more complex in chemical terms, but normally requires the precipitation of magnesium hydroxide from a solution rich in magnesium, typically solution-mining brines or (more dilute) seawater. The former is exemplified at Veendam, Netherlands, where water is injected into a MgCl₂ rich salt formation, and returned to the surface under hydrostatic pressure. Though varying from region to region, seawater contains on average ~1.29-1.35 g/L Mg [155-156], thus constituting

a vast resource of magnesium. The concentrated brines or seawaters can be de-borated *via* ion exchange resins, and sulfate concentrations reduced *via* the addition of CaCl₂ brines to precipitate CaSO₄·2H₂O and yield a purified MgCl₂-rich brine [157-158]. This is then reacted with slaked lime or dolime (Ca(OH)₂ or CaMg(OH)₄, obtained by calcination then hydration of limestone or dolomite respectively) to precipitate magnesium hydroxide according to Eqs. 3.2 and 3.3.



The resultant Mg(OH)₂ slurry is then filtered, washed and calcined to form MgO. This can be briquetted then further sintered if required [159-160].

The wet route can also occur *via* the pyrohydrolysis of magnesium chlorides in superheated steam up to 1000 °C [158, 160]. A current commercial-scale example is the Aman spray roasting process [160-161], Eq. 3.4.



The MgO produced in either wet or dry processes can be further calcined at varying temperatures depending on the end purpose. Increasing the residence time within calciners and increasing temperature reduces MgO surface area, increases crystallite size and reduces reactivity due to sintering [154, 162-165]. This enables a range of magnesia products to be produced depending on the degree of reactivity required. MgO is typically labelled by calcination temperature, which has resulted in varying overlapping definitions. The European Commission has defined grades of MgO as [152]:

- Caustic calcined (600-1300 °C)
- Dead burned (1600-2200 °C)
- Fused (>2800 °C)

While a producer of magnesia [166], in common with much of the technical literature, uses:

- Light burned (700-1000 °C)
- Hard burned (1000-1500 °C)
- Dead burned (1500-2000 °C)

Dead burned magnesia is typically used in the refractories industry to form linings and bricks, principally due to its high melting point. Caustic calcined / light burned magnesia finds a range of applications including as a feed supplement and fertilizer within agriculture, the paper industry, pharmaceuticals, fire proofing, and many more [152, 158]. The reactivity of magnesia tends to decrease with increasing processing temperature, and magnesias processed at the lower end of the light burned range are also described, particularly within the cements community, as ‘reactive magnesia’, see section 2.1.

The determination and optimization of the reactivity of MgO for cement applications has been the subject of much discussion, and a variety of tests are used to determine magnesia reactivity. These include the time taken to neutralize an organic acid, and surface area as determined by gas sorption, iodine adsorption, and other techniques [153, 167-169]. The effect of variations in reactivity due to calcination conditions and magnesia impurities will be further discussed below in relation to the respective magnesium cements presented in this review, as much of the research pertains to the optimization of chemical reaction processes taking place in specific cements.

3.2 Magnesium carbonate and reactive magnesia cements

Magnesium carbonate and reactive magnesia cements have gained significant popularity over the past decade, largely due to concerns over climate change, and particularly the intention and need to mitigate the CO₂ emissions associated with conventional PC manufacture. Magnesium can form a wide range of carbonates and hydroxy-carbonates (Table 3.1), leading some to propose that it is possible to develop large-scale production of cements with reduced CO₂ emissions, or even ‘CO₂ negative’ cements, by uptake of atmospheric CO₂ to form such products [170-172]. Carbonation of magnesia (MgO) can be described in general as the formation of magnesite from MgO *via* uptake of carbon dioxide as in Eq. 3.5, or with the incorporation of water to form nesquehonite as in Eq. 3.6:

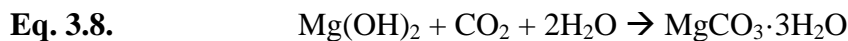


Table 3.1 Magnesium minerals identified in magnesia cements

Mineral	Composition	Density (g/cm³)
Brucite	$\text{Mg}(\text{OH})_2$	2.38 [173]
Magnesite	MgCO_3	3.01 [174]
Nesquehonite	$\text{MgCO}_3 \cdot 3\text{H}_2\text{O}$	1.85 [175]
Lansfordite	$\text{MgCO}_3 \cdot 5\text{H}_2\text{O}$	1.70 [176]
Artinite	$\text{Mg}_2(\text{CO}_3)(\text{OH})_2 \cdot 3\text{H}_2\text{O}$	2.03 [177]
Hydromagnesite	$\text{Mg}_5(\text{CO}_3)_4(\text{OH})_2 \cdot 4\text{H}_2\text{O}$	2.25 [178]
Dypingite	$\text{Mg}_5(\text{CO}_3)_4(\text{OH})_2 \cdot 5\text{H}_2\text{O}$	2.15 [179]
Huntite	$\text{CaMg}_3(\text{CO}_3)_4$	2.70 [180]

3.2.1 Reactive magnesia

The materials described in the technical literature as reactive magnesia cements often involve the addition of fine reactive MgO to conventional PC systems, resulting in the formation of $\text{Mg}(\text{OH})_2$, then subsequent carbonation to a hydrated magnesium carbonate, as exemplified for the case of nesquehonite in Eqs. 3.7 & 3.8.



This cementing system has been envisaged to replace either a large fraction, or the majority, of PC in a binder system, thus resulting in a lower carbon footprint for the cement as a whole. However, regulatory standards currently place tight restrictions on the MgO content of PC-based cements due to the long-term dimensional instability experienced when MgO grains are present within the PC, see Section 3.2.2.

3.2.2 Expansive MgO cements

It should be noted that the materials described as reactive magnesia cements are quite distinct from the use of smaller quantities of reactive magnesia as an expansive additive in cement binders, which is used in dam construction and other large civil engineering projects, particularly in China, to compensate for the slight natural shrinkage of PC during hydration, which can continue for months or years in service [181-182]. The emplacement of large cement/concrete monoliths presents challenges associated with cooling shrinkage of cement paste after hardening. Such large volumes of concrete can reach high temperatures, extending long after the concrete has hardened, up to 6 months after pouring. As the concrete cools it contracts, leaving a dam liable to cracking.

Shrinkage compensating and expansive cements have long been used for various civil engineering projects [183-185]. These are typically based on increasing the aluminate and sulfate concentrations of cements by adding ye'elimite ($\text{Ca}_4\text{Al}_6\text{O}_{12}\text{SO}_4$) and anhydrite (CaSO_4), forming expansive ettringite ($\text{Ca}_6\text{Al}_2(\text{SO}_4)_3(\text{OH})_{12}\cdot 26\text{H}_2\text{O}$) crystals upon hydration [182, 184-186]. Recently cements based on calcium sulfoaluminate, dicalcium silicate and calcium ferrite phases [187-188] have gained interest, with the degree of expansion controlled by water content in the mix. These cements are typically used where it is essential that the cracks do not form upon autogenous or drying shrinkage, such as in water towers, pipes, and runways [189].

In large structural applications, however, where shrinkage is often observed due to cooling after an initial exothermic hydration reaction rather than autogenous or drying shrinkage of the cement hydrates, conventional shrinkage compensating cements are unsuitable, as shrinkage occurs long after the desired expansive products have formed. For this purpose, MgO expansive cements have been gaining momentum. These rely on the expansive hydration of MgO to $\text{Mg}(\text{OH})_2$, resulting in a 117% molar solid volume expansion [190]. The use of MgO requires careful calcination, control of fineness and dosage to ensure that expansion is delayed to occur during cooling, but not so delayed as to cause long term dimensional stability issues within these cements [191-194]. Further details about these expansive

magnesia-containing cements are provided in a concise review by Du [181], and a recent comprehensive review by Mo et al. [195].

3.2.3 Development of reactive magnesia cements

In recent years there has been considerable interest in reactive magnesia cements containing a very high content of MgO, although much of the work has appeared in the patent literature or online sources rather than peer reviewed publications [196-200]. It has been claimed that reactive magnesium cements can be carbon negative [201] when a carbon recycling cement kiln is used in the production of the reactive magnesia, and when also considering the later CO₂ uptake by the cement in service. The US patent awarded to Harrison of the Australian company TecEco, based on a 2001 submission [197], describes the use of extended curing durations and sometimes steam curing to produce strong blocks based on blends of MgO, a pozzolan and PC. The MgO used is produced by calcination of MgCO₃ at a relatively low temperature, ~650 °C, which induces lattice strain and porosity in the MgO particles that would be annealed out if processed at higher temperatures.[154] This enables control of the reactivity of the MgO according to the treatment conditions and particle size, to ensure that it hydrates at the same time as the other cementitious components, and is thus defined as ‘reactive’. Importantly, this MgO reacts much more rapidly than dead burnt sources of MgO (low reactivity MgO calcined >1500 °C), such as the free MgO in Portland clinker, which are fired at much higher temperatures and thus typically hydrate slowly, causing cracking within conventional cements as an expansive chemical reaction is induced locally within a material that has already hardened [202].

It is also claimed [197] that the addition of ferrous sulfate can improve the durability and strength of the reactive magnesia cements. This is likely to be due to the formation of magnesium oxy-sulfate phases (cf. section 6.1) during steam curing, in parallel with the magnesium hydroxides and carbonates.

This line of inquiry was further developed by Vandeperre et al. [203-204] who studied the hydration and microstructure of cements made from coal fly ash (FA) with the addition of up to 50 wt.% (MgO + PC) and confirmed that the addition of reactive MgO does not induce the delayed expansive cracking normally associated

with less-reactive MgO in PC systems. However, lower compressive strengths were observed when MgO was added due to the lower PC content in these mixes, as well as higher water demand and higher porosity. For example, one formulation using commercial super-fine reactive (“XLM”) MgO and FA with the formulation (FA:PC:MgO) 50:50:0 achieved an unconfined compressive strength of 34 MPa. Replacing half of the PC with MgO (50:25:25) gave a strength of 20 MPa, and further reducing the PC content (50:10:40) yielded only 8.5 MPa [204]. The MgO was observed to hydrate to form $\text{Mg}(\text{OH})_2$ alone, with no magnesium carbonate phases detected, resulting in a poorly connected microstructure, as shown in Figure 3.2. The MgO was observed to have no influence on the PC hydrate phases formed up to 35 days of hydration [204]. These studies confirmed that at least during the first month of curing, these reactive MgO-PC blended cements do not take up a measurable quantity of environmental CO_2 and thus are unlikely to be ‘carbon-negative’, or even carbon-neutral, in the short to intermediate term. Cwirzen & Habermehl-Cwirzen [205] also observed that the freeze-thaw resistance, flexural and compressive strengths were reduced due to increased capillary porosity when MgO is added to a PC-based system.

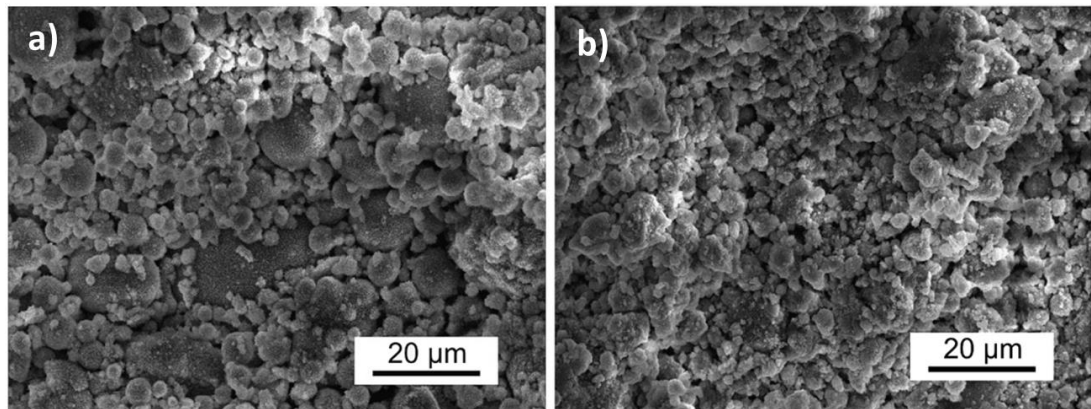


Figure 3.2 Secondary electron micrographs of MgO:FA binders after 14 days curing under ambient conditions with varying compositions: a) 90 FA : 10 MgO, b) 50 MgO : 50 FA, showing little development of a cohesive binding phase in either case [203]

The application of accelerated carbonation curing conditions to reactive MgO systems, however, provided a very different outcome. MgO:PC:FA and MgO:FA systems were exposed to a controlled atmosphere comprising of 5% or 20% CO₂ by volume, at ambient pressure, at both 65% and 95% relative humidity (RH), for 21 days [206]. Samples were pre-cured for 14 days at 98% RH, atmospheric CO₂, then cut into 5 mm thick plates and cured for a further 21 days in the specified environments. Under natural conditions neither of these systems formed magnesium carbonates, however under accelerated carbonation conditions nesquehonite formed in both systems (Table 3.2) along with calcite, CaCO₃, resulting from the carbonation of PC hydration and pozzolanic FA reaction products.

Table 3.2 Key phases identified *via* XRD in FA:PC:MgO samples by Vandeperre et al. [206], after 21 days of curing in controlled CO₂ environments at ambient pressure. X denotes identification of the phase.

Sample (wt. %) FA:PC:MgO	% RH	Vol.% CO ₂	Brucite	Nesquehonite	Calcite
90:0:10	98	0.04	X	-	-
		20	-	X	X
	65	20	X	-	minor
90:5:5	98	0.04	X	-	X
		20	-	X	X
	65	20	-	-	X
50:0:50	98	0.04	X	-	minor
		5	X	X	X
		20	X	X	X
	65	5	X	-	X
		20	X	X	X
50:25:25	98	0.04	X	-	X
		5	X	X	X
		20	X	X	X
	65	5	X	-	X
		20	X	-	X

The proportion of MgO in each cement evidently controlled the ability to form identifiable quantities of carbonated magnesium phases: for the samples containing 90% FA, only at 98% RH and 20% CO₂ was nesquehonite formed. This does, however, show the potential for forming both PC-free and PC containing low-binder materials which can then be carbonated. The samples containing 50% FA were more amenable to carbonation, with the PC-free system (50:0:50) producing substantial amounts of nesquehonite at both 5% and 20% CO₂ and 98% RH, although 20% CO₂ was required in a lower humidity environment (65% RH). The addition of PC to this system reduced carbonation of the magnesium-containing phases, requiring a 98% RH environment to form nesquehonite, although this was achieved with both 5% and 20% CO₂ concentrations. This demonstrates that carbonation of these reactive magnesia cements is possible, both when formulated PC-free and containing PC, however greatly increased levels of CO₂ are required during curing, and control of humidity is paramount.

The PC-free system (MgO:FA) showed a significant increase in fracture toughness in three-point bending geometry following accelerated carbonation when compared to the low values of toughness obtained under natural curing conditions, while the physical properties of the MgO:PC:FA systems appeared unaffected by carbonation [206]. It must, however, be noted that these samples were thin plates (5 mm thick), which are much more amenable to accelerated carbonation than units with a higher wall thickness such as blocks due to limitations on the diffusion rate of CO₂ into a thicker element.

Unfortunately, there have been no published long-term studies of reactive magnesia cements, meaning that the durability performance of these materials is difficult to validate. Specifically, it is unclear whether the Mg(OH)₂ formed within the MgO:PC systems will actually undergo the postulated carbonation processes over a timeframe of several years under natural atmospheric exposure conditions. If not, this calls into question the overall environmental advantages of reactive magnesia cements without the implementation of accelerated carbonation.

Recently, studies on reactive magnesia have been undertaken by Mo & Panesar, who focused on the accelerated carbonation of MgO:PC blends with and without addition of ground granulated blast furnace slag (BFS) [207-209]. These cements contain up

to 40 wt.% MgO, with the major carbonate phases formed being nesquehonite, calcite and aragonite. These studies employed rather extreme carbonation conditions for cements: samples were vacuum dried to remove capillary moisture, before being exposed to a 99.9% CO₂, 98% RH atmosphere, enabling rapid carbonation of the specimens. It was claimed that the presence of MgO altered the calcite formation, resulting in formation of a magnesian calcite, which along with the deposition of nesquehonite reduced sample porosity, densifying the microstructure and increasing microhardness. Due to the relatively extreme carbonation conditions, it remains to be determined whether this carbonation regime could be employed on a commercial scale or is viable in larger products.

There does remain open discussion about the role of Mg during the formation of calcite in carbonation of MgO-containing PC systems. Although the formation of magnesian calcite has been claimed by Mo & Panesar, the work of Vandeperre et al. [203, 206] did not indicate the incorporation of Mg within calcite during atmospheric or mildly accelerated carbonation of reactive magnesia cements. The effect of Mg:Ca ratios on the formation of calcite and related CaCO₃ polymorphs (vaterite and aragonite) are the subject of extensive literature with regards to seawater: increasing Mg:Ca ratios are known to influence aragonite formation instead of calcite in seawater, and magnesian calcites can precipitate from Mg-enriched seawaters and chloride solutions [210-216]. However, due to the low solubility of Mg in carbonate-enriched alkaline media, the mechanisms taking place in cementitious systems may differ, and this requires further analysis.

Questions have also been raised about the thermodynamic stability of nesquehonite, which is identified as the main hydrous magnesium carbonate binding phase in many reactive magnesia cements. Nesquehonite itself has been widely studied as a mineral phase for carbon sequestration (along with magnesite and hydromagnesite) within geological formations and Mg bearing wastes [217-222] due to the ready formation of nesquehonite by interaction of magnesium-bearing minerals and CO₂. Claims have been made that nesquehonite is a stable product up to ~100°C [223-224], but others have asserted that nesquehonite is instead metastable [225]. Recent research on nesquehonite highlights the differing effects of the analytical conditions under which nesquehonite is studied on its reported thermal stability. There is compelling evidence that dehydration can occur <100 °C [226], with mass loss beginning at 55

°C [227] under an atmosphere of flowing nitrogen, while decomposition in water can occur at ~50 °C [228]. Several studies have also noted the transformation of nesquehonite to hydromagnesite at ~52 °C [229-230].

Earlier experimental research by Robie & Hemingway has indicated that nesquehonite is unstable at room temperature, decomposing to release CO₂ and H₂O over time when it is held under ambient CO₂ conditions [231]. The authors sealed a 43 g sample in a flask with a rubber stopper, which upon opening four months later was reported to be “...accompanied by a violent expulsion of gas and some sample, much like that of a bottle of warm champagne which had been shaken before opening.” [231]. In 1999 Königsberger undertook thermodynamic modelling of the MgO-CO₂-H₂O system, concluding that under conditions of $P_{\text{CO}_2} \leq 1\text{atm}$, nesquehonite is never more stable than hydromagnesite [232]. Recent thermodynamic calculations by Chaka & Felmy are in agreement with these observations, indicating that hydromagnesite is more stable at room temperature [233]. This has been recently discussed in the context of reactive magnesia cements [234], concluding that caution is required in the application of such cementing systems, as the changes in crystal composition, volume and morphology which would take place during conversion of nesquehonite into hydromagnesite may be expected to fundamentally weaken the structure of these binders during their service life (cf. densities in Table 3.1), as well as leading to dimensional instability of the materials as a whole (Figure 3.3.).

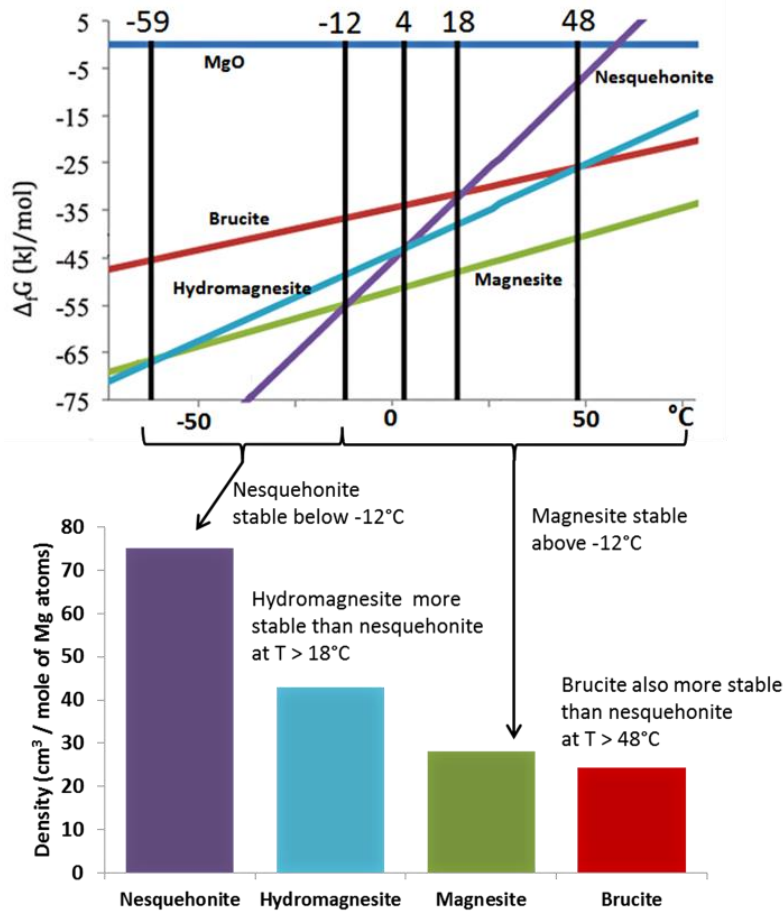


Figure 3.3 Free energy phase diagram for hydrous magnesium carbonates per mole of Mg [234] adapted from Chaka and Felmy [233], under conditions of $p\text{CO}_2 = 400$ ppm and $p\text{H}_2\text{O} = 32$ mbar (saturation vapour pressure at 298 K), along with the density per mole of Mg atoms of stable magnesium phases

3.2.4 Carbonated magnesia blocks

The formation of PC-free carbonated MgO binders was demonstrated by Dheilily, et al. [235] who studied the influence of $\text{Mg}(\text{OH})_2$ in lime mortars. This study involved three mortar formulations; $\text{Ca}(\text{OH})_2$ only, 50:50 $\text{Ca}(\text{OH})_2:\text{Mg}(\text{OH})_2$ blend, and $\text{Mg}(\text{OH})_2$ only, which were cured for 120 days either in air or in a CO_2 atmosphere (98% RH). Higher compressive strengths were obtained in the $\text{Mg}(\text{OH})_2$ only mortars (8.1 MPa) after carbonation than in the $\text{Ca}(\text{OH})_2$ only mortars (5.3 MPa). This was credited to the precipitation of hydromagnesite in the higher strength mortars *via* carbonation of $\text{Mg}(\text{OH})_2$, forming an interlocking network which

improved cohesion. De Silva et al. [236] also studied compacted $\text{Mg}(\text{OH})_2/\text{Ca}(\text{OH})_2$ blocks, carbonated using CO_2 at 2 MPa (approx. 20 atm) pressure. It was found that when using mostly $\text{Mg}(\text{OH})_2$, stronger blocks were formed than with $\text{Ca}(\text{OH})_2$ (as shown in Figure 3.4), with nesquehonite identified as the major carbonated Mg phase at this very elevated partial pressure of CO_2 . This stands in contrast with the results of Dheilily et al.[235], who identified hydromagnesite as the major carbonate phase when treatment was carried out at atmospheric pressure. The long-term stability of these blocks has not been studied beyond the observation from the data in Figure 3.4 that the carbonated systems based on $\text{Mg}(\text{OH})_2$ alone, or with 10:1 $\text{Mg}(\text{OH})_2:\text{Ca}(\text{OH})_2$, decreased in strength from 1 to 28 days of age. The findings discussed in the preceding section regarding the thermodynamic stability of hydromagnesite over nesquehonite under ambient conditions may be important in understanding such behavior.

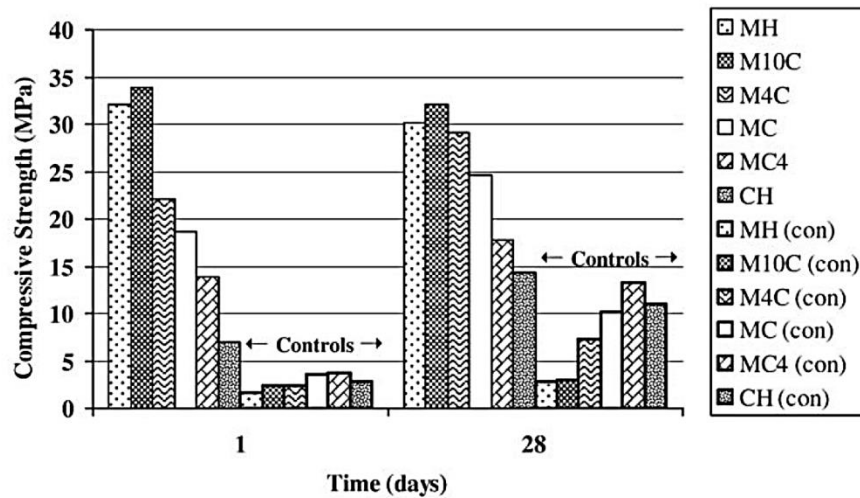


Figure 3.4 Compressive strengths at 1 and 28 days of $\text{Mg}(\text{OH})_2\text{-Ca}(\text{OH})_2$ compacts, with molar ratios as denoted in the legend, exposed to CO_2 at 2 MPa for 0.5 h (denoted *con* for control), then 24 h at 24 °C, 50% RH. The 10:1 $\text{Mg}(\text{OH})_2:\text{Ca}(\text{OH})_2$ compact (M10C) attains the highest strengths under this carbonation regime [236].

Research on the use of reactive magnesia cements to produce masonry blocks continued through the work of Liska and Al-Tabbaa, who studied $\text{MgO}:\text{FA}$ blends

which were mixed with sand and gravel to make blocks of sufficient porosity to enable their complete carbonation. Investigations began using MgO blended with FA or Lytag (synthetic aggregate formed from sintered coal ash) which was pressed into blocks and exposed to both natural and accelerated (20% CO₂, 98% RH, ambient pressure) carbonation conditions [237]. In samples cured for up to 196 days under natural conditions, no magnesium carbonates were formed; instead, consistent with the work of Vandeperre et al. [204], Mg(OH)₂ was the primary phase formed. Under accelerated carbonation conditions nesquehonite and Mg(OH)₂ were identified, with compressive strengths of up to 20 MPa achieved in some samples [237]. Further refinement of processing conditions led to the production of MgO-based blocks reaching strengths of 22 MPa after only 14 days [170], which is similar to the strength of many commercially available masonry units and thus offers a pathway for the uptake of this technology as a replacement for bricks or PC-based masonry blocks. The detailed identification of the phase equilibria, and particularly the nature and stability of the magnesium carbonates present as a function of sample curing and conditioning, is still under discussion in some of these systems [234], with nesquehonite and dypingite sometimes difficult to identify conclusively from the available data.

These papers do, however, confirm that elevated CO₂ conditions are required for the production of a useful product, with limited strengths observed under atmospheric curing conditions. This would limit the technology to precasting applications, where curing can be controlled in a factory, rather than application on-site.

3.2.5 Novacem

Another group who attracted significant attention to their work on magnesium carbonate binders was the company Novacem, which was born out of research conducted at Imperial College London, based on ‘carbon negative’ cement technology [238]. The Novacem company was liquidated in 2012, but its technology and intellectual property were sold to Calix, an Australian carbon capture and minerals processing company.

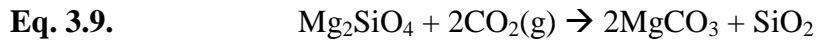
The publicly accessible information regarding the technology behind Novacem was presented in a series of patent applications. The patent granted under the title “Binder composition” [172] described a porous MgO cement which takes up CO₂ during hardening, and which contains no PC. The particular improvements Novacem claim over other MgO blocks are the ability to use either MgO or Mg(OH)₂ (or a blend thereof) as starting materials, along with the addition of a magnesium hydroxycarbonate (which can itself be produced through partial re-carbonation of magnesia[239]) and a hygroscopic salt. The patent claims that the hydration of MgO in presence of these carbonates produces brucite crystals with larger surface area, and thus higher early strength. The addition of magnesium hydroxycarbonates was also believed to increase the rate of MgO hydration and provide nucleation sites for carbonation [240]. The material carbonates over time, under atmospheric conditions, assisted by the high humidity induced due to the presence of the hygroscopic salt. The high surface area Mg(OH)₂ in this application was claimed to be more susceptible to carbonation, a desirable characteristic when compared to previously developed MgO-based blocks. It was claimed that a net absorption of 0.59 tonnes of CO₂ per tonne of MgO can be achieved by this processing pathway, hence the advertising of the material as a ‘carbon negative’ cement [172]. The examples provided show a maximum compressive strength of 25 MPa, and the example applications were limited to use as mortars, masonry block replacements, roof tiles and bricks, which do not require high strengths and are sufficiently porous to allow carbonation.

The addition of hygroscopic salts was a key step in the success of this process, as the formation of nesquehonite from Mg(OH)₂ (Eq. 3.8) requires both CO₂ and H₂O, meaning humidity is an important factor, which many academic studies do not take into consideration.

Unfortunately, the chloride salts which are described as offering attractive hygroscopic properties may induce corrosion in steel, and can also become mobile under wicking action leading to efflorescence, meaning that care is required in specifying these materials for use under appropriate service conditions.

Novacem also applied for a patent which outlined the production of MgO from magnesium silicates such as olivine (Mg,Fe)₂SiO₄ [241], *via* supercritical

carbonation (temperatures of 100-225 °C, under a >75% CO₂ atmosphere at pressures of 7.1-9.7 MPa) to form a magnesium carbonate or hydroxy-carbonate, and silica or metal silicates. For forsterite, which is the magnesium end-member of the olivine family, this process is summarized by Eq. 3.9:



The magnesium carbonate can be calcined to produce MgO, the silica either utilized or discarded, and the CO₂ recycled. The energy requirements, and consequent commercial viability of this process, have yet to be demonstrated on an appropriate scale. However, the carbonation of magnesium silicates, especially serpentine minerals (such as chrysotile, lizardite and antigorite), for CO₂ capture in geological formations is a fast moving area of research, which may drive down costs due to innovation [221, 242-243]. If this process is viable, and implemented using clean sources of energy, this has the potential to produce a low carbon cement which could be applicable for preformed blocks and tiles. Recent papers by Gartner & Macphee [244] and Gartner & Hirao [245] provide detailed reviews of the early work of Novacem, and offer further insight into magnesia cement carbonation in context with work on other novel binders, in both thermodynamic and practical senses.

3.2.6 Limitations of carbon sequestration

Other than under extreme carbonation conditions, reactive magnesia added to PC has not been observed to carbonate at a sufficient rate to enable utilization of the higher strength (generally by a factor of approximately 4-5) of carbonated compared to uncarbonated magnesia-based blocks in a practical sense. Porous MgO blocks without PC addition have, however, been shown to carbonate under mildly elevated CO₂ partial pressures. To ensure the green credentials of these blocks would require the commercial production of the blocks to take place alongside a large point-source CO₂ emitter (i.e. a PC plant or fossil fuel fired power station), and considerable storage capacity would be needed for extended-duration CO₂ curing. To date research has focused on porous blocks for masonry applications, which tend to be commodity products of low economic value, meaning that the economically viable construction of a facility to produce low-margin products would seem to depend on

external drivers such as carbon taxation rather than being profitable on a simple product-for-product basis.

A common argument in favor of magnesia cements is based on the perceived green credentials of MgO compared to PC due to the amount of CO₂ released during production of the latter. Most commercially available MgO is produced *via* the calcination of magnesite (Eq. 3.1). To produce reactive magnesia, magnesite is typically calcined at <750 °C [197] (see section 1.2), which is lower than the processing temperature used in PC production, which must usually be around 1450 °C to convert limestone and silica to the tricalcium silicate (Ca₃SiO₅) which comprises ~60% of a modern PC, in a rotary kiln [84, 185], Eqs. 3.10 & 3.11. The use of magnesite is therefore a potential source of CO₂ savings *via* reduced energy requirements.



On a molar basis magnesite and calcite release the same amount of CO₂ during calcination. However, on a mass basis magnesite calcination will produce more CO₂ than calcite calcination (522 kg CO₂/t MgCO₃ v 439.7 kg CO₂/t CaCO₃), due simply to the higher atomic mass of calcium than magnesium. Therefore magnesite is not an inherently ‘green’ material, and so unless MgO is obtained from calcination of naturally occurring brucite deposits, which are uncommon, or obtained from magnesium silicates, then CO₂ is produced during manufacture. Production of MgO for these cements from seawater or brine has also been proposed, but as earlier noted this process is very energy intensive and utilizes limestone or dolomite, which release CO₂ during processing into lime or dolime.

Further to this, confusion in the academic and commercial literature related to MgO production has led to some inflated assumptions regarding CO₂ savings. For example, the Novacem (now Calix) patent [172] claims that the “*high CO₂ absorption ability of MgO (up to 1.09 tonne of CO₂/tonne MgO) offers the unique potential to develop “carbon negative” cements – however this assumes little or no CO₂ emission during manufacture of MgO. At best, reactive MgO cements derived*

from carbonate precursors will be able to absorb as much CO₂ as is released during calcination of MgCO₃, assuming that renewable energy is used during calcination, that no other emissions occur during the supply chain, and that 100% of the MgO is carbonated during curing or in service.

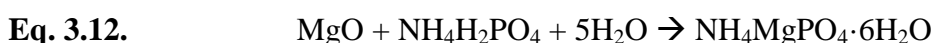
3.2.7 Conclusions

Reactive magnesia cements have not yet been proven to successfully perform under ambient conditions, as they require production as porous units or structures, control of internal humidity, and enhanced levels of CO₂ to form binding magnesium carbonate phases. Once produced these cements have been shown to form strong enough products for usage as precast materials, especially blocks or tiles, although the long-term durability of the formed phases is currently in question. It is imperative for the success of these cements that MgO can be produced economically and sustainably from either magnesium silicate or brines, at a commercially sustainable throughput. Ultimately, reactive magnesia cements are not so simply classified as 'eco cements' as has been done in some areas of the literature, although there is certainly scope for this to be achieved. Examples which have been proven to carbonate are (for the moment) confined to porous products exposed to elevated CO₂ curing conditions. These do have some potential for becoming carbon neutral, if produced from naturally occurring brucite deposits, using renewable fuels for calcination and ensuring carbonation throughout the product. Carbon negative cements could potentially be produced from magnesium silicate sources, offering interesting scope for replacement of PC in production of non-reinforced blocks and other pre-cast or factory-produced units, but with limitations in large-scale in situ concreting or where mechanical loading necessitates the use of steel reinforcing.

3.3 Magnesium phosphate cements

3.3.1 Phosphate bonding of magnesia

Magnesium phosphate cements are formed *via* an acid-base reaction between MgO and a soluble acid phosphate (typically an ammonium or potassium phosphate), forming a magnesium phosphate salt with cementitious properties as exemplified by Eq. 3.12. This class of materials is known broadly as magnesium phosphate cements, or MPCs.



The application of phosphate bonding to produce cementitious materials has long been known, with some of the earliest such records from the late 19th century describing zinc phosphate dental cements [246-247]. Phosphate bonded refractories are also in widespread use, exploiting the property of cold setting to form products which are stable at high temperatures. One of the first systematic studies of the phosphate bonding process was published by Kingery in 1950 [248-250], who remarked that acid phosphates are responsible for bonding in cold-setting systems, and stated that “*For optimum bonding, a weakly basic or amphoteric cation having a moderately small ionic radius is required...*”. Describing the then-existing literature on oxide reactions with phosphoric acid, Kingery noted that acid or inert oxides do not react with phosphoric acid, whereas highly basic oxides react violently, forming porous structures with decreased strengths. Weakly basic or amphoteric oxides performed the best, with oxides of Be²⁺, Al³⁺, Fe³⁺ and Mg²⁺ giving the best results in order of bond strength [249-250].

Considerable literature exists for zinc phosphate cements, due to their use as dental cements [251-253]. However, these set much too rapidly for use as cements for construction purposes, whereas the ability to produce dead burnt magnesium oxide, with reduced reactivity, has opened the possibility for production of MPCs suitable for structural applications. Such MPCs have been the subject of several patents for use as refractory investments, commonly to cast alloys, and often for use in dentistry. For example, Prosen in 1940 outlined a dental investment using silica, MgO and a blend of ammonium and sodium phosphates [254].

Formation of magnesium phosphates through this acid-base process can be simply achieved *via* the reaction of MgO with H₃PO₄ [249, 255]. Finch & Sharp [255] found that when starting from a 1:1 molar MgO:H₃PO₄ aqueous mixture, a hard though water-soluble product was formed and the reaction stoichiometry deviated from the theoretical 1:1 case through incomplete reaction of the MgO, Eq. 3.13.



To form an insoluble product with a 1:1 ratio of Mg:P, an excess of MgO is typically required [256], with the reaction instead proceeding *via* Eq. 3.14.



These reactions are highly, often violently, exothermic, which raises practical challenges regarding the use of this process on a large scale.

3.3.2 Application as cements

Applying the magnesium-phosphate bonding process to the production of cementitious products requires a system which reacts more slowly and with a more gradual heat evolution. In the 1940s, Every and Prosen each filed patents using MgO and ammonium phosphates to form molded products [254, 257], which reacted more slowly than systems using phosphoric acid, and these ammonium-containing compositions formed the focus of much development in the ensuing decades. The combination of magnesia with phosphoric acid and Al(H₂PO₄)₃ has also been used in some refractories, forming a moldable product consisting of MgHPO₄·3H₂O and an amorphous aluminum phosphate phase [255, 258].

A key step towards the formulation of modern MPCs was provided by Limes & Ponzani of the Republic Steel Corporation. Their 1966 patent [259] outlines a refractory cement which can be sprayed onto furnace walls, and is tolerant of both high and low temperatures. As MgO mixed with phosphoric acid reacts too rapidly for spray application, they proposed the use of a blend of liquid ammonium ortho-, pyro- and poly-phosphates with dead burnt magnesia, and succeeded in producing a cold-setting sprayable composition [259].

The ability to use these quick setting cements for other purposes was realized some 8 years later, when a number of patents were published in 1974-1977 describing the use of magnesium ammonium phosphates as rapid patch repair cements for roads and highways [260-263]. Among these, Stierli et al. of W.R. Grace & Co. proposed the addition of a boron compound such as borax to control the rate of reaction, which was claimed to delay setting for up to 1 hour to offer a more convenient working time [263]. These rapid repair cements began to be marketed under various trade names by the early 1970's [264], and were generally shipped as a dry powder mix, to which a liquid phosphate solution was added.

Several reports in the 1980's show that interest remained in MPCs for repair of damaged runways, pavements and bridges [265-266]. Notably, a report detailing the use of MPC to repair a runway after the Falklands War described compositions setting in ~30 mins, enabling patching of over 1000 "scabs" to enable rapid re-commissioning of Port Stanley Airport [267].

However, continued development of lower-cost options, such as blended PC compositions, rapid setting high alumina cements and epoxy resins, has left MPC as a marginal player among currently marketed rapid setting mortars. A more recent evaluation of proprietary rapid repair mortars showed many non-magnesia mortars equaling or exceeding the properties of leading MPCs [268]. The release of gaseous ammonia from the hardening and hardened cements also places some restrictions on the use of these materials on environmental and hygiene grounds.

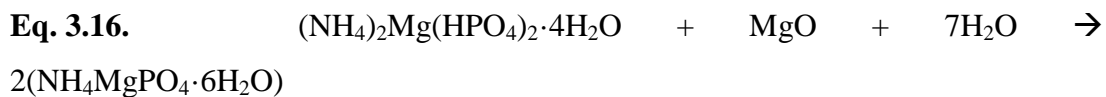
3.3.3 Method of action

Scientific literature on the chemical specifics of MPCs did not emerge until the early 1980's. Among the early publications were two papers by Sugama and Kukacka in 1983 [269-270], where cements made from MgO and diammonium phosphate solutions, and MgO and ammonium polyphosphate solutions, were tested. The principal products formed were claimed to be struvite ($\text{MgNH}_4\text{PO}_4 \cdot 6\text{H}_2\text{O}$) and $\text{Mg}_3(\text{PO}_4)_2 \cdot 4\text{H}_2\text{O}$, along with small quantities of newberyite ($\text{MgHPO}_4 \cdot 3\text{H}_2\text{O}$) and $\text{Mg}(\text{OH})_2$ [269-270].

Abdelrazig & Sharp [271] disagreed with these findings, claiming that mixtures of MgO and monoammonium phosphate form dittmarite ($\text{MgNH}_4\text{PO}_4 \cdot \text{H}_2\text{O}$), while the addition of sodium tripolyphosphate as a setting retarder resulted in the formation of struvite and schertelite ($\text{Mg}(\text{NH}_4)_2\text{H}_2(\text{PO}_4)_2 \cdot 4\text{H}_2\text{O}$) [271]. This was clarified by Popovics et al. in 1987 [272], who identified that dittmarite forms as the principal product if setting is rapid (i.e. without a setting retarder), while struvite is the principal product if setting is slow.

Although earlier patents and papers used liquid polyphosphates or diammonium phosphate, by the late 1980's magnesia and powdered monoammonium phosphate were the preferred materials, shipped as dry powders, principally forming a crystalline struvite binding phase when mixed with water, according to Eq. 3.12 [273].

Further investigations by Abdelrazig et al. [273] of an MPC retarded with sodium tripolyphosphate showed struvite to be the main phase, though with some schertelite and minor traces of dittmarite and stercorite. It was suggested that schertelite is an intermediate phase in the formation of struvite, first forming *via* Eq. 3.15, then reacting with more MgO and H_2O *via* Eq. 3.16.



The formation of minor quantities of dittmarite in MPCs is thus related either to the presence of insufficient water during hydration, or *in-situ* dehydration of struvite due to autogenous heating of the cement due to its highly exothermic hydration reaction process.[274-275], which can induce an increase in temperature up to at least 80 °C [274]. Struvite was demonstrated to be unstable from 50 °C in air, decomposing *via* Eq. 3.17. [275]



The MgHPO_4 thus formed, which is often X-ray amorphous, can rehydrate to form newberyite. However, boiling of struvite in water leads only to the loss of water, forming dittmarite, which can then rehydrate to re-form struvite at room temperature

[275]. Depending on the heat evolved by hydrating MPC, and the availability of water, such a process could account for the dittmarite identified in some rapid setting MPC formulations [272]. The minerals phases identified within various MPCs are displayed in Table 3.3.

Table 3.3 Magnesium phosphate minerals reported in MPCs

Mineral	Formula
Struvite	$\text{NH}_4\text{MgPO}_4 \cdot 6\text{H}_2\text{O}$
Newberyite	$\text{MgHPO}_4 \cdot 3\text{H}_2\text{O}$
Hannayite	$(\text{NH}_4)_2\text{Mg}_3\text{H}_4(\text{PO}_4)_4 \cdot 8\text{H}_2\text{O}$
Schertelite	$(\text{NH}_4)_2\text{MgH}_2(\text{PO}_4)_2 \cdot 4\text{H}_2\text{O}$
Dittmarite	$\text{NH}_4\text{MgPO}_4 \cdot \text{H}_2\text{O}$
Stercorite	$\text{NaNH}_4\text{HPO}_4 \cdot 4\text{H}_2\text{O}$
Struvite-K	$\text{MgKPO}_4 \cdot 6\text{H}_2\text{O}$

The principal sources of variation in performance and properties between modern MPC systems relate to quantity of water used, the magnesium/phosphate ratio, the addition of diluents and the usage of setting retarders. The water content, and effect of these on the cements is notable. As typical for cements, increasing the water content of a mix is reported to decrease the compressive and flexural strength [272, 274, 276], as demonstrated in the results of Hall et al. [274] shown in Figure 3.5. The addition of water beyond 20 wt.% has been reported to cause MPC to ‘split’, meaning that the cement remains as a slurry and does not functionally set [277], distinct from the case for PC where the addition of an excess of water means that the paste segregates and ‘bleeds’ excess water, forming a solid (although porous) hydrate product and a clear supernatant solution.

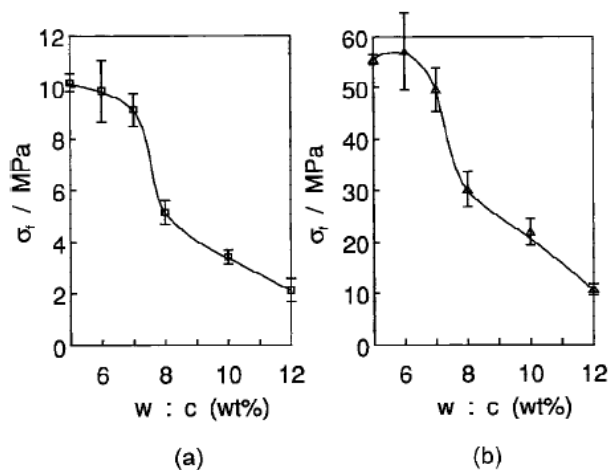


Figure 3.5 Effect of water content (expressed as water:cement mass ratio, in percentage) at 7 days on (a) flexural and (b) compressive strength of MPC mortars [274].

To form the maximum possible amount of struvite as a binding phase, a stoichiometric 1:1 molar ratio of $\text{MgO} : \text{NH}_4\text{H}_2\text{PO}_4$ would theoretically be preferred. In typical usage however, MgO is used in significant excess, as excess unreacted phosphate would be soluble, leaching out of the cement during service, potentially compromising structural integrity but also leading to unappealing efflorescence on the cement surface. Although numerous studies have been undertaken on this topic, comparison of published research into struvite-based cement systems is hampered by a wide variation in the use of retarders and proportions of water used, along with a disinclination to report whether molar or weight ratios are used [278-279].

Within struvite-K systems (cf. section 3.4) a few more detailed studies have been undertaken, with Mg:P molar ratios of 4-6 producing the highest compressive strengths, and ratios above this yielding a reduction in strength [280-282]. These did not, however, study low or equimolar ratios of Mg:P, which remains a notable gap in the understanding of these cements.

The use of high Mg:P ratios results in the presence of large quantities of unreacted MgO in these cements once set. In general construction practice, the presence of free MgO in hardened cements is considered highly undesirable and a harbinger of future expansive cracking as it slowly hydrates to $\text{Mg}(\text{OH})_2$ [283]. Long-term studies of MPC durability and dimensional stability are not prominent in the open literature,

however, the presence of MgO might not be a major issue in these cements, as it is reported that struvite forms around MgO grains, effectively entombing them [271, 284]. An excess of magnesia is thus required to react with all of the phosphate, as a significant fraction of the magnesia remains inaccessible for reaction, with the optimal ratio depending on the particle size and reactivity of the MgO.

3.3.4 Struvite-K cements

Crystalline magnesium ammonium phosphates are well known mineral phases occurring in nature, principally in bat guano. The main crystalline phase in modern MPCs is struvite. This phase was first described by Teschemacher in 1845, occurring as crystals in guano at Saldanha Bay, now in South Africa, and named the mineral *Guanite* [285]. Also in 1845 Ulex [286-288], reported the discovery of this mineral in Hamburg during the reconstruction of St Nicholas church on the site of the former Neue Burg, which had been destroyed in 1072. Crystals up to 2.5 cm long were unearthed in a buried ditch, presumed to have been used to store waste, manure and as an open dung-pit. Ulex postulated that the crystals formed due to “*infiltrations of urine through a soil consisting of vegetable matter*”, and named the new mineral after Heinrich von Struve, a well-known diplomat and mineralogist at the time [286-288].

Struvite was later reported in 1870 in bat guano from the Skipton caves in Victoria, Australia [289]. Several other magnesium phosphates were also discovered in this guano over the next few decades, including hannayite, newberyite, schertelite and dittmarite [290-292]. As listed in Table 3.3, these are all also important phases in synthetic MPCs.

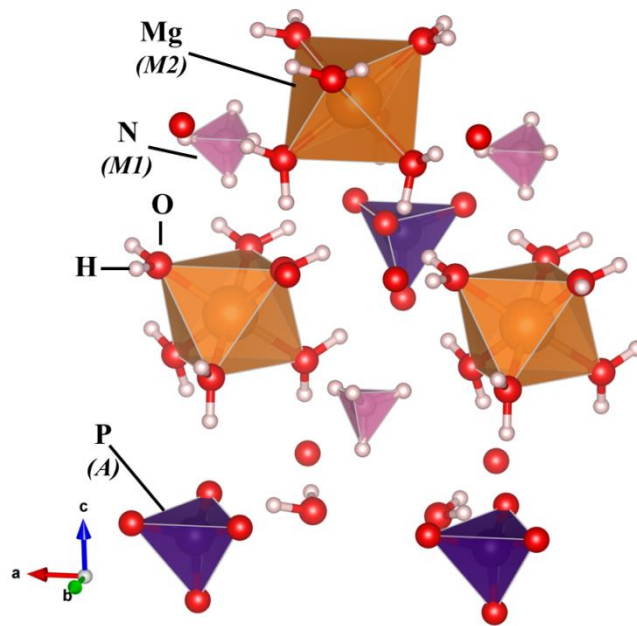


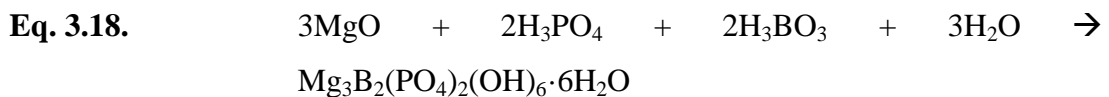
Figure 3.6 Crystal structure of struvite, drawn from [293], and with M1, M2 and A sites identified in italics

The struvite mineral family is known to accept a wide range of substituents within the $M^1M^2A \cdot 6H_2O$ structure (Figure 3.6). These include substitutions of monovalent cations on the M1 site (NH_4^+ , K^+ , Rb^+ , Cs^+ , Tl^+), divalent cations on the M2 site (Mg^{2+} , Ni^{2+} , Zn^{2+} , Co^{2+} , Cd^{2+} , Cr^{3+} , Mn^{2+} , VO_2^+) and trivalent oxyanions on the A site (PO_4^{3-} , AsO_4^{3-}) [294-302].

A considerable quantity of struvite research pertains to its role in urinary stones [303], and as a precipitate which causes blockages in wastewater works [304-305]. The tendency of struvite to precipitate from municipal wastewater has led to commercial recovery of phosphate and nitrogen from water works as struvite for sale as a fertilizer, but this can lead to problems related to the co-precipitation of heavy metals within the struvite structure [306-310]. Although potentially problematic for the phosphate recovery industry, this ability is of interest for the immobilisation of heavy metals and radionuclides within MPCs, particularly those based on an ammonia-free magnesium potassium phosphate binding phase such as struvite-K. This phase ($MgKPO_4 \cdot 6H_2O$) has been found as a naturally occurring alteration mineral [311-312], but has been popularized over the last 20 years as an alternative MPC cement binder.

Ammonia-free MPCs were popularized by Wagh, Singh and other workers from Argonne National Laboratory as an encapsulant for various nuclear wastes arising from clean-up of legacy nuclear sites in the USA. This began in the early 1990s with research on the use of MPCs which can tolerate ash and salt bearing wastes, combined with radioactive and heavy metal contaminants. Typically these wastes might include pyrophoric materials, requiring a low temperature encapsulation process, but also contain salts or materials which are unsuitable for cementation in conventional PC blends.

Initial development focused on the use of a Zr-phosphate matrix to chemically immobilize wastes, with encapsulation of this phase in a magnesium phosphate binder formed from MgO, boric acid (as a set retarder) and phosphoric acid [313-314]. In a quick-setting (15 minutes) reaction, newberyite and lüneburgite ($\text{Mg}_3\text{B}_2(\text{PO}_4)_2(\text{OH})_6 \cdot 6\text{H}_2\text{O}$) were reportedly formed [313-314] *via* Eqs. 3.14 & 3.18.



Although this newberyite-based wasteform reportedly performed well during leach testing, the use of phosphoric acid generated too much heat during setting (large-scale systems showed boiling of the mix), and its acidity was problematic in a processing sense [315]. This issue was overcome through the use of KH_2PO_4 instead of H_3PO_4 [315], creating struvite-K *via* Eq. 3.19:



The reduced acidity of KH_2PO_4 yields a slower and more controlled reaction, and therefore resolves issues with heating [316]. Being a dry powder, it can also be pre-bagged with MgO similar to $\text{NH}_4\text{H}_2\text{PO}_4$ in modern ammonium-MPC repair mortars, but avoiding the evolution of ammonia gas during setting. It is also one of the least soluble of the commercially available acid phosphates, Table 3.4, which is advantageous compared to the sodium analogue.

Table 3.4 Solubility of selected acid phosphates in water [317]

Phosphate	Solubility (g in 100g H₂O) at 25 °C, 1 bar
KH ₂ PO ₄	25.0
NH ₄ H ₂ PO ₄	40.4
NaH ₂ PO ₄	94.9

These magnesium potassium phosphate cements (MKPCs) were also described as “chemically bonded phosphate ceramics (CBPCs)” [318], or by the trade name ‘Ceramicrete’, and have been extensively developed and trialed in the USA and Russia for conditioning of various challenging nuclear wastes [319] including:

- Plutonium contaminated ash [96]
- Heavy metal and radium wastes [320]
- ⁹⁹Tc bearing wastes, using SnCl₂ as a reductant [95]
- Liquid Hanford vitrification wastes [321]
- Mayak salt wastes [322]

Alongside this application, other MKPC patents have been granted to Wagh & Singh [323-325], including for sprayable compositions and oil-field applications.

MKPCs have also been proposed as lower-pH binders for reactive metal wastes, such as aluminum wastes arising from nuclear operations. Aluminum corrodes in alkaline media, such as conventional PC blends [326], reacting expansively and cracking the cement, while producing flammable hydrogen gas. This means that the lower internal pH of struvite-K based cements may be advantageous in reducing corrosion of aluminum [318, 327-328]. For this application, MKPCs have been tested for *in-situ* cementation of the P-reactor vessel at the Savannah River Site in the USA during decommissioning, but ultimately a sulfoaluminate cement was preferred for large-scale use [329-330]. In the UK, MKPCs have been investigated for encapsulation of reactive metallic aluminum, magnesium and uranium-containing nuclear wastes [91]. The low water content at which MKPC can be formulated [91] also reduces the availability of free water for corrosion of Mg and U [328].

Interest in MKPCs has, however, extended beyond the nuclear industry, and most current literature focuses on MKPCs rather than ammonia MPCs.

3.3.5 Retardation of MPCs

The ability to control the rate of reaction in MPCs is crucial to the application of these cements, whether in rapid patch repair or low temperature waste encapsulation. With NH_4 -MPCs, the need to produce a premixed 'just add water' bag of cement led to the development of retarders. Addition of water to a blend of monoammonium phosphate and MgO results in a mass which sets too rapidly to be of use, and thus early MAP patch repair cements used a separately packaged ammonium polyphosphate solution which reacted more slowly with the MgO . Several alternative methods have been used over the years, though the addition of borates has now come to be favored.

3.3.5.1 Temperature

Although MPCs are capable of setting at temperatures below freezing, the acid-base reaction is considerably slowed. This has been practically encountered during patch repair in Alaska [331], and studied by Yang [278], who demonstrated an MPC mortar capable of setting at $-10\text{ }^\circ\text{C}$ in a period only three times longer than at $25\text{ }^\circ\text{C}$, as illustrated in Figure 3.7. Such low temperature pose a challenge to most other cementing systems, as the setting of many cements is problematic below $0\text{ }^\circ\text{C}$, but the inherently rapid reaction and low water content of MPCs are advantageous in this context

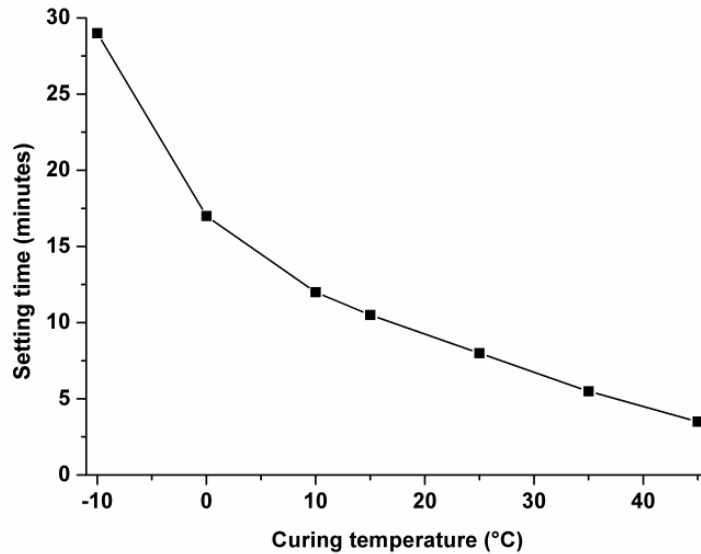


Figure 3.7 Effect of temperature on ammonia-MPC setting time (with 5% borax), drawn from data presented in [278]

3.3.5.2 Sodium tripolyphosphate

Sodium tripolyphosphate ($\text{Na}_5\text{P}_3\text{O}_{10}$) was an early retarder used in NH_4 -MPC, and was generally added into the mixes as a powder, to increase MPC setting times from 4-7 minutes up to 15 minutes [273, 332]. $\text{Na}_5\text{P}_3\text{O}_{10}$ has been proposed to chelate Mg^{2+} ions from the MPC slurry [273], but its effectiveness is restricted by the limited solubility of $\text{Na}_5\text{P}_3\text{O}_{10}$ in an already saturated acidic phosphate solution during MPC setting reactions [332]. The addition of $\text{Na}_5\text{P}_3\text{O}_{10}$ also has the side effect of promoting the formation of stercorite ($\text{NaNH}_4\text{HPO}_4 \cdot 4\text{H}_2\text{O}$) in ammonium phosphate cements [333], though the effects of this phase on MPC properties and performance are unknown.

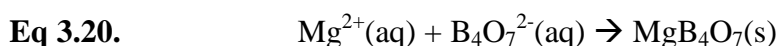
3.3.5.3 Borates

More recently, borate has become the de facto standard retarder for MPCs due to its effectiveness and the relatively low doses required compared to $\text{Na}_5\text{P}_3\text{O}_{10}$. Both borax ($\text{Na}_2\text{B}_4\text{O}_7 \cdot 10\text{H}_2\text{O}$) and boric acid (H_3BO_3) have been widely used, with similar effects, though boric acid has been more widely used in recent years. With the

inclusion of both borax and boric acid in the EU ‘Candidate List of Substances of Very High Concern for Authorisation’ [334] due to reproductive toxicity, the use of these substances in Europe is becoming restricted, but this is not yet the case globally.

This retarding mechanism was originally developed to extend the pot life of NH₄-MPC in high temperatures (e.g., road patching in the summer sun), with Stierli’s patent [263] reporting the use of ammonium pentaborate ((NH₄)B₅O₈·8H₂O), borax, boric acid and trimethyl borate (B(OCH₃)₃) as retarders. With several wt.% boron compounds added, setting times of up to 30 minutes could be achieved, allowing the marketing of a pre-blended one-bag cement. The addition larger quantities of borax (20 wt.%) reduced compressive strength development at early age, although the reduction was only 8% after 28 days of curing [335].

The precise retarding mechanism of boron compounds in MPCs is currently unclear. Yang & Wu [278] concluded that the Mg:B ratio effects setting but the B:P ratio does not, indicating that the borates are reacting with the MgO. Sugama & Kukacka [270] initially suggested that retardation was due to the Mg²⁺ ions being chelated by B₄O₇²⁻ ions, forming a colloidal precipitate around MgO grains, reducing further dissolution and thus retarding strength development [270]. This would follow the known action of borax as a water softener, Eq. 3.20 [336]:



Conversely, Hall et al. [332] suggest that B₄O₇²⁻ ions are unlikely to form in the acidic phosphate (pH ~5) solution of a freshly mixed MPC slurry, and instead proposed that B(OH)₃ or B(OH)₄⁻ adsorb to the magnesia surface, reducing its dissolution. A more recent suggestion from Wagh is that boric acid reacts with MgO and the acidic phosphate solution to form a solubility-limiting coating of lüneburgite (Mg₃[B₂(OH)₆](PO₄)₂·6H₂O [337]) around MgO grains. This was claimed to occur in both phosphoric acid-MgO and KH₂PO₄-MgO systems using 4 wt.% or less H₃BO₃ [314, 318, 338], but it appears likely from solubility arguments that such a mechanism would require a higher boron concentration to be truly effective.

3.3.5.4 Diluents

Diluents are typically unreactive filler materials added to cements to save on material costs, and/or to reduce exothermic output for a massive pour. Traditional NH_4 -MPCs utilize sand as a diluent to produce a mortar, while MKPC mortars (often for nuclear applications) make use of finer materials such as coal fly ash [91, 281, 339], blast furnace slag [340-341] and wollastonite (CaSiO_3) [340].

Among these materials, fly ash is the most popular, as its addition to an MKPC mix also enhances fluidity *via* the ‘ball-bearing’ type effect of the spherical fly ash particles. The addition of fly ash to an MPC mortar can more than double setting times (though ≥ 50 wt.% replacement of MPC is required), with a corresponding increase in fluidity [339]. Although this reduces early (<24 hour) strength, the 28 day strength is reported to be slightly higher, with the material with no fly ash addition achieving 72 MPa, and with 50 wt.% fly ash replacement achieving 75.5 MPa [339]. Although these diluents are often described as being nominally inert, Gardner et al.[341] have noted the potential formation of potassium aluminophosphate gels when fly ash or blast furnace slag are combined with MKPC, suggesting that there is in fact a chemical interaction taking place rather than a simple dilution process. This highlights the need for this chemical reaction process to be more fully understood if these composite MKPC-based cements are to be used in critical applications such as nuclear waste immobilization.

3.3.6 MKPC expansion

An under-reported, yet potentially serious issue with MKPCs is that of significant deleterious expansion during setting, which affects pastes seemingly at random. Although not noted in the scientific literature, this issue has been illustrated in several PNNL/SRNL reports [321, 329]. During trials to scale up Ceramicrete, Josephson et al. noted severe expansion after casting small samples, popping lids off the containers used for casting the cement [321]. Stefanko et al. reports expansion of MKPC grouts after 24 hours of curing. Attempts to determine the cause of expansion was inconclusive, with only crystalline struvite-K identified [329]. Gardner has recently reported the expansion of MKPC-slag and MKPC-fly ash blends affecting

roughly 1 in 10 batches [342], of which Figure 3.8 shows two particularly badly affected batches.



Figure 3.8 Photographs of 50 mm cubes of MKPC-blast furnace slag (left) and MKPC-fly ash (right), each with 1:1 ratios of MKPC to diluent, suffering from expansion and cracking 3 days after casting [342]

Singh et al. have attributed expansion to carbonates or bicarbonates in simulant waste streams reacting with the phosphoric and boric acids, evolving CO_2 during setting [340]. It should, however, be noted that expansion has also been observed in absence of any carbonates [342], including in pure MKPC, as well as the materials blended with FA or BFS in Figure 3.8 which are unlikely to show significant thermal cracking effects due to their low heat output. This expansion has only been reported in the MKPC system, not in ammonia-MPCs, but it does represent a serious issue with MKPCs, requiring further research before these cements can be used with full confidence at an industrial scale.

3.3.7 Conclusions

MPCs were popularized as rapid patch repair materials using a blend of mono-ammonium phosphate and magnesium oxide, generally binding through an acid-base formation of struvite. This enabled rapid setting and use in cold environments, which might preclude other cements. Various retarders have been implemented to extend setting times, with borates the most popular retarder today. Over the past 15-20 years

interest in these has waned in favor of potassium-struvite cements, due largely to reduced heat output and the elimination of ammonia liberation during setting. These have found a niche as prospective nuclear waste immobilization matrices, especially for treatment of reactive metals unsuitable for conventional PC blends. The internal pH of MPCs is, however, too low and the cost too high to allow for their use in structural steel-reinforced concrete, which will continue to restrict these cements to lower-volume niche applications.

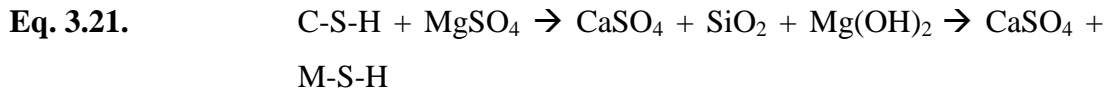
3.4 Magnesium silicate hydrate (M-S-H) cements

The concept of using a magnesium-silicate bond to form a cementitious product has existed for over 100 years. In 1889, Cummings claimed to produce a magnesium silicate cement by mixing and calcining MgCO_3 and finely pulverized silica to form a hydraulic powder [343], while in 1899 Steiger proposed a cement consisting of MgCl_2 , MgO , potassium or sodium silicate and water, which formed a “*hydrosilicate of magnesium and chlorid (sic) of alkali*” [344]. Various other patents describe additions of soluble silicates to magnesium oxychloride cements [345], powdered asbestos derived cements [346-348], or simply the fusion of talc or asbestos and silica into refractory articles [349-350]. Though proposed in many of these patents, the use of the magnesium silicate bond as a cement-forming system remained relatively unresearched for over 50 years, and are still not well understood.

The reaction of magnesia with a soluble source of silica generally forms a poorly crystalline talc-like or serpentine-like phase, the precise structure of which is still under investigation, and which appears to depend significantly on the Mg/Si ratio. Modern M-S-H cements are generally formed from a source of magnesium (typically MgO) and a source of highly reactive silica (e.g. silica fume) *in-situ*, rather than forming from the hydration of a magnesium silicate clinker, as magnesium silicates are non-hydraulic as mentioned above.

Within modern cements, M-S-H first came to attention during investigations into the degradation of maritime concretes produced from PC. In 1953, Cole observed the presence of a crystalline hydrated magnesium silicate (reported as $4\text{MgO}\cdot\text{SiO}_2\cdot 8.5\text{H}_2\text{O}$) in a severely degraded sea-wall [351], and postulated that this

had formed as magnesium salts in the seawater reacted with silica gel within the degraded cement; these results were supported by several later observations on PC-based materials damaged by MgSO_4 attack [352-357], according to Eq. 3.21 which schematically (and without intending to define stoichiometries of any of the reactions or silicate gels) describes the degradation of calcium silicate hydrate (C-S-H) and formation of M-S-H [358]:



The loss of strength associated with formation of M-S-H during MgSO_4 attack on hydrated PC led Cohen & Bentur to label M-S-H as a ‘noncementitious’ phase [359]. However, although its presence is not usually seen as beneficial to cements, M-S-H has been postulated to act as an extra binding phase for cations in cements blended with blast furnace slag, which tends to be richer in Mg than is PC [360].

3.4.1 M-S-H as a cementitious phase

The first major systematic studies of M-S-H began in the late 1980s for use as a non-PC binder in refractory castables [361], driven by Elkem as a major producer of microsilica (also known as silica fume, an amorphous silica by-product of silicon and ferrosilicon production). This binder was based on a blend of jet-milled fine periclase (dead burnt MgO) and microsilica, which is able to be sprayed onto a substrate, providing good resistance to temperatures up to 1500 °C [362-363]. The high compressive strength of these materials, up to ~130 MPa (Figure 3.9), proves that M-S-H is not “non-cementitious” as was previously claimed, but rather can form a strong bond. Szczerba et al. [364] also reported that M-S-H could be a useful material for refractory castables due to the high melting temperatures of MgO and forsterite (Mg_2SiO_4), two products of the thermal degradation of M-S-H.

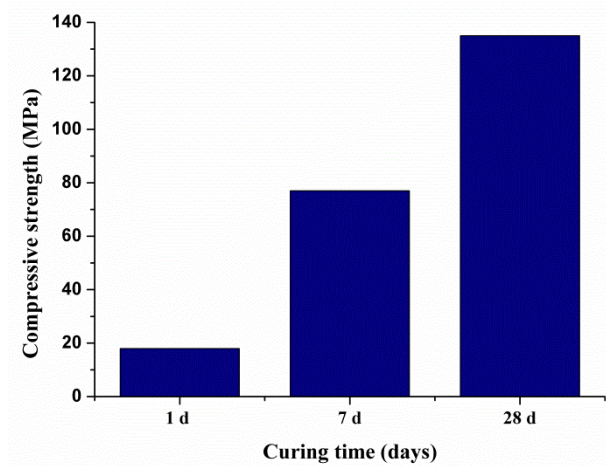


Figure 3.9 Compressive strength of M-S-H prisms cured underwater at 20 °C, plotted from data in [361]

The use of MgO and silica fume to form M-S-H was applied to cement systems in China in the mid-2000s, when patents were granted to Chen & Wei for M-S-H mortars made using MgO, silica fume and various industrial by-products including steel slags and coal fly ashes [365-366]. Several mortars were claimed to reach over 70 MPa in compressive strength after 28 days of curing, verifying the ability of this binder to form a cementitious mass.

Sandberg & Mosberg [361] and Wei et al. [367-368] validated the use of sodium hexametaphosphate (NaPO_3)₆ to increase the fluidity of M-S-H forming systems in the fresh state, to reduce the water/solids ratio required to achieve mixing and casting. Szczerba et al.[364] also described a factor of 10 decrease in the time required to form M-S-H when increasing the curing temperature from 20 to 40 °C. Each of these studies led to the production of a characteristically poorly-crystalline M-S-H, with an X-ray diffraction pattern similar to that shown in Figure 3.10.

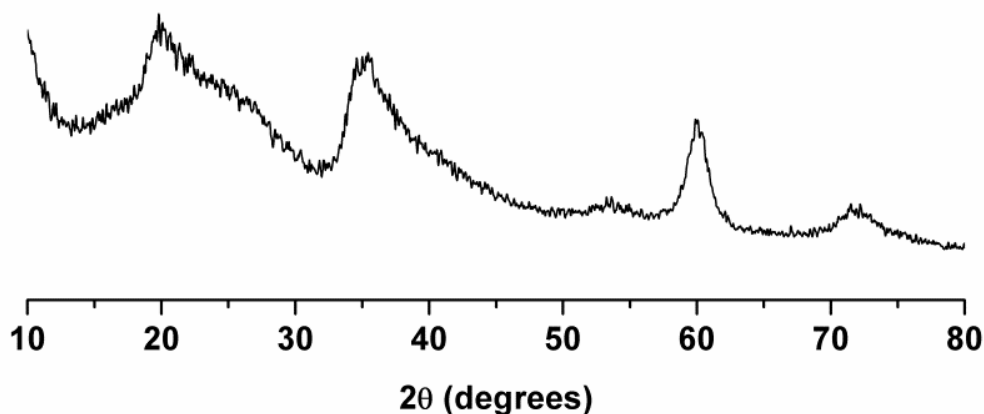


Figure 3.10 XRD pattern of a $\text{Mg}(\text{OH})_2$ -silica fume cement, cured at 40 °C for 8 months, showing formation of a poorly crystalline M-S-H phase.

Recently, M-S-H cements have been studied for their potential as cements for nuclear waste immobilization, with particular focus on the less-alkaline pH characteristics of M-S-H cements compared to PC. This is considered a disadvantage in reinforced concrete applications, as the moderate pH of M-S-H does not offer effective passivation of mild steel reinforcing in the same way as the highly alkaline PC pore solution environment. However, this same moderate pH could enable M-S-H to be used as an encapsulation matrix for metallic aluminum wastes resulting from the nuclear industry. Zhang et al. [369] studied M-S-H cements made from dead burnt MgO and silica fume, finding that the pH of these cements varied from 9.5 to 10.5, which would enable usage as a lower pH binding system, and later extended that work to the addition of MgCO_3 to reduce initial pH, finding the corrosion of reactive aluminum to be greatly reduced [370-372].

The use of M-S-H cements has also been studied for the immobilisation of $\text{Mg}(\text{OH})_2$ rich Magnox sludges, a legacy waste from the UK nuclear industry. This motivated the use of $\text{Mg}(\text{OH})_2$ as a precursor, rather than MgO as is typically used in M-S-H cements, with the aim of using this waste as an integral part of the cementitious matrix and thus achieving a very high waste loading [373].

Several countries including France, Switzerland, Belgium, Sweden and Finland [57-58, 374-375] are proposing radioactive waste repositories based on a multi-barrier concept utilizing clay backfills. These will require cements during construction and plugging, the alkaline nature of which is known to locally degrade the clays,

resulting in an array of alteration products and physico-chemical changes over extended periods of time [56, 376-380]. It is instead envisaged that construction cements will be lower pH (<11) cements to reduce dissolution of the clays and improve overall cement-clay compatibility, likely PC-SF or ternary PC-SF-FA/BFS [376, 381-384] blends. Although these have improved compatibility with the clays, studies of the interfacial zone between these low-pH cements and clays note the formation of M-S-H along with hydrotalcite [385-386]. This research has pushed forward research into the structure of M-S-H in recent years, but also poses the question as to whether M-S-H binders themselves could be used as low-pH shotcrete and stabilizing cements in clay-based repositories. As noted earlier, research by Zhang et al. [369] into M-S-H binders produced cements with pH values of 9.5-10.5, well within the range required for lower-pH cements to be considered for this usage.

3.4.2 Structure of M-S-H

Although the understanding of M-S-H as a binding phase is in its infancy, a significant quantity of literature does exist related to the structure and nature of the M-S-H system. The minerals linked to M-S-H and selected crystal structures are noted in Table 3.5. Interest in the synthetic formation of chrysotile asbestos encouraged the study of the MgO-SiO₂-H₂O system from the early 1950s, although these studies often used high pressure and temperatures using hydrothermal techniques. In 1954 Kalousek & Mui [387] studied mixtures of MgO and silicic acid at temperatures between 75 and 350 °C, with Mg/Si ratios between 0.5 - 2.0. The solid reaction products were reported to be a mixture of talc (Mg/Si 0.75) and chrysotile (Mg/Si 1.5), exhibiting diffuse scattering in X-ray diffraction patterns. In 1960 Yang studied the MgO-SiO₂-H₂O system from 100-300 °C [388], conducting hydrothermal synthesis of phases at pressures up to 138 MPa. A number of products were formed which were reported to resemble talc and serpentine. Both of these papers suggest that several solid M-S-H gels with differing compositions can precipitate, although whether these co-precipitate or form *via* an intermediate gel is a point of discussion.

Table 3.5 Minerals linked to M-S-H

Mineral	Group	Formulation
Lizardite	<i>Serpentine</i>	$\text{Mg}_3(\text{Si}_2\text{O}_5)(\text{OH})_4$
Antigorite	<i>Serpentine</i>	$\text{Mg}_3(\text{Si}_2\text{O}_5)(\text{OH})_4$
Chrysotile	<i>Serpentine</i>	$\text{Mg}_3(\text{Si}_2\text{O}_5)(\text{OH})_4$
Sepiolite	<i>Phyllosilicate</i>	$\text{Mg}_4(\text{Si}_6\text{O}_{15})(\text{OH})_2 \cdot 6\text{H}_2\text{O}$
Saponite	<i>Phyllosilicate</i>	$\text{Ca}_{0.25}(\text{Mg,Fe})_3(\text{Si,Al})_4\text{O}_{10}(\text{OH})_2 \cdot n\text{H}_2\text{O}$
Talc	<i>Phyllosilicate</i>	$\text{Mg}_3(\text{Si}_4\text{O}_{10})(\text{OH})_2$

In 1998, Temuujin et al. [389-390] formed M-S-H through a mechanochemical process, rather than *via* hydrothermal synthesis: $\text{Mg}(\text{OH})_2$, MgO and silicic acid were combined in a high-energy grinding method to form gels, which were aged prior to analysis. The resulting M-S-H was reported to be a poorly crystalline mixture of talc and chrysotile-like materials (as observed in the XRD patterns in Figure 3.11), similar to M-S-H produced hydrothermally.

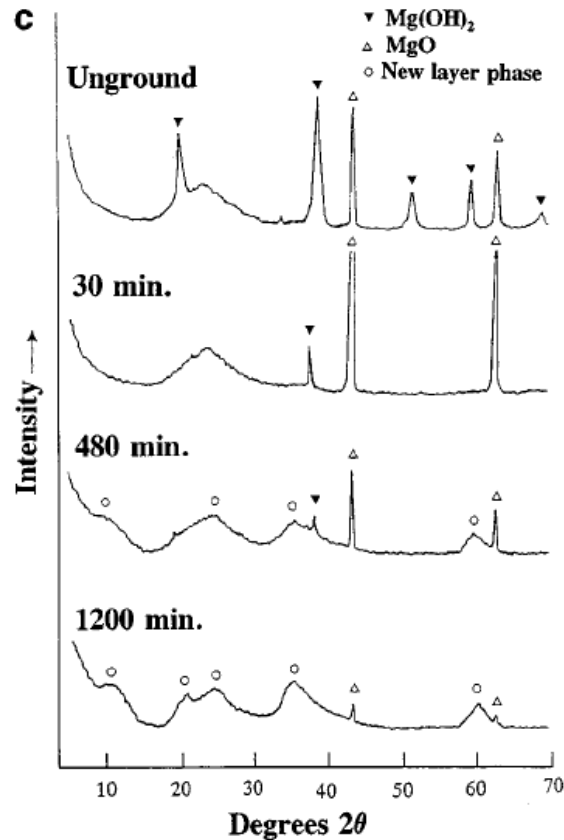


Figure 3.11 X-ray diffraction patterns of an MgO-silicic acid mix ground for various times then aged. The pattern labelled 1200 min displays a characteristic M-S-H diffraction pattern, which was identified by the authors as a ‘new layer phase’ [390]

There is also evidence that disordered M-S-H can be found to occur naturally. Mitsuda [142] discovered veins of M-S-H in association with 11 Å tobermorite from Heguri, Japan, believing it to be an intermediate product in the formation of talc. This theory was further explored by Mitsuda and Taguchi whilst studying hydrothermally produced M-S-H [391] (up to 600 °C) until the poorly crystalline phase crystallized and transformed into talc. The formation of M-S-H in nature under hydrothermal conditions was also reported by Gunnarsson et al. [392], who noted the formation of poorly crystalline Mg silicate scale with an antigorite-like structure in geothermal installations in Iceland.

Focusing on M-S-H formation within cements, Brew & Glasser [393] undertook a study to synthesize and analyze M-S-H gels precipitated by mixing $\text{Mg}(\text{NO}_3)_2 \cdot 6\text{H}_2\text{O}$

and $\text{Na}_2\text{SiO}_3 \cdot 5\text{H}_2\text{O}$. Solid state ^{29}Si NMR analysis of these gels revealed only slight structural differences as a function of Mg/Si ratio. These gels were also aged at 85°C over 6 months, which resulted in structural changes, as the two highest-Mg gels (Mg/Si molar ratios 0.89 and 0.94) developed different structural motifs upon ageing compared to the lower-Mg gels, resulting in a shift in the position of the Q^3 peak in ^{29}Si MAS NMR spectra of the gels with higher Mg/Si ratios. This suggested the formation of a serpentine-like material at higher Mg content, whilst the lower Mg/Si gels more closely resembled a talc-like structure.

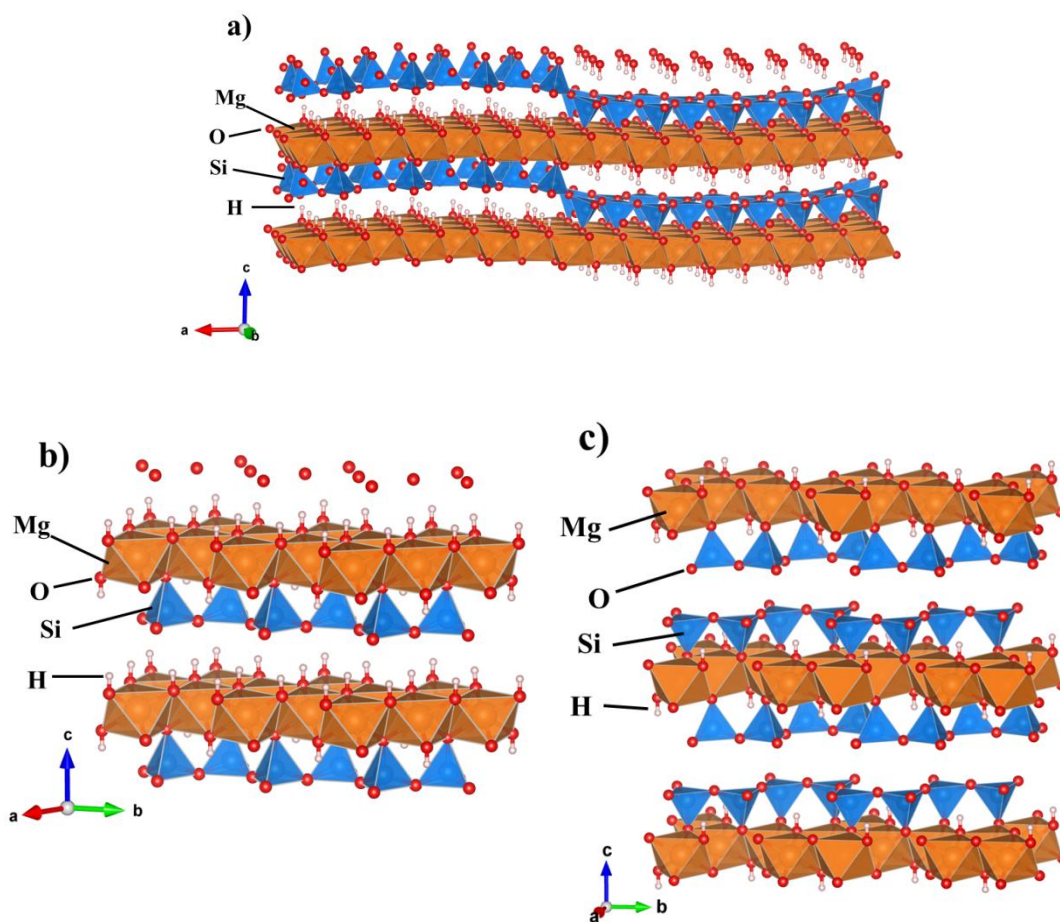


Figure 3.12 Crystal structures of a) antigorite, b) lizardite and c) talc, drawn from [394-396]

The precise nature of this serpentine-like material has until recently proven difficult to elucidate. The Mg-rich end of the serpentine group encompasses three minerals (antigorite, chrysotile and lizardite), each polymorphs of $\text{Mg}_3(\text{Si}_2\text{O}_5)(\text{OH})_4$. The crystal structures of antigorite, lizardite and talc are shown in Figure 3.12 above.

Several studies have looked at the amorphized structure of these three minerals, which tend to be structurally very similar [397-400], and thus the poorly crystalline mineral phases are difficult to differentiate from one another. Walling et al. [373] recently studied the structure of M-S-H cements derived from $\text{Mg}(\text{OH})_2$ and silica fume at an Mg/Si ratio of ~ 0.95 , and through the application of ^{29}Si and ^{25}Mg solid state NMR spectroscopy, found the structure of this gel to resemble poorly crystalline lizardite rather than an antigorite or talc-like assemblage, as depicted in Figure 3.13. A recent detailed study of M-S-H and C-S-H gels by Lothenbach et al. noted the existence of M-S-H gels with Mg/Si ratios from 0.7-1.3, both M-S-H and C-S-H forming separate gels, with little probability of a solid solution between the two [143]. This is complimented by the work of Roosz et al. who synthesized M-S-H with Mg/Si ratios of 0.57 and 1.07, finding the former gel structurally similar to 2:1 Mg-Si phyllosilicates [401].

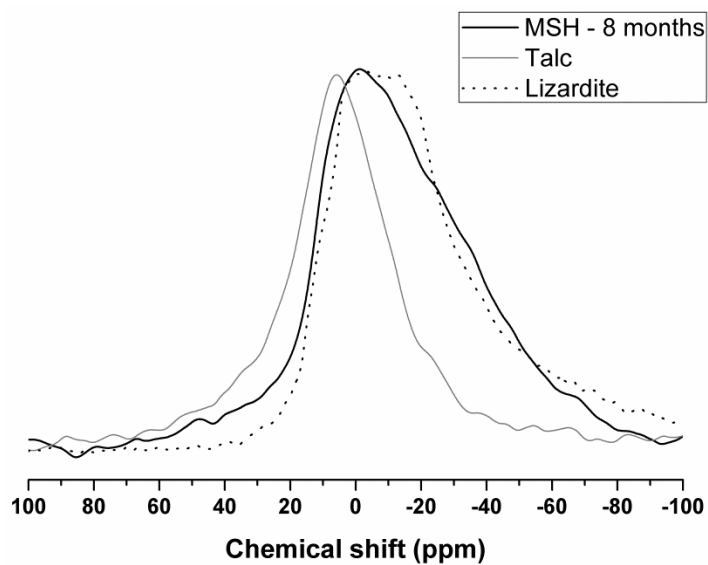


Figure 3.13 ^{25}Mg MAS NMR spectra of 8 month cured M-S-H, talc and lizardite.

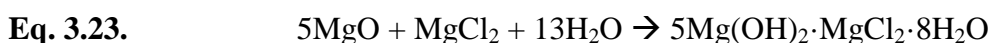
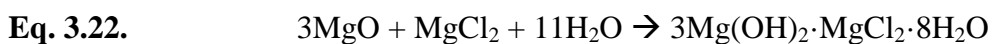
Adapted from [373]

3.4.3 Conclusions

No studies have to date described the scale-up of M-S-H for commercial cementing applications, and little work has been undertaken on the mechanical properties of M-S-H other than compressive strength, or its long-term durability. As a cement, M-S-H appears to be restricted by its very slow setting at ambient temperatures which may limit large-scale utilization in construction, but which is likely to be somewhat less problematic in specific applications involving the immobilization and disposal of nuclear waste. The precise structural details of the gel phase(s) forming in M-S-H binder systems also remain to some extent unclear. The relatively high cost of highly reactive silica compared to PC means that for the foreseeable future, it is likely that M-S-H will remain a niche cement unless more economic sources of silica can be utilized, with research likely instead focusing on M-S-H alteration products within PC-based cementitious systems. The potential, however, for improvements in mechano-chemical properties and reaction speeds are significant, and might possibly herald a brighter future for this cement through application of improved chemical and microstructural-level understanding to the optimization of engineering properties.

3.5 Magnesium oxychloride (Sorel) cements

Magnesium oxychloride (MOC) cements are based on the aqueous reaction between MgO and MgCl₂ (e.g. Eqs. 3.22 & 3.23), forming a variety of phases which are highly dependent on the precursor molar ratios, temperature and magnesium reactivity.



First reported by Sorel in his 1866 patent [402], and further elucidated in a widely-recognized journal publication by the same author in 1867 [403], these cements initially proved popular due to their attractive, marble-like appearance. Binding phases corresponding to those formed in MOCs can be synthesized through the dissolution of MgO into an aqueous solution of MgCl₂, forming a homogeneous gel

from which basic magnesium chloride salts precipitate. These salts are often expressed as $x\text{Mg}(\text{OH})_2 \cdot y\text{MgCl}_2 \cdot z\text{H}_2\text{O}$ or $x\text{MgO} \cdot y\text{MgCl}_2 \cdot (z+x)\text{H}_2\text{O}$. This leads to the abbreviations ‘3 phase’ and ‘5 phase’, derived from the ratio (x/y) of brucite to magnesium chloride in each phase.

The ability of MOCs to bind and consolidate large quantities of diverse filler materials ranging from granite to sawdust, with good compressive and tensile strengths, has furthered their adoption. Historical uses have varied from ornamental (imitation ivory, billiard balls, door handles), to floors, stucco [404], grinding wheels [405] and even burial vaults [406]. Various sources note widespread usage as a wood substitute in flooring for ships from the early 1900s to the 1950s [407-408], including the RMS Olympic and RMS Titanic ocean liners [409], where fire resistance and acoustic damping properties were desired. However, the popularity of MOC cements has precipitously declined in the last half century due to their poor water resistance and subsequent degradation during service.

Typically, MOC cement is made by first combining magnesia (MgO), generated through calcination of magnesite, with filler materials. This mix is then packed into a shape and moistened with a solution of MgCl_2 (typically at a concentration of $\sim 1.5\text{-}3$ mol/L [403, 410]), and left to harden *via* Eqs. 3.22 & 3.23. The variation in reactivity of MgO due to different impurities and calcination temperatures, combined with differing concentrations of MgCl_2 solution, has resulted in considerable variability in the reaction products formed and consequently the physical properties [411-412] of the hardened cements. Heat, whether applied externally or generated during hydration, alters the phases formed [413-414], as does carbonation [415], further complicating the discussion of which are the precise binding phases present in hardened MOC cements.

Although discussed here as a cementing system in its own right, magnesium oxychloride phases have also been found to exist as degradation products in high alumina cements and PCs due to chloride attack [416-417].

3.5.1 Phase composition

Early attempts to determine the composition of the MOC binding phase began with a series of experiments by Bender in 1871 [418], who concluded that $5\text{MgO}\cdot\text{MgCl}_2\cdot 17\text{H}_2\text{O}$ ($14\text{H}_2\text{O}$ when dried) was the binding phase formed, while Krause in 1873 [419] stated that $10\text{MgO}\cdot\text{MgCl}_2\cdot 14\text{H}_2\text{O}$ was the binding phase. This disagreement was resolved by Robinson & Waggaman [420] over 30 years later, who concluded that $3\text{MgO}\cdot\text{MgCl}_2\cdot 10\text{H}_2\text{O}$ is the stable product formed in the $\text{MgO}\text{-HCl}\text{-H}_2\text{O}$ system at $25\text{ }^\circ\text{C}$ when MgO is in excess.

The 3 phase was thus accepted as the key binding phase, supported by research by Paterson [407] and by Lukens [421], although reservations were stated regarding its actual water content. The crystalline water content of the 3 phase, and thus its full chemical makeup, was determined as $3\text{Mg}(\text{OH})_2\cdot\text{MgCl}_2\cdot 8\text{H}_2\text{O}$ by Walter-Lévy and de Wolff [422-423].

However, the 3 phase is not the only phase formed during the formation of MOC cements. A series of papers by Feitknecht [424-426] from 1926-30 analyzed the formation of MOC phases with varying MgCl_2 concentrations, and postulated that various phases (including 3-1-10 and 5-1-10) were forming, based on the first optical micrographs of needle-like crystals of MOC phases (as shown in Figure 3.14), and X-ray diffraction patterns for these phases. In 1944, Feitknecht once again confirmed the existence of the 5 phase, and revised the description of crystalline water content within the composition to $5\text{Mg}(\text{OH})_2\cdot\text{MgCl}_2\cdot 7\text{H}_2\text{O}$ [427], which is now known as the 5 phase.

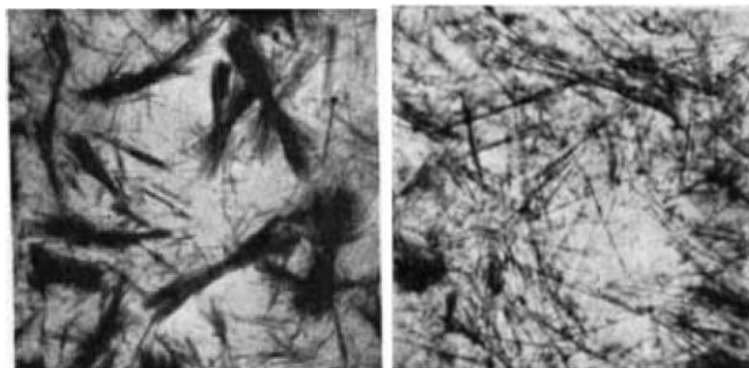


Figure 3.14 Optical micrographs of MOC phases precipitating from solution [424].

The formation of these two phases (3 and 5 phase) was reviewed by Walter-Levy [423] in 1949, who noted that the 5 phase formed principally in solutions containing >1.5 M MgCl_2 , although the excess MgCl_2 in solution gradually transformed the 5 phase to the 3 phase, while the use of MgCl_2 solutions <1.5 M instead yielded $\text{Mg}(\text{OH})_2$. The crystallographic details of these two phases were then accurately analyzed for the first time by de Wolff and Walter-Lévy [428-429], considering 8 crystal-bound water molecules to be present in both the 3 and 5 phases, with the 3 phase found to be triclinic, while the 5 phase was reported as monoclinic.

Much later, in 2007, Sugimoto et al. [430] provided crystal structure descriptions for both the 3 and 5 phases. The 3 phase was described as consisting of two $\text{Mg}(\text{OH})_4(\text{OH}_2)_2$ octahedra, forming chains with Cl and H_2O intercalated between them, forming the $\text{Mg}_2(\text{OH})_3\text{Cl}\cdot 4\text{H}_2\text{O}$ crystal. The 5 phase consists of two $\text{Mg}(\text{OH})_4(\text{OH}_2)_2$ and one $\text{Mg}(\text{OH})_6$ octahedra, forming a triple chain, with disordered intercalated Cl and H_2O , forming the $\text{Mg}_3(\text{OH})_5\text{Cl}\cdot 4\text{H}_2\text{O}$ crystal. Both crystal structures are displayed in Figure 3.15, along with the chlorocarbonate phase.

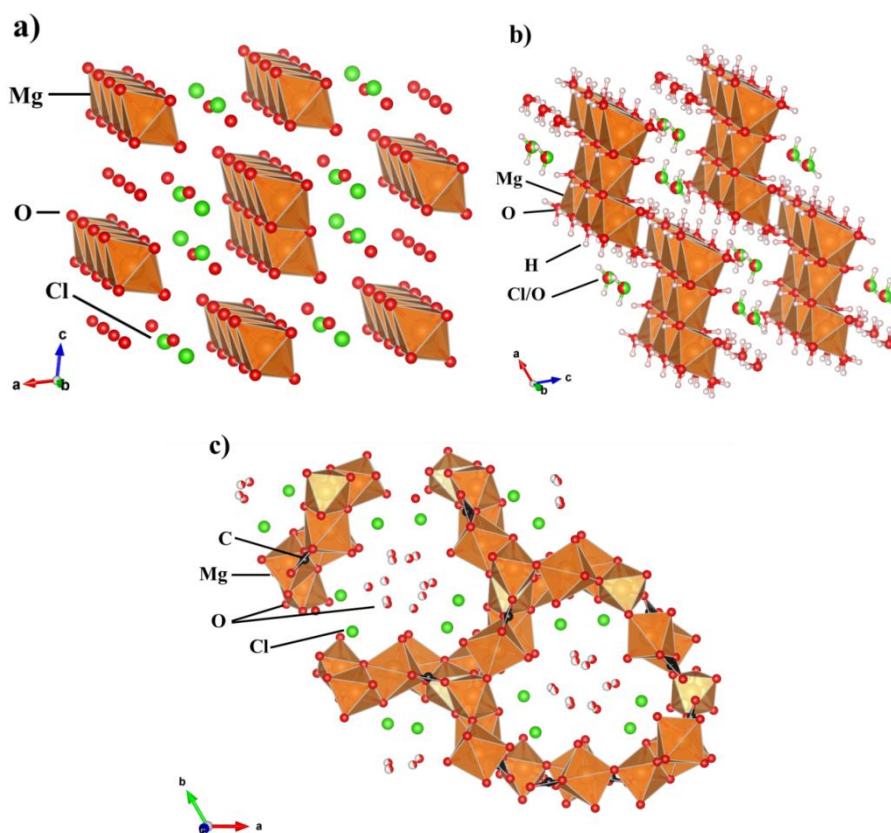


Figure 3.125 Crystal structures of the a) 3 phase b) 5 phase, and c) chlorocarbonate drawn from [429-431] (note that hydrogen positions are not defined in a) or c))

Another complicated and disputed matter is the proposed carbonation of MOC phases. The chlorocarbonate phase (sometimes called ‘chlorartinite’), was noted by Walter-Lévy [422] and defined by de Wolff [428] as $\text{Mg}_2(\text{OH})\text{Cl}\cdot\text{CO}_3\cdot 3\text{H}_2\text{O}$. This was much later clarified by Sugimoto et al. in 2006 [431], where chlorartinite was found to have a structure entirely different from that of artinite ($[\text{Mg}_2(\text{CO}_3)(\text{OH})_2]\cdot 3\text{H}_2\text{O}$ with Mg octahedra in zig-zag double chains), and was instead refined as $[\text{Mg}_2(\text{CO}_3)(\text{H}_2\text{O})(\text{OH})]\text{Cl}\cdot\text{H}_2\text{O}$ with Mg octahedra in 15-membered puckered rings. The importance of this phase in practical application of MOC cements will be discussed in more detail in section 5.2 below.

The understanding of phase composition became yet more complicated when in 1951 Walter-Lévy & Bianco [432] noted the appearance of two new phases that formed above 100 °C. These were characterized as 2-1-4 and 9-1-5, of which the 2 phase was not stable at room temperature, converting back to 3-1-8. The structure of the 9 phase was much later refined to 9-1-4 by Dinnebier et al. [433]. Bianco [414] performed an extended study of higher temperature phases, from 50 to 175 °C, suggesting the additional formation of 2-1-2 and 3-1-1; due to the significant heat of hydration evolved during the initial setting and hardening of MOC cements, the phases formed at temperatures greater than 100 °C have the potential to form within large blocks of the cement, even when poured at room temperature. While studying the 9-1-4 phase, Dinnebier et al. [433] postulated that this phase existed only as an intermediate strength-giving phase which rapidly formed during MOC hydration, and eventually transformed to the 3 phase (Figure 3.16). It was suggested that this was also true of the 5 phase, proposed to exist essentially as a metastable phase at room temperature, before stabilizing as the 3 phase [433].

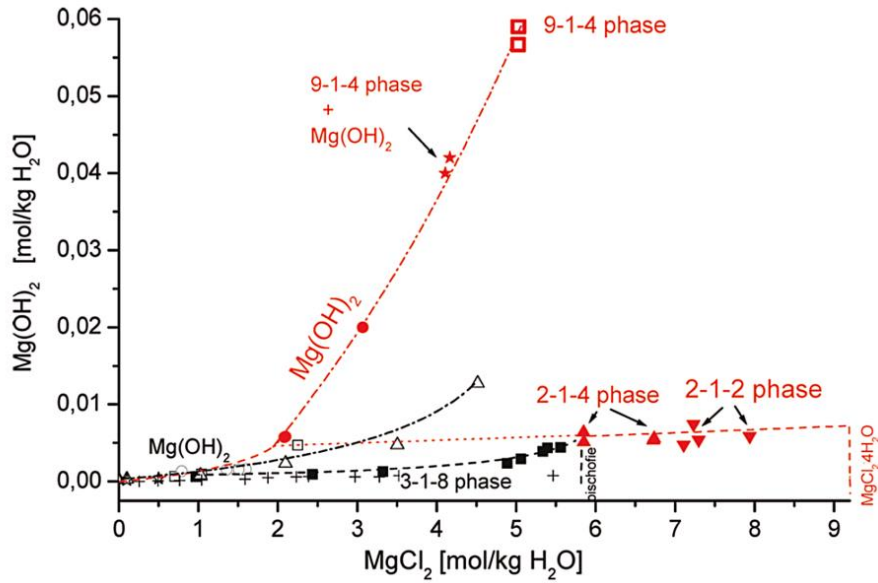


Figure 3.16 Phase equilibria at 120 °C (red) compared to literature data at 25 °C (black), as compiled by Dinnebier et al. [433]

The potential formation of these higher temperature phases was particularly highlighted by Newman et al. [434], where the heat generation of MOC was studied using a formulation that was likely to generate the 5 phase (expected to be the most exothermic). The internal sample temperature reached up to 147 °C, with a deleterious effect on strength. This leads to a complicated situation where MOC monoliths may experience spatial variations in phase assemblages as a function of the temperatures experienced during curing, as the high-temperature phases tend to persist for some time at room temperature upon cooling.

The thermal stability of the then-known MOC phases was analyzed by Cole & Demediuk in a 1955 thermogravimetric (TG)/differential thermal analysis (DTA) study [415]. Heating yielded a variety of stable hydrate forms of each phase, formed through stepwise dehydration, Figure 3.17. The proposed stable hydrate forms of each phase were:

- 2 phase: 4H₂O, 2H₂O, anhydrous
- 3 phase: 8H₂O, 5H₂O, 4H₂O, anhydrous
- 5 phase: 8H₂O, 5 or 4H₂O, 3H₂O, anhydrous
- 9 phase: 5H₂O, 2H₂O, anhydrous

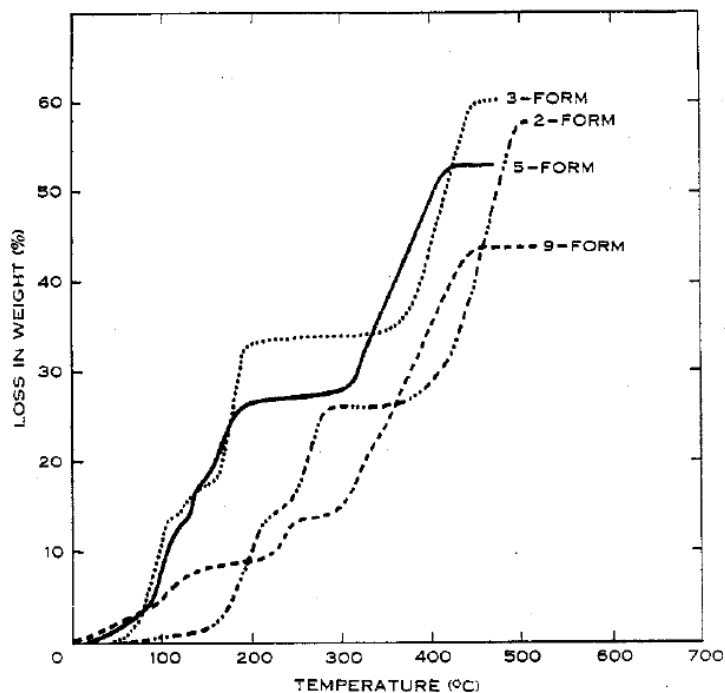


Figure 3.17 Thermogravimetric data for 2, 3, 5, and 9 phases up to ~500 °C [415].

Among the dehydrated phases proposed by Cole & Demediuk, the formation of lower hydrates of the 3 phase was again shown by Runčevski et al. in 2014 [435], who during synchrotron XRD & TG dehydration studies, observed and characterized 3-1-5.4 and 3-1-4.6 hydrates [435]. The high temperature phase 2-1-2 was confirmed in 2012 by Dinnebier et al. [413], as a lower hydration state of 2-1-4 formed by *in-situ* dehydration, with both phases forming as fine needles. These were both produced at elevated temperature in ~7 M MgCl₂ solutions, with lower concentrations resulting in 9-1-4 formation (as shown in Figure 3.18) [413]. Phases which have to date been identified are listed in Table 3.6:

Table 3.6 Phases observed in magnesium oxychloride cements

Phase	Composition	Characterized	Powder Diffraction File (PDF) card #	$\Delta_f G_m^\circ$ (kJ mol ⁻¹)
3-1-8	3MgO·MgCl ₂ ·11H ₂ O 3Mg(OH) ₂ ·MgCl ₂ ·8H ₂ O	de Wolff & Walter-Lévy [428-429]	00-07-0412	-2552 [436]
5-1-8	5MgO·MgCl ₂ ·13H ₂ O 5Mg(OH) ₂ ·MgCl ₂ ·8H ₂ O	de Wolff & Walter-Lévy [428] Sugimoto et al. [430]	00-07-0420	-3385 [437]
Chlorocarbonate (Chlorartinite)	Mg ₂ CO ₃ (OH)Cl·2H ₂ O (Sugimoto) Mg ₂ CO ₃ (OH)Cl·3H ₂ O	de Wolff & Walter-Lévy [429] Suigimoto et al. [431]	00-07-0278 00-50-1690	-
2-1-2	2Mg(OH) ₂ ·MgCl ₂ ·2H ₂ O	Dinnebier et al. [413]	00-012- 0133	-
2-1-4	2Mg(OH) ₂ ·MgCl ₂ ·4H ₂ O	Dinnebier et al. [413]	00-012- 0116	-
9-1-4	9Mg(OH) ₂ ·MgCl ₂ ·4H ₂ O	Dinnebier et al. [433]	00-007- 0409	-

Based on the development of this crystallographic understanding of the phases formed, it has also become possible to design and manipulate the phase equilibria within MOC binders, particularly to improve the durability and/or strength of the cements. High strengths are typically achieved through maximizing the rapid formation of the 5 phase, where the interlocking crystalline needles of this phase have long been believed to be the source of strength [415, 438]. Matković & Young

[439], however, suggested that needle interlocking was not the major source of strength, but rather that the needles formed in areas of porosity, which can result in the early stiffening of the paste. These authors state that once the voids are filled with crystallites, the MOC microstructure begins to densify, which was proposed to be responsible for the main strength gain.

In 1976 Sorrell & Armstrong published the first comprehensive phase diagram for MOC binders at room temperature [440], with formation of the 5 phase occurring only in a narrow window in the phase diagram. MOC is unstable in the presence of excess water, breaking down to MgCl_2 and $\text{Mg}(\text{OH})_2$, and conversion to hydromagnesite ($\text{Mg}_5(\text{CO}_3)_4(\text{OH})_2 \cdot 4\text{H}_2\text{O}$) may also result from chloride leaching [440]. Unreacted MgCl_2 can migrate to the surface of a monolithic sample, leading to unsightly white deposits (efflorescence), and unreacted MgO can cause dimensional stability issues, further affecting the durability of these cements.

In 1980 Urwongse & Sorrell [441] published a key paper on the solubility of MgO in HCl solutions at 23°C , that further refined the MgO - MgCl_2 - H_2O ternary diagram for a sealed system, Figure 3.18. They noted that due to the tendency of the 5 phase to form more rapidly than the 3 phase (as in Figure 3.19), previous experimental studies which analyzed samples after a few days of reaction might have concluded that the 5 phase has a greater range of stability than is truly the case at equilibrium, as it is metastable with respect to the 3 phase under various conditions. Urwongse & Sorrell also note that initial cement setting happens prior to evident crystallization of either the 3 or 5 phase, and therefore gel formation is crucial, suggesting that crystallization happens from a supersaturated solution; this may be related to an Ostwald step rule-like process. It was also noted that formulations aiming to produce the 3 phase react more slowly, and have a greater tendency to form the less soluble chlorocarbonates, than those dominated by the 5 phase.

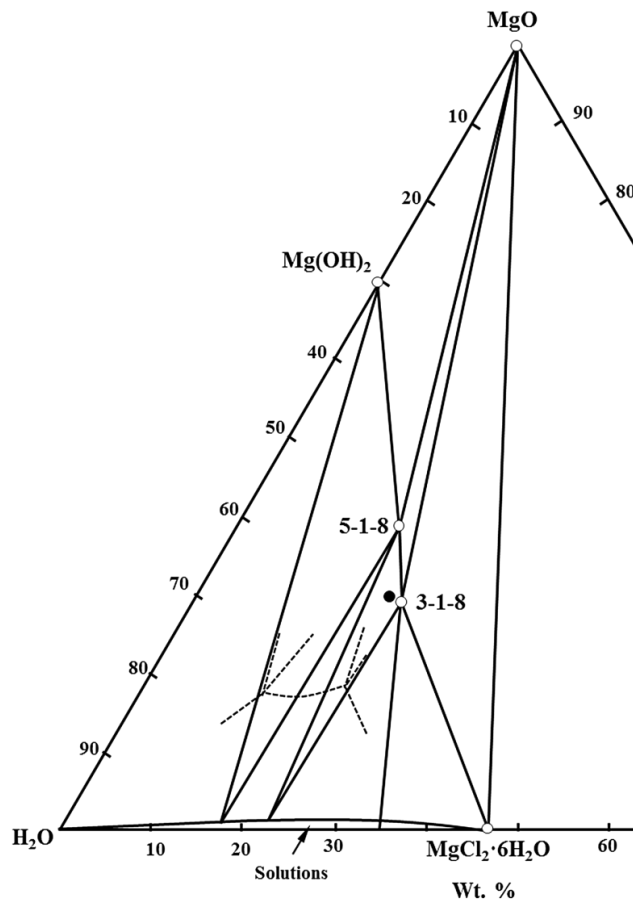


Figure 3.18 Phase diagram at 23 ± 3 °C of $\text{MgO-MgCl}_2\text{-H}_2\text{O}$, drawn from the findings of Urwongse and Sorrel [441]. The composition marked • corresponds to the time-resolved analysis presented in Figure 3.19.

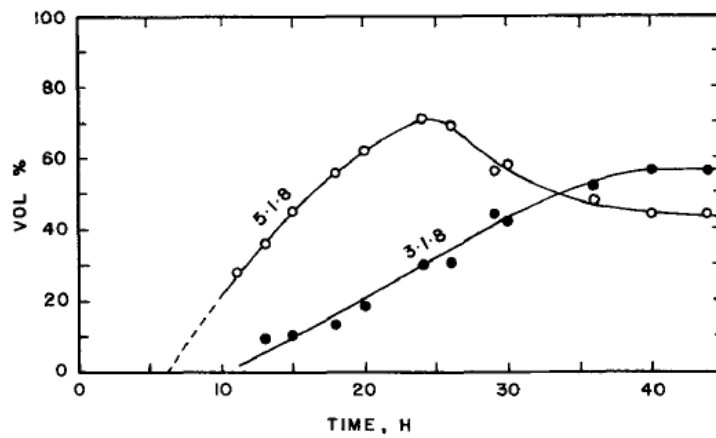


Figure 3.19 Relative amounts of 5-1-8 and 3-1-8 phases as a function of time, in the composition marked • in Figure 3.18 [441].

Chau and Li [412, 442-443] studied the varying effects of molar ratios on the strength and phase development in MOC binders within the ternary MgO-MgCl₂-H₂O system. These formulations were chosen to form MOC binders containing appreciable quantities of the 5 phase, to achieve void filling and early strength development. Very high strengths (up to 155 MPa) were achieved after 14 days of curing using excess MgO, leading the authors to state that this was required for a ‘good’ cement. However, a dead burnt magnesium oxide was used, resulting in non-equilibrium conditions due to the presence of remnant MgO. The authors stated that “excess or unconsumed MgO powder acts as a filler...”, however care should be taken as unreacted MgO can cause serious unsoundness (dimensional instability) in cements due to its slow hydration to Mg(OH)₂, which occupies a substantially larger volume.[444] It should thus be carefully considered whether the optimum formulation for MOC binders should contain substantial quantities of unreacted dead burnt MgO.

3.5.2 Chlorocarbonate: Relation to strength and durability

The tendency of the 3 phase to transform into a chlorocarbonate phase (Mg(OH)₂·MgCl₂·2MgCO₃·6H₂O) when exposed to ambient air,[415, 441] and the relationship of this process to strength and durability, raises important questions regarding the in-service properties of MOC cements. There are tentative indications that chlorocarbonate formation is welcome due to its lower solubility than the oxychloride phases, thus forming a semi-protective skin on top of the MOC cement [440]. This indicates that such a process may be desirable for external applications, especially when the material is used as a stucco, however few studies exist on the protective (or otherwise) nature of this phase.

Of these few studies, however, those that focus on the application of MOC during restoration of the Acropolis site in Athens are particularly insightful. MOCs (also named ‘Meyer stone glue’ in Greece) were used during restoration of the Erechtheion temple, partly due to the marble-like appearance achieved, during the 1970s. However, the subsequent degradation of the MOC has caused substantial damage to the Pentelic marble [445-446] due to staining and expansion. In 1999

Maravelaki-Kalaitzaki & Moraitou [447] studied some of these mortars, and noted that in line with the literature, mortars exposed to water were destabilized, dissociating to $\text{Mg}(\text{OH})_2$ and MgCl_2 in solution and with associated loss of strength. Although the chlorocarbonate phase could reduce leaching, its formation caused a large volume change which induced cracking in surrounding marble, causing considerable damage. This corroborates an earlier study by Castellar et al.[448], who found cracks in MOC polishing bricks which they assigned to dimensional changes during carbonation. Maravelaki-Kalaitzaki & Moritou also noted the presence of hydromagnesite in leached, carbonated mortars, potentially as a degradation product of chlorocarbonate [447].

The effect of chlorartinite (magnesium chlorocarbonate) on MOC durability was clarified somewhat in 2006, when Sugimoto et al.[431] found that although the presence of chlorartinite was not damaging *per se*, this phase can rapidly exchange water with the environment. Particularly, crystal water was lost simply through exposure to an inert gas atmosphere at room temperature, accompanied by a density change of >15%. This makes MOC binders containing chlorartinite highly susceptible to changes in humidity, with potential for associated cracking. This suggests that the chlorocarbonate phase is not as protective as has been proposed, especially if the cement is exposed to wide variations in humidity, as in an external service environment.

3.5.3 Influence of MgO calcination

The effect of MgO reactivity, and therefore the conditions of magnesite calcination, is crucial in defining MOC formation. Calcination for longer durations and at higher temperatures produces a less reactive MgO (i.e. ‘dead burnt’) [160], as noted in section 1.2. These effects were noted in the work of Harper [410], where increased calcination temperatures and various impurities were shown to delay the setting and exothermic events in MOC pastes. This significant retardation highlights the need for careful control and characterization of the magnesia used in the production of MOC binders.

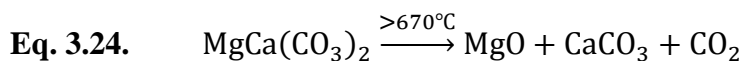
These findings were echoed by Bilinski & Alegret [449-450], who observed that the setting times and strengths of MOC varied widely as a function of magnesia calcination conditions. The calcination conditions can influence water demand (due to surface area), therefore affecting the ionic strength of the MgCl_2 solution used to achieve a binder with a given Mg/Cl ratio, and thus the phase formation. Generally, cements produced using magnesite calcined at 800-1000 °C produced substantially stronger cements than those calcined at less than 800 °C [410, 451], with reports of up to a factor of 10 increase in strength when comparing magnesia calcined at 600 °C to 1000 °C [410].

3.5.4 Cost-effective production

Shaw & Bole [404], writing in 1922, noted that the high production costs, and the frequent cracking and buckling of MOC floors, were significant disadvantages restricting MOC uptake at that time. The latter is now able to be better controlled due to the improved understanding of phase equilibria in the MOC system, but the former continues to be a problem. Attempts have been made to make use of locally available substitutes to reduce costs, including the use of bittern water (solutions left after sodium chloride precipitation from brines) instead of pure MgCl_2 solutions [452]. This has led to numerous regional revivals of MOC binders in areas where brines were abundant, especially around Salt Lake City, USA [453-454] and as evidenced by current research by the Qinghai Institute of Salt Lakes, China [412, 455-457].

Alongside the availability of MgCl_2 , the lack of widely distributed high-grade magnesite deposits has also historically severely hampered the adoption of MOC binders. This has resulted in several studies of the use of dolomite ($\text{CaMg}(\text{CO}_3)_2$) instead of magnesite for economic reasons [458-459], as it is much more widely distributed and easily available [404]. Several early patents claimed that dolomite could be used to produce MOC binders if the dolomite was carefully calcined by controlling CO_2 pressure and firing at ~750 °C to produce MgO and CaCO_3 [458-461].

Typically the thermal decomposition of dolomite is reported as a two stage decomposition, with Eq. 3.24 yielding MgO and CaCO₃, followed by CaCO₃ decomposition at higher temperature according to Eq. 3.10 [462]



These reactions often merge into an apparently single-step process in air [462], and varying decomposition temperatures are reported depending on mineral purity and decomposition conditions [459, 463-464], posing difficulties for CaO-free production of MgO. This is illustrated in the combined thermal analysis / XRD undertaken by MacKenzie & Reinhold [462] (Figure 3.20) where CaO begins to form very shortly after MgO is detected within the samples.

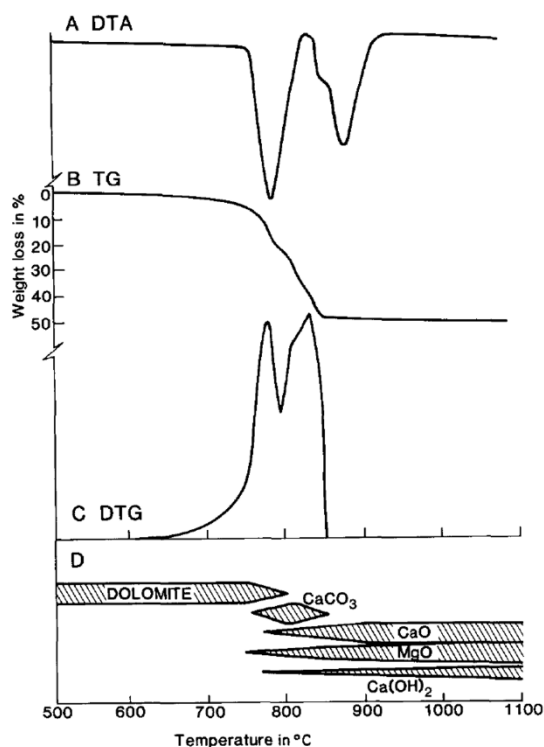


Figure 3.20 Thermal analysis of dolomite, including semi-schematic X-ray phase compositions in panel (D). DTA (panel A) was undertaken in a static autogenous atmosphere, TG/DTG (B and C) in flowing Ar, resulting in the differences in decomposition temperatures between the techniques [462].

If, however, the partial pressure of CO₂ is increased, the resulting decomposition regions are able to be separated [463]. The initial decomposition associated with magnesia formation can occur at a lower temperature (fully decomposing by

~800 °C) while CaCO₃ decomposition is pushed to a higher temperature, ~950 °C. McIntosh et al. ³²⁹ illustrated this (Figure 3.21), undertaking DTA analysis on dolomite under flowing N₂, then incrementally increasing the atmospheric concentration of CO₂ up to 100%. This clearly separates the constituent peaks [465], which would enable production of MgO without CaO co-formation.

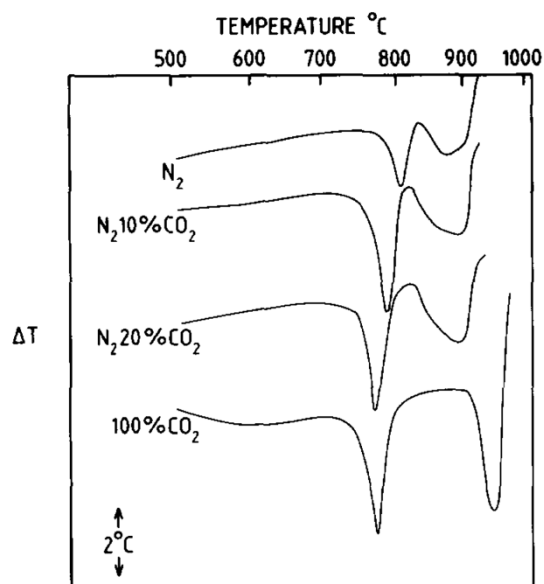


Figure 3.21 DTA curves for calcination of dolomite in varying atmospheres of N₂ to pure CO₂ [465].

The presence of impurities in dolomite has been shown to severely affect its reaction and usability as a source of MgO [466], and the avoidance of free CaO formation is imperative, as even as little as 2 wt.% of this impurity is detrimental to the service life of MOC binders [459].

Other attempts to improve MOC binders include co-formation of other oxychloride salts. Cations with a similar charge and crystal ionic radius to VI-coordinated Mg²⁺ (0.86Å), such as Zn²⁺ (0.88Å) and Cu²⁺ (0.87Å) [467], can also form oxychloride binders, as described for the first time in the patent literature in 1872, where MOC cements with partial or full replacement of MgO with ZnO were used for production of various articles [468-470]. The zinc oxychloride system was later characterized by

Sorrell [471], and was observed to form 4-1-5 and 1-1-2 phases, the latter of which is unstable in water.

In 1937 Hubbell added finely divided copper to MOC binders, forming cupric oxychloride and atacamite ($3\text{CuO}\cdot\text{CuCl}_2\cdot 3\text{H}_2\text{O}$) [472-473]. This was claimed to increase strength, reduce solubility and reduce efflorescence of the excess MgCl_2 . Various patents by Hubbell described the use of additions of finely divided copper metal or copper oxide [474-476], while copper sulfate and carbonate were later used by Whitehead [477]. Farrell & Wolff [478] demonstrated the antiseptic properties of these materials, and this characteristic is now exploited in the use of cupric oxychloride-containing flooring materials for commercial kitchens and work surfaces [479].

3.5.5 Water resistance

Another principal reason for the decline in usage of MOC binders has been the susceptibility of these materials to deleterious processes induced by exposure to moisture [420]. In moist conditions, the binding phases dissolve into a solution of $\text{Mg}(\text{OH})_2$ and MgCl_2 , resulting in the loss of the strength of the cement. Zhou [480] calculated that the 3 phase is unstable in a solution with $m_{\text{Mg}} < 2.25$ mol/kg, while the 5 phase is unstable where $m_{\text{Mg}} < 1.47$ mol/kg. Additionally, the release of MgCl_2 is particularly unwelcome near any structures containing steel reinforcing due to the risk of the chlorides causing significant steel corrosion. Additions of ‘waterproofing’ fillers have ranged from paraffin soaked sawdust [461] and Solvay process residues [481] at the turn of the 20th century, to additions of amorphous silica [482], and more recently coal fly ash [457, 483]. Melamine formaldehyde [484], latex (combined with glass fibers) and other polymers [485-486] have also both been used to shield MOC phases from water.

A promising development illustrated by several papers has been the use of small quantities of phosphates to improve the stability of MOC phases. This ability was claimed by Stewart in 1932 [487], however little substantial literature existed until the 21st century. Deng [488] investigated the effect of small phosphate additions (up to 1.7 wt.% phosphoric acid, NaH_2PO_4 or $((\text{NH}_4)\text{H}_2\text{PO}_4)$) on the properties of MOC

binders during immersion in water for 60 days. Phosphates were found to greatly improve compressive strength retention; up to 96 % of dry cured strength was retained when 0.74 wt.% H_3PO_4 was added, compared to 6.4% retention for the unmodified MOC. This was not attributed to the formation of insoluble magnesium phosphates, but rather it was observed that the phosphates reduced the level of free Mg^{2+} ions required in solution, and thus stabilized the 5 phase [488-489]. This was confirmed by Zhou et al., who found that a 0.5 wt.% addition of NaH_2PO_4 altered the conditions of phase formation in MOC, promoting the formation of the 5 phase and $\text{Mg}(\text{OH})_2$ [480], as demonstrated in Figure 3.22, where the phase boundaries are altered when phosphate is added. However, the precise mechanisms involved in enhancement of the water resistance of MOC cements by the addition of phosphate require substantial further research.

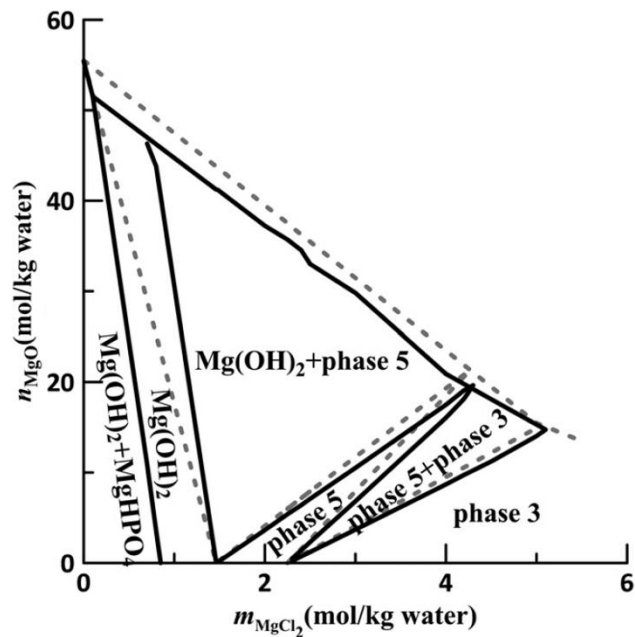


Figure 3.22 $\text{MgO-MgCl}_2\text{-H}_2\text{O}$ equilibrium phase diagram with 0.5% NaH_2PO_4 at 25 °C, 0.1MPa, with the phosphate-free diagram represented by dotted lines, edited from ref. [480].

3.5.6 Current uses for MOC

In the past decades, MOC binders have become less popular as flooring and stucco materials due to the issues related to their susceptibility to water damage, and their high costs relative to water-resistant PCs, or gypsum plasters which are similarly susceptible to water damage but usually less expensive. Nonetheless, there is continuing interest related to the fire resistance of MOCs, with particular interest in their use as a paintable substrate or internal plasterboard replacement. It is postulated that the large amount of crystalline water (typically ~35 % hydrated water by weight) in MOC phases, which requires a large amount of energy to liberate, combined with the ability of MgO to effectively reflect heat, gives MOC binders good heat resistance [490]. Both the 3 and 5 phases decompose *via* stepwise dehydration, followed by dissociation and degradation to MgO and HCl by 600 °C [456]; this release of hydrochloric acid upon heating must be considered as a point of caution related to the use of MOC binders for fire protection in domestic applications.

The ability of MOCs to incorporate wood filler was exploited to produce ‘woodstone’ panels, which have the appearance of chipboard and ability to hold screws and nails, but are fire resistant [491-492]. Closely related are ‘magnesium oxide boards’, which are often MOC blended with perlite, and used to replace plaster boards [493-495]. Although fire resistant, these boards are often marketed as carbon neutral or ‘eco’ products, due to the use of magnesia and the low temperatures used in production. Though magnesia is not an eco-material *per se*, a reduction in the heat required to form these boards has the potential to offer energy savings. Alongside wood fillers, the lower alkalinity of MOCs compared to PCs also enables the incorporation of glass fiber reinforcement. Several patents exploit this characteristic to produce reinforced cement boards [496-498].

Several niche industrial applications for MOC cements also exist, such as:

- Temporary oil-well cements, accommodating varying additives, which are acid soluble when the need for their removal arises [499-502]
- Usage during rock salt and potash mining to seal brine intrusions [433, 503-504]

- Stabilization of nuclear waste repositories hosted in salt mines. MOCs are currently being used in the Asse II geological repository in Germany, where saline intrusions and instability require the use of a highly salt tolerant cement [505-506]. These are also proposed for use in a future high level waste repository in a salt dome in Gorleben, Germany [507-508].

3.5.7 Conclusions

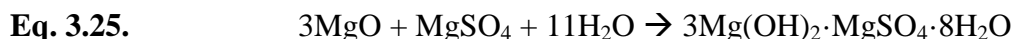
Beyond these technical uses and applications in wall-board production, there is probably little prospect for a large-scale resurgence in MOC binders. The continuing complexity associated with ensuring a well-developed binding system, combined with the inherent instability and solubility issues of the major phases when in contact with water, will continue to limit their applicability. In wall-board applications, the market is more accustomed to gypsum-based products, which are produced on a much larger scale and a lower cost in many countries. Carefully quality controlled production and blending of a ‘just add water’ MgO-MgCl₂ mix at an industrial plant can certainly lead to production of a viable cement for production of precast items, however the deliquescent nature of MgCl₂ severely affects the ability to store and market such a cement. Magnesium oxychloride cements are, therefore, likely to remain a niche product for specialized applications, other than in areas where magnesium salts are very inexpensive and where they may offer cost savings compared to gypsum.

3.6 Magnesium oxysulfate cements

3.6.1 Phase composition

Magnesium oxysulfate (MOS) cements are similar in concept to MOC cements, except that MgSO₄ is used instead of MgCl₂. A similar nomenclature scheme is applied to the $x\text{Mg}(\text{OH})_2 \cdot y\text{MgSO}_4 \cdot z\text{H}_2\text{O}$ phases, which are thus described analogously as the ‘3-phase’, ‘5-phase’ and so on, however these phases are not isostructural to those formed in oxychloride cements which share the same names.

Typically, formation will follow Eqs. 3.25. & 3.26 (the latter if heated), though several other phases can also be formed.



The history of these cements began with a patent granted in 1891 to Enricht for “Artificial stone or cement” [509], which specified a combination of magnesium oxide, magnesium sulfate and water, which “*forms an oxysulphate (sic.) of magnesium, which on drying becomes a very hard cement or stone*”. This was quickly followed by a similar 1892 patent, which included egg albumen, and claimed to form a cement which was not attacked by the climate [510].

MOS cements gained interest due to the less hygroscopic nature of magnesium sulfate compared to magnesium chloride [487, 511-512], and hence claimed superior resistance to weathering [513]. This enabled easier shipping and a longer shelf life for bagged cements. These cements, however, find fewer applications and consequently there is much less literature available compared to MOC cements. MOS cements are more difficult to form due to the limited solubility of $\text{MgSO}_4 \cdot 7\text{H}_2\text{O}$ at room temperature, but the development of these materials based on sulfates does avoid the use of chlorides, making them significantly less damaging to steel reinforcing, although they still suffer from poor water resistance.

In 1892 Thugutt undertook a study on basic sulfates of magnesium and zinc [514], reporting the formation of $6\text{Mg}(\text{OH})_2 \cdot \text{MgSO}_4 \cdot 3\text{H}_2\text{O}$, but little further literature emerged until the 1930s, when Walter-Lévy [515] studied the formation of carbonated magnesium sulfates. This work entailed additions of potassium carbonate or bicarbonate to a concentrated solution of magnesium sulfate, yielding $\text{Mg}_4(\text{OH})_2(\text{CO}_3)_2\text{SO}_4 \cdot 6\text{H}_2\text{O}$, which reverted to an oxysulfate over time. The authors identified in particular the formation of $3\text{Mg}(\text{OH})_2 \cdot \text{MgSO}_4 \cdot 8\text{H}_2\text{O}$ (the 3-1-8 MOS phase) [516], later characterized in crystallographic detail by Dinnebier et al. [517].

In 1957, Demediuk & Cole [518] undertook a comprehensive study of the MgO - MgSO_4 - H_2O system by analyzing precipitates from saturated solutions of MgSO_4 to which MgO was added, at temperatures from 30 to 120 °C. They identified four

magnesium oxysulfate phases, (3-1-8, 5-1-3, 1-1-5 and 1-2-3) which are among the known MOS phases detailed in Table 3.7.

Table 3.7 Phases observed in magnesium oxysulfate cements

Phase	Composition	Most detailed crystallographic characterization	PDF card #
3-1-8	$3\text{Mg}(\text{OH})_2 \cdot \text{MgSO}_4 \cdot 8\text{H}_2\text{O}$	Dinnebier et al. [517]	00-07-0418
5-1-3 (or 2)	$5\text{Mg}(\text{OH})_2 \cdot \text{MgSO}_4 \cdot 3\text{H}_2\text{O}$ (or $2\text{H}_2\text{O}$)	Demediuk & Cole [518]	00-07-0415
1-1-5	$\text{Mg}(\text{OH})_2 \cdot \text{MgSO}_4 \cdot 5\text{H}_2\text{O}$	Demediuk & Cole [518]	00-13-0341
1-2-3	$\text{Mg}(\text{OH})_2 \cdot 2\text{MgSO}_4 \cdot 3\text{H}_2\text{O}$	Demediuk & Cole [518]	00-13-0349
5-1-7	$5\text{Mg}(\text{OH})_2 \cdot \text{MgSO}_4 \cdot 7\text{H}_2\text{O}$	Runčevski et al. [519]	

The formation of these phases is strongly influenced by temperature, as is the solubility of MgSO_4 , which greatly increases with temperature. This increases the concentration of MgSO_4 in solution, enabling the precipitation of the 1-1-5 and 1-2-3 phases which contain higher proportions of MgSO_4 . The construction of a phase diagram (Figure 3.23) identified several conditions where pure phases could precipitate, and many mixed-phase areas, although the as-drawn shapes of the boundaries of some of the regions identified do appear unusual in a thermodynamic sense.

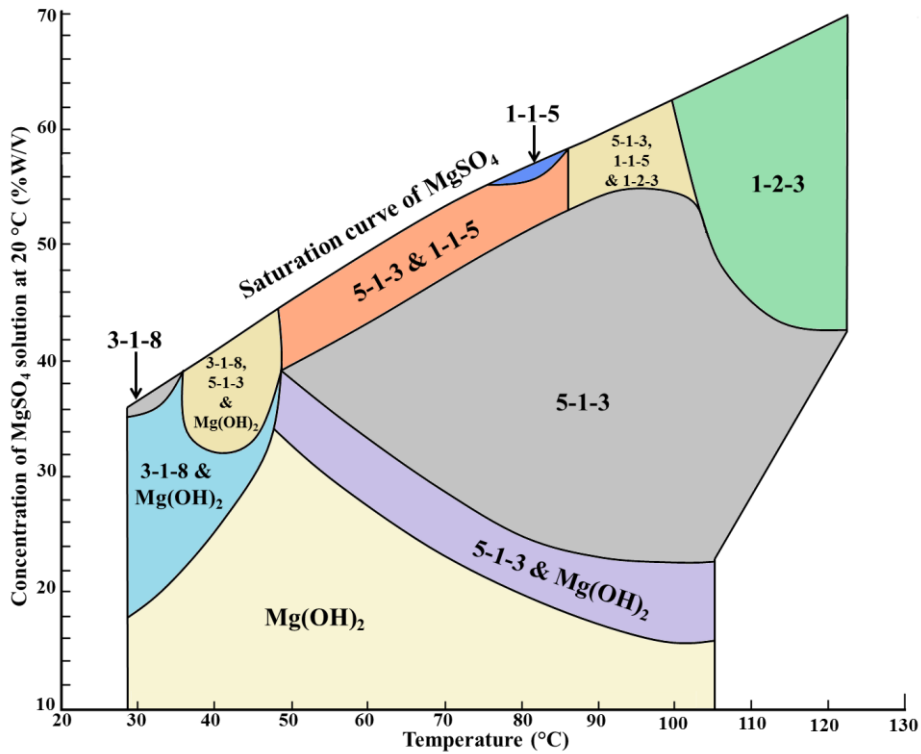


Figure 3.23 Phase equilibria in the system MgO-MgSO₄-H₂O, redrawn from [518]

Of particular interest is the existence of a single-phase Mg(OH)₂ region at low concentrations of MgSO₄, as this conclusively shows that MOS phases are not water-resistant, with phases liable to dissociate to Mg(OH)₂ in weak MgSO₄ solutions or pure water. The degree of instability depends on temperature, reaching a maximum in solubility at ~47 °C.

Urwongse & Sorrell [520] developed a ternary phase diagram for MgO-H₂SO₄-H₂O at 23°C, Figure 3.24, where H₂SO₄ was used instead of the MgSO₄ in Figure 3.23. It was determined that the 3-1-8 phase was the main phase formed under a broad range of conditions, along with Mg(OH)₂ and hydrated forms of MgSO₄. The 1-1-5 phase was also observed, however it was metastable at 23 °C. It was postulated that in commercial cements, the 5-1-3 phase is the most desirable in terms of strength development characteristics, but also noted that this can be only formed as a stable phase under steam curing conditions.

The formation of only a limited number of stable phases at near-ambient temperature is in good agreement with the results published by Demediuk [518], where only the 3 phase and $\text{Mg}(\text{OH})_2$ were observed at 30 °C (Figure 3.23). The 5 phase exists alone in a stable range between 50-120 °C, with a peak in stability at 100 °C, and in combination with the 3 phase and $\text{Mg}(\text{OH})_2$ at 40 °C. Given the wide range of phases formed at elevated temperatures, there is a clear need for further ternary studies at temperatures of up to 120 °C.

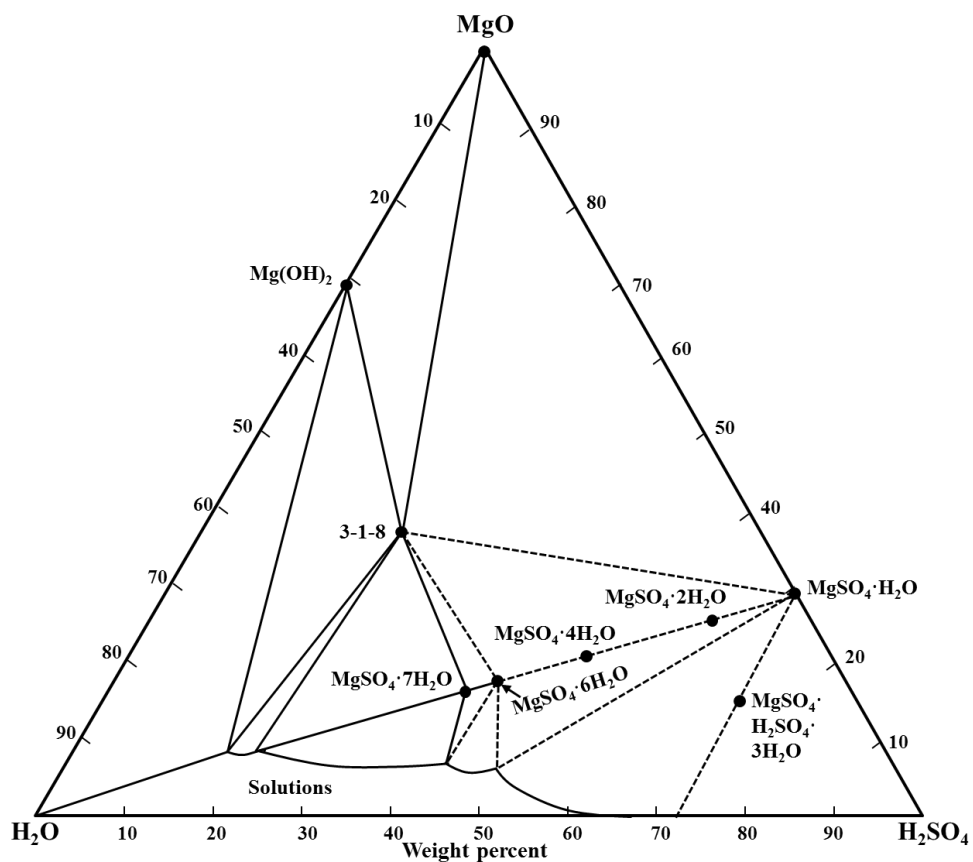


Figure 3.24 Phase diagram for the system $\text{MgO-H}_2\text{SO}_4\text{-H}_2\text{O}$ at 23 ± 3 °C, drawn from [520]

More recently, Dinnebier et al. [517], Runčevski et al. [519] and Wu et al. [521] revisited the field of MOS cements with modern analytical techniques. Dinnebier et al. [517] carried out equilibrium experiments in the MOS system, from which it was concluded that the 3-1-8 phase was unstable at room temperature, with the 5-1-2 phase reported as being the most stable. The 3-1-8 phase was found to form from a

solution supersaturated in Mg^{2+} , while the 5-1-2 phase could be induced to form from an undersaturated solution *via* equilibration of an MgSO_4 solution with 3-1-8 precipitates (Figure 3.25). This suggests that the 3-1-8 phase is actually a metastable phase at room temperature, not the final stable product as previously believed. Those authors also undertook detailed high resolution synchrotron X-ray diffraction characterization of the 3-1-8 phase, refining its structure (Table 3.7). It was also determined that the 5-1-3 and 5-1-2 phases were essentially the same structure, with 5-1-2 being a more correct description of the basic chemistry of this phase. Scanning electron micrographs of 5-1-2 and 3-1-8 crystals showed that the former consists of long needles, whilst the 3-1-8 phase forms flaky crystals. This interlocking needle-like structure (as previously discussed in the MOC section), and its space filling properties, are now understood to be the reasons why the 5-1-*n* phase is preferred for strength gain in industrial applications.

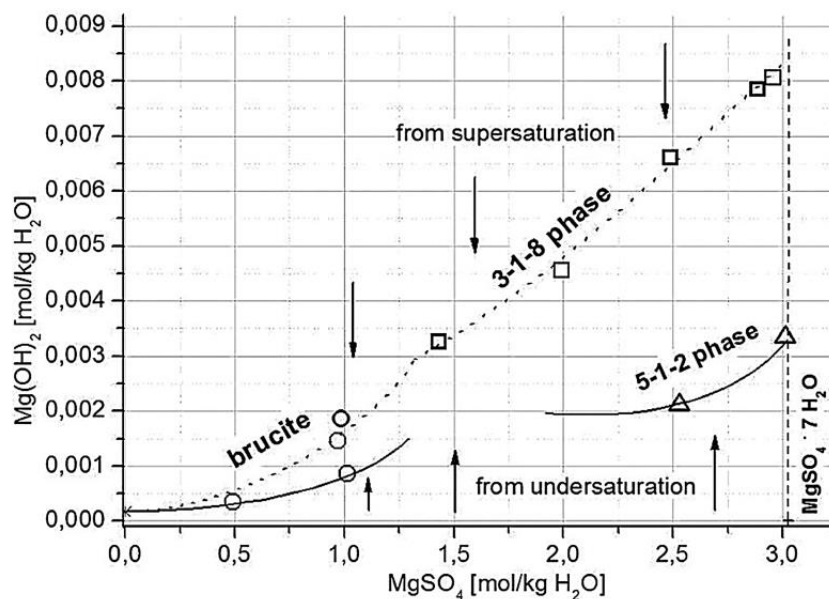


Figure 3.25 Solubility diagram at 25 °C for the MOS system [517].

Wu et al. [521] reported the effects of phosphate additives in MOS cements at 23 °C, and postulated that a 5-1-7 phase formed from high levels of MgO when phosphates were added to an MOS system. The approach used in this study differs from most of the MOS literature, as very high levels of MgO were used, whereas it is typical in

most studies to slowly add MgO into solutions of MgSO₄, and investigate the precipitated phases. However, the MgO used by Wu et al. was only 80% pure, and the impact of impurities on the results is not known. This paper was followed by crystallographic analysis of the 5-1-7 phase [519], where it was shown to form needle-like crystals. It was claimed that the new 5-1-7 phase could be produced by adding quantities of MgSO₄·7H₂O to water, then adding MgO and citric acid, and curing at 20 °C for a week. However, there has not yet been confirmation of the thermodynamic stability of this phase which would enable it to be incorporated into the phase diagram of the system, and the fact that additives (phosphate or citric acid) seem to be required for its synthesis indicate that it is likely to be a metastable rather than stable phase.

3.6.2 Hydrothermal production of magnesium oxysulfates

The temperature-dependent solubility of MgSO₄ has been shown to result in the formation of different phases, which has been studied in cements up to 120 °C [518]. The formation of MOS phases at higher temperatures has been reported, especially around hydrothermal vents on ocean floors, where it was discovered that the heating of seawater to 325 °C resulted in MOS phase precipitation [522]. This was followed by numerous studies on varying MOS phases found around hydrothermal vents (therefore exposed to higher temperatures and/or pressure), or from heating seawater compositions, including 1-3-1 [523], 5-1-4 [524], 2-1-0 [525], 1-2-2 [526] and caminite (2-5-1) [527]. Although none of these have been used for cementitious purposes, their existence demonstrates the potential to push the MOS system beyond the limit of saturated steam curing. Also related to these topics are various papers on hydrothermal preparation of magnesium oxysulfate whiskers, for use as precursors for MgO nanowires *via in-situ* thermal decomposition, resulting in the formation of the 5-1-2 / 5-1-3 phase at temperatures of up to ~200 °C [528-531].

3.6.3 Current uses for MOS

Usage and analysis of MOS cements in the last 50 years has been largely confined to patent applications, with many patents describing the use of oxysulfate binders in the production of steam cured panels or sheets, where steam curing is applied to reduce the solubility of MgSO_4 by favoring formation of more MgO-rich hydrates, and also to accelerate strength development. The earliest of these was by Biefield in 1955 [532], who patented a method of producing MOS structural sheets, heating these to 77 °C in order to form a strong product. This patent also makes use of the lower pH of MOS than PC to enable the use of glass fiber reinforcement, as is also done in MOC systems. Pressurized steam at temperatures up to 121 °C can also be used to form 5-1-3 phase cubes [533] with a curing time of less than 20 minutes, to enable rapid production of potentially commercially viable products.

3.6.4 Conclusions

Magnesium oxysulfate cements are extremely niche products, although at present there are very few applications that utilize MOS as a modern cementitious material. These materials appear to suffer from the same susceptibility to water as MOC binders, and are therefore not useful as structural cements. The low solubility of MgSO_4 necessitates steam curing to produce many of the phases. This quite possibly limits MOS cement usage to internal boards or faux-wood panels which can be quickly produced, as well as sprayable fireproof coatings. However in this instance there are few obvious benefits over using alternative existing commercial products, such as gypsum based internal boards.

3.7 Perspectives: What is the future of Mg-based cements?

The outlook for magnesia-based cements is one of cautious optimism. In their various guises, these cements are sometimes raised on pedestals as potential saviors of the built environment in the 21st century, but generally without appreciation of their inherent physical and economic limitations. These cements will continue to find a place in niche applications, where PC is unsuitable due to required physical or

chemical properties. Magnesium phosphate cements have applications in environments requiring near-neutral pH cements and for rapid repair, especially in cold environments. Magnesium silicate cements will likely be hindered by a lack of commercially viable sources of reactive silica, unless coupled with carbonate cements in a multi-phase binder. These are also very technically immature, with fundamental physical properties of this binder yet to be understood. Large scale reinforced concrete applications are unrealistic due to the inability of both magnesium phosphate and silicate cements to passivate mild steel, and also the significant cost premium over well-established PC blends. Oxysalt based cements are likely to remain very low-volume products due to poor water resistance, despite over 100 years of research. For dry internal applications these cements compete against now well established gypsum-based cements, such as plaster of Paris, with few benefits which justify the added complexity of producing a Sorel or oxysulfate cement binder.

Magnesium carbonate cements appear to hold the strongest prospect for the future, especially in lower-value precast applications such as blocks or tiles which can be produced and cured close to point-source emitters of CO₂ such as fossil fuel power stations. These cements need to be properly formulated, however, with appreciation of magnesite calcination emissions and the degree to which carbonation might occur throughout the material. CO₂ savings are possible through the use of these materials, especially if magnesia can be produced from widely distributed magnesium silicate minerals, however detailed life-cycle validation and optimization are required before these can truly be claimed to be carbon neutral cements. Equally, durability testing is essential, as the long-term properties of most magnesium cements are unknown, reducing their appeal as modern building materials.

The global push for other alternative cements such as geopolymers, CSA cements and more eco-friendly blended optimized PC systems will provide strong competition against Mg cements. The future of the construction industry is likely to be one in which the norm becomes a suite or toolkit of cements tailored to specific applications, as Portland-based cements come under increasing environmental pressure. Magnesium based cements can form part of this suite, but are unlikely to provide a magic bullet in terms of large-scale like-for-like replacement of PC in key

construction applications. Nonetheless, the future of this class of cements does on balance appear promising.

3.8 Conclusions

This review has presented an overview of current and historical research and applications of magnesia based cements, including oxysalt, silicate, phosphate and carbonate systems. The manufacture and durability of these cements has been discussed in relation to their formulations and constituent materials. These cements occupy niche positions within industry today, but have in recent years gained increasing attention as solutions are being sought for the challenges facing the cement and construction industries in the 21st century. Although magnesia cements have been researched for nearly 150 years, fundamental issues remains concerning their long-term durability and cost-effectiveness, especially regarding more recent additions to this family such as magnesium silicate and carbonate cements. Production of reinforced concrete or large-scale cast-*in-situ* construction work would seem to pose significant technical challenges across the class of magnesia-based cements, but there are certainly smaller-scale applications involving production of unreinforced elements under controlled conditions which are promising and approachable. However, care should be taken before magnesia-based cements can be heralded as environmental saviors for the construction industry, as considerable research and development efforts are required before any of these cements could come close to providing a sustainable alternative binding system fit for large-scale usage in the 21st century.

Within the content of Magnox sludge, this review has highlighted the disparate nature of magnesium cements, which are not a homogeneous body of chemistries. Oxysalt based cements are unlikely to be of use due to their susceptibility to water, despite countless attempts over the years to improve their resistance. Phosphate systems are likely to react far too rapidly with fine Mg(OH)₂ bearing sludge material, as these typically require dead burnt, calcined MgO to slow down reactions. Carbonate cements are more promising, but currently require extensive *in-situ* elevated carbonation, often in the form of aerated or porous blocks. Although

potentially suitable for some precast applications, this is unlikely to work with nuclear wastefoms. This leaves magnesium silicate cements as the remaining magnesium-based cement system which holds some promise. The feasibility of this is, however, likely to be determined by the availability of reactive silica sources and as to whether $\text{Mg}(\text{OH})_2$ rich sludges can be induced to react to form such a binder.

4 Experimental

4.1 Analytical Methods

4.1.1 X-Ray Diffraction (XRD)

X-ray diffraction is a powerful tool for identification of crystalline phases, and in this thesis is used in the form of powder X-ray diffraction for often complex materials containing many natural and synthetically produced mineral phases. The principles of X-ray diffraction involve the diffraction of X-rays by a crystalline lattice in a manner that is characteristic of that crystal. When a crystalline sample is exposed to an X-ray, incident X-rays are scattered by the atoms within the lattice planes, interfering either destructively or constructively when diffracted. This interference produces characteristic diffraction intensities which are the basis of phase identification. This is described in Bragg's law, Eq 4.1:

$$\text{Eq. 4.1} \quad 2d\sin\theta = n\lambda$$

Where θ is the angle of scatter, d is the distance between lattice planes, and λ is wavelength, as shown in Figure 4.1. The lower X-ray depicted in Figures 4.1 travels an extra distance equal to $2d\sin\theta$, which if this is an integer multiple (n) of the wavelength of the X-ray, will constructively interfere. Waves out of phase with one another will destructively interfere, and will not appear as intense regions on the diffraction pattern.

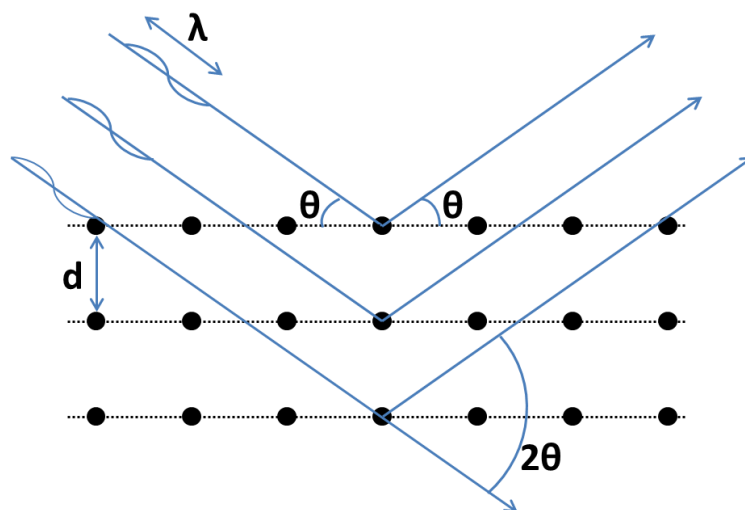


Figure 4.1 X-ray diffraction in a crystal lattice

This crystalline diffraction is able to occur with X-ray radiation as the wavelengths involved are typically smaller than the crystal lattice d spacing (e.g. 1.54 Å for Cu $K\alpha$ radiation). X-ray radiation is generated in an X-ray tube, containing a source of electrons and a high voltage maintained across two electrodes. Electrons are drawn to the anode (target), producing X-rays on impact [534]. The X-ray spectrum produced depends on the anode material, which for cements is typically Cu, or Co if used for samples containing high levels of Fe [535-536]. The anode material ejects electrons from the K shell, resulting in electrons from mainly the L shell, but also from the M shell dropping down to fill this energy level, de-exciting the nucleus. This movement from the L or M shells down to the K shell is accompanied by a release of energy in the form of characteristic X-rays, noted chiefly as $K\alpha$ (both $K\alpha_1$ and $K\alpha_2$) and $K\beta$, as in Figure 4.2.

This resulting X-ray radiation consists of sharp peaks ($K\alpha$ doublet and $K\beta$), but also polychromatic bremsstrahlung radiation caused by deceleration of the electrons. This, along with the $K\beta$ is typically filtered out with a monochromator (typically Ni for a Cu source), resulting in nearly monochromatic radiation remaining [534-535].

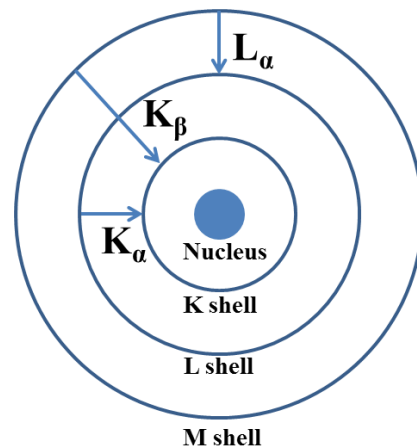


Figure 4.2 Electronic transitions in the atom (adapted from [534])

This radiation is then used for the diffraction experiments, be it powder (as typical for cements) or single crystal analysis. The diffraction patterns collected can be checked against known patterns for phases of interest, provided that the material in question is crystalline. X-ray diffraction is not as useful for semi-crystalline or amorphous material, resulting in broad, diffuse diffraction patterns due to the lack of long range order in these materials.

All the samples analysed in this thesis *via* X-ray diffraction were studied using a STOE STADI P diffractometer, using an imaging plate detector (IP-PSD). Cu K α (1.5418 Å) radiation was used, collecting data between $10^\circ < 2\theta \leq 70^\circ$, and angle corrected using a silicon standard (NIST 640d) to ensure accurate determination of peak positions.

Samples were prepared *via* grinding in an agate mortar and passing the resultant powder through a 63 μm brass sieve. This powder was sandwiched between two pieces of Scotch® Magic Tape, which is X-ray transparent. This enabled sample mounting without requiring glue, which might have re-hydrated the cement powders, and was fastened within the sample holder. The resultant diffraction patterns were analysed *via* STOE Win XPOW 2.1, using the ICDD PDF-2 database [537].

4.1.2 Fourier Transform Infra-Red Spectroscopy (FTIR)

Infrared spectroscopy is the observation of the vibrations of bonds in molecules through excitation by infrared radiation. Bonds between atoms vary between molecules, dependent on the strength of the bond and the size of the atoms involved. Not all bonds are useful in FTIR, however, molecule must be “infrared-active”, meaning it requires a dipole which changes due to expansion and contraction of the molecule. An example is the water molecule, H_2O , some of the vibrations of which are shown in Figure 4.3. The vibrational modes of diatomic molecules are relatively simple, only having one mode due to one bond (although this may not be IR active if symmetrical, such as in N_2), whereas polyatomic molecules can have many bending and stretching modes [538-539].

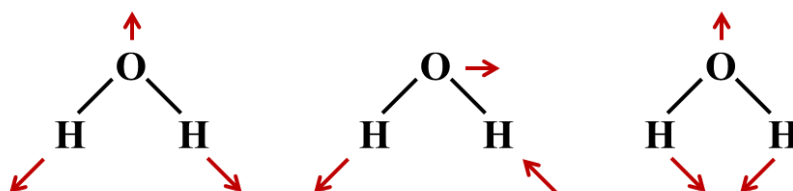


Figure 4.3 Vibrations within H_2O (drawn from [540])

FTIR utilises a two-beam interferometer as the basis for spectroscopy. In this infrared radiation is emitted, then split in half by a beam splitter. Half is sent to a fixed mirror, while the other half is sent to a moveable mirror. These both reflect back, and recombine. The beams interfere either constructively or destructively depending on the location of the moveable mirror, resulting in a beam which contains many frequencies of IR radiation at once, rather than just a monochromatic source. This enables scanning over a wide range of frequencies very quickly.

Molecules absorb infrared radiation at frequencies corresponding to the vibrational frequency of the infrared active bonds within the molecules. This allows a comparison between the emitted and transmitted IR spectra to be obtained, with absorption occurring where there is a corresponding vibration of a bond within the material. As the beam contains many wavelengths, the transmitted beam is Fourier transformed to process the data into a usable plot of data. Typically this is displayed

as a plot of transmittance against frequency, the latter of which is usually displayed as wavenumber (cm^{-1} : the number of waves occurring within 1 cm) [538, 540].

In this thesis all samples were analysed using the KBr disc method. This consists of grinding and pressing a pellet consisting of 2 wt. % powdered dried sample in anhydrous KBr. This allows a support matrix for the powdered sample, while the KBr does not exhibit absorption of any IR radiation within the mid-IR region of interest ($4000\text{-}400\text{ cm}^{-1}$).

Most of the samples analysed within this thesis were studied using a Perkin Elmer Spectrum 2000 spectrometer in mid-IR mode, using the KBr method above. The only exceptions are 18 month cured samples in Chapter 8, which were analysed on a Perkin Elmer Frontier FTIR using the KBr method in transmittance mode. This change was due to the previous instrument being retired from service, and replaced with a more modern instrument.

4.1.3 Nuclear Magnetic Resonance (NMR)

This technique is used to provide structural information about local ordering at an atomic level, which is especially useful for poorly crystalline or amorphous materials that are not structurally identifiable using X-ray diffraction or other characterisation techniques [541]. NMR spectroscopy takes advantage of the natural magnetic moment of certain nuclei to obtain information about the nuclei in question, and the effects of neighbouring nuclei. This technique can only be undertaken on nuclei with a non-zero spin (I), such as (typically within cements) ^1H (spin $+1/2$), ^{27}Al (spin $+5/2$) and ^{29}Si (spin $+1/2$). This excludes common nuclei such as ^{12}C or ^{16}O , which have a spin of 0, however ^{13}C can be used instead, with a spin of $-1/2$ [542-543].

This spin results in a magnetic moment within the nuclei, the energy levels of which can be split in a strong magnetic field. The nuclear magnetic moment is quantised into $2I+1$ levels, which for a spin- $1/2$ nuclei results in two energy levels between which the magnetic moment of the nuclei are split. The energy difference between these levels is the basis behind NMR spectroscopy, with transitions between the levels only possible by the absorption or emission of photons in the radiofrequency (rf) region [543-544]. The nuclei themselves do not all experience the same rf resonances, as they are magnetically shielded by surrounding electrons, which vary due to structural or geometric differences within the material. This results in a different resonant frequency, which is recorded as a change in chemical shift. This makes NMR especially useful for studying short-range order within materials.

A simple NMR experiment consists of preparing the nuclei by placing it within a magnetic field, then exposing it to a pulse of rf radiation at the Larmor frequency of the nuclei in question. Each nucleus has a different Larmor frequency, meaning each experiment is highly selective to the nuclei being studied. Once the rf pulse is switched off, the nuclei relax back to thermal equilibrium. This relaxation induces a voltage in the surrounding coil within the NMR instrument. This is known as the Free Induction Decay (FID), recorded over time. This can be Fourier transformed to give a plot of amplitude against frequency, the latter of which is recorded as a chemical shift relative to a known standard. As noted above, this chemical shift is highly dependent on the local structure around the nuclei in question [543].

NMR experiments undertaken on solid state materials have an added complication compared to liquid state NMR. Within the liquid state, the constant movement of the atoms results in an averaged magnetic shielding applying across all the nuclei evenly, resulting in narrow NMR spectra. In the solid state the uneven magnetic moment distribution, both direct and indirect spin-spin coupling, and quadrupolar coupling, all conspire to produce broad spectra [541, 543]. It was found, however, that physically spinning the samples at 54.74° to the axis of the magnetic field, at extremely fast rates ($\sim 10,000$ revolutions per second) vastly reduces the effect of these interactions on the NMR spectra. As many of the interactions disappear, this is called the 'Magic Angle' (and thus Magic Angle Spinning, MAS). Although this can even out many of the interactions, quadrupolar interactions between nuclei still have a large effect. These are nuclei with a spin $>1/2$, resulting in more than two energy levels, and complicated interactions between these [543-544].

NMR is a very flexible technique, allowing detailed study of many nuclei. There exist a wide array of experimental conditions which can relay more information about the nuclei in question, and closely related nuclei. One such of these techniques used in this thesis is Cross Polarisation (CP). This utilises the ability to transfer magnetisation from one closely-bonded nucleus to another. An experiment using this technique will typically couple one nucleus (such as ^{29}Si) with another which has a faster relaxation (such as ^1H). Longer relaxation times result in a lower signal to noise ratio for an experiment over a set time due to the ability to perform fewer scans. Exciting both nuclei with their Larmor frequencies at the same time enables magnetisation from the ^{29}Si nuclei to be transferred to the ^1H nuclei, but using the ^1H relaxation time. This enables much more rapid experiments to be undertaken, with greater signal strength. As this preferentially occurs for nuclei closer to the ^1H nuclei, this technique can also reveal more information about the structure of the material in question.

The signal to noise ratio is also affected by the natural abundance of the nuclei in question. ^{27}Al has a 100% natural abundance, resulting in very rapid data acquisition, whereas ^{25}Mg has a 10% natural abundance, making it much slower. Within ^{25}Mg this is also combined with a large quadrupole moment, low susceptibility and a low resonance frequency, typically requiring a higher magnetic field instrument to obtain meaningful data.

The NMR data collected were undertaken at external facilities. ^{29}Si & ^{27}Al data were collected at the University of Durham using the EPSRC solid-state NMR service, while the ^{25}Mg data collection was undertaken at the University of Warwick as part of the EPSRC high-field NMR referral service. The specific acquisition parameters are noted below by chapter:

Chapter 5: Solid state ^{29}Si NMR spectra were collected on a Varian VNMRS 400 (9.4 T) using a 6 mm outer diameter (o.d.) zirconia rotor. Chemical shifts were externally referenced to tetramethylsilane (TMS) at 0 ppm. ^{29}Si MAS NMR spectra for M-S-H were collected at 79.435 MHz, with a spinning speed of 6.8 kHz, a pulse duration of 6.2 μs (90°) and a relaxation time of 30 s, for a minimum of 2000 scans. M-S-H samples for NMR analysis were produced using analytical grade $\text{Mg}(\text{OH})_2$ (Alfa Aesar, 95-100% purity) to eliminate any possibility of Fe contamination. ^{29}Si MAS NMR spectra for mineral samples (lizardite and antigorite) were collected at 79.438 MHz, with a spinning speed of 6 kHz, a pulse duration of 4.5 μs (90°) and relaxation time of 1 s for 43200 scans.

^{25}Mg MAS NMR spectra were obtained on a Bruker Advance III 850 spectrometer (19.96 T), using a 4 mm zirconia rotor, with a spinning speed of 10 kHz (M-S-H, lizardite and talc) and 14 kHz (antigorite – required due to signal broadening from iron). Spectra were collected at 52.05 MHz with a pulse duration of 5 μs (90°) and relaxation time of 2 s. Higher iron contents in these two samples enabled a faster relaxation time to be used than with the M-S-H materials. Chemical shifts were externally referenced to either MgO (26 ppm) or a 1 M MgCl_2 (0 ppm) solution.

Chapter 7: ^{27}Al and ^{29}Si MAS NMR spectroscopy was performed on a Varian VNMRS 400 (9.4 T) spectrometer. ^{27}Al MAS NMR spectra were collected at 104.198 MHz, spinning at 14 kHz (12 kHz for 720 day samples) using a 4 mm o.d. zirconia rotor with a pulse duration of 1.0 μs , acquisition time of 10 ms and recycle of 0.2 s for a minimum of 1900 scans. Chemical shifts were referenced to 1.0M aqueous $\text{Al}(\text{NO}_3)_3$. ^{29}Si MAS NMR spectra were collected at 79.435 MHz at a spinning speed of 6.8 kHz (6 kHz for 720 day samples) with a pulse duration of 6.2 μs (4.5 μs for 720 day samples), acquisition time of 20 ms (30 ms for 720 day samples) and a recycle delay of 60 s, for a minimum of 47 scans (912 for 720 day

samples). Chemical shifts were externally referenced to tetramethylsilane (TMS) at 0 ppm.

^{25}Mg MAS NMR spectra were collected on a Bruker Advance III 850 (19.96 T) spectrometer using 4 mm o.d zirconia rotors, collected at 52.042 MHz at a spinning speed of 10.0 kHz, pulse duration of 5.0 μs and recycle time of 2.0 sec for 5800 scans. Simulations were performed using Bruker Topspin 3.2 software. Chemical shifts were externally referenced to MgO.

Chapter 8: Solid-state ^{29}Si MAS nuclear magnetic resonance (NMR) was collected on a Varian VNMRS 400 (9.4 T) at 79.438 MHz using a 6 mm zirconia rotor, at a 6 kHz spin rate. Pulse duration was 4.5 μs (90°), with a 10s relaxation time for a minimum of 6000 repetitions, with chemical shifts externally referenced to tetramethylsilane (TMS) at 0 ppm. ^{27}Al MAS NMR was collected on a Varian VNMRS 400 (9.4 T) at 104.199 MHz using a 4 mm zirconia rotor, at a 14 kHz spin rate. Pulse duration was 1 μs (25°), with a 0.2s relaxation time for a minimum of 5200 repetitions. Chemicals shifts were referenced externally to 1 M aq. $\text{Al}(\text{NO}_3)_3$.

4.1.4 Scanning Electron Microscopy (SEM) & Energy Dispersive X-Ray Spectroscopy (EDX)

Scanning electron microscopy (SEM) is an imaging technique that enables high resolution image production to μm resolution, which when coupled with energy dispersive X-ray spectroscopy (EDX), enables qualitative and quantitative chemical analysis of surface features.

A typical electron microscope consists of a sample mounted on a metal stub which is placed into a vacuum chamber. Above this is an electron gun (typically a tungsten filament or field emission source), producing electrons which are scanned over the surface of the sample. An electron detector displays the resulting secondary and backscattered electrons on a visual display unit, building up an image of the same being scanned [545-546].

The electrons scanned over the sample surface interact with the matter in varying ways, visually represented in Figure 4.4. Electrons can undergo inelastic collisions with specimen electrons, ejecting these from the nucleus. These are called secondary electrons, and typically emanate from only the top few nanometres of the sample surface. Displaying only these secondary electrons in the display unit gives detailed information about the surface topology. Incident electrons may also undergo scattering within the sample, these are backscattered electrons, penetrating further into the bulk of the sample before re-emerging [545, 547].

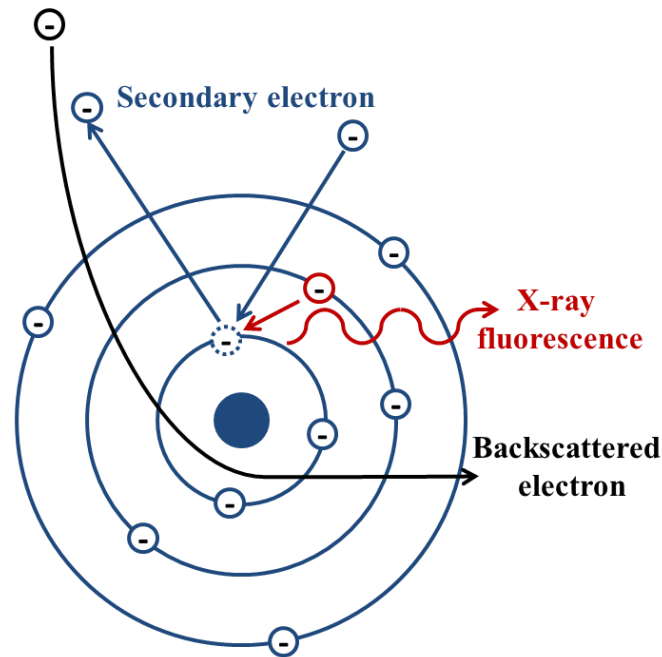


Figure 4.4 Electron interactions including backscattered electrons, release of secondary electrons and X-ray fluorescence

Typically an SEM will operate under a vacuum between the sample and electron gun to reduce damage to the electron gun and avoid scattering of the electrons before reaching the sample. This usually requires the coating of samples with a conductive material (such as carbon) to avoid charge build-up on the sample. However, low vacuum and ‘environmental’ SEMs can operate without the need for a high vacuum or the requirement for sample coating due to the positively ionised gases within the sample chamber.

Energy dispersive X-ray spectroscopy (EDX) is an additional bolt-on tool to SEM analysis, enabling chemical analysis. This utilises the principle of X-ray fluorescence from samples subjected to incident electrons, as shown in Figure 4.4. Incoming electrons occasionally undergo collisions with electrons within the inner K shell of the nucleus. Ejection of these electrons will leave the nucleus in an excited state, which causes electrons from outer shells (such as L or M shells) to drop down (similar to the process noted in Figure 4.2). This is accompanied with a release of X-rays which are characteristic of the emitting nucleus. This X-ray radiation can be detected, and the energies plotted to build up a qualitative and quantitative

representation of the elements within the material. Combined with SEM, this can be spatially resolved, resulting in an ‘elemental map’ of the sample [545, 547].

Sample preparation is very important for SEM and EDX analysis. Typically a solid sample is used, either as a fractured surface or a cut and polished surface. The latter is usually preferable for cement samples, as it enables a clear slice through the cement to be observed, with features represented on a flat plane. Uneven surfaces pose issues with focussing, resulting in partially blurry images and unreliable EDX analysis.

Chapter 5: Analysis was undertaken on a JEOL JSM 6400, using a 15 kV accelerating voltage and a 15mm working distance. Samples were resin mounted, ground and polished to a 1 micron finish using diamond paste, before being carbon coated.

Chapter 6: Analysis was conducted on freshly fractured sample surfaces mounted on carbon tabs, using a low vacuum Hitachi analytical Benchtop SEM TM3030 with integrated Bruker Quantax 70 EDX system, at an accelerating voltage of 15 kV.

Chapter 8: Analysis was carried out on monolithic samples sliced using a diamond wafering blade, the specimen was mounted in epoxy resin, ground and polished using diamond paste to a 1 micron finish. Analysis was undertaken on a Hitachi TM3030 desktop SEM at 15 kV accelerating voltage, operating under a low vacuum, precluding the requirement for carbon coating. This was coupled with energy dispersive X-ray analysis (EDX) using a Bruker Quantax 70 Energy Dispersive X-Ray Spectrophotometer for elemental mapping and spot analysis.

4.1.5 Thermal analysis (TGA, DTG and DTA) & coupled mass spectrometry (TG-MS)

Under the umbrella term of ‘thermal analysis’ there exist a wide range of techniques, of which TGA, DTG and DTA are of importance within this thesis. Each of these techniques relates to the controlled heating of crushed samples and determining either the change in mass (TGA/DTG) or the variation in temperature between the sample and a reference material (DTA). These techniques allow the identification and quantification of materials through determining events such as dehydration, decarbonation, melting, recrystallization or oxidation). The nature of these events, and the temperature at which they occur within a sample, can enable identification of phases or transitions which might not be identifiable using other techniques [548].

Thermogravimetric Analysis (TGA) is the simplest of these techniques, measuring the change in mass of a sample at either a fixed temperature, or during heating at a predetermined heating rate [549]. The instrumentation is simply a microbalance within a furnace, typically controlled by a computer interface to allow programmable heating control. An inert gas atmosphere (typically flowing nitrogen or argon) is usually used, to remove the potential for oxidation (or burning) within an air or oxygen atmosphere, which might complicate the interpretation [550].

A useful adaptation of TGA is Differential Thermogravimetry (DTG), in which the numerical derivative of the TGA output curve is taken. This allows easier resolution and identification of double or overlapping decomposition regions, and is easily produced from the TGA data.

Differential Thermal Analysis (DTA) is somewhat different in that the change in temperature of a sample relative to a reference is recorded, not the change in mass. This is useful in case of reactions which do not involve mass change (such as crystallisation). In a DTA instrument both the sample and reference are subjected to the same heating or cooling regime, and the difference in temperature between them is recorded.

Coupled to thermal analysis is a technique called mass spectrometry (TG-MS) which allows real time analysis of the evolved gases from a TGA instrument. This is undertaken through non-intrusive sampling of the evolved gases from within the furnace. The gas particles are ionised, typically stripping them of electrons, resulting

in charged particles (usually a singular positive charge). A mass spectrometer then separates and measures the mass of these ions, giving a charge to mass ratio. As the charge is typically 1, this is simply m , resulting in easy identification of species [551-552].

Within this thesis samples were analysed using several different thermal analysis instruments, detailed below for each chapter:

Chapter 5: Selected samples were analysed *via* thermogravimetric analysis (TGA) using a Pyris 1 TGA and differential thermal analysis (DTA) using a Perkin Elmer DTA 7, both using an alumina crucible, at a heating rate of 10 °C/min up to 1000 °C in a flowing nitrogen atmosphere.

Chapter 7: Thermogravimetric analysis (TGA) was carried out using a Perkin Elmer TGA 4000 coupled with a Hiden Analytical mass spectrometer (HPR-20 GIC EGA). The mass spectrometer signals for H₂O and CO₂ were continuously recorded. The samples were assessed at a heating rate of 5°C/min up to 900 °C, using alumina crucibles and nitrogen as a purge gas (20 mL/min).

Chapter 8: 28 day cured samples were analysed using a Pyris 1 TGA in an alumina crucible, heating at 10 °C/min up to 1000 °C in a nitrogen atmosphere. Aged samples were analysed in a Perkin Elmer TGA 4000 instrument in an alumina crucible, heating at 5 °C/min up to 950 °C in a nitrogen atmosphere. Composition of the gases released during the TGA test was determined using a Hiden Analytical mass spectrometer (HPR-20 GIC EGA) attached to the thermogravimeter. Both 28 day and aged samples were flushed with nitrogen for 30 minutes prior to analysis to remove surface water.

4.1.6 Compressive strength

Compressive strength testing is a simple test, in which the strength of a sample is determined by uniaxial compression between two parallel planes until the sample fails (i.e. cracks). By determining the strength of a material, inferences can be made about the degree of hydration which has occurred within the cementitious material, and can be easily compared to known strengths for a typical Portland cement matrix.

To ensure reproducible results, specific criteria are required to be met regarding sample shape and preparation. In this thesis the directions laid out in BS EN 12390-1:2012 and BS EN 12390-3:2009 for testing of concrete have largely been followed, with the exception of a smaller sample size (50 mm paste cubes) [553-554].

Samples were prepared using three gang cast iron 50mm cube moulds, prepared with an organic release agent, into which cement paste was cast. The filled moulds were sprinkled with water and placed into inflated plastic bags which were sealed, ensuring the bags did not touch the wet cement paste. After the samples set, cubes were de-moulded and placed back into the sealed bags until testing. Samples were tested using a Controls Automax 5 (Figure 4.5), using a loading rate of 0.25 MPa/s up to failure. Samples were tested in triplicate unless otherwise noted.



Figure 4.5 Automax 5 with door closed and empty chamber

The experimental conditions used are detailed below by chapter:

Chapter 5: Sample paste was poured into 50 mm steel cube moulds, compacted with the use of a vibrating table, sealed and cured in a 40 °C environmental chamber. Cubes were demoulded after 3 days and returned to the environmental chamber.

Chapter 8: As per Chapter 5, except that manual tamping was undertaken to remove entrained air instead of a vibration table, and samples were left for 5 days prior to demoulding in a 20 °C environmental chamber.

4.1.7 Mini-Slump

The mini-slump testing method was used to provide an indication of workability in small paste samples. This method is similar to a flow table test used in concrete consistency testing, except scaled down for cement pastes and excluding the need for sample agitation to flow.

Within the mini-slump test, a scaled down cone is placed in the centre of a flat surface, then filled with cement paste. The cone is then removed vertically, and cement paste allowed to flow outward. The dimensions of the post-slump paste are taken, resulting in a slumped surface area value. This is a very simple, reproducible test in which the more fluid the paste, the larger the slump area.

The cone geometry used in this thesis is that proposed by Kantro [555], in one of the first and most popular mini-slump papers. The shape was a scaled down Abrams cone, with the internal cone dimensions of 19 mm top opening, 38 mm bottom opening and 57 mm in height (Figure 4.6). This cone was manufactured from a single cylinder of PTFE, resulting in straight sides which could easily be held. The slump board was a sheet of poly(methyl methacrylate) marked with 2 x 2 cm grids underneath for ease of measurement.

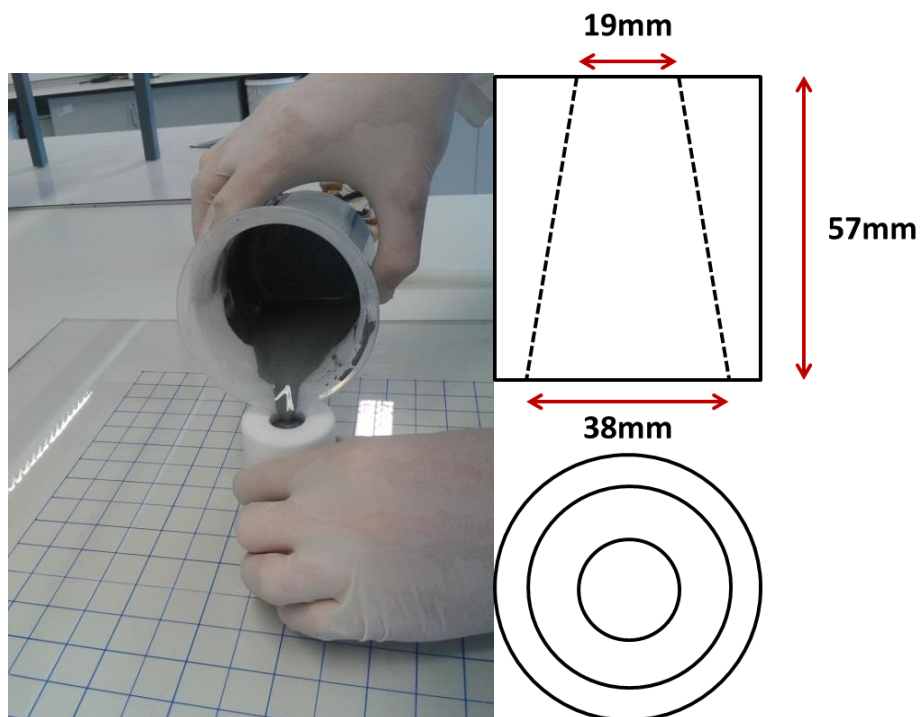


Figure 4.6 Filling the mould (left) and mould dimensions (right)

For slump analysis, the cone was placed central to the board, and slowly filled with the sample paste to the top. This was tapped several times to ensure no bubbles. The cone was then lifted upwards with one movement rapidly. The sample was left to spread for 5 seconds before a photograph was taken from directly above. The surface area was measured *via* ImageJ software [556] from the photograph, calibrated to the grid lines behind the sample, as demonstrated in Figure 4.7. Each paste slump test was repeated in triplicate, with triplicate measurement calibration and analysis undertaken per photograph.

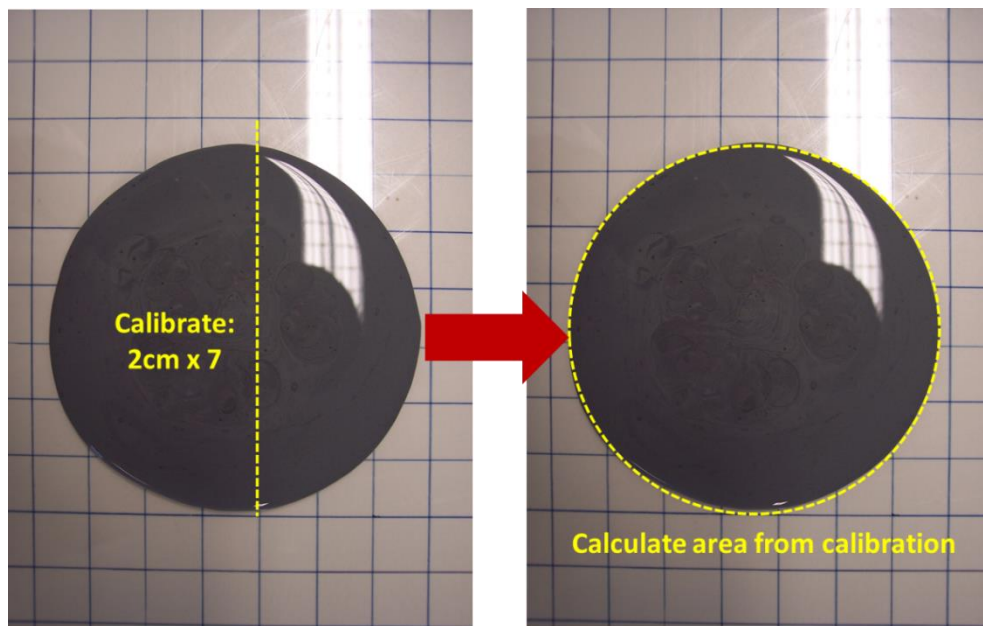


Figure 4.7 Calculation of mini-slump area

4.1.8 Isothermal calorimetry

Isothermal (conduction) calorimetry allows the measurement of cement heat of hydration over extended periods of time (weeks to months) and the effect of varying additions or changes to the cements on the rate of hydration and total reaction. This test relies on the principle of chemical reactions undergoing either exothermic or endothermic events. Typically in cementitious materials hydration is an exothermic process, meaning that the rate of heat output, and total amount of heat can be correlated back to certain hydration events, such as (in Portland cements) silicate dissolution of sulphate depletion [557].

This testing typically requires a material (cement paste, or liquid) to be placed inside a container (ampoule), which is lowered into a channel within a calorimeter. Inside this channel is a heat flow sensor, which is also connected to a heat sink kept at a constant temperature. Heat produced in the sample ampoule registers as a temperature gradient over the sensor, producing a voltage which is measured. This voltage is proportional to the heat rate and total heat generated [558].

Alongside each sample in a parallel channel is a reference material, preferably with a similar specific heat capacity (typically a simple material, such as sand or water). This allows any non-sample heat disturbances to be filtered out, as they will act equally on both the sample and reference.

The analytical conditions used are detailed below by chapter:

Chapter 7: Isothermal calorimetry was undertaken for fresh pastes using a TA Instruments TAM Air calorimeter at 40 °C. Raw materials and water were brought to 40 °C using an oven, then mixed externally and weighed into a plastic ampoule. This was placed into the calorimeter, and the heat output measured for 30 days (720 hours), with heat flow normalised to the total content of aluminosilicate materials (silica fume plus sodium aluminate) in each sample.

Chapter 8: In fresh pastes, isothermal calorimetry experiments were carried out using a TA Instruments TAM Air isothermal calorimeter at 25 °C ±0.02 °C. The materials were mixed externally, 20 g of paste was weighed into plastic ampoules and placed into the calorimeter. Heat output was measured for 14 days (336 hours), and normalised considering the sample weight tested in each case.

4.1.9 Blaine

Powder fineness was determined using a Controls 62-L0041/A Blaine fineness apparatus. This instrument uses the principle of air permeability through a compacted bed of powder to determine powder fineness.

Using the instrument in Figure 4.8, a given quantity of material (calculated via BS EN 196-6 [559], and varying by sample surface area) is compacted to a specific size and placed at the top of the instrument. Light mineral oil is present in a glass u-bend, which is drawn up on one side to a marked point using a plunger to draw out air. The plunger is then sealed off, and air allowed to permeate into the cell through the compacted bed held at the top of the instrument. Fineness is determined by measuring the time required for enough air to permeate (in general, the finer the material the longer the time required) to cause the oil to level out. Due to the construction of the apparatus, the test is not absolute, and requires calibration to a known standard prior to testing (NIST SRM 114q). The time taken can be used to calculate the fineness (expressed as cm^2/g or m^2/kg) using other known parameters in EN 196-6 [559]. This test is repeated in triplicate for each material.



Figure 4.8 Blaine fineness apparatus

4.1.10 Particle Size Distribution (PSD)

Laser particle size analysis is a quick, easy to repeat analysis method which exploits the variation in laser scattering as a function of particle size. Typically a liquid suspension is produced containing the powder to be analysed, through which a laser beam is passed. The angular scattering of the light from this laser is proportional to particle size, with smaller particles scattering the light more, and vice versa. Using the known optical properties of the materials being analysed, this can be calculated back into a distribution of the particle size, rather than just a singular value.

Analysis in this thesis was undertaken using a Malvern Mastersizer 3000 PSA (with a Hydro EV flexible volume wet dispersion unit), using a 4mW He-Ne 632.8nm red light source, and a 10mW LES 470nm blue light source. This enables particle size analysis of between 0.001 – 3500 μm [560]. 10 scans were performed per sample, with each sample repeated in triplicate and an average of the samples.

Typically a suspension is produced using water and a dispersant, however due to the risk of cement hydrating isopropanol was used as the liquid medium, employing sonication to break up agglomerating particles.

4.1.11 Automatic Vicat

Cement setting times were determined through the use of an automatic vicat apparatus. This test simply measures the depth to which a needle with a fixed weight can penetrate into a sample of cement. As the cement begins to set the needle will be able to penetrate less, until setting has completed and penetration is not possible.

The instrument used for this thesis was a Mastrad E040 Automatic Recording Vicat Apparatus, consisting of a weighted needle attached to a pencil which draws verticle lines on a sheet of paper. This is located above a turntable, onto which a sample of wet cement paste is placed (inside a truncated cone shaped plastic mould). If the needle penetrates all the way thourgh the cement to the bottom of the mould, the cement has not set. The instrument repeats this needle dropping procedure once every 30 minutes, rotating the mould slightly each time so as not to test the same position twice.

For Portland cement pastes EN 196-3 [561] requires this to be undertaken with at least 5mm water covering the mould and cement. This was not adhered to in this thesis, as there was uncertainty as to the effect of excess water on the true setting of the alternative cements presented here. Equally, within EN 196-3 ‘Final set’ typically requires a different needle to be attached and the mould turned upside down. In this instance instead initial set was taken as the point at which the needle stopped penetrating the full distance, and final as being when the needle did not penetrate into the cement, as illustrated in Figure 4.9.

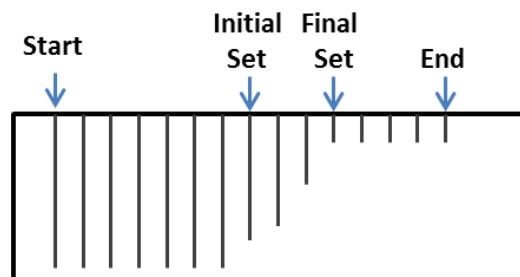


Figure 4.9 Illustration of automatic vicat experiment paper, showing vicat pencil marks at 30 minute intervals

4.2 Materials

The materials used within this thesis varied between chapters. The analysis undertaken on these, and the purity / origin of these are detailed below by chapter.

4.2.1 Chapter 5

The raw materials used were dead burnt MgO from Richard Baker Harrison (89% purity), light burnt MgO and heavy burnt MgO from Sigma Aldrich (technical grade), Mg(OH)₂ from Intermag Company Ltd (<95% purity), silica fume (SF) 181 (Microsilica 940-U, >90% SiO₂) supplied by Elkem as an undensified dry powder, and sodium hexametaphosphate ((NaPO₃)₆, 65-70% P₂O₅ basis) supplied by Sigma-Aldrich.

4.2.2 Chapter 6

The primary raw materials used were Mg(OH)₂ from Alfa Aesar (>95% purity), silica fume (Microsilica 940-U, >90% SiO₂) supplied by Elkem as an undensified dry powder, and sodium aluminate (Fisher Scientific, technical grade).

4.2.3 Chapter 7

The principal raw materials were silica fume (Microsilica 940-U, Elkem, >90% SiO₂); sodium aluminate (NaAlO₂, technical grade, Fisher Scientific); Mg(OH)₂ (>95% purity, Alfa Aesar) and distilled water

4.2.4 Chapter 8

The slag used in this chapter was a commercial GGBS supplied by Civil and Marine Ltd., the chemical composition of which is reported in Table 4.1. Commercial magnesium hydroxide (Mg(OH)₂, Alfa Aesar, >95% purity, Blaine fineness 1179 ± 6 m²/kg) was used to simulate the Magnox sludge, and as an alkaline activator a commercial sodium carbonate (Na₂CO₃ (>99.5% purity), Sigma-Aldrich) was used.

The GGBS had a particle size between 0.5 and 59 µm (D₅₀ = 13.2 µm, measured by laser particle analysis (Malvern Mastersizer 3000 in 2-propanol)) and a measured fineness of 515 ± 1 m²/kg by Blaine analysis. This slag has a basicity coefficient (K_b

= $(\text{CaO}+\text{MgO})/(\text{SiO}_2+\text{Al}_2\text{O}_3)$ [562-563]) of 1.01, making this a basic slag, with a quality coefficient ($Q_c = (\text{CaO}+\text{MgO}+\text{Al}_2\text{O}_3)/(\text{SiO}_2+\text{TiO}_2)$ [563]) of 1.70

Table 4.1 Chemical composition of the GGBS determined by X-ray fluorescence (XRF)

Oxide	Quantity (wt.%)
MgO	8.4
Al ₂ O ₃	12.6
SiO ₂	35.4
CaO	40.3
TiO ₂	0.6
Others	2.48

5 Magnesium silicate hydrate cementitious systems

5.1 Introduction

This chapter investigates the incorporation of $\text{Mg}(\text{OH})_2$ into the primary binding phase of a magnesium silicate hydrate (M-S-H) cement. Chapter 2 highlighted the chemistry of Magnox sludges, which were found to consist primarily of $\text{Mg}(\text{OH})_2$ with a few minor corrosion and carbonation products such as hydrotalcite ($\text{Mg}_6\text{Al}_2(\text{CO}_3)(\text{OH})_{16}\cdot 4\text{H}_2\text{O}$), artinite ($\text{Mg}_2\text{CO}_3(\text{OH})_2\cdot 3\text{H}_2\text{O}$) and UO_2 . These sludges were highly heterogeneous in nature, varying considerably between sampling sites but generally consisting of fine particles and colloids. These were found to be largely unreactive in conventional Portland cement composite cements, being encapsulated rather than chemically immobilised [65, 134]. This chapter investigates the use of this material as a core component in the formation of a cementitious binder, with the aim of producing a cementitious material with a higher concentration of waste per unit volume than when using conventional Portland composite encapsulants.

There are a range of magnesium-based cements that could be investigated for the incorporation of $\text{Mg}(\text{OH})_2$ into their structure, however, as the review of these cements in Chapter 3 highlights, many would be unsuitable. Oxysalt based systems (both oxychloride and oxysulphate) are degraded by water, losing mechanical strength and structural integrity over time, while magnesium phosphate cements require careful control and calcination of magnesia to avoid flash setting. It would be possible to calcine the Magnox sludge, however fewer steps are preferable, especially considering the highly active nature of the sludges and the shielded facilities which would be required to undertake this compared to a conventional calciner. Equally, the inhomogeneous nature of the sludges would make controlling the end product more difficult, which along with pieces of metallic uranium present poses a challenge. This process is suggested for certain glassy and ceramic wasteforms proposed for Magnox sludge [564], and would be technically feasible, but presumably at a higher cost. Magnesium carbonate cements are possible, but require curing in elevated CO_2 conditions, and has to date only been proven to work with porous blocks. This method of curing is not compatible with an in-drum mixing

method, or direct grouting inside drums/boxes. Magnesium silicates are a promising option since they are compatible with ambient temperature (and slightly elevated) curing, require no external CO₂ curing, and react more slowly than magnesium phosphates. They are believed to form poorly crystalline forms of stable minerals, which are likely more resistant to water than magnesium oxysalt cements. These magnesium silicate cements are the focus of this chapter, by building on the known properties on these from the existing literature, and adapting them to utilise Mg(OH)₂ as a raw material.

In this chapter, hydrated Mg(OH)₂-silica fume (SF) blends are produced and characterised up to 28 days of curing, with a focus on assessing workability, strength, phase development and gel structure of the M-S-H system. Due to industry and regulatory concerns about the possibility of organic superplasticisers enhancing radionuclide solubility within nuclear wasteform cements [565-566], the application of an inorganic deflocculant (sodium hexametaphosphate (NaPO₃)₆), as used in castables and for clay dispersions [567-568], was also investigated as a means to reduce water demand. This additive has previously been used in M-S-H cements [368-369], but its effect on fluidity and phase formation within these cements has not yet been described in detail. The structural composition of M-S-H, and the effect of the phosphate dispersant on this structure, was analysed up to 8 months of curing using solid state NMR spectroscopy.

5.2 Preliminary experiments

When this study commenced, there was little openly available literature describing the production of M-S-H cements. More literature existed on the properties of M-S-H gels than on their practical usage. Literature related to cement production was limited to M-S-H monoliths produced and described in publications by Zhang et al. [369-370, 372] and by Wei et al. [367-368]. This necessitated a short experimental programme to determine the optimum M-S-H composition, source of Mg and curing conditions relative to those identified by other authors.

From the literature, the most common method of producing an M-S-H binder is to blend dead burnt MgO with silica fume (amorphous SiO₂) and water to produce a paste. This is often augmented with an inorganic dispersant, usually sodium

hexametaphosphate (NaPO_3)₆, due to the use of very high levels of silica fume, which has a high water demand. This dispersant lowers the amount of water required, producing a less porous and denser structure.

The choice of which MgO to use was crucial within this study. As noted in Chapter 3, the calcination temperature of MgO affects the reactivity of the material, as does the fineness. From the existing literature, Zhang et al. [369] used Magchem 30, a light burnt MgO produced from brines, while Wei et al. [367-368] used a heavier burnt MgO (calcined at ~800 °C). Here it was decided to begin with a ‘dead burnt’ MgO, which although less reactive, was likely to entail a reduced water demand and thus a more workable composition which sets. Higher water contents are typically associated with lower compressive strengths, and a higher porosity in conventional cements [569]. Any way in which water content can be lowered is likely to produce a denser, more durable wasteform. A sodium hexametaphosphate dispersant was also used, in line with the literature.

Different formulations are used for these experiments, although most follow the general setup in Table 5.1. To prepare the following pastes, the specified amount of (NaPO_3)₆ was fully dissolved in distilled water, then MgO (or Mg(OH)₂) was gradually added over 1 minute, and this suspension was mechanically mixed using a bench top Kenwood mixer for 3 minutes before adding the silica fume. Mixing continued for an additional 5 minutes, and pastes were then poured into 50 mL centrifuge tubes, sealed, placed in an environmental chamber at the required temperatures, 95% relative humidity, and cured for up to 28 days. Hardened samples which had been cured for 7, 14 and 28 days were crushed and immersed in acetone for 2 days to arrest hydration, then dried in a vacuum desiccator for a further 2 days. These were then ground with an agate mortar and sieved to <63 μm using a brass sieve for analysis.

Table 5.1 Typical M-S-H formulation (weights in grams) for preliminary experiments

MgO	SiO₂ (silica fume)	H₂O	(NaPO₃)₆
50	50	40	2

5.2.1 MgO-SiO₂-H₂O

5.2.1.1 Effect of dead burnt magnesia

For ease of testing, a 50:50 wt. % blend of MgO:SiO₂ (SiO₂ as silica fume) with an additional 2 wt. % (NaPO₃)₆ as a dispersant was used. Through the use of this dispersant, despite the high level of silica fume utilised, a water / binder (w/b) ratio of 0.4 was achieved. Samples were cured at 20 °C in sealed centrifuge tubes.

The samples did not set within 1 month, only hardening after 2 months of curing. The results of XRD analysis of this hardened product, and the same formulation after 1 year of curing, are shown in Figure 5.1. This displays the characteristic poorly crystalline features of M-S-H at ~25°, ~35° and 60° 2θ, showing that there has been reaction between the MgO and silica fume to form a hydrated magnesium silicate material. The sharp reflections at 36.9°, 42.9° and 62.3° show the presence of large quantities of unreacted MgO. Silica fume typically presents a diffuse reflection at ~22°, which overlaps with a key M-S-H reflection at 25°, making XRD unsuitable for determining the presence or absence of residual SiO₂.

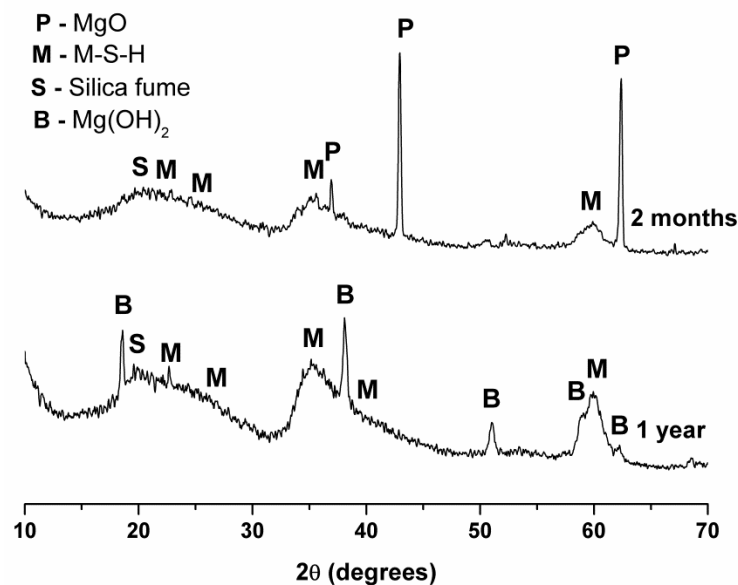


Figure 5.1 X-ray diffraction patterns for 50:50 wt.% dead burnt MgO:SiO₂ (w/b = 0.4) with 2 wt. % (NaPO₃)₆, cured at 20 °C for 2 months and 1 year

This cement was unusual in appearance, visually exhibiting a very low porosity and properties more closely resembling a glass, as photographs of a broken sample demonstrate (Figure 5.2). Although the ability to form a solid monolith and chemically incorporate magnesium appeared attractive for the encapsulation of $\text{Mg}(\text{OH})_2$ wastes, the long setting time is potentially of concern for industrial applications. Wei et al. [368] showed that an increase in curing temperature (from 25 to 50 °C) increases the formation of M-S-H within a 28 day period, with a curing temperature of 100 °C increasing this substantially.



Figure 5.2 Photographs of 50:50 wt. % $\text{MgO}:\text{SiO}_2$ ($w/b = 0.4$) with 2 wt. % $(\text{NaPO}_3)_6$, cured at 20 °C for 1 year (sample fractured to remove material for XRD analysis)

Curing the same system at an increased temperature (40 °C, 95% RH) improved the setting time, with this sample setting within 2 weeks. Upon analysis after 28 days (Figure 5.3) however, it is unclear if more M-S-H has been produced, as there are still strong reflections for MgO. Although setting times were improved, 2 weeks is likely to be too long for use as an encapsulating cement. Current cement formulations for waste encapsulation typically set within 24 hours, which ensures fair throughput of waste packages within an encapsulation facility. There needs to be confidence that these products can solidify before exporting to an engineered facility, and long curing times would add extra interim storage costs or significantly reduce throughput. This however is not set in stone, more stringent specifications exist for fluidity, heat output and ability to be vibrated [68-69] – which are requirements specific to wastes being encapsulated (such as swarf in MEP [68]).

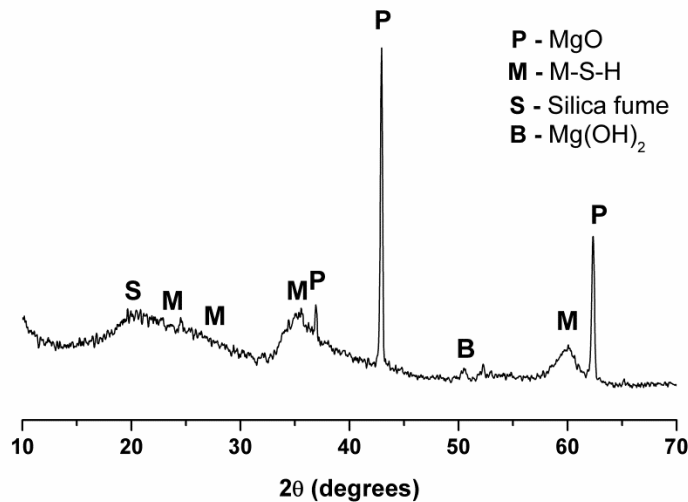


Figure 5.3 X-ray diffraction pattern of 50:50 wt.% dead burnt MgO:SiO₂ (w/b = 0.4) with 2 wt. % (NaPO₃)₆, cured at 40 °C for 28 days

5.2.1.2 Effect of light burnt magnesia

To reduce setting times, a more reactive, finer MgO was acquired, closer in characteristics to that used by Zhang et al. [369]: “light burnt” MgO was selected from Sigma-Aldrich. The same formulations were chosen (50:50 wt. % MgO:SiO₂, with 2 wt. % (NaPO₃)₆). The MgO powder exhibited a much higher water demand than expected, requiring a water/binder mass ratio of 1.44 to form a mixable paste. However, despite this extremely high water content, automatic Vicat analysis revealed an initial set of 4 ½ hours, and a final set of 6 hours.

Despite this quicker setting, the MgO appeared to predominantly form Mg(OH)₂, rather than being consumed to form M-S-H, with XRD analysis showing only limited M-S-H formation (Figure 5.4). Figure 5.5 illustrates a reduction in the [102] plane reflection at 50.8° up to 28 days of curing, which is suggestive of Mg(OH)₂ itself being consumed to form M-S-H over time.

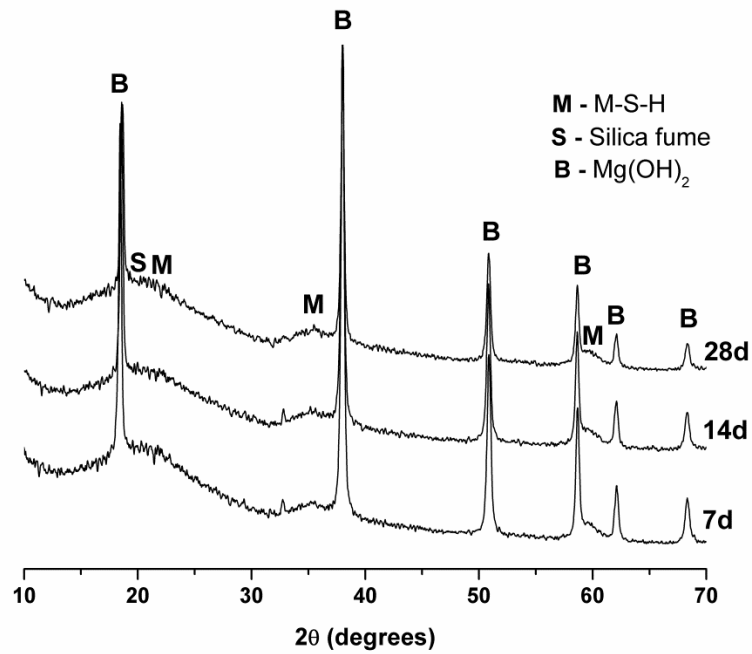


Figure 5.4 X-ray diffraction patterns of 50:50 wt. % light burnt MgO:SiO₂ (w/b = 1.44) with 2 wt. % (NaPO₃)₆ cured at 20 °C for up to 28 days

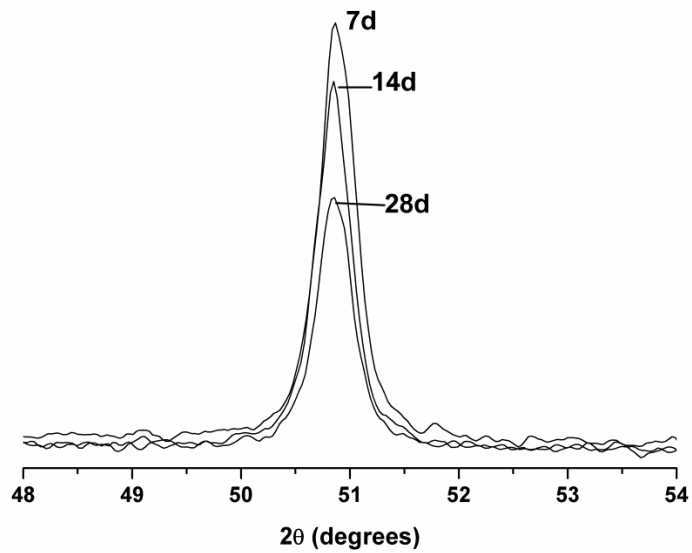


Figure 5.5 Expanded X-ray diffraction patterns in Figure 5.4, focussing on 48-54° 2θ to highlight the consumption of brucite

5.2.1.3 Heavy burnt magnesia

To reduce the setting times, a more reactive MgO was chosen. Using a “heavy burnt” MgO, again from Sigma-Aldrich, was intended to strike a balance between reactivity and workability. The same formulation was tested (50:50 wt. % MgO:SiO₂, with 2 wt. % (NaPO₃)₆), with the apparent MgO fineness necessitating a water content of w/b = 0.8 for a mixable composition to be produced. Unlike the dead burnt MgO samples, this mix set in under 24 hours. Using an automatic Vicat test, an initial set of 5 ½ hours and final set of 9 hours was determined. XRD analysis of this sample after 28 days of curing is displayed in Figure 5.6, in which M-S-H and Mg(OH)₂ are prominent, with no residual MgO detected.

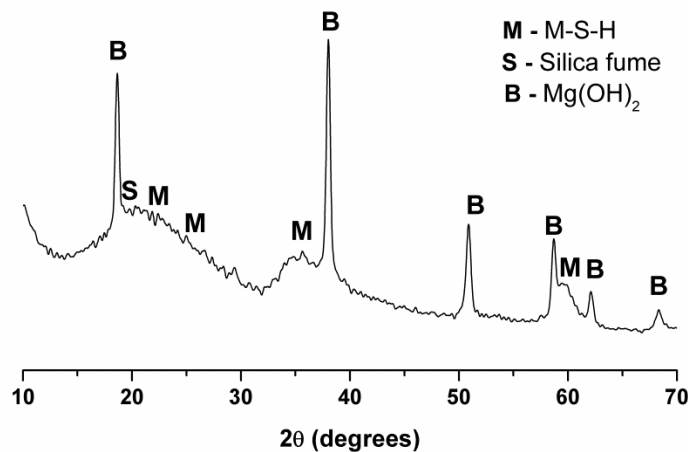


Figure 5.6 X-ray diffraction pattern of 50:50 wt.% heavy burnt MgO:SiO₂ (w/b = 0.8) with 2 wt. % (NaPO₃)₆, cured at 20 °C for 28 days

Although this formulation required a much higher water content, this did not inhibit the formation of a relatively strong product. Compressive strength measurements were undertaken in triplicate on 50mm cubes of hardened paste (Figure 5.7), where an average strength of 23 MPa was achieved at 28 days. Also of interest was that despite a high water content, no bleed was noted in any of these samples, although samples less than 14 days old were prone to drying cracking once removed from humidity chambers.

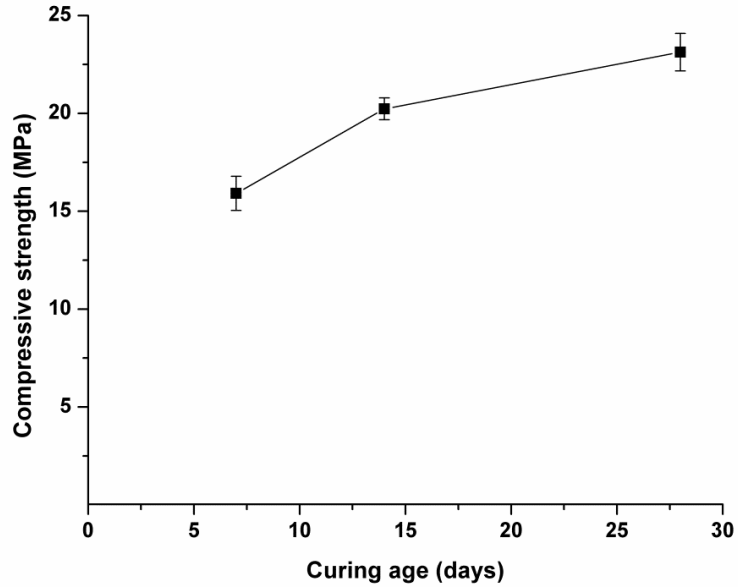


Figure 5.7 Compressive strength data for 50:50 wt.% heavy burnt MgO:SiO₂ (w/b = 0.8) with 2 wt. % (NaPO₃)₆ cured at 20 °C for up to 28 days

5.2.1.4 Blended dead-heavy magnesia

In an attempt to lower the w/b ratio, but retain the early setting characteristics, a blend of dead burnt and heavy MgO was trialled using a 1:1 dead burnt : heavy burnt blend with the same formulation (50:50 MgO:SiO₂, with 2 wt. % (NaPO₃)₆, w/b = 0.6). The sample failed to set within 28 days, but eventually formed a solid monolith after ~6-8 months. XRD analysis after 1 year of curing showed remnants of MgO, along with M-S-H (Figure 5.8).

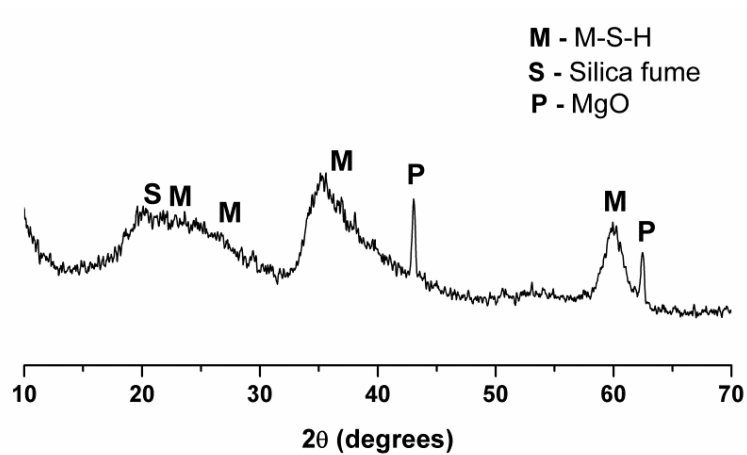


Figure 5.8 X-ray diffraction pattern of blended dead burnt-heavy burnt 50:50 wt. % MgO:SiO₂ blend (w/b = 0.6) with 2 wt. % (NaPO₃)₆, cured at 20°C for 1 yr

5.2.1.5 Heavy burnt magnesia with elevated curing temperature

The heavy burnt MgO was chosen for optimisation, with the success achieved using 40 °C as a curing temperature guiding this further investigation. Increasing from 20 °C to 40 °C curing was very beneficial in the production of M-S-H, resulting in very little Mg(OH)₂ remaining after 28 days curing, and increasing intensity of M-S-H reflections, postulated to represent increasing M-S-H formation (Figure 5.9). The sample cured at 40 °C was sectioned and polished for SEM analysis (Figure 5.10), showing a crinkled and pitted, yet cohesive binder with little evidence for unreacted MgO or Mg(OH)₂.

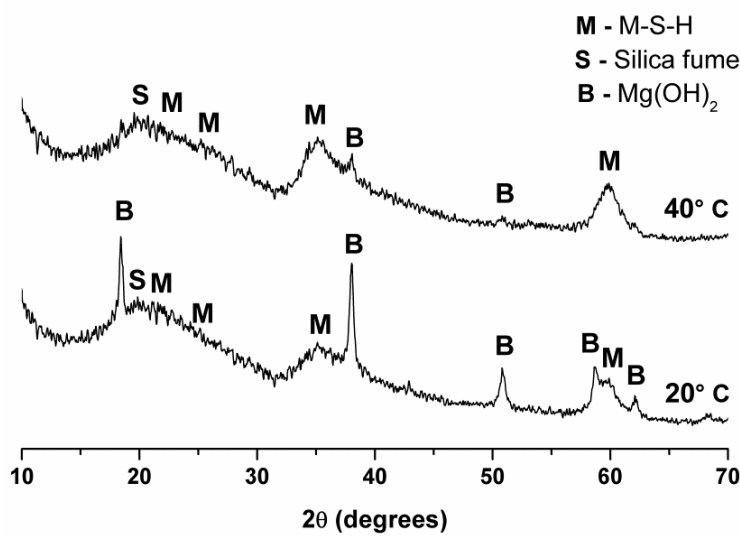


Figure 5.9 X-ray diffraction patterns of 50:50 wt. % heavy burnt MgO:SiO₂ (w/b = 1) with 2 wt. % (NaPO₃)₆ cured at both 20 and 40 °C for 28 days

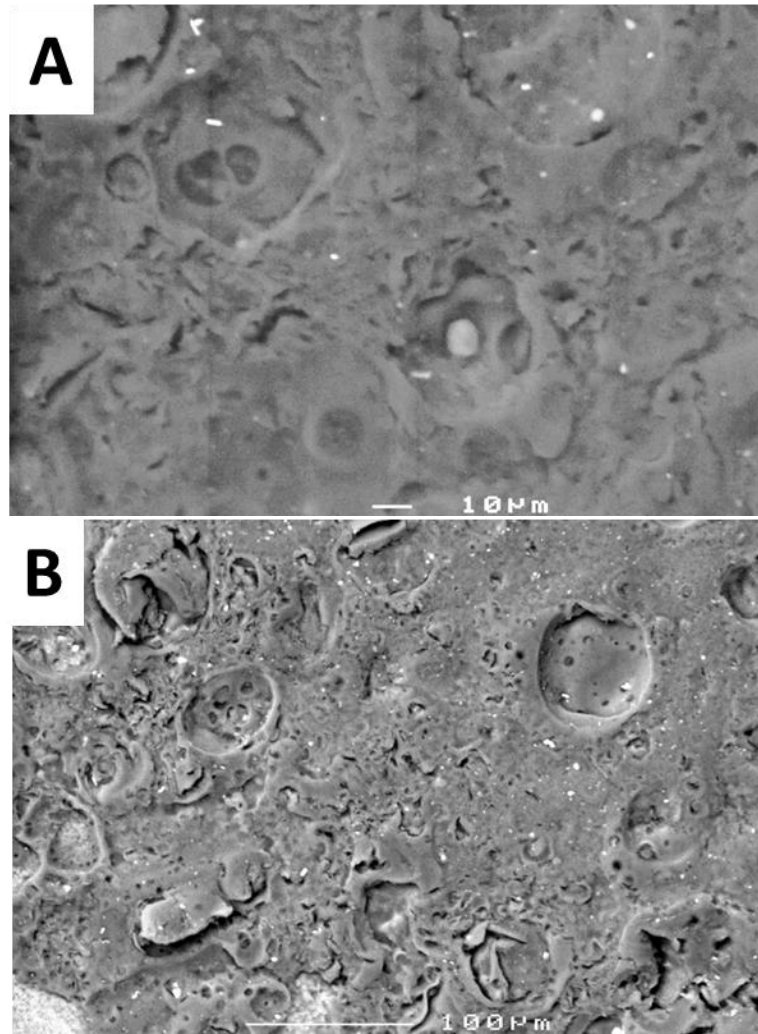


Figure 5.10 SEM micrograph of a cut, polished surface of 50:50 wt. % MgO:SiO₂ (w/b = 0.8) with 2 wt. % (NaPO₃)₆ cured at 40 °C for 28 days at two different magnifications

5.2.1.6 Varying MgO-SiO₂ ratios

All the trial samples used a 50:50 blend of MgO:SiO₂ for simplicity. Ultimately the strength of the binder is determined by M-S-H formation. The effects of raising the heavy burnt MgO content to 60:40 and 70:30 mass ratios MgO:SiO₂ were investigated to determine if this might increase M-S-H formation, as shown in Figure 5.11.

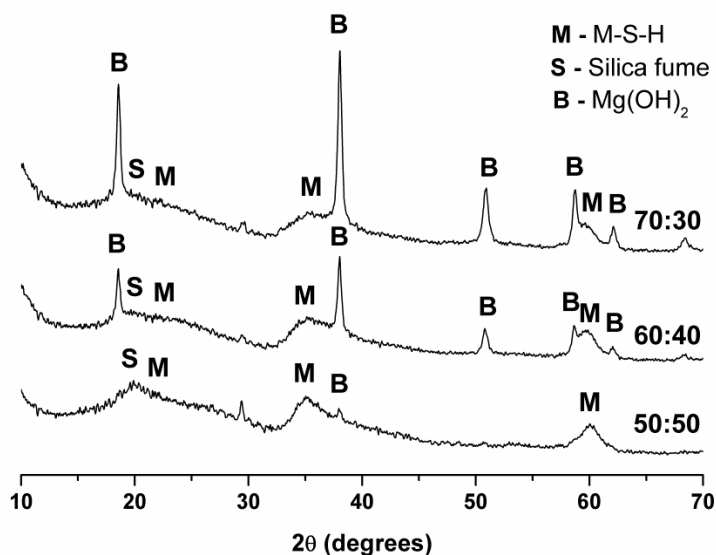


Figure 5.11 X-ray diffraction patterns of heavy MgO:SiO₂ blends of varying ratios (w/b = 0.9) with 2 wt. % (NaPO₃)₆ cured at 40 °C for 28 days

Increasing the content of MgO beyond 50 wt. % did not appear to increase the production of M-S-H, and results in residual Mg(OH)₂. A short series of experiments were also undertaken where the SiO₂ content was increased up to a 20 MgO : 80 SiO₂ blend. Although all the MgO reacted with no residual Mg(OH)₂ there was significant diffuse scattering remaining associated with unreacted SiO₂. Due to this the 50:50 blend was chosen as the optimum, as this conferred the benefit of ease of use and utilised the most MgO.

5.2.2 Mg(OH)₂-SiO₂-H₂O

5.2.2.1 Varying Mg(OH)₂-SiO₂ ratios

A solid M-S-H binder was quite easily produced under the elevated temperature curing conditions tested for the MgO-SiO₂-H₂O system. Also from testing of the finer light burnt MgO, it was noted that Mg(OH)₂ appears to be able to directly form M-S-H (albeit slowly). Due to this, a switch was made to using Mg(OH)₂ directly. In line with the testing on the MgO system, varying levels of Mg(OH)₂:SiO₂ were tested (50:50, 60:40 and 70:30 wt. %), to check if, similarly to the MgO:SiO₂ system, a 50:50 blend was appropriate.

The major difference from the materials based on MgO was the increase in water ratio required due to the very fine nature of the Mg(OH)₂ powder. Aside from this, the ultimate results were largely similar, with most of the Mg(OH)₂ being consumed during the formation of M-S-H in the 50:50 system (Figure 5.12). This system was also left to set at 20 °C, however this failed to harden within 3 months. After 1 year of curing the sample had set, and fully consumed the Mg(OH)₂ to form M-S-H, as shown in Figure 5.13. Though successfully demonstrating the ability to form M-S-H at ambient temperature, in the context of Magnox sludge disposal a setting time in excess of 3 months is an unacceptable time, which would severely limit cementation plant operations.

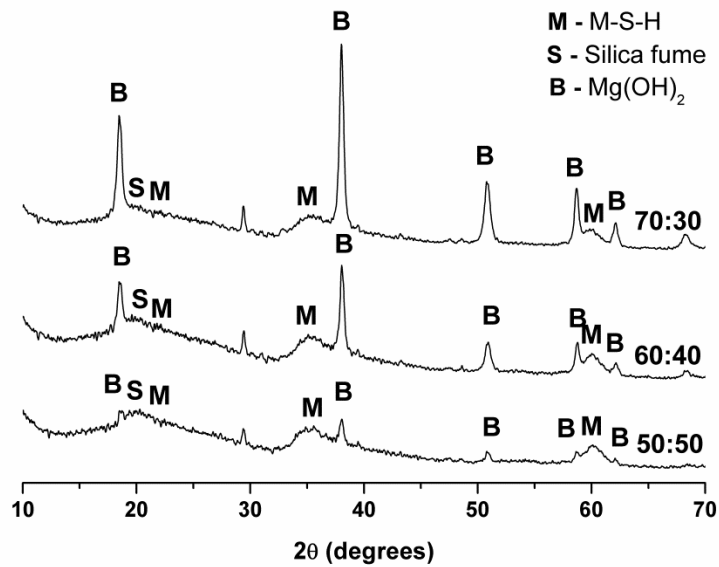


Figure 5.12 X-ray diffraction patterns of varying Mg(OH)₂:SiO₂ mass ratios (w/b = 1) with 2 wt. % (NaPO₃)₆ cured at 40 °C for 28 days

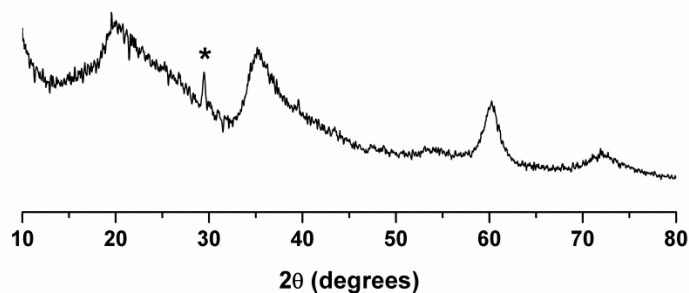


Figure 5.13 X-ray diffraction pattern of 50:50 wt. % Mg(OH)₂:SiO₂ (w/b = 1) with 2 wt. % (NaPO₃)₆ cured at 20 °C for 1 year

5.2.2.2 Effect of curing temperature

Although 40 °C was selected as the curing temperature, further investigations were undertaken to study the effect of 60 °C curing, and to analyse the 20 °C Mg(OH)₂:SiO₂ blends that did not set within 28 days of curing. The results of these are shown in Figure 5.14.

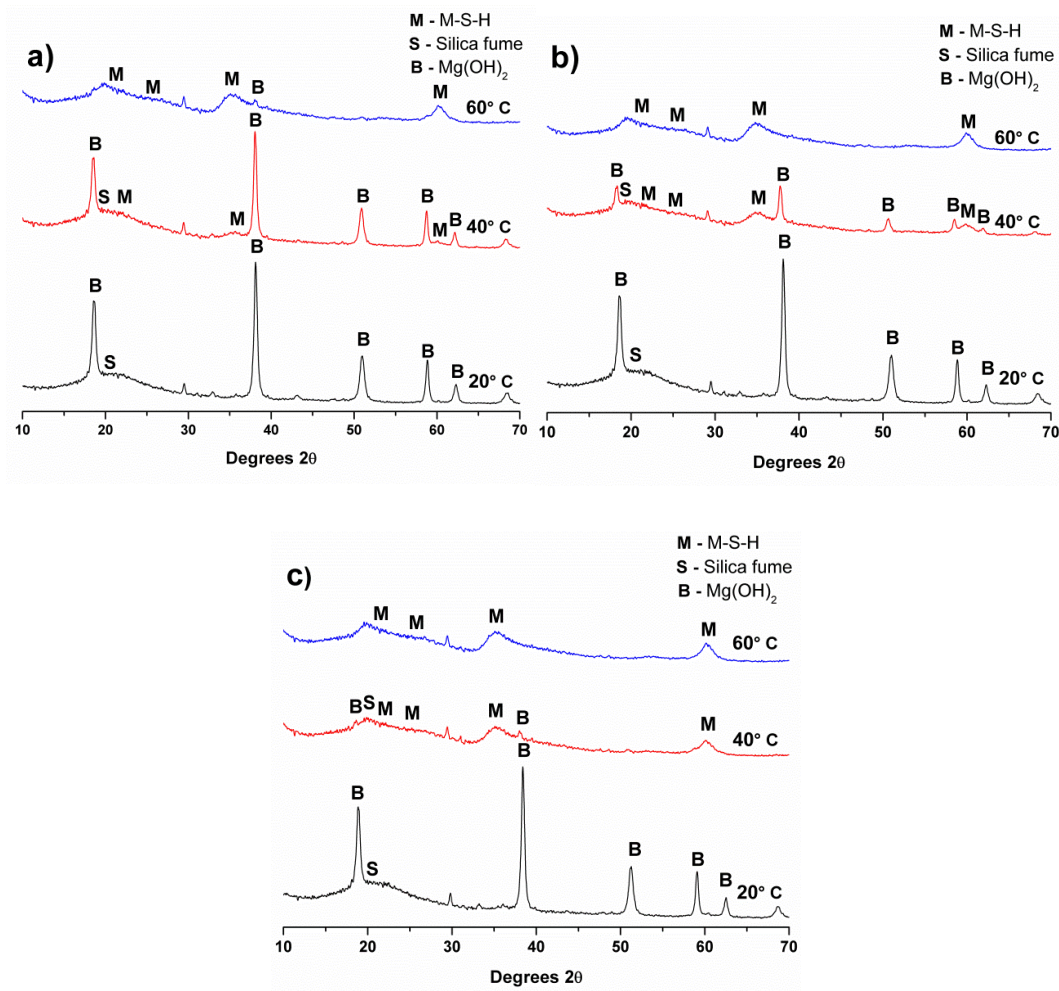


Figure 5.14 X-ray diffraction patterns of 50:50 wt. % Mg(OH)₂:SiO₂ with 2 wt. % (NaPO₃)₆ cured at 20°, 40° and 60 °C for; a) 7, b) 14, c) 28 days

No diffuse reflection associated with formation of M-S-H was observed in the 20 °C cured samples even after 28 days of curing, corresponding to a lack of setting. The other two samples both set, forming diffuse reflections of M-S-H. Curing at 40 °C produced some M-S-H by 7 days, and almost completely consumed the Mg(OH)₂ by

28 days. Curing at 60 °C, however, almost completely consumed the Mg(OH)₂ by 7 days of curing, fully using up the Mg(OH)₂ by 14 days.

Due to the poorly crystalline nature of the M-S-H formed, FTIR analysis was undertaken to determine if the curing temperatures resulted in structural variations in the M-S-H (Figure 5.15); further details of structural identification are explained below, in Section 5.3.2.2.2. The characteristic sharp –OH vibration of Mg(OH)₂ is present at ~3800 cm⁻¹ [570] when curing at 20 °C, largely disappearing from the 40 °C and 60 °C samples, in line with the behaviour observed *via* XRD analysis. Helpfully, FTIR can reveal more information about the presence (or not) of silica fume, which within XRD analysis overlaps with a major M-S-H reflection at ~20°. Focussing on the region 1500-500 cm⁻¹ (Figure 5.16) shows a clear shift in the Si-O bending region. Here silica fume typically exhibits vibrations at ~1200 cm⁻¹ and ~810 cm⁻¹ [570], while M-S-H Si-O units vibrate at ~1000 and ~680 cm⁻¹. This demonstrates that most, if not all, of the silica fume was consumed in both the 40 °C and 60 °C samples by 28 days of curing.

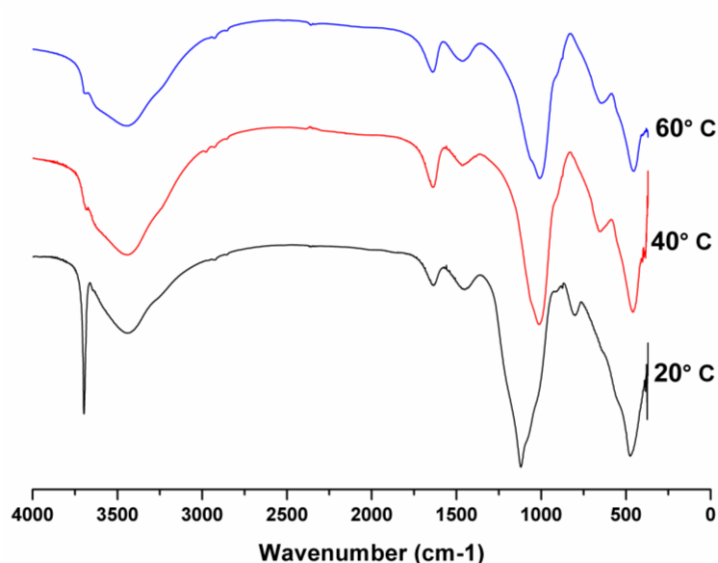


Figure 5.15 FTIR spectra of 50:50 wt. % Mg(OH)₂:SiO₂ with 2 wt. % (NaPO)₆ cured for 28 days at 20, 40 and 60 °C

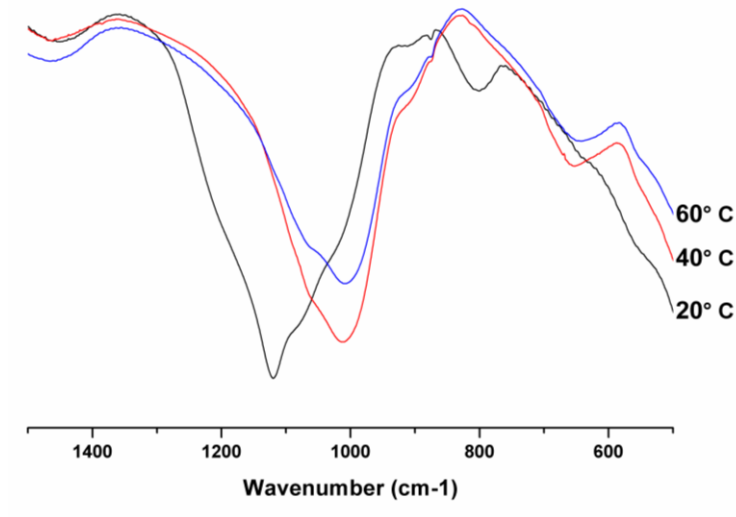


Figure 5.16 Enlarged FTIR spectra of Figure 5.15, focussing on 1500-500 cm⁻¹

Although curing at 60 °C resulted in a faster setting system, 40 °C is a more realistic curing temperature, and results in a similar M-S-H gel forming (from FTIR and XRD analysis).

As a result of these preliminary studies, the use of slightly elevated 40 °C curing temperatures was confirmed, along with the use of a 50:50 wt.% Mg(OH)₂:SiO₂ formulation, rather than requiring blending with a pre-prepared MgO-derived M-S-H cement.

5.3 In-depth study of structure and properties of the M-S-H binder

This section details a more in-depth study of the workability and structural properties of a cementitious binder produced in the $\text{Mg}(\text{OH})_2\text{-SiO}_2\text{-H}_2\text{O}$ system. This section is an extension of the published paper:

Walling, S.A., Kinoshita, H., Bernal, S.A., Collier, N.C., Provis, J.L. (2015) “Structure and properties of binder gels formed in the system $\text{Mg}(\text{OH})_2\text{-SiO}_2\text{-H}_2\text{O}$ for immobilisation of Magnox sludge”, *Dalton Transactions*, **44**, 8126-8137.

5.3.1 Formulation design

Throughout the experiments, a mix design of 1:1 $\text{Mg}(\text{OH})_2\text{:SiO}_2$ (silica fume, SF) was utilised. The influence of the $(\text{NaPO}_3)_6$ in the range 0 to 5 wt.% of the binder, and the water/binder (w/b) ratio, on the workability of the M-S-H system was investigated *via* mini-slump testing. An initial w/b ratio of 1.2 (defined on a mass basis) was tested at different $(\text{NaPO}_3)_6$ levels, and then this was systematically reduced by 0.1 unit increments until the samples were no longer fluid (i.e. a mini-slump value of 11.3 cm^2 , corresponding to the base area of the cone), to identify the lowest w/b ratio at which the samples could reasonably be mixed and poured. For the system without $(\text{NaPO}_3)_6$ the w/b ratio was also increased systematically by 0.1 unit increments from 1.2 due to the low mini-slump values recorded, until stopping at 1.6 (a level arbitrarily decided as too high without risking drying shrinkage), where a value of $\sim 80 \text{ cm}^2$ was achieved. Once an optimal level of phosphate addition was identified, the structural development of this paste was then studied over the time of curing.

5.3.2 Results and discussion

5.3.2.1 Influence of $(\text{NaPO}_3)_6$ addition

5.3.2.1.1 Mini-slump

The addition of $(\text{NaPO}_3)_6$ as an inorganic dispersant led to vast differences in the workability between the samples produced, as shown in Figure 5.17. With no phosphate addition, the paste was thick and lacked fluidity. The validity of this test at very low slump values is of issue, due to material sticking to the inside of the test vessel (as in Figure 5.18, which shows a zero slump formulation). This is however, only a problem with samples exhibiting a ‘zero’ slump, as material does not stick when any higher slump is achieved. Overall a w/b ratio of 1.6 was the highest tested, only achieving a mini-slump value of $\sim 80 \text{ cm}^2$. For comparison, using a mini-slump test in this geometry, a typical Portland cement paste with a w/b ratio of 0.36 and no organic admixtures achieved 27 cm^2 , and with a w/b ratio of 0.5 achieved 68 cm^2 [555].

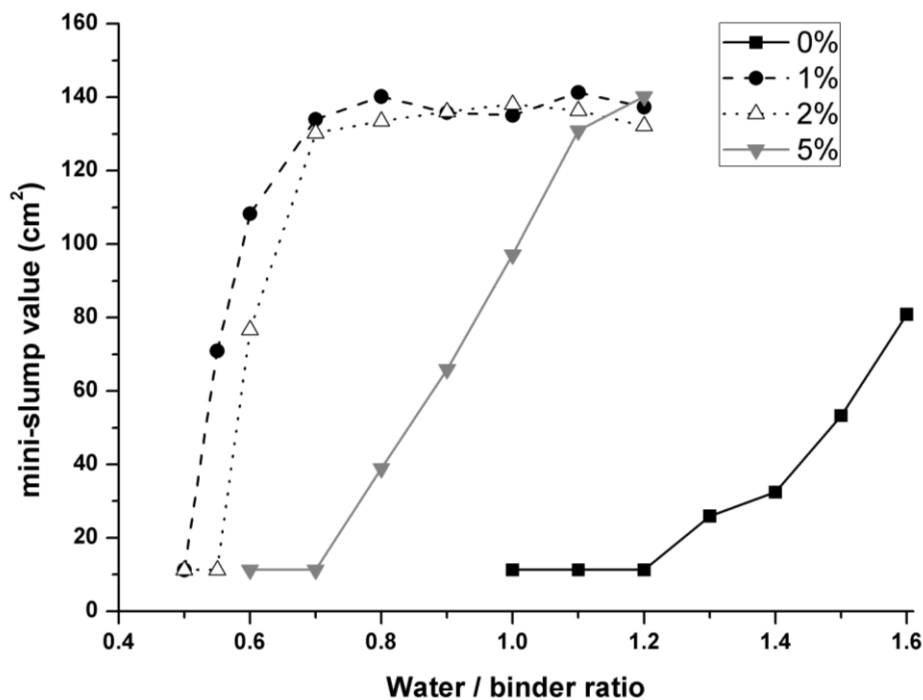


Figure 5.17 Mini-slump values for 1:1 $\text{Mg}(\text{OH})_2:\text{SiO}_2$ with 0-5 wt.% $(\text{NaPO}_3)_6$ as shown in the legend, as a function of water/binder ratio. A measurement of 11.3 cm^2 indicates no slump, as this is the initial slump cone area

The addition of 1 wt.% $(\text{NaPO}_3)_6$ consistently produced a higher fluidity than the other formulations, though only marginally more than the 2 wt.% formulation. Both 1 and 2 wt.% enabled retention of a high fluidity, $\sim 130 \text{ cm}^2$, down to $w/b = 0.7$, with zero slump only reached at $w/b = 0.50$ using 1 wt.% $(\text{NaPO}_3)_6$, and $w/b = 0.55$ using 2 wt.%. Some loss of fluidity was observed at 5 wt.% $(\text{NaPO}_3)_6$ addition, with higher w/b ratios required in order to achieve similar mini-slump values compared to the formulations with 1 and 2 wt.% $(\text{NaPO}_3)_6$. This indicates that a threshold limit exists, beyond which the dispersion is no longer as effective, when too much phosphate is added.

Sodium hexametaphosphate is widely used as a deflocculant and dispersant in minerals processing and the clay industry [567, 571-572]. It is known to adsorb onto mineral surfaces, and is likely performing in the same way within these M-S-H cements. Once adsorbed the phosphate increases the zeta potential of the slurry, increasing the repulsion between the particles and resulting in a more stable suspension [568]. Lower zeta potentials result in flocculation, coagulation, and an increased viscosity [572].

The ability to maintain a high workability over a wide range of w/b ratios by using $(\text{NaPO}_3)_6$ as a dispersant enables a wider range of sludges to be used as feedstocks, due to their variable water content. Correspondingly, significantly less water is required to fluidise the system, compared to the phosphate-free system. This is important, as the w/b ratio has a key impact on porosity in cementitious systems, and reducing water content is the most straightforward way to lower the porosity of the hardened material. Porosity of a cementitious binder is intrinsically linked to permeability, and consequently plays a major role in determining the mobility of radionuclides in the long-term leaching of cementitious wastefoms.[3]

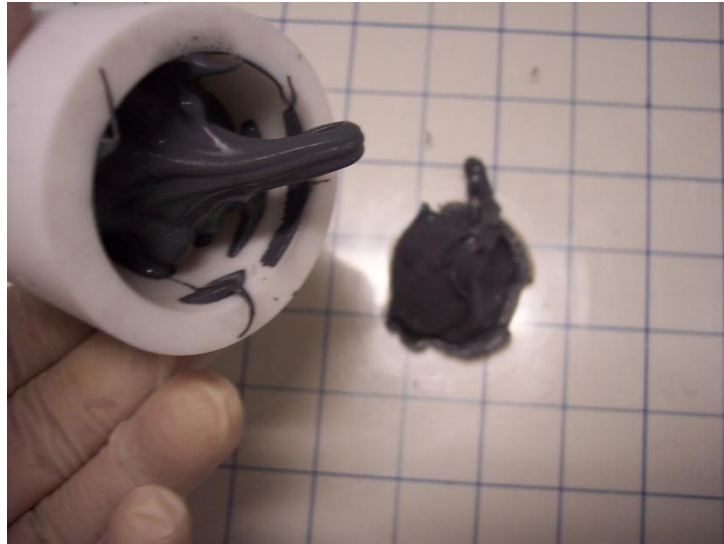


Figure 5.18 Photograph of 1:1 $\text{Mg}(\text{OH})_2:\text{SiO}_2$ sample (2 wt. % $(\text{NaPO}_3)_6$, w/b = 0.5) exhibiting a value of 11.3 cm^2 , showing the highly viscous nature of the paste upon removal of the slump cone

5.3.2.1.2 Compressive strength

In the hardened state, the physical effects of changing the dose of $(\text{NaPO}_3)_6$ had only minor effects for a given w/b ratio. Figure 5.20 shows the development of compressive strength as a function of curing duration for samples with a w/b ratio of 1.0, with representative cubes shown in Figure 5.19. All samples exhibited slow strength gain during the first 28 days, with the samples containing any amount of $(\text{NaPO}_3)_6$ producing similar compressive strengths at each age of curing. The low strengths shown here are related to the high water/binder ratio of this sample set, which prevents the development of a strong microstructure. The sample formed in the absence of $(\text{NaPO}_3)_6$ produced the lowest strength after 28 days. This is likely to be a consequence of the presence of voids and bubbles within the samples caused by the extremely viscous paste produced, which was difficult to cast into the moulds despite the use of a vibrating table.



Figure 5.19 Photograph of 1:1 $\text{Mg}(\text{OH})_2\text{:SiO}_2$ sample cubes, with 5 wt. % $(\text{NaPO}_3)_6$, after 28 days of curing

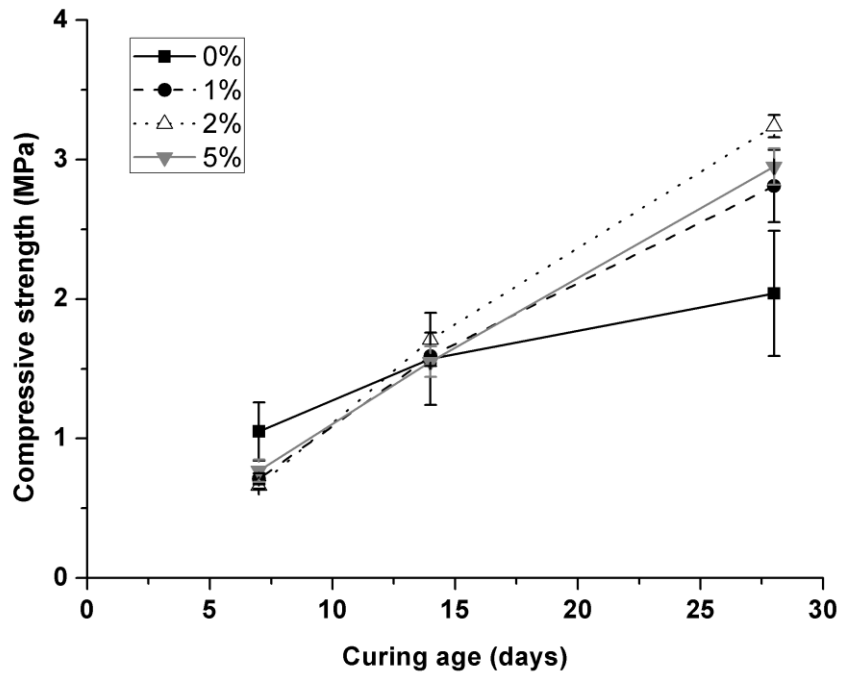


Figure 5.20 Compressive strength of 1:1 $\text{Mg}(\text{OH})_2\text{:SiO}_2$ pastes, w/b = 1.0, with 0–5 wt.% $(\text{NaPO}_3)_6$

All of the samples produced with w/b = 1.0 exhibited lower compressive strengths than is recommended for use in a typical nuclear waste package (4 MPa for a 500 L drum) [72], but at 14 and 28 days did exceed the 0.7 MPa which is the baseline performance requirement for material handling. On this basis, and to offer chemical

consistency throughout all samples, this w/b ratio was selected for use in characterisation of the hardened binder products.

5.3.2.1.3 X-ray diffraction

Figure 5.21 shows similar hydration products to those formed in the tested samples (Section 5.2), with brucite ($\text{Mg}(\text{OH})_2$, PDF # 74-2220) and silica fume consumed to varying degrees at different levels of phosphate addition, to produce M-S-H. Calcite (CaCO_3 , PDF # 05-0586) was identified as a minor impurity in the commercial-grade $\text{Mg}(\text{OH})_2$. In the XRD patterns, poorly crystalline M-S-H is clearly observed *via* diffuse scattering at 20° , 36° and 61° 2θ , with a minor diffuse reflection at 28° 2θ . These diffractograms are similar to those observed for other M-S-H systems [367, 391], as well as for mechanically amorphised talcs [397] and for ground chrysotile; these phases are both considered potential structural models for M-S-H [398]. Excess silica fume is identified *via* a diffuse reflection centred at 20° 2θ , partially overlapping one of the M-S-H reflections. The formation of M-S-H appeared to be retarded when $(\text{NaPO}_3)_6$ was added beyond 1 wt.%; this was clearly observed in the XRD data for the 2 wt.% and 5 wt.% samples after 28 days of curing.

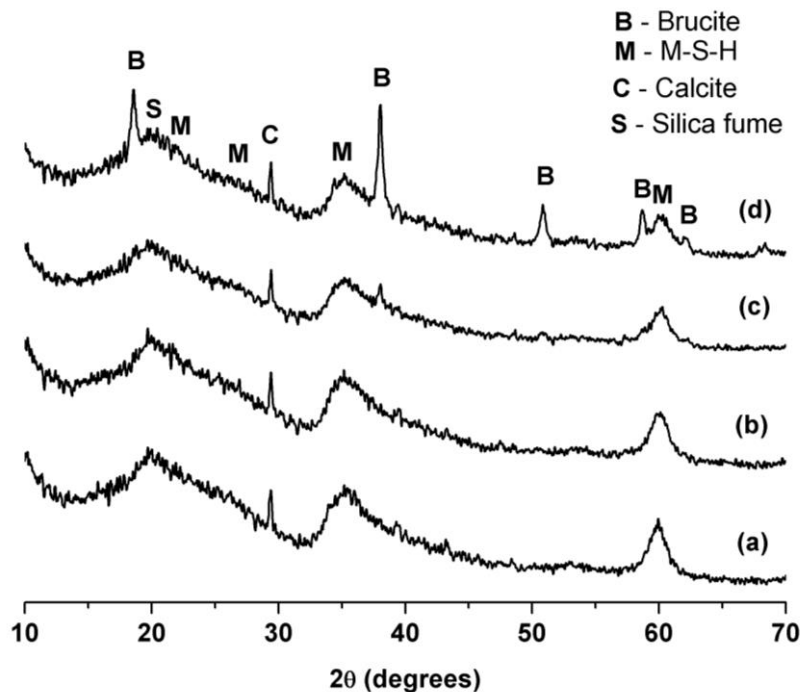


Figure 5.21 X-ray diffraction patterns of 28 day-cured 1:1 $\text{Mg}(\text{OH})_2$: SiO_2 (w/b = 1.0) binders, with (a) 0, (b) 1, (c) 2 and (d) 5 wt.% $(\text{NaPO}_3)_6$ addition

5.3.2.1.4 Thermal analysis

The differential thermogravimetry (DTG) data presented in Figure 5.22 (and total TG in Figure 5.23) correlate well with the diffractograms in Figure 5.21, recording higher residual contents of $\text{Mg}(\text{OH})_2$ (decomposition peak at $\sim 400^\circ\text{C}$ [573]) in the samples with increasing addition of phosphate. The weight loss at temperatures up to $\sim 150^\circ\text{C}$ is assigned to the release of adsorbed water from the surface of the M-S-H [574], as well as free water held in the pores of the hardened gel. Any crystalline talc present would lose structural water at $875 - 1000^\circ\text{C}$ [573], and thus is identifiably absent from these samples (consistent with the XRD data), while poorly crystalline talcs, ground chrysotile, ground antigorite and M-S-H are known to lose water slowly over a wide temperature range below 700°C [389, 391, 398-400, 574].

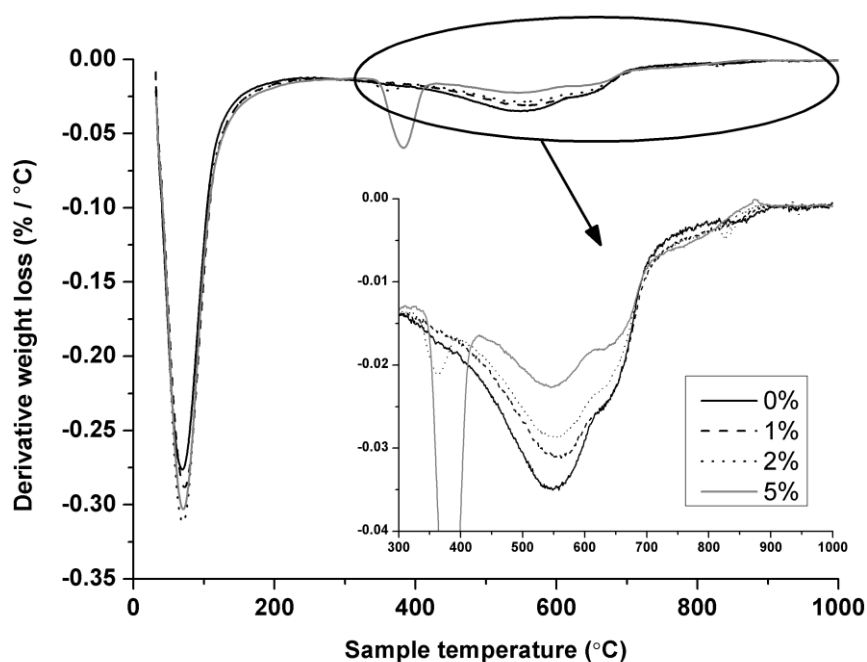


Figure 5.22 DTG data for 1:1 $\text{Mg}(\text{OH})_2:\text{SiO}_2$ (w/b = 1.0) with 0 – 5 wt.% $(\text{NaPO}_3)_6$, samples cured for 28 days. Inset shows the data above 300°C with an expanded vertical scale

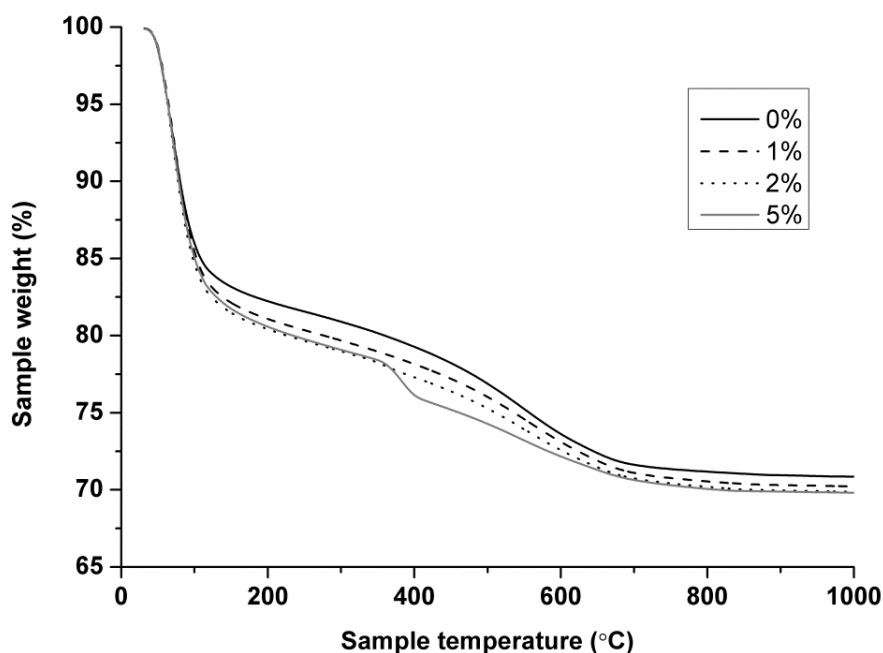


Figure 5.23 TG data for 1:1 Mg(OH)₂:SiO₂ (w/b = 1.0) with 0 – 5 wt.% (NaPO₃)₆, samples cured for 28 days

Table 5.2 shows a quantitative breakdown of the thermogravimetric data in key temperature regions of interest, for samples cured for different durations. The mass loss between 340 – 440 °C represents the quantity of unreacted Mg(OH)₂, and it is evident that even at 1 wt.% addition of (NaPO₃)₆, the rate of Mg(OH)₂ consumption was reduced compared to the phosphate-free sample. More unreacted Mg(OH)₂ was present after 7 and 14 days of curing in the presence of phosphate, although for 1 and 2 wt.% (NaPO₃)₆, parity with the phosphate-free system was reached after 28 days. Addition of 5 wt.% phosphate reduces Mg(OH)₂ consumption at all ages studied, which is consistent with the XRD analysis in section 5.3.2.1.3; the mass loss peak is much more prominent in this sample than in the others shown in Figure 5.22.

Table 5.2 Mass loss (%) determined by TGA in different temperature ranges for 1:1 Mg(OH)₂:SiO₂ (w/b = 1.0) with 0 – 5 wt. % (NaPO₃)₆, at different curing durations. Uncertainty in calculated mass loss is approximately ± 0.2%. Full data are displayed in Appendix I, along with XRD and DTA data for up to 28 days of curing.

Mass loss (%)				
Temperature range (°C)	Na(PO₃)₆ (wt. %)	Curing duration (days)		
		7	14	28
25 to 1000	0	27.2	27.9	29.2
	1	27.2	28.0	29.8
	2	26.1	27.4	30.1
	5	26.0	27.2	30.2
340 to 440	0	7.2	3.6	2.3
	1	10.2	5.5	2.2
	2	11.1	6.6	2.3
	5	10.6	7.6	4.1
450 to 1000	0	5.8	7.0	7.4
	1	5.4	6.2	7.0
	2	4.9	5.8	6.5
	5	4.2	4.8	5.4

In Figure 5.22, the region between 450 and 700 °C was seen to consist of two peaks, located at 550 °C and 640 °C. The peak at 550 °C is identified as being due specifically to M-S-H decomposition, with the peak at 640 °C assigned to the decomposition of calcite (CaCO₃) [575], which is introduced into each sample in equal proportions as an impurity in the Mg(OH)₂. As previously mentioned, the M-S-H loses water slowly and over a very wide temperature range, and thus the mass loss event at 450–1000 °C is treated as characteristic for its analysis in Table 5.2, assuming a constant CaCO₃ contribution in all samples.

Magnesite (MgCO₃) decomposes at 527-615 °C [464, 575], but this phase was not identified by FTIR or XRD analysis, and so is not considered to contribute significantly to the DTG profile. Other (hydrous) magnesium carbonates would show

distinctive low-temperature decomposition peaks, and also were not identified by XRD or FTIR.

The inset in Figure 5.22 demonstrates a clear difference between the samples at 28 days of age, which is also quantified in Table 5.2 for each curing age. If it was assumed that M-S-H was structurally similar between the samples, this would indicate that M-S-H formation increased with curing age, and was retarded by the phosphate additions. This is in agreement with the differences observed in the diffraction patterns (Figure 5.21). However, when comparing between the 0 and 1 wt.% $(\text{NaPO}_3)_6$ data, the mass loss in Table 5.2, for $\text{Mg}(\text{OH})_2$ decomposition (340-440 °C) remains the same (and XRD analysis (Figure 5.22) suggests complete $\text{Mg}(\text{OH})_2$ consumption), however the mass loss for M-S-H is different between these two. This suggests there might be a structural difference in the M-S-H gels forming due to the effect of the phosphate additive.

This potential structural difference is highlighted within the differential thermal analysis of the samples. The data for these follow the DTG curves, except for the presence of an exotherm at 800-850 °C which does not correspond to any weight loss within the DTG plot (Figure 5.22). Figure 5.24 displays these data, focussing on the region 700-1000 °C. In these data it can be observed that at 14 days (Figure 5.24 B) and 28 days (Figure 5.24 C) of curing an increase in phosphate content appears to shift the major exothermic peak ~800-850 °C to a slightly lower temperature. The nature of this exotherm is discussed in more detail in Section 5.3.2.2.1 below.

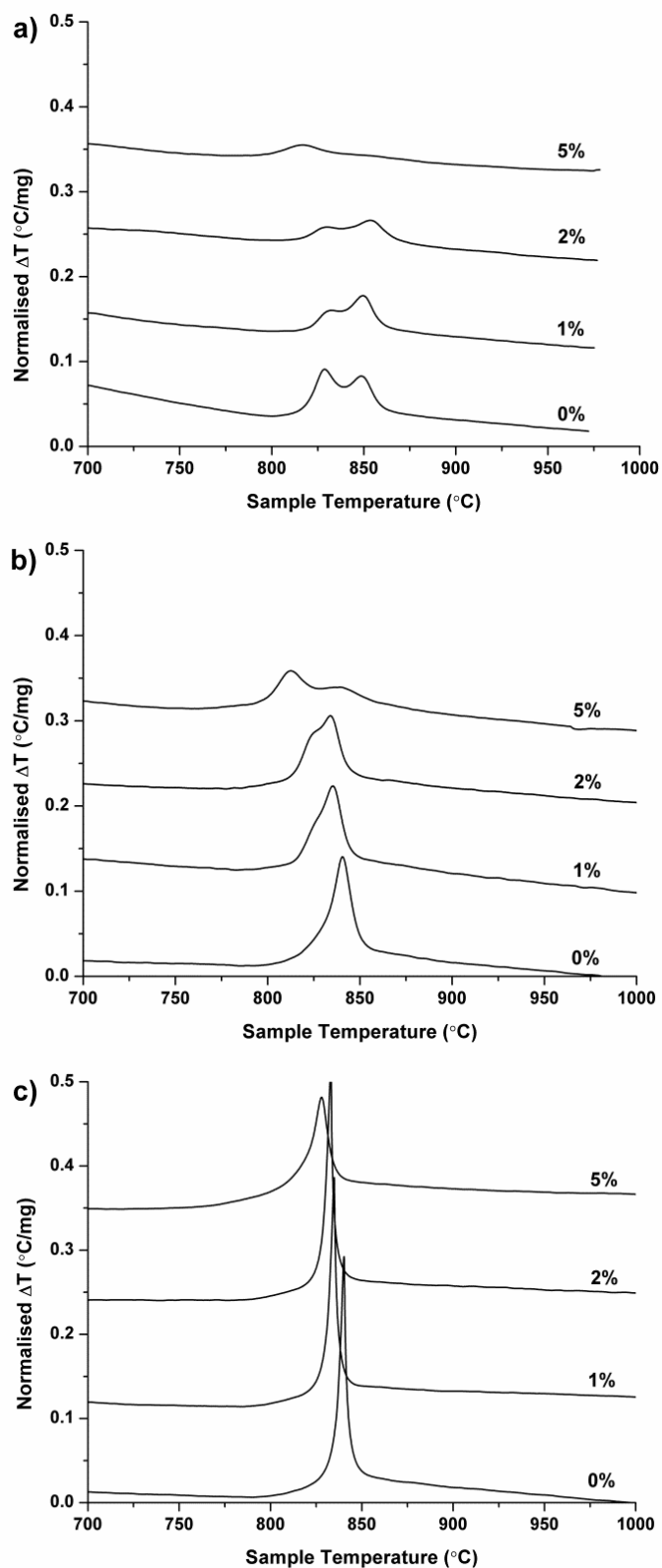


Figure 5.24 DTA data for 1:1 $\text{Mg}(\text{OH})_2:\text{SiO}_2$ ($w/b = 1.0$) binders with 0-5 wt.% $(\text{NaPO}_3)_6$, at curing ages of (a) 7, (b) 14 and (c) 28 days curing (n.b. spectra stacked and offset, y axis given for comparison)

5.3.2.2 Structural evolution

5.3.2.2.1 X-ray diffraction and thermal analysis

Based on the discussion in the preceding section, further analysis was undertaken to understand the structural evolution of a phosphate modified system. A 1:1 $\text{Mg}(\text{OH})_2:\text{SiO}_2$ blend, using a w/b ratio of 1.0 and 2 wt. % $(\text{NaPO}_3)_6$, was used as it developed the highest compressive strength among the samples tested at this w/b ratio.

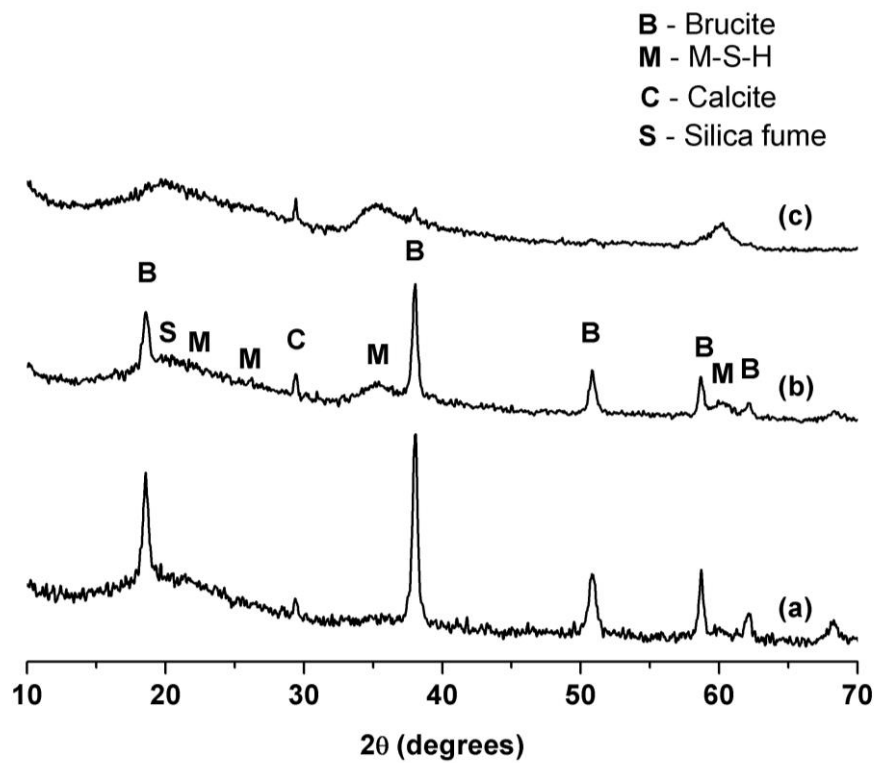


Figure 5.25 X-ray diffractograms of 1:1 $\text{Mg}(\text{OH})_2:\text{SiO}_2$ (w/b = 1.0) with 2 wt.% $(\text{NaPO}_3)_6$ at curing ages of (a) 7, (b) 14 and (c) 28 days

The development of the binder can be seen in the diffractograms in Figure 5.25, where decreasing intensity of the brucite ($\text{Mg}(\text{OH})_2$) reflections is evident, along with increasing intensity of M-S-H reflections as the curing process progresses. This correlates well with the DTG data for samples with different curing durations (Figure 5.26), demonstrating that longer-term curing led to lower mass loss at $\sim 400^\circ\text{C}$

(Mg(OH)₂ decomposition), and larger mass losses in the regions 25 – 150 °C and ~550 °C, both of which can be used as indicators of M-S-H formation. As in Figure 5.22, these DTG data also show a double peak in the region 450-700 °C. At early ages both peaks appear to have a similar intensity, but the peak at 550 °C increases at later curing ages, while that for the calcite decomposition at 650 °C remains constant.

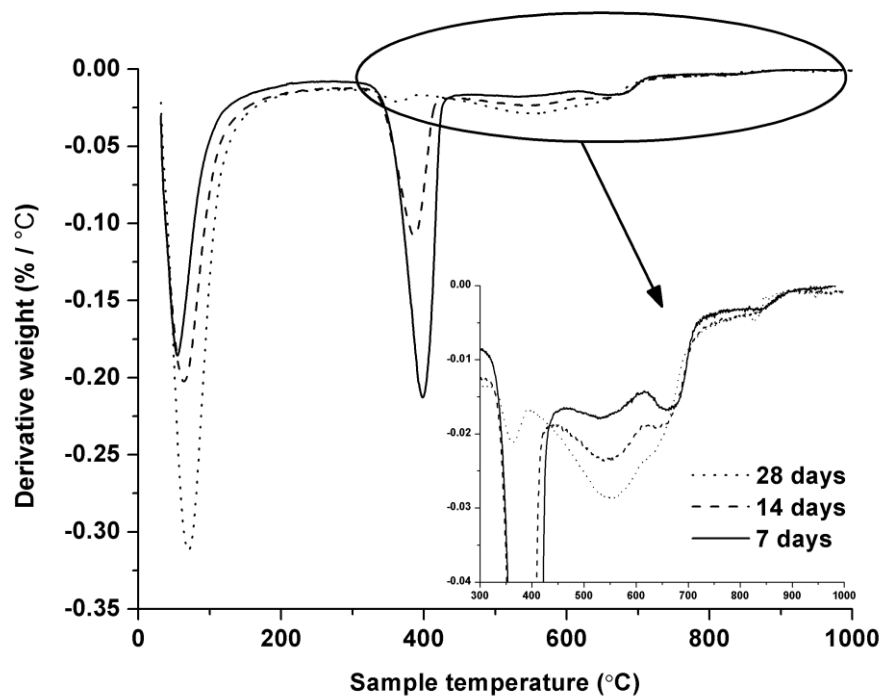


Figure 5.26 DTG data for 1:1 Mg(OH)₂:SiO₂ (w/b = 1.0) with 2 wt.% (NaPO₃)₆, at curing ages of 7, 14 and 28 days

The DTA data for the M-S-H binder (Figure 5.27) show endothermic heat flow features in similar temperature ranges to those observed as mass loss peaks in DTG, but with an additional exotherm at 800-850 °C, which becomes sharper and more intense with greater sample maturity. This signal changes from two shallow exotherms (826 and 853 °C) after 7 days, to one strong sharp exotherm at 833 °C after 28 days. This change is not associated with a mass loss event in the DTG data, and therefore has been identified as the crystallisation of M-S-H [389, 391]. Similar crystallisation events have been observed in thermal treatment of amorphised talc [399], which is converted to enstatite (MgSiO₃) at this temperature [397] (overview

of minerals linked to M-S-H reported again in Table 5.3). Comparable exotherms are noted in natural serpentine minerals, with chrysotile exhibiting a particularly sharp exotherm, forming a mixture of enstatite and forsterite (Mg_2SiO_4) upon heating [576].

Table 5.3 Minerals linked to M-S-H

Mineral	Group	Formulation
Lizardite	<i>Serpentine</i>	$\text{Mg}_3(\text{Si}_2\text{O}_5)(\text{OH})_4$
Antigorite	<i>Serpentine</i>	$\text{Mg}_3(\text{Si}_2\text{O}_5)(\text{OH})_4$
Chrysotile	<i>Serpentine</i>	$\text{Mg}_3(\text{Si}_2\text{O}_5)(\text{OH})_4$
Sepiolite	<i>Phyllosilicate</i>	$\text{Mg}_4(\text{Si}_6\text{O}_{15})(\text{OH})_2 \cdot 6\text{H}_2\text{O}$
Saponite	<i>Phyllosilicate</i>	$\text{Ca}_{0.25}(\text{Mg,Fe})_3((\text{Si,Al})_4\text{O}_{10})(\text{OH})_2 \cdot n\text{H}_2\text{O}$
Talc	<i>Phyllosilicate</i>	$\text{Mg}_3(\text{Si}_4\text{O}_{10})(\text{OH})_2$

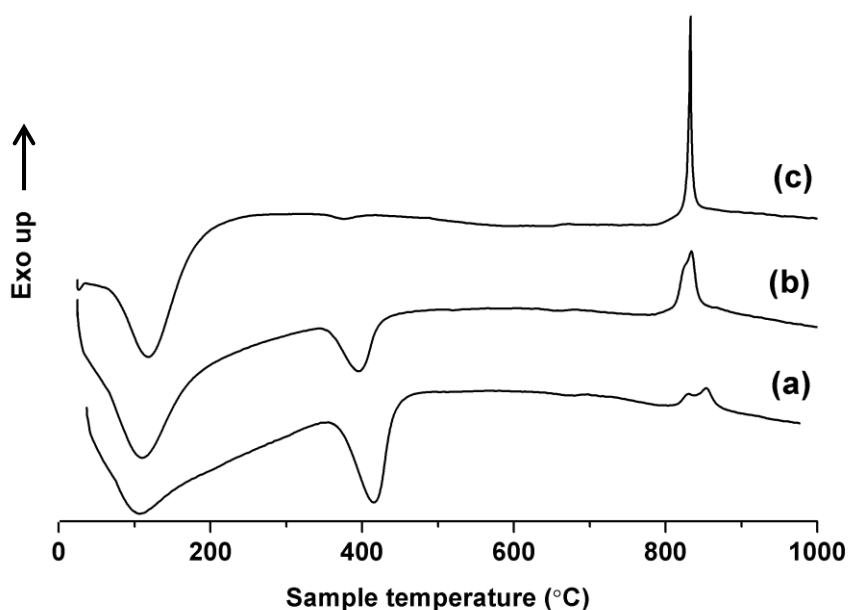


Figure 5.27 DTA data for 1:1 $\text{Mg}(\text{OH})_2:\text{SiO}_2$ (w/b = 1.0) with 2 wt.% $(\text{NaPO}_3)_6$, at curing ages of (a) 7, (b) 14 and (c) 28 days

To further understand the exotherms observed in the DTA data, samples cured for 7 and 28 days were heated to 900 °C and analysed by XRD to determine the crystalline

phases formed (Figure 5.28). There is a clear difference observed between the samples. For the 28 day cured sample, only enstatite (MgSiO_3 , PDF # 73-1758) was present, similar to the thermal treatment of amorphised talc as noted above. On the other hand, for the 7 day cured sample, in addition to enstatite, forsterite (Mg_2SiO_4 , PDF # 34-189), periclase (MgO , PDF # 89-4248) and a broad band around $\sim 22^\circ 2\theta$ assigned to low-crystallinity silica were also observed.

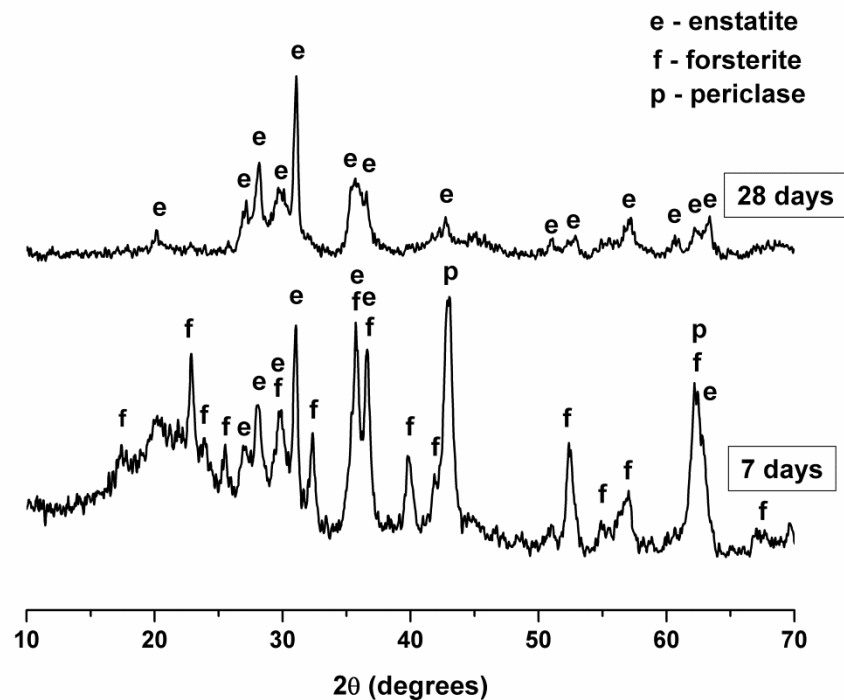


Figure 5.28 XRD patterns of 1:1 $\text{Mg}(\text{OH})_2:\text{SiO}_2$ (w/b = 1.0) heated to 900°C after 7 and 28 days of curing

The presence of a single, sharp exotherm in the DTA data for the 28 day cured M-S-H (Figure 5.27) can be explained by the presence of only enstatite after heating (Figure 5.28). The shallower double peak observed in the DTA data for the 7 day cured sample could be attributed to a less developed and less homogeneous M-S-H gel structure, which crystallised into enstatite and forsterite at slightly different temperatures. The significant amount of periclase in the 7 day cured sample is due to the dehydroxylation of remnant $\text{Mg}(\text{OH})_2$ upon heating.

5.3.2.2.2 Fourier transform infrared spectroscopy

The FTIR data shown in Figure 5.30 demonstrate the evolution of phases with time, from the raw materials to the 28 day cured sample. The silica fume used in the present study (Figure 5.30a) had a spectrum similar to that of vitreous silica, with broad bands at 1110 cm^{-1} and 803 cm^{-1} arising from Si-O stretching, and at 475 cm^{-1} arising from O-Si-O bending [577-578]. $\text{Mg}(\text{OH})_2$ (Figure 5.b) displayed a characteristic OH vibration at 3698 cm^{-1} and libration at 415 cm^{-1} , with adsorbed water at $\sim 3400\text{ cm}^{-1}$ and the broad carbonate vibration of the calcite impurity at 1450 cm^{-1} [579-580]. The anhydrous mix (Figure 5.c) naturally showed the features of these raw materials combined.

Upon reaction, some of these features from the raw materials became less prominent (Figure 5.30d,e), and the spectrum of the 28 day sample (Figure 5.30f) became very similar to those previously reported for other M-S-H gels [393]. The crystal structures of some important M-S-H minerals are shown in Figure 5.29 below.

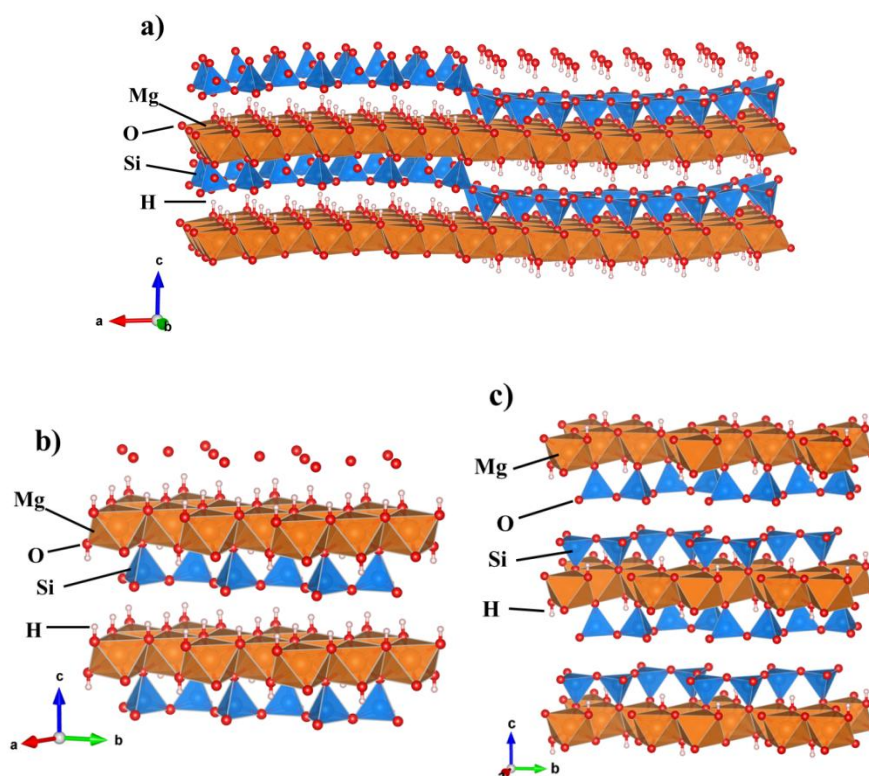


Figure 5.29 Crystal structures of a) antigorite, b) lizardite, c) talc, drawn from

It is noted that the spectrum of the 28 day curing sample also resembles those for partially amorphised talc [397, 399], ground chrysotile [398], and ground antigorite [400]. Libration of the Mg_3OH unit in talc has been observed at 669 cm^{-1} , along with a vibration of chrysotile at 608 cm^{-1} (shoulder at 645 cm^{-1}) [581], and similar modes are likely to be causing the peak seen in the M-S-H at 642 cm^{-1} . The Si-O-Si vibrations of the tetrahedral sheets within the talc structure are recorded at 1018 cm^{-1} and 1047 cm^{-1} [582], while amorphised chrysotile exhibits in-plane Si-O and out-of-plane Si-O stretching at 1025 cm^{-1} and 1082 cm^{-1} respectively, with asymmetric Si-O stretching at 960 cm^{-1} [398]. The broad band centred at 1009 cm^{-1} , with a broad shoulder at 1052 cm^{-1} , in the M-S-H is likely to be related to similar structural motifs.

The broad bands at $\sim 3400\text{ cm}^{-1}$ and 1640 cm^{-1} , which increase in intensity with age, are suggestive of water adsorbed to surfaces or incorporated in disordered reaction products. Some contribution in this region may also be from Si-OH vibrations due to the hydrated residual silica, which may also be producing the shoulder seen at $\sim 885\text{ cm}^{-1}$.

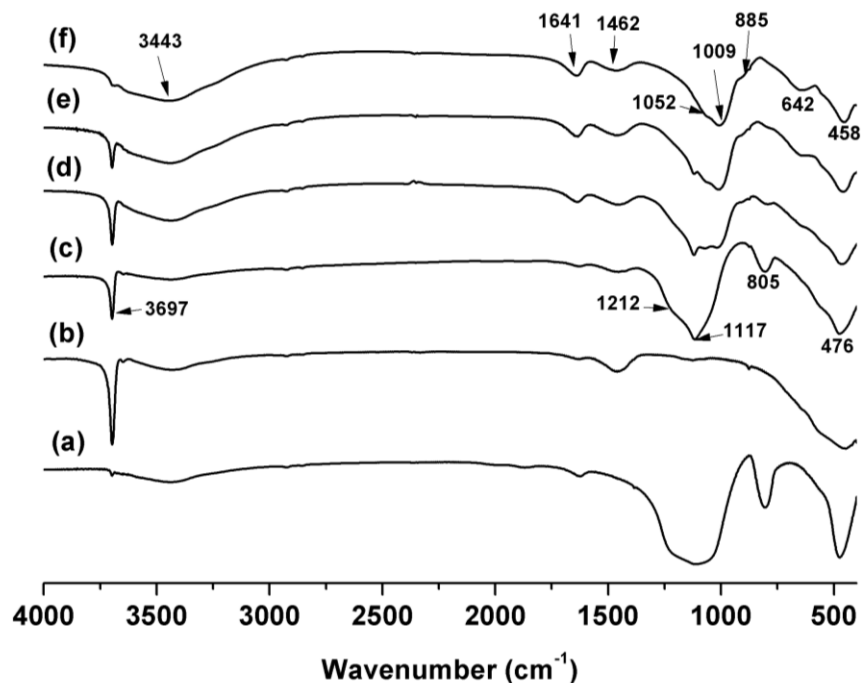


Figure 5.30 FTIR spectra of (a) silica fume, (b) $\text{Mg}(\text{OH})_2$, (c) 1:1 $\text{Mg}(\text{OH})_2:\text{SiO}_2$ with 2 wt.% $(\text{NaPO}_3)_6$ as an anhydrous powder mix, and hydrated samples cured for (d) 7, (e) 14 and (f) 28 days ($w/b = 1.0$ for all hydrated samples)

5.3.2.3 Nuclear Magnetic Resonance (NMR) spectroscopy

^{29}Si and ^{25}Mg MAS NMR experiments were carried out to identify any structural changes occurring in these binders at advanced times of curing (up to 8 months), and the effect of $(\text{NaPO}_3)_6$ addition on the structure of the M-S-H formed in the 1:1 $\text{Mg}(\text{OH})_2:\text{SiO}_2$ binder system. The ^{29}Si NMR spectra of M-S-H samples with 0% and 2% $(\text{NaPO}_3)_6$ after 1 and 8 months of curing are reported in Figure 5.31.

The ^{29}Si MAS NMR spectra in Figure 5.31 are in good agreement with previously reported spectra for synthetic M-S-H type gels produced using MgO as the main Mg source [368, 389, 583]. Both the 1 and 8 month data sets resemble most closely the aged (6 months) high-Mg samples produced at 85 °C by Brew and Glasser [393], and the peak assignments presented here follow the general trends identified by those authors.

Deconvolution of the spectra enabled the identification of five peaks, with very minor shifts between spectra (Table 5.4). For the two spectra obtained after 1 month of curing, Q^1 and Q^2 peaks centred at around -81 and -86 ppm respectively were identified, with the Q^3 region split between two peaks centred at (a) -93 and (b) -97.7 ppm, respectively. It is noted that the ^{29}Si MAS NMR spectra of serpentine minerals and talc typically exhibit peaks in the Q^3 region, while broader Q^1 and Q^2 bands signify a less structured gel. The major $\text{Q}^3(\text{a})$ peak at -93 ppm was consistent with the Q^3 resonance typically identified in both chrysotile [584] and antigorite [585-586], while the smaller $\text{Q}^3(\text{b})$ peak at -97.7 ppm was assigned to a Q^3 site environment similar to those typically present in talc [573].

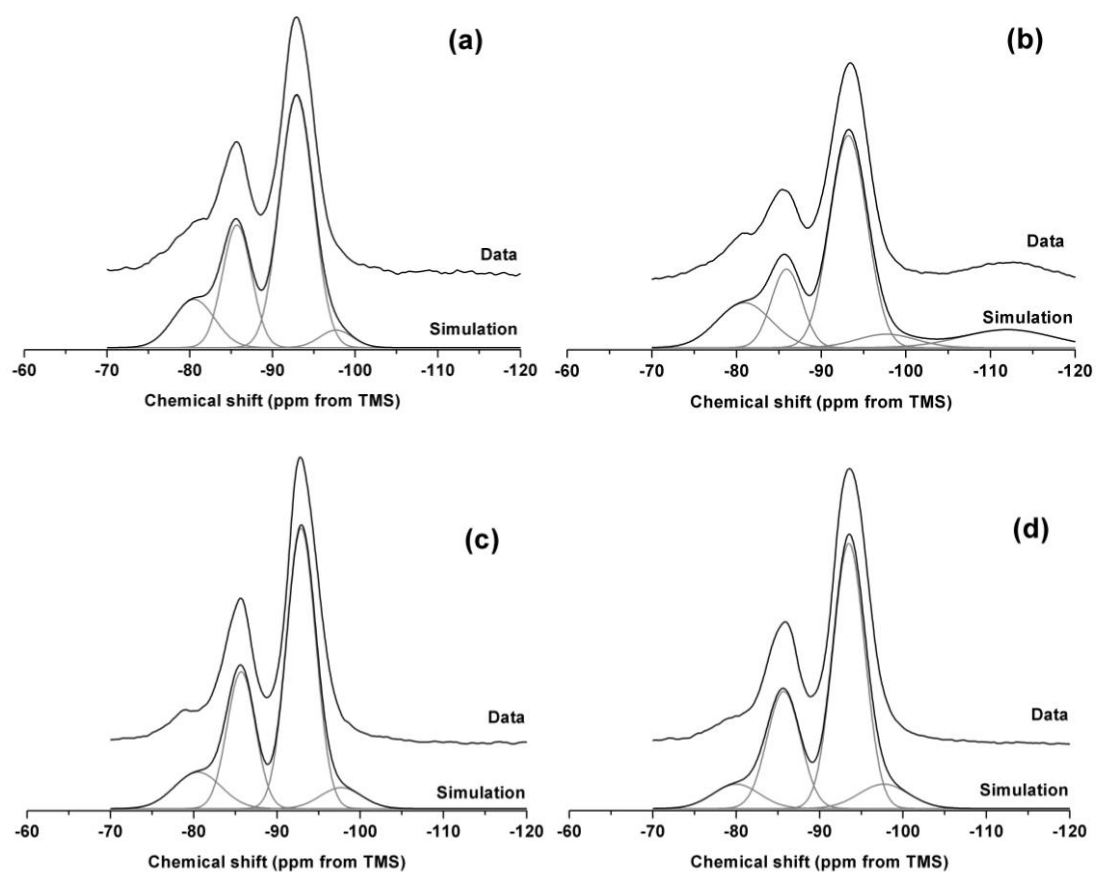


Figure 5.291 ^{29}Si MAS NMR spectra for 1:1 $\text{Mg}(\text{OH})_2:\text{SiO}_2$ (w/b 1.0) with (a) 0 and (b) 2 wt. % $(\text{NaPO}_3)_6$ at a curing age of 1 month, (c) 0 and (d) 2 wt. % $(\text{NaPO}_3)_6$ after 8 months of curing. The data presented include a simulation and constituent peaks underneath.

Table 5.4 Peak positions and widths (ppm) for deconvolutions shown in Figure 5.31

Estimated uncertainty in calculated intensities $\pm 1\%$

$(\text{NaPO}_3)_6$		1 month					8 months				
		Q ¹	Q ²	Q ^{3(a)}	Q ^{3(b)}	Q ⁴	Q ¹	Q ²	Q ^{3(a)}	Q ^{3(b)}	Q ⁴
0 wt. %	Centre	-80.5	-85.7	-92.9	-97.7	-	-80.5	-85.7	-92.9	-97.7	-
	FWHM	5.9	4.1	4.8	4.7	-	6.6	4.0	4.1	5.9	-
	Intensity (%)	13.7	24.4	57.9	4.0	-	11.6	26.5	55.9	6.0	-
2 wt. %	Centre	-80.9	-85.9	-93.2	-97.7	-112	-80.0	-85.7	-93.5	-97.7	-
	FWHM	7.5	4.2	5.2	8.2	12.7	6.6	4.7	4.5	7.1	-
	Intensity (%)	16.1	15.8	52.1	5.3	10.7	7.7	26.6	57.3	8.3	-

The relatively high $Q^3(a+b)/Q^2$ intensity ratio in Table 5.4 is indicative of a high level of structural development in the gel. The addition of 2 wt.% $(NaPO_3)_6$ leads to the presence of a peak centred at -112 ppm after 1 month, attributed to Q^4 species in unreacted silica fume [587] and indicating a lower extent of reaction, resulting in lower intensity Q^3 and Q^2 peaks. This indicates that with no addition of $(NaPO_3)_6$ the silica fume had completely reacted, while the presence of phosphate had retarded the conversion of silica fume to M-S-H.

After 8 months of curing, the spectra had changed slightly compared with those observed in the specimens after 1 month of curing. There was a decrease in the Q^1 region for both 0 and 2 wt. % phosphate samples, which suggests that further structural development of M-S-H occurred in the samples, leading towards the formation of a more cross-linked structure. After 8 months of curing the resonance assigned to the Q^4 sites of unreacted silica fume was no longer present in the phosphate-containing sample, indicating that the silica fume in these binders had been fully consumed at this time.

The structure of M-S-H has previously been proposed to resemble a poorly crystalline talc-like material (Figure 5.29) [142]. Talc typically exhibits a single ^{29}Si peak at -97.7 ppm [573], however this peak was only a minor Q^3 component within the binders produced in this study. The major Q^3 component was identified at -93 ppm, which corresponds to that typically found in the serpentine group of minerals (polymorphs of $Mg_3(Si_2O_5)(OH)_4$, such as chrysotile, lizardite and antigorite). The reported ^{29}Si NMR peak locations for these minerals vary slightly from publication to publication, potentially due to the slight variations in chemical composition of each natural sample due to Fe, Ca and Al inclusions. Both chrysotile [584] and antigorite [586] have reported values close to -93 ppm, although the antigorite spectrum is broad, while data for lizardite is difficult to obtain.

To clarify the details of the M-S-H structure formed here, natural mineral samples of lizardite and antigorite were obtained and analysed *via* ^{29}Si and ^{25}Mg MAS NMR. These samples contained traces of iron (7.0 wt.% in antigorite, 3.4 wt.% in lizardite, on an oxide basis as determined by X-ray fluorescence), broadening the signal and affecting the relaxation times. This was more severe for the antigorite sample. The

lizardite was also slightly aluminous (7.1 wt.% Al₂O₃), as Al often substitutes for Si in natural samples [395, 588-589]. These spectra are shown in Figure 5.32, both exhibiting strong signals within the Q³ region at around -90 ppm. The broad antigorite spectral feature at -87.8 ppm is downfield of the principal Q³ peaks in the M-S-H, although the spectrum is not of high resolution, whereas the main lizardite peak at -93.7 ppm matches very closely to the Q³(a) site observed within the M-S-H samples. There does exist a broad feature downfield of this peak, which significantly reduces in area when cross polarised with ¹H (Figure 5.33), suggesting these may resemble less ordered, less hydrated lizardite-like assemblages than the primary Q³(a) site.

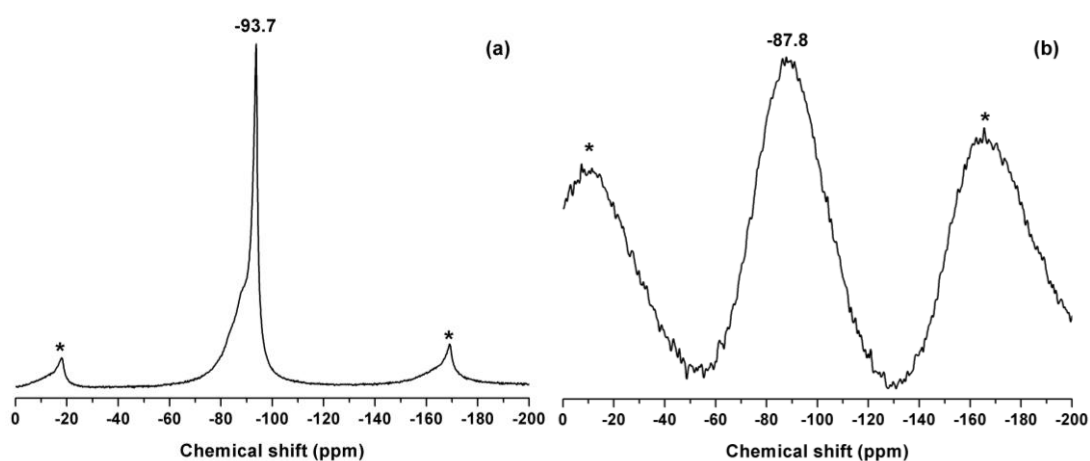


Figure 5.32 ²⁹Si MAS NMR spectra for: (a) lizardite, (b) antigorite. Spinning sidebands marked with *

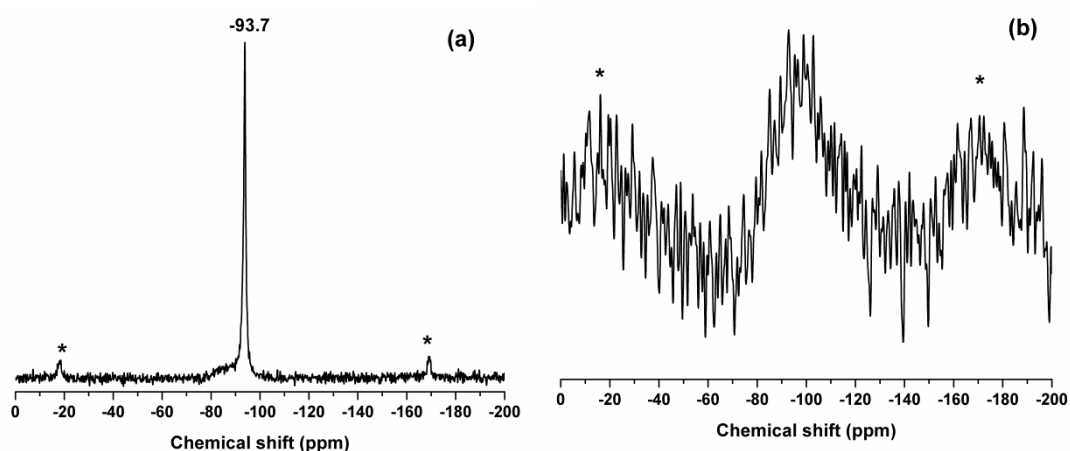


Figure 5.33 ²⁹Si-¹H CP-MAS NMR spectra for: (a) lizardite, (b) antigorite. Spinning sidebands marked with *

^{25}Mg MAS NMR data are significantly more difficult to obtain and interpret than is the case for ^{29}Si . The low natural abundance (10%) and low resonance frequency often necessitates the use of very high field instruments (e.g. 20 T used here) [590]. Combined with its quadrupolar nature (spin $5/2$), this makes the interpretation of spectra complicated, though recent advances in this field are shedding more light on this less well studied nucleus [590-594].

^{25}Mg MAS NMR spectra of lizardite, antigorite and talc are overlaid with the spectra of 1 and 8 month cured M-S-H samples (with 0% $(\text{Na}_3\text{PO}_4)_6$) in Figure 5.34. A clear change in lineshape is observed in the M-S-H samples as curing progresses, with the spectrum shifting upfield. The 8 month M-S-H sample specifically aligns well with the lizardite spectrum (as compared in Figure 5.35), compared to the antigorite or talc spectra. It should be noted that being a natural sample, the lizardite contains an impurity of ~12 wt.% $\text{Mg}(\text{OH})_2$, which will modify the ^{25}Mg spectrum. At this field strength, second-order quadrupolar interactions of the central transition cause $\text{Mg}(\text{OH})_2$ to exhibit a split double peak from its single Mg site [595]. This double peak is centred at -9 ppm, which is in the central part of the lizardite spectrum. Though contributing to the peak, this is unlikely to significantly alter the peak position.

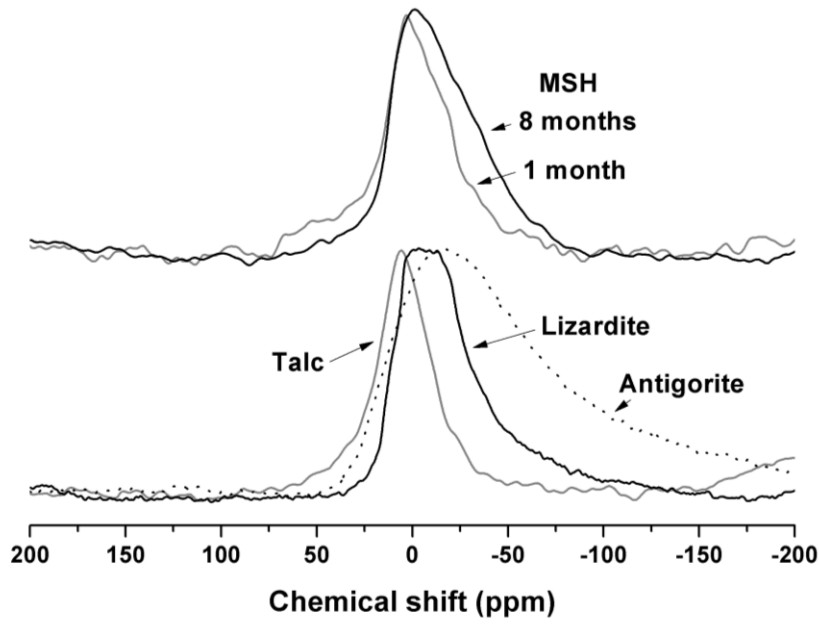


Figure 5.34 ^{25}Mg MAS NMR spectra of 1 and 8 month cured M-S-H with reference materials. Note that the antigorite spin rate was increased from 10 to 14 kHz due to line broadening from iron.

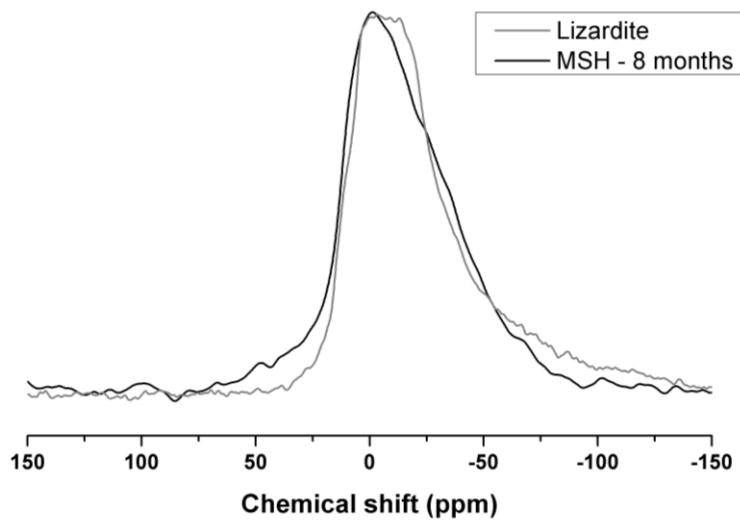


Figure 5.35 ^{25}Mg MAS NMR spectra of 8 month cured M-S-H, and comparison with lizardite

Studies of mineral formation in the M-S-H system have evolved significantly over time, as thermodynamic and kinetic data are refined. Previous papers have included chrysotile as a stable phase, or exclude lizardite from calculations, leading to

predictions that either antigorite or chrysotile are stable at low temperatures [596-597]. Recently, however, it has been concluded that lizardite is the stable phase in the M-S-H system below ~ 300 °C, with antigorite only stable at temperatures exceeding 250 °C [598]. Chrysotile is postulated to only form from supersaturated solutions as a kinetic effect [599-600], having no thermodynamically stable range within the M-S-H field [598]. Given this assessment, it seems reasonable to conclude that the serpentine-like feature in the M-S-H gel is likely to be structurally similar to the thermodynamically most stable phase; this is lizardite, given the formation conditions.

This assignment fits well with the chemistry of the binders produced within the $\text{Mg}(\text{OH})_2\text{-SiO}_2\text{-H}_2\text{O}$ system studied; assuming complete reaction of $\text{Mg}(\text{OH})_2$ and SiO_2 in these samples, the molar Mg/Si ratio of this binder should be ~ 0.95 . This ratio is between those of talc (0.75) and lizardite (1.5), and thus suggests that the structural motifs of both mineral types are likely to be present in the gel structure. It does, however, appear that ageing of the gels produces a gel which is closer in structure to lizardite than talc, as evidenced by the aforementioned NMR data.

Analysis of M-S-H gels at different Mg/Si ratios by Brew and Glasser [393] showed that increasing the Mg/Si ratio of the M-S-H gel induced changes in the peak positions of the ^{29}Si MAS NMR resonances towards less negative chemical shift values. In that study, aged M-S-H gels formulated with Mg/Si ratios of 0.82 and 0.89 exhibited Q^3 bands at chemical shifts of -98.8 ppm and -97.7 ppm respectively, whereas M-S-H gels produced with an Mg/Si ratio of 0.94 showed a peak shifted to -94.6 ppm. Brew and Glasser noted that their FTIR and ^{29}Si NMR data more closely resembled chrysotile than talc. This suggests that there is a shift from the formation of a poorly crystalline talc-like structure to a poorly crystalline serpentine-like material when the Mg/Si ratio is increased. It is important to understand this structural shift as a function of composition, as knowledge of the structure of the M-S-H can help to predict its future behaviour, likely stability, and the quantity of $\text{Mg}(\text{OH})_2$ which can be accommodated into this system, and this is central to its use as a nuclear wasteform. The addition of phosphate to enhance fluidity does not appear to significantly alter the final M-S-H structure, although it retards the kinetics of conversion of amorphous silica to M-S-H in the first month of curing.

5.4 Conclusions

5.4.1 Scientific findings

Chapter looked at varying ways in which M-S-H cements could be made using both MgO and Mg(OH)₂. Initially scoping experiments determined that a 50:50 blend of MgO:SiO₂ produced cements which formed appreciable amounts of M-S-H and formed solid monoliths. The strength of these cements was lower than a typical Portland cement, and water/solids ratios was significantly higher. The type of MgO used was crucial, with dead burnt MgO reactive very slowly, although forming solid cements after a year of curing. The M-S-H gel formed was poorly crystalline in nature, very much in agreement with existing literature from MgO-silica fume cements. Crucial information about the effect of curing temperature was elucidated from these initial experiments, with increasing temperature significantly accelerating the formation of M-S-H. Curing at 60 °C resulting in nearly full conversion of Mg(OH)₂ to M-S-H after 7 days, with curing at 40 °C taking 28 days. Curing at 20 °C resulted in no observable M-S-H formation after 28 days. This resulted in a slightly elevated temperature of 40 °C used for all further M-S-H experiments, balancing speed of formation with the risk of desiccation at higher temperatures.

It was found that Mg(OH)₂ could be used to successfully form an M-S-H cement, something what has not before been reported in open scientific literature. The properties of this cement were studied, using the already determined 50:50 wt. % blend (Mg(OH)₂:SiO₂). An inorganic phosphate dispersant (NaPO₃)₆ was utilised to reduce the water content and to produce a more fluid cement. This was highly effective up to 2 wt.% of the total solids, producing very fluid cements down to a water / binder ratio of 0.6, down from 1.6 without any phosphate addition. Aside from increasing fluidity, the phosphate addition slightly retarded M-S-H formation up to 2%, and retarding more heavily at a 5% loading. As a result of this it would be advisable to keep (NaPO₃)₆ loadings at, or below 2 wt. % in M-S-H cements.

The development of the M-S-H gel within these Mg(OH)₂-SiO₂-(NaPO₃)₆ binders was followed in more detail up to 28 days of curing, using XRD, FTIR and NMR analysis. The gel itself resembled that of a poorly crystalline talc or chrysolite-like material from initial XRD and FTIR analysis. Detailed ²⁹Si and ²⁵Mg solid state

NMR revealed structural features more closely resembling lizardite than other related magnesium silicate minerals (such as antigorite or chrysotile), however the Mg/Si ratio of 0.95 within this binder points towards structural features of both lizardite and talc. Although the precise nature of the M-S-H gel is still not fully understood, the work here has contributed new knowledge to this area.

5.4.2 Industrial application

This chapter has ultimately successfully proven that $\text{Mg}(\text{OH})_2$ can be utilised to produce an M-S-H cement without the need for a pre-existing MgO based M-S-H cement binder. The developments presented here will enable M-S-H to be used as an encapsulant for both low and high-water content sludges without the occurrence of bleed water, which would otherwise need to be decanted and treated as a secondary waste stream if Portland cement-based grouts were used to treat these sludges. The implementation of these cements for Magnox sludge encapsulation is likely to be hindered by slow strength development in samples with a high water/binder ratio, despite providing an effective method of converting this waste into a cementitious binder. Application of this cement would also be highly dependent on the Mg/Si ratio in the resultant cementitious slurry, which is a major concern as retrieved sludges can vary widely in their $\text{Mg}(\text{OH})_2$ contents. This would require extensive characterisation, and potential homogenisation of sludges prior to cementation if M-S-H cements were chosen as a wasteform. Although this is not impossible, it would add an extra step of complexity in utilising this type of binder.

Ultimately these binders are also highly dependent on an elevated curing temperature for formation of M-S-H within a suitable time period. It would therefore be crucial that wasteforms are kept at or above 40 °C until solidification, unless waste packages could be stored for several months before moving from cementation facilities. The ability of these cements to compete with existing Portland cement based binders for waste immobilisation would also highly depend on their long-term stability, which is as yet unknown. This cement is not yet a suitable candidate for Magnox sludge immobilisation, however it does hold some promise as a slower setting cement which is controllable, fluid, and ultimately produces a solid wasteform.

6 Aluminosilicate – Mg(OH)₂ binders

Note: This chapter is an extended version of the published paper:

Walling, S.A., Bernal, S. A., Kinoshita, H., Collier, N.C., Provis, J.L. (2014) “Cementitious binders in the system Mg(OH)₂-NaAlO₂-SiO₂-H₂O”, *Advances in Applied Ceramics*, **113**, 496-501.

6.1 Introduction

M-S-H binders have attracted the attention of both industry and academia as potentially environmentally friendly and alternative cements that can be a suitable matrix for the immobilisation/encapsulation of ILW [369]. The formation conditions of M-S-H products and their properties from existing literature have been studied in detail within Chapter 3. In the previous chapter, it was demonstrated that M-S-H can also be produced through the chemical reaction between silica fume and Mg(OH)₂ under non-hydrothermal conditions, rather than requiring the use of MgO as a precursor. These M-S-H matrices, however, exhibit extended setting times (between 5 and 30 days at 40°C), and develop relatively low compressive strength (≤ 7 MPa) despite forming considerable quantities of the M-S-H binding phase.

There exists the possibility of enhancing the early age properties of the M-S-H systems based on Mg(OH)₂ and silica fume *via* the addition of reactive alumina, which would be expected to produce an aluminosilicate support matrix at early ages, reducing the hardening time and producing solid monoliths. Geopolymer and mixed zeolite monoliths have been successfully produced using sources of reactive silica (silica fume and geothermal silica) combined with sodium aluminate [601-602]. These have been developed as “just add water” one-part mixes, which harden at 40°C without the need for higher temperature ($\geq 85^\circ\text{C}$) curing typical of production of geopolymers and zeolites from fly ash sources [603-604].

In these systems an amorphous aluminosilicate ('geopolymer') type gel is formed, along with a range of crystalline zeolites whose compositions and structures are strongly dependent on the formulation and chemistry of the starting material. These materials have been tested, and used in practice, for the immobilisation of a wide variety of radioactive wastes [102-103, 105], as highlighted in Chapter 2.5.3. In particular, it has been demonstrated that alkali-activated aluminosilicate binders have the capacity to chemically bind cations such as Cs^+ within the proto-zeolitic structure of the geopolymer gel, and in the crystalline zeolites forming in these materials [103-104, 605-606]. This is of significant importance as the immobilisation of Cs^+ in Portland cement composites is limited [607].

Considering the requirement to immobilise $\text{Mg}(\text{OH})_2$ and fission products present in Magnox sludge, this chapter presented the development and characterisation of binders within the system $\text{Mg}(\text{OH})_2\text{-NaAlO}_2\text{-SiO}_2\text{-H}_2\text{O}$, with a particular focus on evaluation of the effect of SiO_2 content. This was achieved through the addition of varying quantities of NaAlO_2 and additional SiO_2 to the $\text{Mg}(\text{OH})_2\text{-SiO}_2\text{-H}_2\text{O}$ system analysed in the previous chapter. This chapter specifically focused on a few key formulations, and their phase development up to 90 days of curing using XRD, FTIR and SEM techniques to determine the influence of formulation parameters on the system.

6.2 Methodology

The specimens presented in this chapter were formulated with varying $\text{SiO}_2/\text{Al}_2\text{O}_3$ molar ratios, at constant $\text{Mg}(\text{OH})_2$ and NaAlO_2 content, as noted in Table 6.1. Dry powders were mixed together until homogeneous, and were then mixed with distilled water at a water / solids mass ratio of 0.60.

Table 6.1 Sample formulations of $\text{Mg}(\text{OH})_2$ - NaAlO_2 - SiO_2 - H_2O binders, molar basis.

Sample ID	$\text{Mg}(\text{OH})_2$	SiO_2	NaAlO_2	$\text{SiO}_2/\text{Al}_2\text{O}_3$ ratio	$\text{Mg}(\text{OH})_2$ content, wt.%
A	3	2.5	1.5	3.3	24
B	3	1.5	1.5	2.0	28
C	3	1	1.5	1.3	33

Samples were cast into 15 mL centrifuge tubes, sealed and cured at 40°C and 95% relative humidity in an environmental chamber until testing at 7, 28 and 90 days. Samples were ground in an agate mortar and sieved to -52 μm prior to analysis with XRD and FTIR instruments.

6.3 Results and Discussion

6.3.1 X-ray diffraction

Figures 6.1-6.3 showed that all the samples form crystalline products within the hardened binder phases, and that in all samples reflections assigned to brucite ($\text{Mg}(\text{OH})_2$, PDF# 7-239) were identified, with no significant variations with the content of silica fume. After 7 days, formation of the zeolite Na-A (LTA; $\text{Na}_{12}\text{Si}_{12}\text{Al}_{12}\text{O}_{48}\cdot 27\text{H}_2\text{O}$, powder diffraction file (PDF) # 00-039-0219) was identified in specimens with the higher SiO_2 content (Figure 6.1A). Intermediate SiO_2 content (Figure 6.1B) promoted the simultaneous formation of a faujasite type zeolite (zeolite Na-X, $\text{Na}_{86}\text{Si}_{103}\text{Al}_{86}\text{O}_{378}\cdot 288\text{H}_2\text{O}$, PDF# 012-0246) along with zeolite LTA, while the lowest SiO_2 content (Figure 6.1C) favoured the formation of a faujasite phase, as well as hydroxysodalite ($\text{Na}_8\text{Si}_6\text{Al}_6\text{O}_{24}(\text{OH})_2\cdot 2\text{H}_2\text{O}$, PDF# 04-009-2429) and minor traces of LTA.

Sample A, containing the highest proportion of silica fume ($\text{SiO}_2/\text{Al}_2\text{O}_3 = 3.3$), also exhibited a diffuse region centred at $\sim 20^\circ 2\theta$, suggesting that excess silica fume remained in the system. This was also potentially present in sample B, but was not visible in sample C, with the lowest proportion of silica fume ($\text{SiO}_2/\text{Al}_2\text{O}_3: 1.3$), which suggested that the silica fume was fully consumed in this formulation.

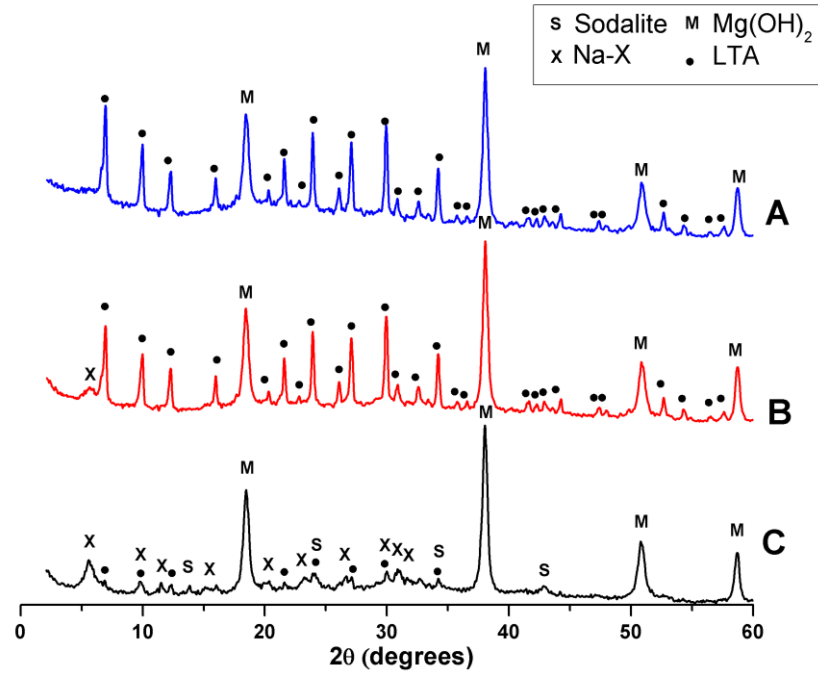


Figure 6.1 X-ray diffractograms of 7-day cured $\text{Mg}(\text{OH})_2\text{-NaAlO}_2\text{-SiO}_2\text{-H}_2\text{O}$ binders with $\text{SiO}_2/\text{Al}_2\text{O}_3$ ratios of (A) 3.3, (B) 2.0 and (C) 1.3.

Similar results to those described for samples cured for 7 days were identified in the specimens cured for 28 days (Figure 6.2) except for sample C, with the lower content of silica fume, where the LTA zeolite was no longer present, and the hydroxysodalite reflections were slightly more intense than observed at 7 days. In all samples, the $\text{Mg}(\text{OH})_2$ reflections remained a dominant feature.

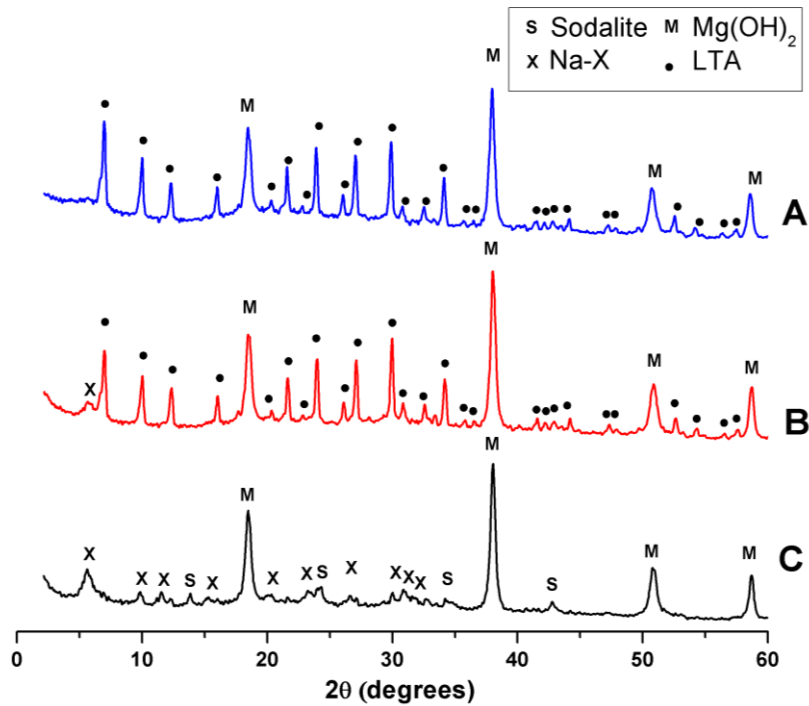


Figure 6.2 X-ray diffractograms of 28-day cured $\text{Mg}(\text{OH})_2\text{-NaAlO}_2\text{-SiO}_2\text{-H}_2\text{O}$ binders with $\text{SiO}_2/\text{Al}_2\text{O}_3$ ratios of (A) 3.3, (B) 2.0 and (C) 1.3

After 90 days of curing, in pastes with the highest silica fume content (Figure 6.3A), only LTA and $\text{Mg}(\text{OH})_2$ were again observed as crystalline reaction products. In the samples with medium and lowest silica fume content (Figure 6.3, B and C respectively), similar crystalline products to those observed at early times of curing (Figures 6.1 and 6.2) were still identified, along with the formation of a small amount of zeolite Na-P1 ($\text{Na}_6\text{Al}_6\text{Si}_{10}\text{O}_{32}\cdot 12\text{H}_2\text{O}$, PDF# 04-009-5257) in sample B.

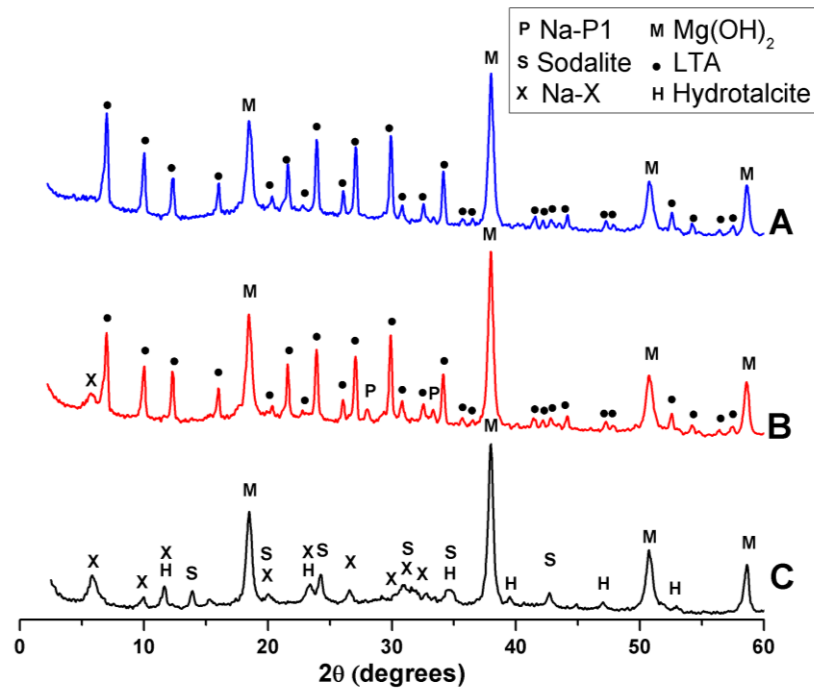


Figure 6.3 X-ray diffractograms of 90-days cured $\text{Mg}(\text{OH})_2\text{-NaAlO}_2\text{-SiO}_2\text{-H}_2\text{O}$ binders with $\text{SiO}_2/\text{Al}_2\text{O}_3$ ratios of (A) 3.3, (B) 2.0 and (C) 1.3

The sample with the lowest silica fume content (Figure 6.3C) underwent the most significant change over the curing period studied here. This binder still showed the presence of zeolite Na-X, however the hydroxysodalite reflections appeared to be more intense than at earlier ages, and a hydrotalcite type phase ($\text{Mg}_4\text{Al}_2(\text{CO}_3)(\text{OH})_{12}\cdot 3\text{H}_2\text{O}$, PDF# 089-0460) was also observed. The most prominent reflections overlap with those of Na-X and sodalite, but the peaks at 39.4° and 46.9° 2θ , also corresponding to this phase, are distinct. As $\text{Mg}(\text{OH})_2$ was the only source of Mg in the system, the formation of hydrotalcite indicated that dissolution of $\text{Mg}(\text{OH})_2$ was taking place. The reflections associated with the formation of an M-S-H type phase (20° , 36° and 61° 2θ) [608], which was the main reaction product of these systems in the absence of NaAlO_2 , as noted in Chapter 5, were not identified in these samples at any curing ages.

It was also noted that the types of zeolites formed in these binders were to some extent converse to what might be expected considering the availability of dissolved

SiO₂ in each system. Sample A contained the highest amount of silica fume, but solely formed LTA (SiO₂/Al₂O₃ = 2.0) during curing, which is the zeolite with the lowest SiO₂/Al₂O₃ ratio identified among the binders assessed. In sample B, the formation of LTA, Na-P1 (SiO₂/Al₂O₃ = 3.30) and Na-X (SiO₂/Al₂O₃ ≥ 2.44) was observed, and sample C predominantly formed Na-X with small quantities of LTA and hydroxysodalite (SiO₂/Al₂O₃ = 2.0). The structure of the zeolites observed here are shown as wireframe structures in Figure 6.4, for reference.

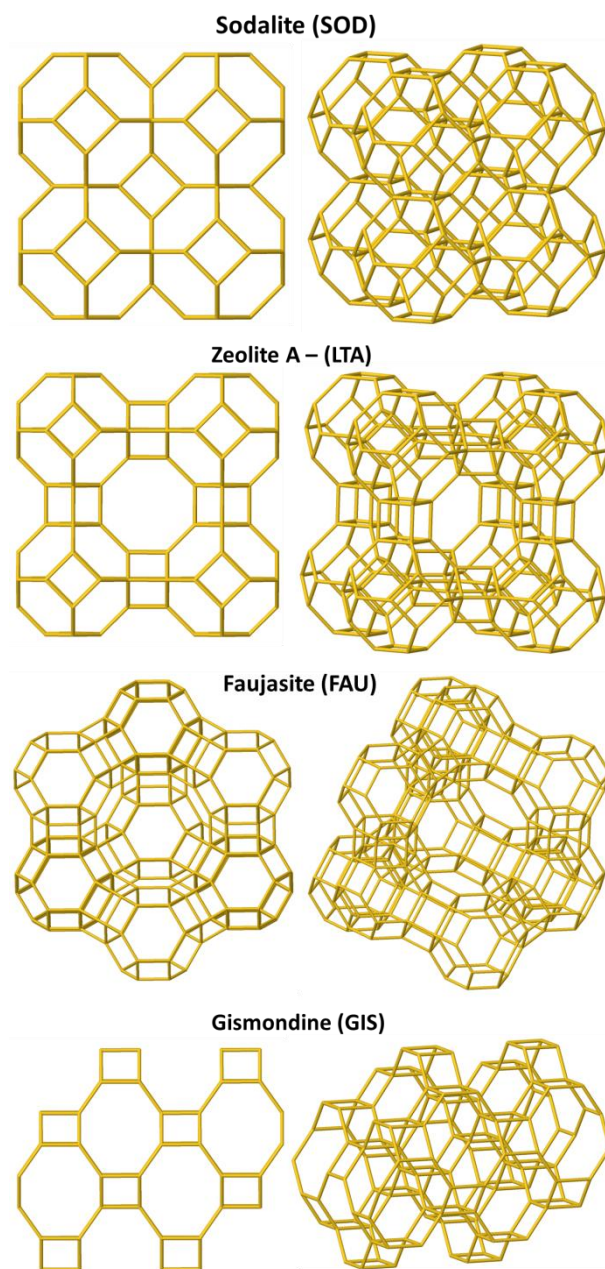


Figure 6.4 Structures of zeolite structures found within these cements (*Na-P1 has a gismondine structure*)

The formation of low silica zeolites, even in SF-rich systems, might be explained by the differences in availability of dissolved Al and the alkalinity of the systems. Iler et al. [609] identified that aluminium incorporated into the silica surface significantly reduces its dissolution, and Chappex et al. [610] noted that the Al/Si ratios reached in the altered surfaces of silica particles were strongly dependent on the solution composition and alkalinity. Considering that all of the binders produced in this study had the same Al and Na contents, any NaAlO_2 that is not reacting with SiO_2 will increase the alkalinity of the system and promote the formation of specific zeolites.

LTA zeolite is usually observed in systems with high Al content [611] and seems to be stabilised at moderately alkaline pH, which suggests that at high SiO_2 content most of the NaAlO_2 has reacted, consuming the available Al and reducing the alkalinity of the binder. Residual unreacted silica fume was clearly visible at early ages in the highest SiO_2 content system (Figure 6.5A). Highly alkaline systems tend towards zeolites with $\text{SiO}_2/\text{Al}_2\text{O}_3$ ratios of 2 such as Na-X and LTA [612], driving the formation of these in the moderate and lower silica systems. Excess alkalinity favoured the transformation of LTA to hydroxysodalite, with a slight excess favouring transformation to zeolite P [613]. This is consistent with the identification of hydroxysodalite in the sample with reduced silica fume content, and Na-P1 in the sample with moderate silica content at advanced ages (Figure 6.3C and 6.3B respectively), where an excess of alkalis might be present as less SiO_2 is available to react with the NaAlO_2 . The proportion of reactive Al in the lowest silica system may be reduced by the formation of an amorphous $\text{Al}(\text{OH})_3$ phase, which at later curing ages contributes to the formation of hydrotalcite. This is, however, speculative as there were several mechanistic phenomena occurring in these binders that modify the availability of different species over the time of reaction, and control the formation of zeolites with different compositions. Further characterisation of these binders is required to gain a better understanding of these aspects of chemistry and structural evolution.

The main constituent of Magnox sludges is $\text{Mg}(\text{OH})_2$, along with significant quantities of radionuclides such as ^{90}Sr , ^{137}Cs and ^{241}Am [108]. The formation of zeolites in the binding system produced here is likely to be of significant benefit for the immobilisation of these radionuclides, particularly ^{137}Cs , which is known to become incorporated irreversibly into sodalite-type and Na-P1 structures [614-615].

The hydrotalcite formed within this system is also of interest in waste immobilisation and cementation due to its exchangeable anion component [616-617]. The safe immobilisation of anions is especially relevant as ^{36}Cl ($t_{1/2}$: 3.02×10^5 y) and ^{129}I ($t_{1/2}$: 1.57×10^7 y) are long-lived radionuclides present in significant quantities in Magnox sludges [618].

6.3.2 Fourier transform infrared spectroscopy

The FTIR spectra of each of the binders after 7, 28 and 90 days curing are displayed in Figures 6.5, 6.6 and 6.7 respectively. In samples cured for 7 days (Figure 6.5), a sharp peak identified at 3698 cm^{-1} was associated with the OH stretching band of the hydroxyl groups in $\text{Mg}(\text{OH})_2$ [570]. The broad band between $3200\text{-}3600\text{ cm}^{-1}$ and centred at approximately 3450 cm^{-1} was assigned to H-OH stretching, with the band centred approximately 1650 cm^{-1} assigned to the bending vibration of the O-H groups present in hydrated reaction products. Significant changes in these bands are not identified as a function of silica fume content or of the time of curing.

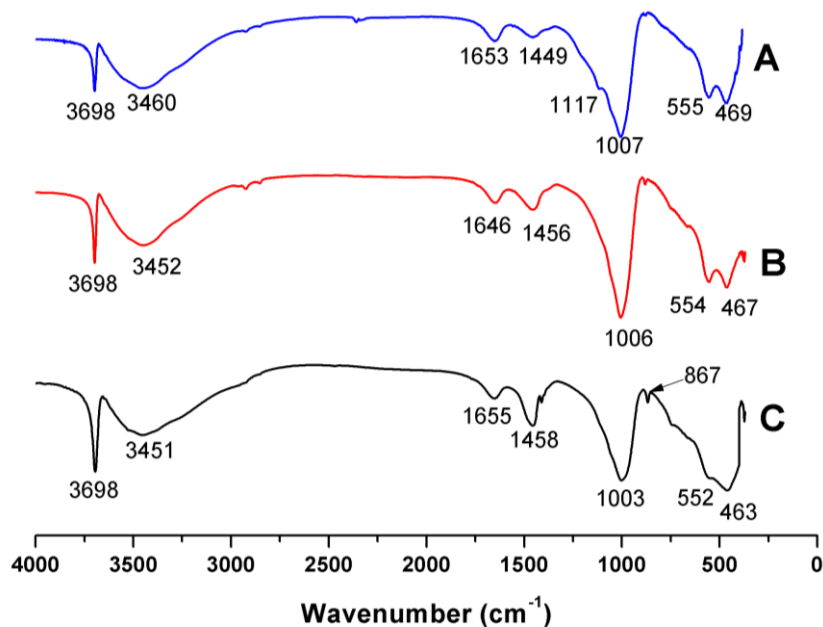


Figure 6.5 FTIR spectra of 7-day cured $\text{Mg}(\text{OH})_2\text{-NaAlO}_2\text{-SiO}_2\text{-H}_2\text{O}$ binders formulated with $\text{SiO}_2/\text{Al}_2\text{O}_3$ ratios of (A) 3.3, (B) 2.0 and (C) 1.3

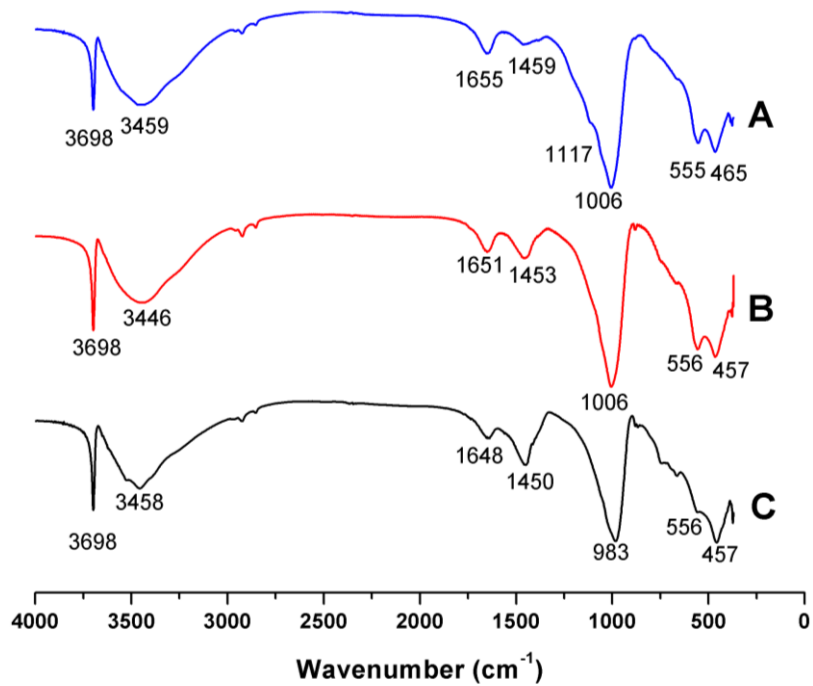


Figure 6.6 FTIR spectra of 28-day cured $\text{Mg}(\text{OH})_2\text{-NaAlO}_2\text{-SiO}_2\text{-H}_2\text{O}$ binders formulated with $\text{SiO}_2/\text{Al}_2\text{O}_3$ ratios of (A) 3.3, (B) 2.0 and (C) 1.3

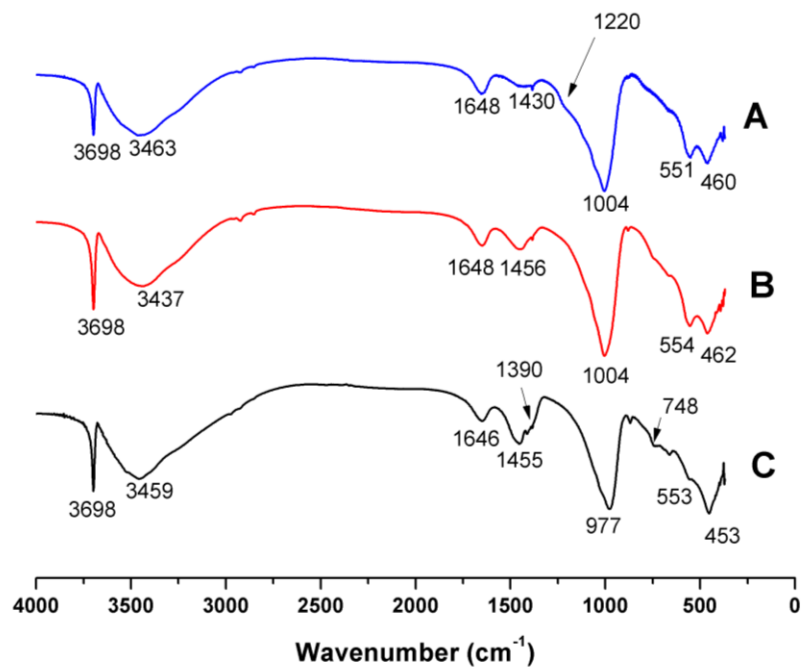


Figure 6.7 FTIR spectra of 90-day cured $\text{Mg}(\text{OH})_2\text{-NaAlO}_2\text{-SiO}_2\text{-H}_2\text{O}$ binders formulated with $\text{SiO}_2/\text{Al}_2\text{O}_3$ ratios of (A) 3.3, (B) 2.0 and (C) 1.3

The band between 1100-900 cm^{-1} is assigned to the Si-O-T asymmetric stretching mode (T: tetrahedral Al or Si) of the reaction products [619]. In binders with high and intermediate SiO_2 contents (samples A and B), this band is identified at 1007 cm^{-1} and 1006 cm^{-1} respectively, along with a shoulder at 1117 cm^{-1} assigned to unreacted silica fume. The identification of the vibration mode corresponding to silica fume in these samples is consistent with the XRD data for samples A and B at 7 (Figure 6.1) and 28 (Figure 6.2) days, and confirms that there is an excess of SiO_2 in these systems. However, this peak completely disappeared at 90 days (Figure 6.7A). The Si-O-T bands at $1007 \pm 1 \text{ cm}^{-1}$ are typical of the zeolite LTA [620], consistent with the XRD data, with bands at ~ 555 and $\sim 460 \text{ cm}^{-1}$ assigned to symmetric stretching of Si-O-T bonds in LTA [621]. Sample A, with the highest proportion of silica, displays an additional peak at 1220 cm^{-1} after 90 days curing. This is potentially related to amorphous silica gel, as no extra associated diffraction features are noted in the XRD data for this sample.

A reduction in the SiO_2 content (sample C) promotes a shift of the Si-O-T band to lower wavenumber. After 7 days (Figure 6.5C), this vibration mode is observed at 1003 cm^{-1} , shifting to 983 cm^{-1} after 28 days, and to 977 cm^{-1} at 90 days (Figure 6.7C). This band is assigned to a combination of the Si-O-T vibration of LTA and asymmetric stretching of Na-X at $\sim 980 \text{ cm}^{-1}$ [622], as identified at early age by XRD, and of hydroxysodalite at 979 cm^{-1} [580], as identified by XRD after 28 and 90 days. An increase in intensity of the two bands at $\sim 755 \text{ cm}^{-1}$ and $\sim 670 \text{ cm}^{-1}$, assigned to Na-X, is also observed [622]. These are most intense in sample C after 90 days of curing, and are also visible in sample B, which also has some Na-X, as identified by XRD (Figure 6.3). The agreement between X-ray diffraction and FTIR results is therefore excellent.

In all systems a band between 1300-1500 cm^{-1} is identified, assigned to the asymmetric stretching mode of the O-C-O bonds of CO_3^{2-} groups. The intensity of this band is inversely proportional to the content of SiO_2 in the samples, with sample C exhibiting the strongest band with a double peak. Alkali or alkali-earth carbonate products were not detected by XRD, but considering the chemistry of the system, it is likely that a hydrotalcite type product is forming in these binders, consistent with the double carbonate peak which is particularly prominent in sample C (Figure 6.7). Hydrotalcite has been identified as a minor phase in XRD analysis of this sample, at

low SiO_2 content, which suggests that an excess of dissolved Al in the system might promote the conversion of $\text{Mg}(\text{OH})_2$ to hydrotalcite-type phases.

6.3.3 Scanning electron microscopy

Backscattered electron micrographs were obtained for fractured surfaces of samples A (Figure 6.8) and C (Figure 6.9). These micrographs clearly show differences in the binders formulated with different SiO_2 contents. In both systems a highly heterogeneous microstructure with little cohesion between agglomerates is observed. In sample A (Figure 6.8) highly crystalline rosette-like agglomerates including hexagonal shaped particles are observed, while the crystallite size seems notably smaller in the binder with the lowest content of SiO_2 (Figure 6.9). The microstructure of sample C is comparable to that observed in aluminosilicate geopolymer gels produced *via* the chemical reaction between NaAlO_2 and geothermal silica [623], suggesting that the formation of a secondary geopolymer gel is possibly taking place in sample C at early curing times.

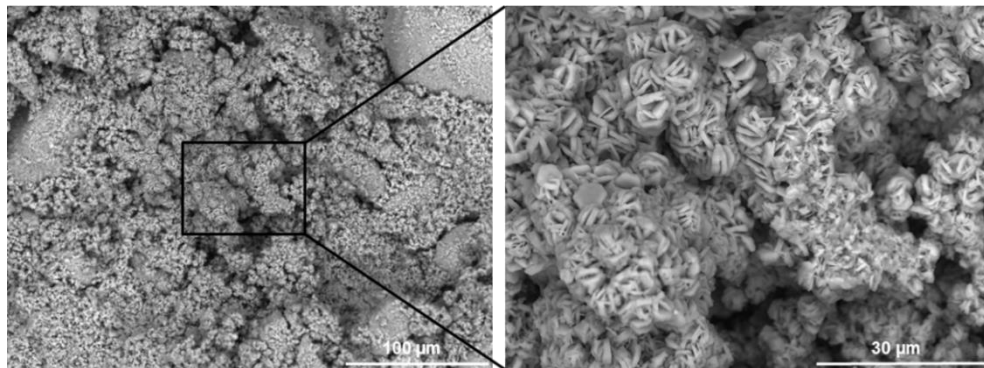


Figure 6.8 Backscattered electron micrographs of sample A after 7 days of curing

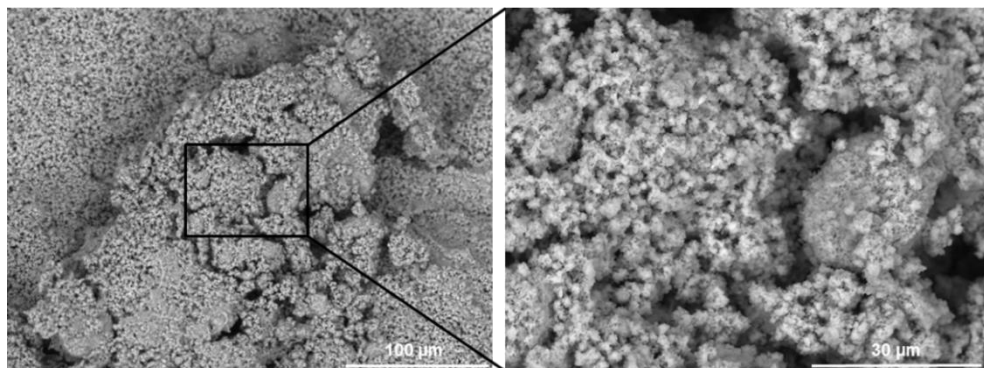


Figure 6.9 Backscattered electron micrographs of sample C after 7 days of curing

6.4 Conclusions

6.4.1 Scientific findings

This chapter focussed on the addition of NaAlO_2 into a $\text{Mg}(\text{OH})_2$ - SiO_2 - H_2O system. These formed solid cementitious products with a variety of zeolites. The chemistry evolves over time, with low silica zeolites forming from early ages as the sodium aluminate precursor reacts with silica fume. The type of zeolite formed is strongly dependent on the SiO_2 content in the binder. The reactivity of $\text{Mg}(\text{OH})_2$ is low although some reaction is occurring as evidenced by the formation of hydrotalcite at later age in the lowest- SiO_2 system studied.

There was no evidence for the formation of an M-S-H or an aluminium substituted M-A-S-H type phase, although this cannot be ruled out at later curing ages due to the partial reaction of $\text{Mg}(\text{OH})_2$ in the lower SiO_2 containing sample. This cementitious binder requires further testing and longer term analysis, combined with more detailed characterisation of the systems to determine whether any reactions are taking place between $\text{Mg}(\text{OH})_2$ and an amorphous component of this binder.

The work undertaken here could be furthered by probing into the mechanisms of the zeolite formations and whether these are likely to be stable over the long term. This is likely to be highly influenced by the solution chemistry, which is as yet unknown. This could feed into geochemical modelling of the stability and ultimate stable mineral assemblages likely to occur within these binders. These questions are of great importance considering the long lived nature of many of the radionuclides within the Magnox sludges.

6.4.2 Industrial application

This chapter has demonstrated the feasibility of producing an alkali-aluminosilicate binder for $\text{Mg}(\text{OH})_2$ rich sludges, which is relevant to the UK nuclear industry. The formation of a variety of zeolites within a stable monolith may be beneficial for waste immobilisation and radionuclide retention. Due to low $\text{Mg}(\text{OH})_2$ reactivity, at this stage of development this system is applicable for the encapsulation of, but not the utilisation of, $\text{Mg}(\text{OH})_2$ as a raw material for the binding phase, although the long term conversion and stability of these systems requires further study.

7 Phase evolution in the $\text{Mg}(\text{OH})_2\text{-NaAlO}_2\text{-SiO}_2\text{-H}_2\text{O}$ system

7.1 Introduction

In the previous chapter cementitious binders within the $\text{Mg}(\text{OH})_2\text{-NaAlO}_2\text{-SiO}_2\text{-H}_2\text{O}$ system were studied up to 90 days of age, and the formation of a range of zeolites was identified, depending on the Si/Al ratio of the binders. Although the inclusion of NaAlO_2 significantly reduced the setting time of these binders, there was no evidence for M-S-H (or M-A-S-H) gel formation. Instead, a layered double hydroxide with a hydrotalcite-like structure was observed in one of the formulations assessed, with little other $\text{Mg}(\text{OH})_2$ reaction.

This chapter further evaluates phase evolution in $\text{Mg}(\text{OH})_2\text{-SiO}_2\text{-NaAlO}_2\text{-H}_2\text{O}$ samples, with an expanded range of formulations and cured for up to 2 years. The reaction of $\text{Mg}(\text{OH})_2$ to form a hydrotalcite-like material within 90 days necessitated a much more detailed analysis of both the initial setting characteristics, and of potential $\text{Mg}(\text{OH})_2\text{-SiO}_2$ or $\text{Mg}(\text{OH})_2\text{-NaAlO}_2$ interactions over an extended timeframe. Particular attention is paid to the elucidation of poorly crystalline phases that are not immediately identifiable using XRD or FTIR techniques employed in the previous chapter.

To establish the nature of this system, an extended range of fresh pastes were assessed through isothermal calorimetry and X-ray diffraction up to 120 hours of curing. The same range of formulations were also aged up to 2 years of curing, and characterised *via* X-ray diffraction, thermogravimetry coupled with mass spectrometry, and solid state ^{27}Al , ^{29}Si and ^{25}Mg magic angle spinning nuclear magnetic resonance (MAS NMR) spectroscopy. The latter was especially useful for determining the presence of amorphous aluminosilicate material and interactions with $\text{Mg}(\text{OH})_2$.

7.2 Methodology

Samples were formulated with a fixed quantity of $\text{Mg}(\text{OH})_2$, but varying quantities of SiO_2 and NaAlO_2 to progressively increase the $\text{SiO}_2/\text{Al}_2\text{O}_3$ molar ratio. Due to the larger number of formulations than the previous chapter, samples have been labelled by their $\text{SiO}_2/\text{Al}_2\text{O}_3$ molar ratios (Rx, where x is between 1.3 and 4.0). The water / solids mass ratio was kept constant at 0.60. The binder compositions are shown in Table 7.1.

Table 7.1 Formulations of samples within the systems $\text{Mg}(\text{OH})_2\text{-NaAlO}_2\text{-SiO}_2\text{-H}_2\text{O}$.
Values reported on a molar basis

Sample ID*	$\text{Mg}(\text{OH})_2$	SiO_2	NaAlO_2	$\text{SiO}_2/\text{Al}_2\text{O}_3$ molar ratio
R1.3	3	1	1.5	1.3
R2.0	3	1.5	1.5	2
R3.0	3	1.5	1.0	3
R3.3	3	2.5	1.5	3.3
R4.0	3	1.5	0.75	4

* Note: Samples tested in previous chapter are A – R3.3, B – R2.0, C – R1.2

Dry powders were mixed together by hand to produce a homogeneous blend, to which the required quantity of distilled water was added, and further mixed for 5 minutes to produce a workable paste. Samples were cast into 15 mL centrifuge tubes and cured at 40 °C and 95% RH in a Sanyo Atmos Chamber MTH-2400, until analysis. Hardened paste samples were removed from the curing chamber at specified ages, and dried in a vacuum desiccator (13.3 kPa) over silica gel and solid NaOH for 6 hours to ensure the cessation of reaction and the removal adsorbed water. Samples were then ground in an agate mortar and sieved to $-63\ \mu\text{m}$ for analysis.

7.3 Results and discussion

7.3.1 Early-age reaction processes

Calorimetric measurement was undertaken on four samples (R1.3, 2.0, 3.0 and 3.3) to determine the kinetics of reaction of binders within the $\text{Mg}(\text{OH})_2\text{-NaAlO}_2\text{-SiO}_2\text{-H}_2\text{O}$ system, and the processes which lead to solidification. All samples were strongly exothermic upon initial mixing, and formed viscous pastes. In the heat release curves (Figure 7.1) it is identified that each sample exhibits four distinct regions of interest, <1 h, 1-20 h, 20-70 h and 70-140 h. The region <1 h, corresponding to the induction period, shows the heat release associated with a combination of instrumentation effects due to loading of samples, and the initial dissolution of NaAlO_2 which produced pastes which were notably hot to touch within minutes of mixing.

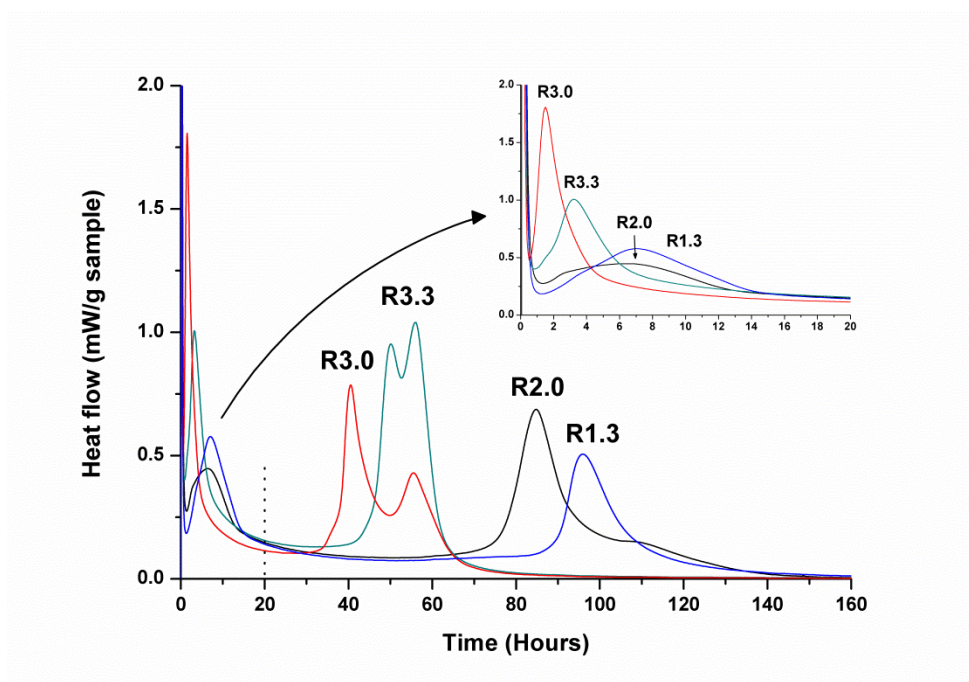


Figure 7.1 Normalised heat flow of pastes within the system $\text{Mg}(\text{OH})_2\text{-NaAlO}_2\text{-SiO}_2\text{-H}_2\text{O}$

Each of the samples exhibited a low intensity exothermic peak in the region 1-20 hours (with R3.0 & R3.3 exhibiting earlier sharper heat output than R2.0 & R1.3), which is assigned to an initial precipitation of reaction products. This is followed by a dormant or induction period of low heat output, lasting 20-60 hours. After the dormant period, a high intensity peak corresponding to the acceleration-deceleration stage of the reaction was observed. During this stage the nucleation and growth of a large amount of reaction products is occurring in all of the samples assessed. The onset of the acceleration period changes significantly as a function of the Si/Al ratio of these binders. The acceleration-deceleration period for samples with a higher silica content (R3.3 and R3.0) is observed between 30-60 hours. The formation of two overlapping but distinctive heat release peaks elucidates that different types of reaction products are precipitating at different times during the reaction process. Conversely, in samples containing less silica (R2.0 and R1.3), a single asymmetric peak corresponding to the acceleration-deceleration period of reaction is observed after 75 to 150 hours of reaction, earlier in R2.0 than in R1.3, which has the lowest silica fume content among the samples tested.

Cumulative heat release curves normalised by the total mass of paste (Figure 7.2) and by the content of silica fume plus sodium aluminate (Figure 7.3) show that the binders with higher contents of silica (R3.0 and R3.3) react faster. However, the heat of reaction is highest in the mix R2.0, with a moderately low (but not the lowest) silica fume content. Differences in the heat of reaction are identified when $\text{Mg}(\text{OH})_2$ is not taken into account as part of the binder (Figure 7.3), compared with the curves of reaction normalised by the total pastes mixed (Figure 7.2), indicating that some $\text{Mg}(\text{OH})_2$ might be participating in the reaction, particularly in the binder R3.3. Viewed in terms of zeolite formation producing heat, R2.0 is close to a 1:1 Si/Al ratio, which are equal to that of the zeolite NaA (LTA structure); this was identified in detail in the XRD analysis below, as being the principal crystalline phase formed in these binders. Therefore, most of the SiO_2 and NaAlO_2 in this sample has the propensity for reaction, whereas in R1.3 there is an excess of Al, and R3.0 and R3.3 have an excess of SiO_2 , which does not fully react.

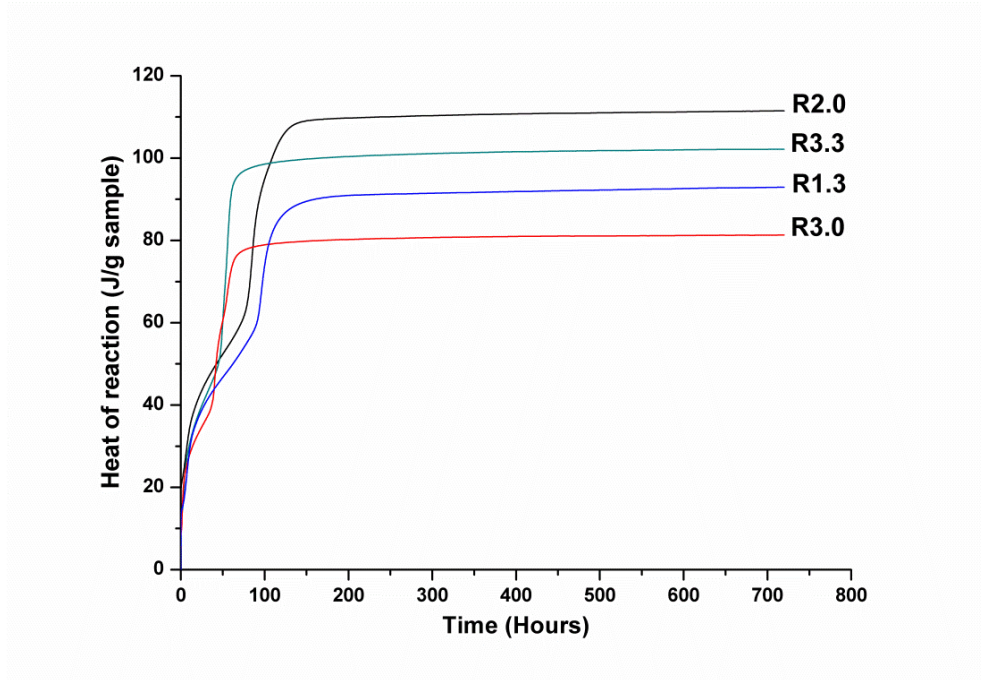


Figure 7.2 Cumulative heat of reaction of pastes within the system $\text{Mg}(\text{OH})_2$ - NaAlO_2 - SiO_2 - H_2O normalised to mass of paste

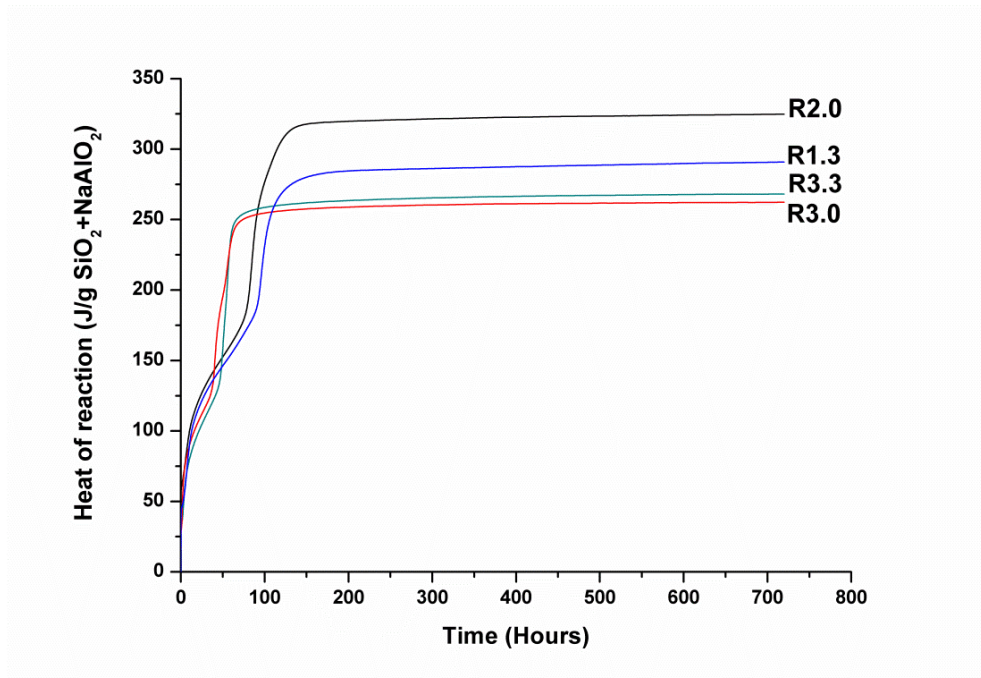


Figure 7.3 Cumulative heat of reaction of pastes within the systems $\text{Mg}(\text{OH})_2$ - NaAlO_2 - SiO_2 - H_2O , normalised to the total mass of SiO_2 + NaAlO_2 in the pastes

In order to identify the phases forming at the early stages of the reaction of these binders, X-ray diffraction (XRD) analysis of pastes cured under identical conditions to those used during the calorimetry test was carried out, at times where the higher heat release was identified (24, 65 and 120 hours). After 24 h of reaction (Figure 7.4A), the only crystalline phases identified in these binders were unreacted brucite ($\text{Mg}(\text{OH})_2$, powder diffraction file (PDF) # 01-074-2220) and traces of poorly crystalline bayerite ($\alpha\text{-Al}(\text{OH})_3$, PDF # 00-020-0011). No crystalline NaAlO_2 is observed, indicating that this compound has fully dissolved, saturating the solution with $\text{Al}(\text{OH})_4^-$ species and resulting in $\text{Al}(\text{OH})_3$ precipitation. This indicates that the first precipitation of reaction products identified by isothermal calorimetry may be associated at least to some extent with the formation of this phase.

No differences are identified between the diffraction patterns of R1.3 and R2.0 (Figure 7.4B) after 65 hours, consistent with the identification of a dormant period in these pastes at this time. Conversely, in samples R3.0 and R3.3 with higher silica content, the precipitation of zeolites of the structure type LTA (zeolite NaA: $\text{Na}_{12}\text{Si}_{12}\text{Al}_{12}\text{O}_{48}\cdot 27\text{H}_2\text{O}$, PDF# 00-039-0219) is observed, consistent with the exothermic event identified *via* isothermal calorimetry. Analysis after 120 hours of reaction (Figure 7.4C) shows the formation of the LTA zeolite in all of the samples assessed, consistent with the identification of the acceleration-deceleration period in all cases by this time. Regardless of chemical composition, after the initial reaction takes place in these binders, the main crystalline reaction products identified are $\text{Al}(\text{OH})_3$ and LTA, although in differing quantities; particularly the reflection peaks assigned to LTA are less intense as the content of silica fume is reduced in the binders.

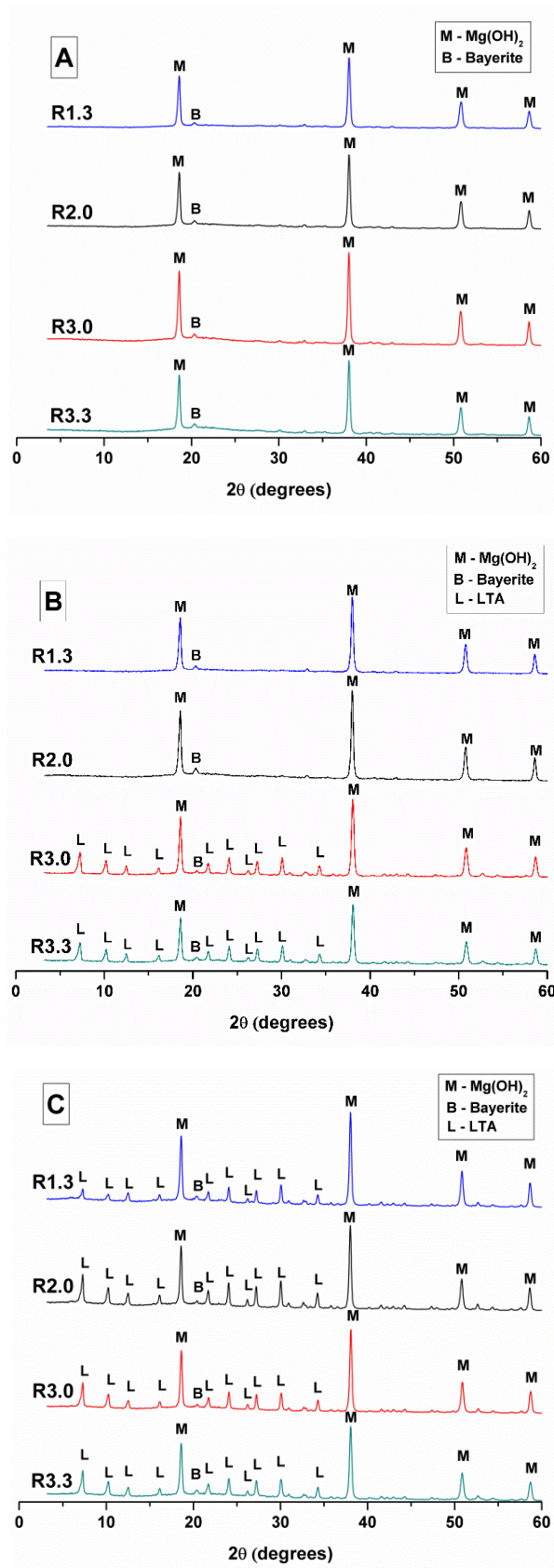


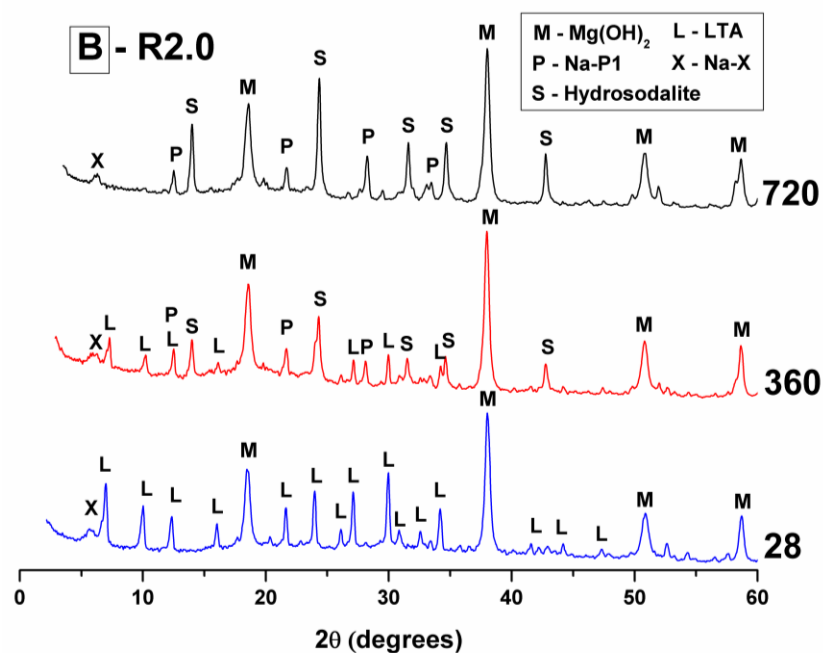
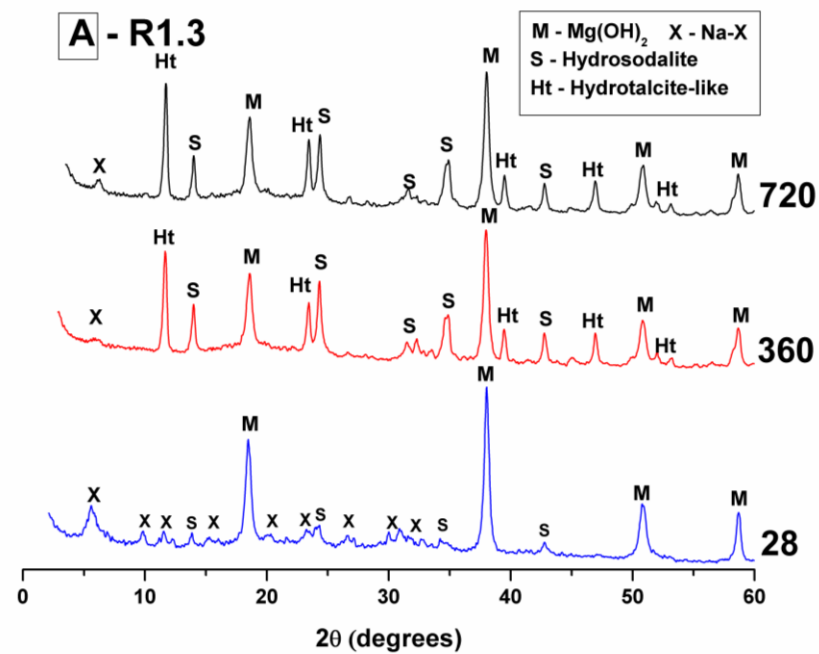
Figure 7.4 X-ray diffraction patterns of samples R1.3, 2.0, 3.0 and 3.3 after (A) 24, (B) 65 and (C) 120 hours of curing

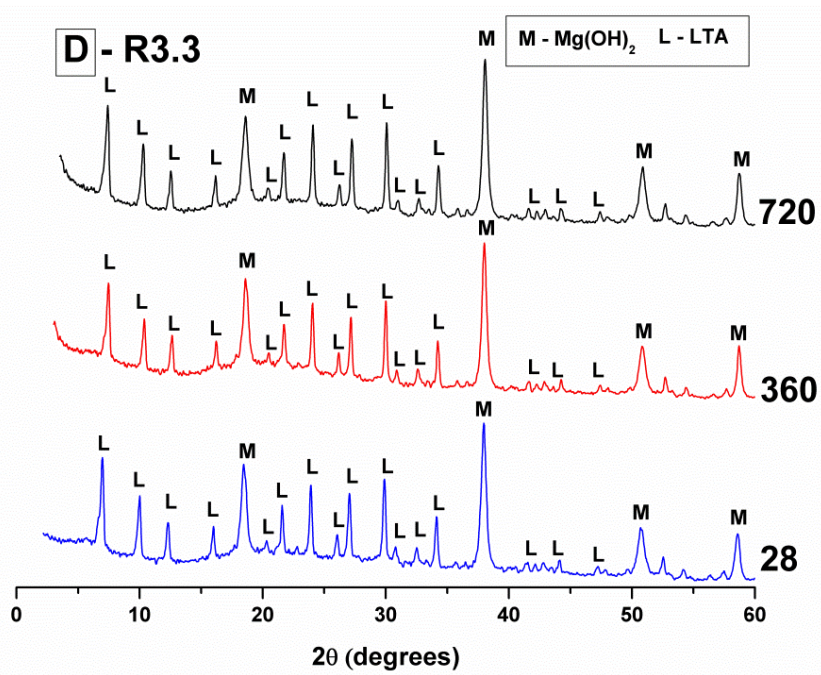
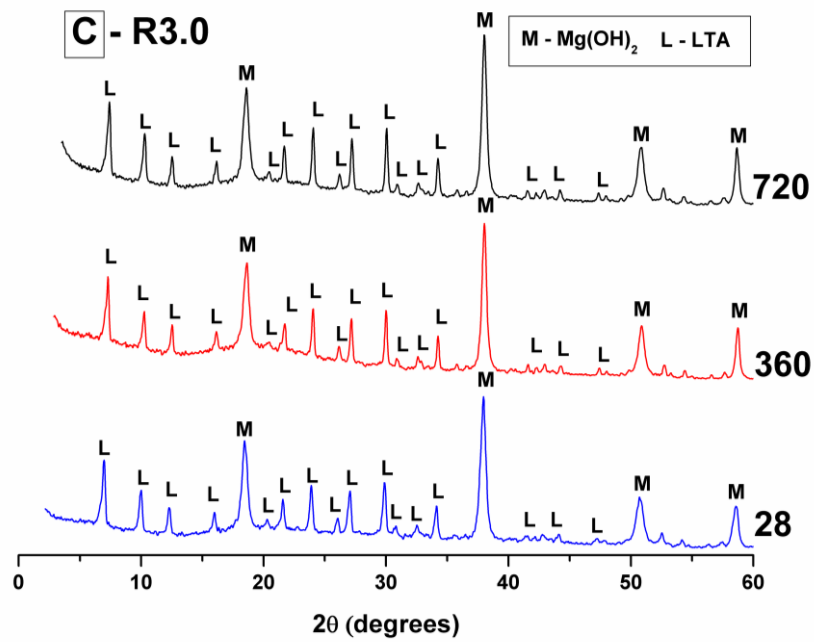
7.3.2 X-ray diffraction analysis of aged samples

The diffractograms of samples R1.3-R4.0 after 28, 360 and 720 days of curing are shown in Figure 7.5. Each of the samples displays an array of crystalline zeolites that varies depending on the bulk $\text{SiO}_2/\text{Al}_2\text{O}_3$ ratio. After 28 days of curing, the higher $\text{SiO}_2/\text{Al}_2\text{O}_3$ samples R3.0, R3.3 and R4.0 exhibit only LTA and $\text{Mg}(\text{OH})_2$ as crystalline features, along with an amorphous component presenting a broad feature around $20^\circ 2\theta$. The lower $\text{SiO}_2/\text{Al}_2\text{O}_3$ samples, R1.3 and R2.0, also contain Na-X (low silica faujasite: $\text{Na}_{86}\text{Si}_{106}\text{Al}_{86}\text{O}_{384}\cdot 175\text{H}_2\text{O}$, PDF# 00-012-0246). In sample R1.3, the LTA that was initially observed to form after 120 h (5 days –Figure 7.4C) was no longer observed, with only Na-X, $\text{Mg}(\text{OH})_2$ and traces of a basic hydro-sodalite (hydroxysodalite, $\text{Na}_8\text{Al}_6\text{Si}_6\text{O}_{24}(\text{OH})_2\cdot 2\text{H}_2\text{O}$, PDF# 04-009-2429) as observable crystalline phases. The metastable nature of LTA in samples R1.3 and R2.0 can be explained by their lower Si/Al ratio induced by a high NaAlO_2 content, which results in more alkaline conditions within the binder. LTA is also known to transform into sodalite type phases [613, 624-625] and/or Na-P (a gismondine structured zeolite, $\text{Na}_6\text{Al}_6\text{Si}_{10}\cdot 12\text{H}_2\text{O}$ [626]) [627] in caustic media, though the process is slower in these cements, possibly due to the limited ionic mobility under the relatively low water/solids ratios used here.

After long curing times the zeolite assemblages within these samples diverge. Samples R3.0, R3.3 and R4.0 (Figure 7.5) do not show any changes in crystalline composition up to 720 days of curing, displaying a considerable degree of stability. Samples R1.3 and R2.0, with lower Si/Al ratios, do however show significant changes. Sample R2.0 shows a change in zeolites, with hydrosodalite and Na-P1 appearing after 360 days of curing, coinciding with a decrease in the intensity of LTA peaks. After 720 days no LTA remained, with the system dominated by hydrosodalite with some Na-P1 ($\text{Na}_6\text{Al}_6\text{Si}_{10}\text{O}_{32}\cdot 12\text{H}_2\text{O}$, PDF # 04-009-5257) and Na-X.

Sample R1.3, with the lowest SiO₂/Al₂O₃ ratio, undergoes a transformation whereby Na-X decreases in intensity, and hydroxysodalite emerges as the dominant zeolite. In addition to this, a hydrotalcite-like magnesium-aluminium layered double hydroxide (LDH), potentially true hydrotalcite (Mg₆Al₂CO₃(OH)·4H₂O, PDF # (00-054-1029) or meixnerite (Mg₆Al₂(OH)₁₈·4H₂O, PDF # 00-038-478) forms by 360 days, increasing in intensity slightly at 720 days of curing. The identity of this phase will be further examined in Section 7.3.3.





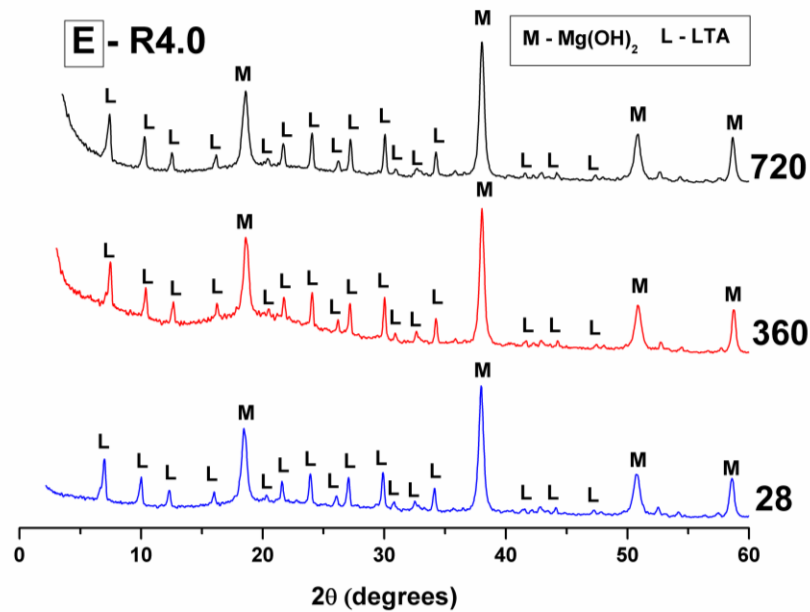


Figure 7.5 X-ray diffractograms of samples (A) R1.3, (B) R2.0, (C) R3.0, (D) R3.3 and (E) R4.0 as a function of the curing time in days. Some of the 28 day data are reproduced from Chapter 6.

Although sample R1.3 forms this additional magnesium-containing phase, all of the samples display strong reflections for $\text{Mg}(\text{OH})_2$, suggesting that little reaction between the aluminosilicate components and $\text{Mg}(\text{OH})_2$ has occurred up to 720 days of curing, except in R1.3. No evidence for the presence of an M-S-H phase can be detected (typically identified from broad features at 20, 35 and 60°, as characterised in Chapter 5), even in R3.3, which was formulated to provide a large quantity of SiO_2 for reaction.

7.3.3 Layered double hydroxide thermal identification

Although a layered double hydroxide (LDH) phase was identified during XRD analysis, this description can encompass a wide range of compositions defined by the formula $[\text{Mg}^{2+}_{1-x}\text{M}^{3+}_x(\text{OH})_2]^{x+}[\text{A}^{n-}_{x/n}] \cdot m\text{H}_2\text{O}$, in which M^{2+} and M^{3+} are di- and tri-valent metallic ions respectively, and A^{n-} can be one of many anions (e.g. CO_3^{2-} , OH^-).

or Cl⁻) [628]. The crystal structure of a typical hydrotalcite intercalated with CO₃²⁻ and H₂O is shown in Figure 7.6 below.

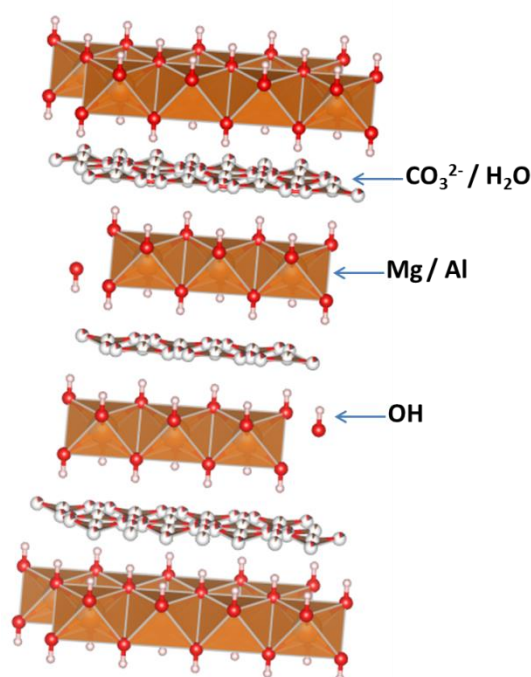


Figure 7.6 Structure of a Mg/Al layered double hydroxide (hydrotalcite), drawn from [629]

For brevity this was labelled a ‘hydrotalcite-like’ phase in Figure 7.5, however as the samples were cured in a sealed container, this is likely to preclude much CO₂ ingress leading to formation of true (carbonate-containing) hydrotalcite. To determine the nature of this LDH, thermogravimetric analysis was undertaken with an attached mass spectrometer to distinguish between H₂O and CO₂ evolution, as shown in Figure 7.7.

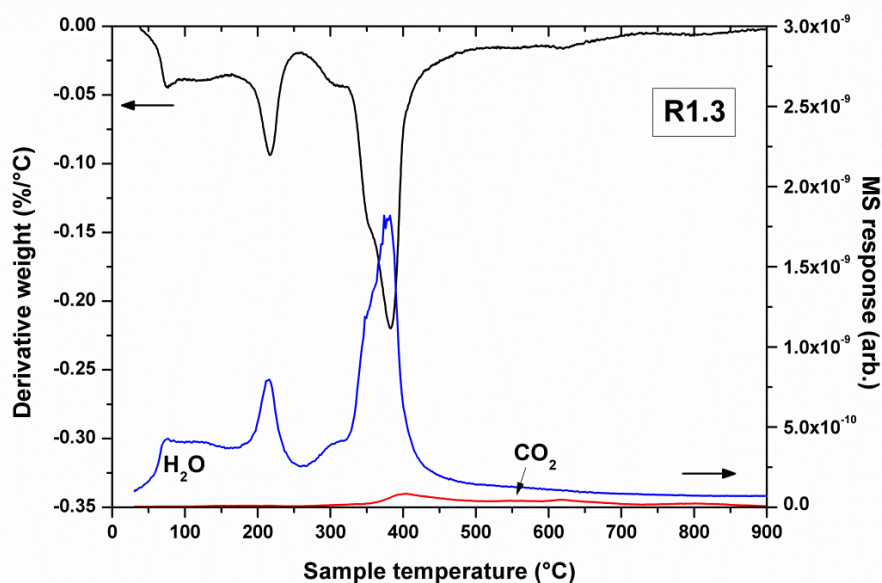


Figure 7.7 TG-MS of sample R1.3 after 720 days of curing, showing DTG (black), H₂O signal (blue) and CO₂ signal (red)

The results of the analysis are complicated, given the multitude of phases observed from XRD analysis within sample R1.3. The weight loss is dominated by the decomposition of Mg(OH)₂ at 383°C [630], and by an Mg-Al layered double hydroxide containing hydroxyl species in the interlayer (denoted OH-LDH) which accounts for much of the remaining weight change, with characteristic decomposition peaks at ~90°C, ~200°C, and as shoulders on the Mg(OH)₂ decomposition peak at ~300°C and 350°C [631]. Some weight loss from bound water will also be due to the release of zeolitic water from Na-X (~167°C) as well as dehydration of hydroxysodalite, which decomposes slowly over a wide range, from ~80-750 °C [632-633]. A small quantity of CO₂ is, however, evolved at ~400°C, pointing to formation of some CO₂-LDH [634-635] albeit as a minor constituent.

The TG-MS decomposition signals observed for the OH-LDH are similar to those of a 2:1 Mg-Al LDH prepared by Valente et al. [631], suggesting that this phase may have a composition similar to Mg₄Al₂(OH)₁₈·*m*H₂O, akin to a carbonate-free form of quintinite.

7.3.4 Solid-state NMR spectroscopy

Although various crystalline phases have formed within this system, the presence of diffuse scattering in many of the XRD patterns (such as $\sim 20^\circ$ in Figure 7.5D & E) suggests either that unreacted silica fume remains, or that non-crystalline reaction products are forming. To further elucidate this possibility, ^{29}Si and ^{27}Al MAS NMR spectroscopy was undertaken on all of the samples after 360 and 720 days of curing, the former of which is initially shown below in Figure 7.8.

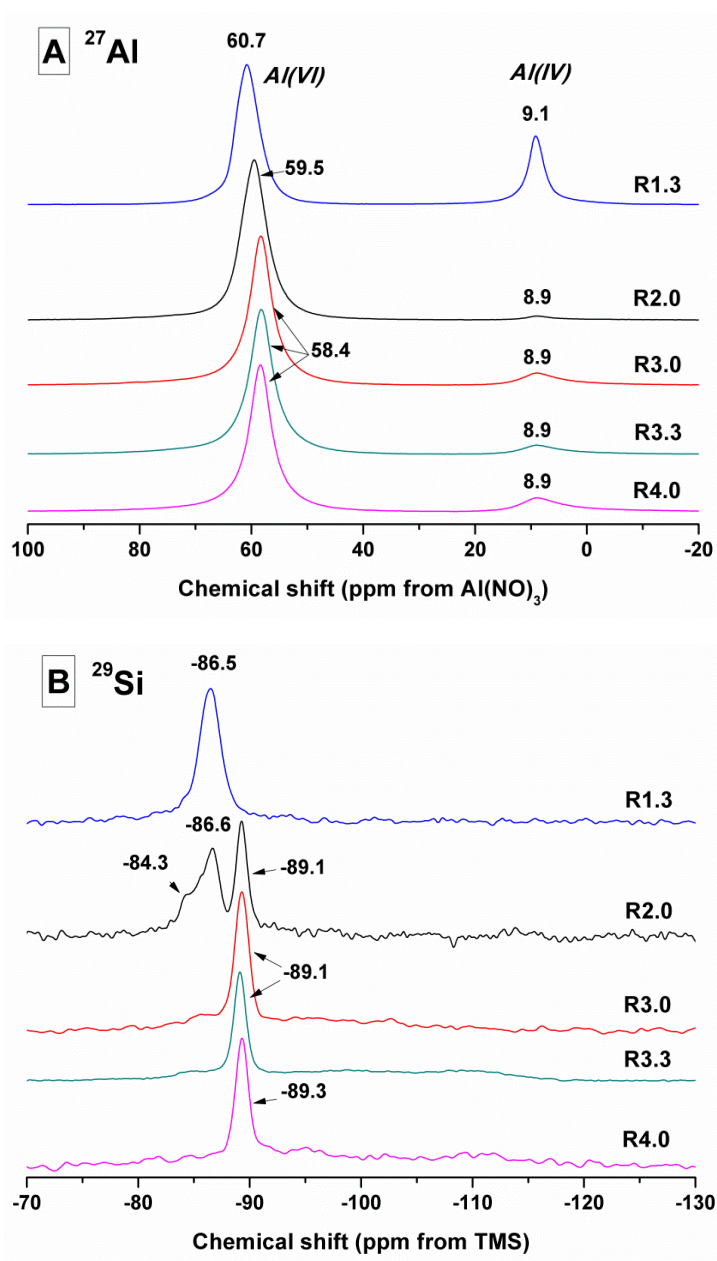


Figure 7.8 (A) ^{27}Al and (B) ^{29}Si MAS NMR spectra of pastes within the system $\text{Mg}(\text{OH})_2\text{-NaAlO}_2\text{-SiO}_2\text{-H}_2\text{O}$, after 360 days of curing

The ^{27}Al MAS NMR spectra of the samples reveal the presence of two Al environments, identified as Al(IV) and Al(VI), at 58-61 and ~ 9 ppm respectively. The peaks close to 60 ppm are characteristic of tetrahedrally coordinated Al in zeolites, consistent with the formation of aluminosilicate zeolites in these samples [636]. The peaks at ~ 9 ppm correspond to octahedrally coordinated Al, typical of non-framework Al species. Sample R1.3 exhibits a stronger signal here, consistent with the identification of a hydrotalcite-like LDH as discussed above [637]. In the remaining samples, although LDH phases have not been observed, the presence of Al(VI) might be evidence of residual $\alpha\text{-Al}(\text{OH})_3$ as postulated through XRD analysis earlier.

^{29}Si NMR further supports the identification of zeolites as observed by XRD. The single peak at -89.3 ppm in samples R2.0-R4.0 is assigned to $\text{Q}^4(4\text{Al})$ units in LTA [636, 638-639]. Sample R2.0 exhibits a more complicated spectrum, with a signal at -86.6 ppm from $\text{Q}^4(4\text{Al})$ units in the sodalite structure [639-640], a small signal at -84.3 ppm associated with $\text{Q}^4(4\text{Al})$ units in low silica Na-X [638], and an LTA signal at -89.3 ppm. R1.3 exhibits a single peak at -86.5 ppm, consistent with the identification of sodalite as the primary zeolite at this curing age.

Although not clearly visible in Figure 7.8, samples R3.0-R4.0 appeared to also present broad features from -85 to -115 ppm. Sample R3.3 was re-analysed with a larger number of scans (increasing from 47 to 892 scans) to reduce noise, with the spectrum subsequently deconvoluted to determine the constituent parts, as shown in Figure 7.9.

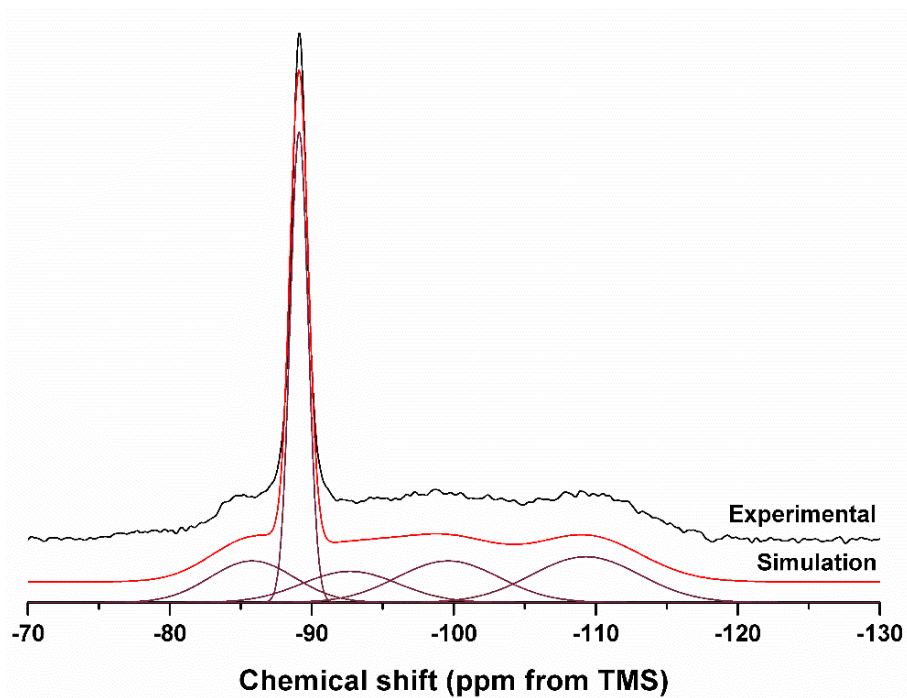


Figure 7.9 ^{29}Si MAS NMR of sample R3.3 at 360 days of curing, featuring both experimental and simulated spectra, and decomposition into component peaks

Alongside the prominent peak at -89.1 ppm assigned to LTA ($\text{Q}^4(4\text{Al})$) are four additional broad peaks centred -85.5, -92.7, -99.6 and -109.3 ppm. Beginning upfield, the peak at -109.3 ppm can be assigned to fully polymerised Q^4 species in unreacted silica fume. The next peak downfield at -99.6 ppm, is assigned to Q^3 species formed through surface hydroxylation of the silica fume due to partial dissolution, forming Q^3 ($>\text{Si-OH}$ single silanol) sites surrounding an unreacted Q^4 silica fume core [641]. The two remaining peaks at -92.7 and -85.5 ppm are assigned to $\text{Q}^3(1\text{Al})$ and $\text{Q}^2(1\text{Al})$ sites respectively. Both of these sites occur as the $\text{Al}(\text{OH})_4^-$ released by sodium aluminate dissociation forms surface $\text{Q}^3(1\text{Al})$, or further depolymerised $\text{Q}^2(1\text{Al})$ units.

There was no evidence provided by these spectra for the formation of an M-S-H gel, which would typically exhibit sharper peaks in the region -85 to -95 ppm, as characterised in Chapter 5 and from existing literature [393]. However, due to the presence of Al within the samples, along with a poorly crystalline component, the potential for an M-A-S-H gel to occur cannot be ruled out. This required the further

the study of this sample (R3.3) under high-field conditions using ^{25}Mg MAS NMR, to determine fully whether any M-S-H or M-A-S-H phases might be present. These data are shown in Figure 7.10. The experimental data were fitted using simulations based on established literature values for magnesium minerals [590] (Table 7.2), and found to consist predominantly of $\text{Mg}(\text{OH})_2$, with some MgO present as an impurity. M-S-H presents a diffuse spectrum centred ~ 0 ppm at this field strength, as demonstrated in Chapter 4. As the experimental data can be fitted well using a simulation of $\text{Mg}(\text{OH})_2$ and MgO alone, no M-S-H can be said to exist within this sample. Equally, as no other Mg sites are observable, the formation of a M-A-S-H phase can also be excluded.

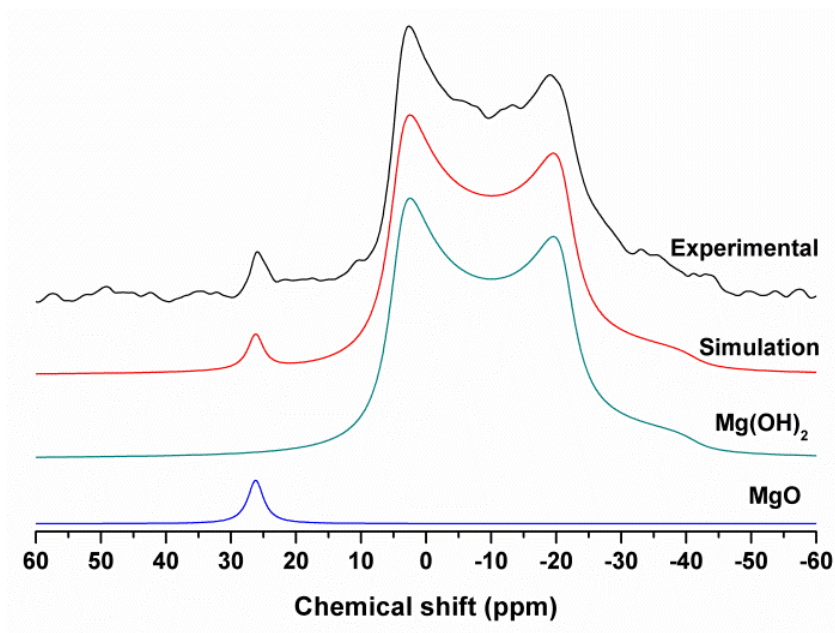


Figure 7.10 ^{25}Mg MAS NMR spectra of sample R3.3 at 360 days of curing, with experimental data, simulation and component parts

Table 7.2 ^{25}Mg MAS NMR simulation parameters for R3.3 at 360 days of curing

	δ_{iso} (ppm)	C_Q (MHz)	η_Q
MgO	26.2	0	0
Mg(OH)₂	11.7	3.1	0

All the samples were analysed again after curing for 720 days, to determine any further changes over time. The NMR spectra remain similar for samples R3.0-R4.0, with only minor shifts in peak positions for both ^{27}Al and ^{29}Si MAS NMR (Figure 7.11). These three all exhibit broad signals in their ^{29}Si spectra, and are deconvoluted below in Figure 7.12 using the same peak parameter values as were used in Figure 7.9. Samples R1.3 and R2.0, however, do show changes, consistent with their changing zeolite assemblages identified by XRD. In sample R1.3, a second peak appeared at -84 ppm, consistent with an increase in the observed Na-X content, while in sample R2.0 the peak at -86.5 ppm (identified as sodalite) increased in intensity, while that for LTA (-89.1 ppm) disappeared entirely; both of these trends are in full agreement with the XRD assignments.

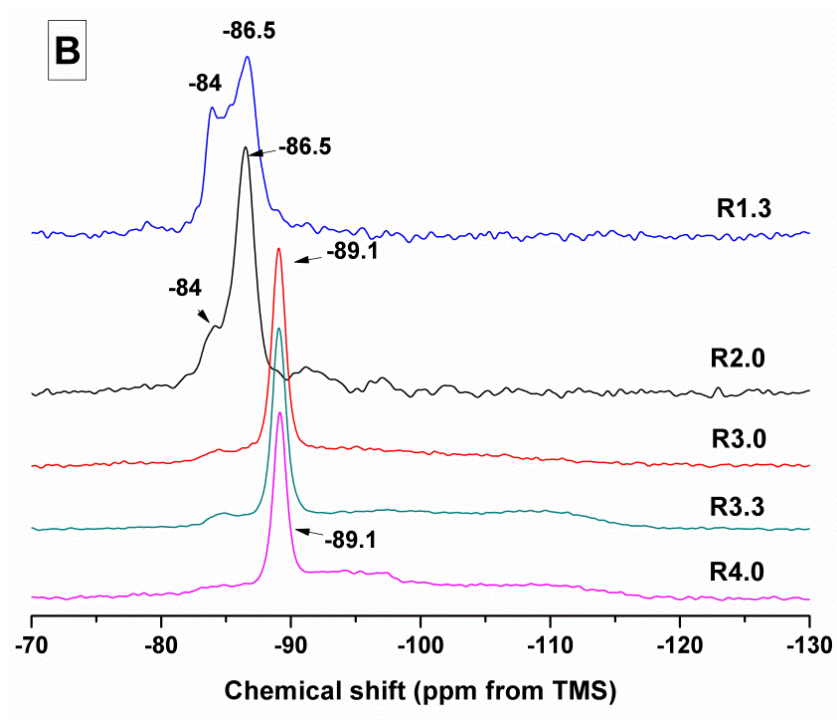
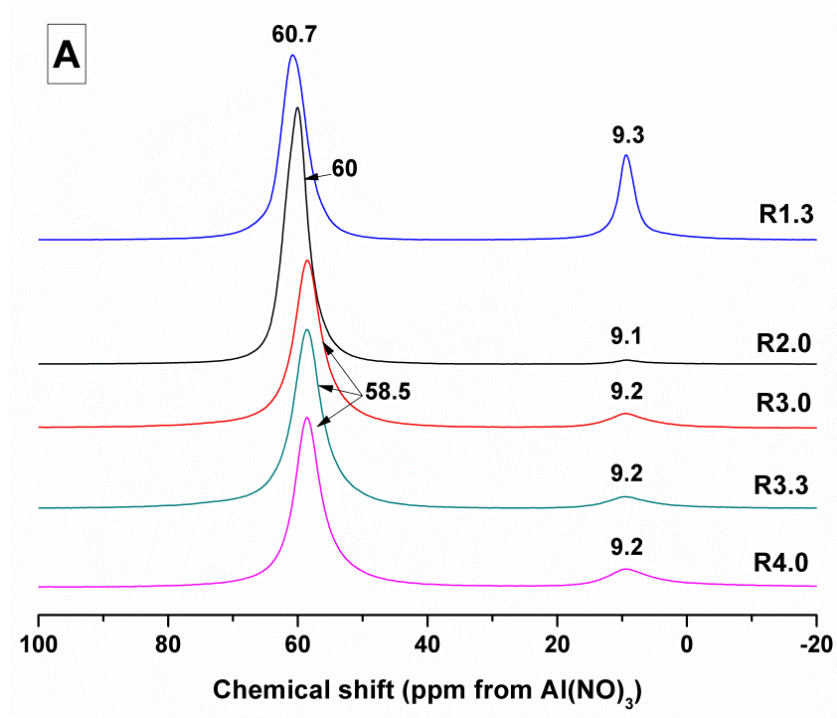


Figure 7.61 (A) ^{27}Al and (B) ^{29}Si MAS NMR spectra of pastes within the system $\text{Mg}(\text{OH})_2\text{-NaAlO}_2\text{-SiO}_2\text{-H}_2\text{O}$, after 720 days of curing

Deconvolution of the ^{29}Si MAS NMR spectra for samples R3.0 – R4.0 was undertaken using the same peak positions and widths as used in Figure 7.9, noted in Table 7.3.

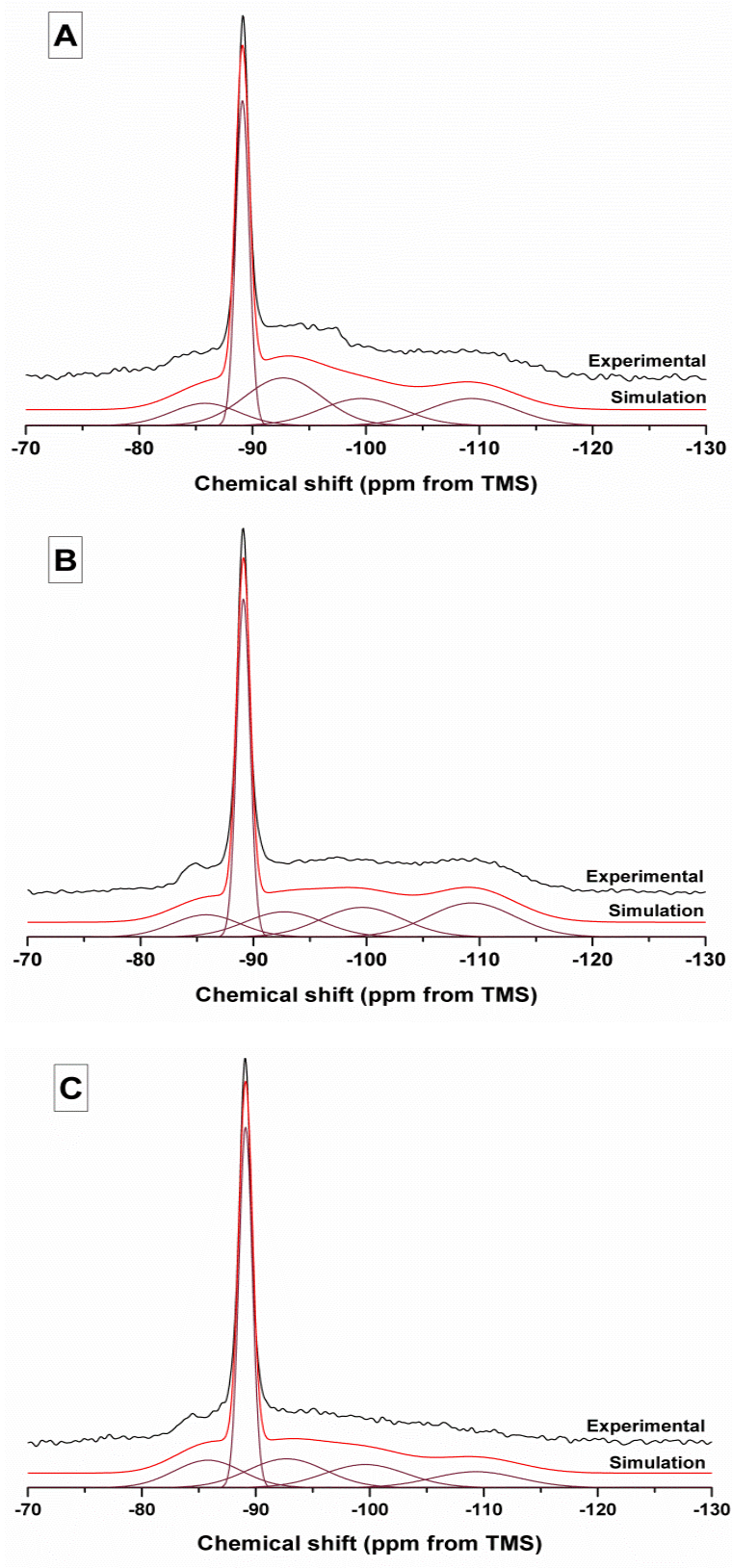


Figure 7.12 ^{29}Si MAS NMR spectra of samples (A) R4.0, (B) R3.3 and (C) R3.0 at 720 days of curing, featuring both experimental and simulated spectra, and decomposition into component peaks

Table 7.3 Peak information for deconvolutions shown in Figure. 7.12. Uncertainty in quantification is $\pm 1\%$ in site percentages

	Disordered phases			Crystalline zeolite		
	Q ² (1Al)	Q ³ (1Al)	Q ³	Q ⁴	Q ⁴ (4Al)	
Centre (ppm)	-85.8	-92.7	-99.6	-89.1	-109.3	
FWHM	7.0	8.0	8.5	1.4	9.0	
R4.0	10.6	31.1	26.0	16.6	15.7	
Peak area (%)	R3.3	11.2	14.5	18.1	22.1	34.2
	R3.0	15.1	18.2	15.5	11.3	39.9

The simulation for each spectrum is largely in line with the observed experimental data, leading me to again believe that no other silicate phases are contributing to these spectra other than those previously described. The fractional integrated peak areas of each site are expressed in Table 7.3. Generally, a higher SiO₂/Al₂O₃ ratio in the formulation favours an increased fraction of the Q⁴, Q³ and Q³(1Al) sites, while a lower SiO₂/Al₂O₃ content results in a larger contribution from the Q⁴(4Al) site of LTA. This is to be expected, as with a higher silica content more unreacted silica is contributing to the spectrum, along with hydroxylated and aluminated silica surface sites.

Overall there is no evidence of a M-S-H or M-A-S-H type phase forming, despite the presence of unreacted and partially aluminated silica. As this has not occurred within 2 years of curing, Mg incorporation is either unlikely to occur, or the kinetics are very slow compared to the zeolite formation.

7.4 Conclusions

7.4.1 Scientific findings

The results of this chapter demonstrate the feasibility of producing an alternative cementitious system which can encapsulate and utilise very high mass fractions of $\text{Mg}(\text{OH})_2$ as a constituent material. The addition of reactive NaAlO_2 into the $\text{Mg}(\text{OH})_2$ - SiO_2 - H_2O system promotes the formation of mixed zeolites, the composition of which varies depending on the $\text{SiO}_2/\text{Al}_2\text{O}_3$ content of the samples.

Initially all samples precipitated $\text{Al}(\text{OH})_3$, followed by zeolites after 20-60 hours. Higher $\text{SiO}_2/\text{Al}_2\text{O}_3$ ratios resulted in faster zeolite formation, although all samples initially exhibited strong heat output during mixing. All samples first form LTA zeolite, before slowly altering the zeolite assemblage over time. High $\text{SiO}_2/\text{Al}_2\text{O}_3$ ratios stabilised LTA, while lower ratios resulted in formation of a low silica faujasite (Na-X) zeolite, Na-P1, sodalite, and a hydrotalcite-type phase in the lowest $\text{SiO}_2/\text{Al}_2\text{O}_3$ ratio sample. This was determined through TG-MS analysis to be a hydroxide containing layered double hydroxide, formed from some $\text{Mg}(\text{OH})_2$ reaction.

^{29}Si and ^{27}Al solid state NMR confirmed the zeolite assignments from the XRD analysis, and also revealed unreacted silica fume, a hydroxylated Q^3 site and aluminated $\text{Q}^2(1\text{Al})$ and $\text{Q}^3(1\text{Al})$ sites, which were not detectable with XRD due to lack of long-range ordering. Further analysis using ^{25}Mg NMR was not able to detect any M-S-H or M-A-S-H formation, despite the presence of large quantities of both $\text{Mg}(\text{OH})_2$ and SiO_2 .

Although no M-S-H or M-A-S-H phases have been identified here, the addition of high quantities of NaAlO_2 promoted the formation of a magnesium-aluminium layered double hydroxide. The potential for ion-exchange between the zeolites, the LDH and any radionuclides may be of benefit for the immobilisation of radionuclide bearing wastes. This ion-exchange potential could be the subject of further work, by loading key elements (such as stable Cs and Sr) into a $\text{Mg}(\text{OH})_2$ slurry prior to formation of the cementitious binders and subjecting the resulting monoliths to semi-static leaching tests.

7.4.2 Industrial application

The possibility of using this cementitious system for waste immobilisation is unlikely in its current format. Despite the ability to utilise $\text{Mg}(\text{OH})_2$ as part of a binding phase, the addition of large amount of NaAlO_2 into the $\text{Mg}(\text{OH})_2$ - SiO_2 - H_2O system is unlikely to be feasible within the context of waste immobilisation due to the extensive exothermic dissolution of SiO_2 and precipitation of $\text{Al}(\text{OH})_3$. Within a larger monolith (such as a 500L drum) this could cause boiling or steam pressurisation of the drum. Equally, the continued evolution of these binders raises questions about the long-term stability. Whether these retain physical stability over a longer (>2 year) timeframe is yet to be answered.

The results of the preceding chapters suggests that the relative stability of more well understood calcium aluminosilicate system is required in the context of waste immobilisation. A system which has the potential for $\text{Mg}(\text{OH})_2$ incorporation, but forms well known phases over a longer timeframe would perhaps be a more suitable encapsulation matrix.

8 Sodium carbonate activated slag – Mg(OH)₂ binders

8.1 Foreword

In this chapter, a study was undertaken on the feasibility of incorporating Mg(OH)₂ within an alternative cementitious system based on alkaline activation of a blast furnace slag. These alternative systems have been of interest for use as nuclear waste encapsulants due to their more flexible chemistry than Portland cement binders [642-643], which can be manipulated by using different alkaline activators and mineral additives [644]. The use of a weakly alkaline activator such as sodium carbonate also enables the slow hydration and setting of such a cement, avoiding issues with thermal gradients within massive samples (such as the 3m³ boxes postulated for use in UK ILW disposal). The slow reaction is typically a limiting characteristic of these cements within the construction field, but does not pose as many limitations within waste management [645]. By utilising a sodium carbonate based activator, there is the potential for magnesium carbonates to form within this system, potentially assisting in the formation of a stable waste monolith. Unlike the other chapters within this thesis, this binding system is not reliant upon the Mg(OH)₂ as an active material for binder formation, and as such can be treated as a relatively ‘safe bet’ for formation of a stable wasteform.

8.2 Introduction

Blast furnace slag rich-binders are beneficial in the encapsulation of radioactive nuclear wastes, as the slag contains sulphides which act as reducing agents, controlling the solubility of key radionuclides, and have been linked to enhanced retention of certain radionuclides [66-67, 360]. Slag-derived binders also often contain layered double hydroxides with a hydrotalcite type structure and a general formula $M_x^{2+}M_y^{3+}(\text{OH})_{2x+3y-nz}(\text{A}^{n-})_z \cdot m\text{H}_2\text{O}$, where A^{n-} is often Cl^- , CO_3^{2-} or NO_3^- , and x/y is generally between 2 and 3 [628, 646], as a reaction product, which is of particular interest for immobilisation of nuclear wastes due to its ability to retain certain long-lived radionuclides such as ^{129}I and ^{36}Cl [617] present in Magnox sludges [618].

Alkali-activated slag binders are Portland cement-free binders produced through the chemical reaction between an alkaline activator and granulated blast furnace slag. The performance of these materials is strongly dependent on the mineralogy and composition of the slag and the nature and concentration of the alkaline activator chosen [647], among other factors. Sodium carbonate activated slags have attracted less attention than other alkali-activated slag cements using sodium hydroxides or sodium silicates as main activators, despite their proven successful usage in Eastern Europe and the CIS as alternative cements for production of mortars and concretes [645]. This is a consequence of the longer setting times identified in these binders (often >5 days) [642, 648], compared when using other alkali-activators. The use of sodium carbonate as activator has advantageous properties compared with sodium hydroxide/silicate solutions, as it is easier and safer to handle due to its powdered and less hygroscopic nature, and when dissolved in water will reach a less elevated pH than that of sodium hydroxide/silicate solutions with an equivalent content of alkalis [642].

Recent studies have demonstrated [644] that the delayed hardening of these cements is strongly dependent on the chemistry of the slag used, and therefore, the general assumption that setting time problems will occur when using this activator is misleading. An increasing MgO content in slag favours hydrotalcite formation in sodium silicate (waterglass)-activated slags [649-650], however, it has been also

suggested [651] that adding reactive MgO to alkali-activated slag binders can have a similar effect, favouring the formation of larger amounts of hydrotalcite. Activation of slag with higher MgO also produces materials that appear to be more resistant to the degradation mechanism referred to as carbonation, potentially opening the door to the development more durable cementitious materials [650].

The addition of Mg(OH)₂ to alkali-activated binders has not been reported in the open literature, although Collier *et al.* [65] identified that the addition of Mg(OH)₂ to Portland cement/slag cement composites potentially promoted the formation of higher contents of hydrotalcite. If this were to hold true for Mg(OH)₂ addition to alternative binders, then these sludges could form part of the binding phase, increasing the achievable waste loadings. The addition of Mg(OH)₂ rather than MgO to alkali-activated cements is also likely to reduce the risk of dimensional instability due to expansive hydration of MgO, while keeping the system saturated with respect to Mg(OH)₂.

In this chapter a sodium carbonate activated slag binder was blended with varying quantities of Mg(OH)₂ (10, 30 and 50 wt.% of the total binder), as a simulant for the solids component of Magnox sludge. Kinetics of reaction were assessed *via* isothermal calorimetry, and hardened samples were evaluated using X-ray diffraction, Fourier transform infrared spectroscopy, thermogravimetry, solid state nuclear magnetic resonance, and scanning electron microscopy, focussing on both early age and longer-term aged samples. Particular emphasis is laid on exploring and understanding the binding gels within this system, and the degree to which Mg(OH)₂ might have influenced their chemistries, and to what level structural substitution might be possible.

8.3 Experimental programme

8.3.1 Sample preparation

All binders were formulated with 10 g of Na_2CO_3 per 90 g of GGBS + $\text{Mg}(\text{OH})_2$ binder, with the ratio of $\text{Mg}(\text{OH})_2$:GGBS treated as a key experimental parameter (Table 8.1). Although the overall Na_2CO_3 content remained constant, the equivalent wt. % Na_2O as a proportion of slag increased as more GGBS was replaced with $\text{Mg}(\text{OH})_2$.

Table 8.1 Formulation of sodium carbonate activated slag cements – mass % basis

Sample ID	$\text{Mg}(\text{OH})_2$	GGBS	Na_2CO_3	w/s ratio	g Na_2O / 100g GGBS
M0	-	90	10	0.30	6.50
M10	10	80	10	0.35	7.31
M30	30	60	10	0.50	9.75
M50	50	40	10	0.60	14.62

Samples were prepared in a Kenwood benchtop mixer by adding the required quantity of water and solid sodium carbonate. After dissolution of the solid activator the GGBS was added to the mix over 2 minutes, followed by the addition of the $\text{Mg}(\text{OH})_2$ over a further 2 minutes of mixing. The amount of water added was increased commensurately with $\text{Mg}(\text{OH})_2$ addition, to maintain an empirically consistent workability between samples. The pastes were cast in 50 mL centrifuge tubes and stored at 20 °C, >90 % relative humidity until analysis at ages of 28 days and 18 months. These samples were then characterised with isothermal calorimetry, XRD, FTIR, compressive strength testing, TG-MS, SEM & EDX mapping.

8.4 Results and discussion

8.4.1 Early age evolution of a $\text{Mg}(\text{OH})_2$ modified sodium carbonate activated slag cement

The effects of GGBS replacement with $\text{Mg}(\text{OH})_2$ on the reaction kinetics of the sodium carbonate activated slag cements were determined by isothermal calorimetry of fresh pastes up to 336 hours (14 days) after mixing, with results as shown in Figs. 8.1 & 8.2, along with XRD analysis (Figure 8.3) of the pastes during the first week of curing. Calorimetry data have been normalised to both overall weight of sample (Figure 8.1), and to content of dry GGBS (Figure 8.2) for further interpretation.

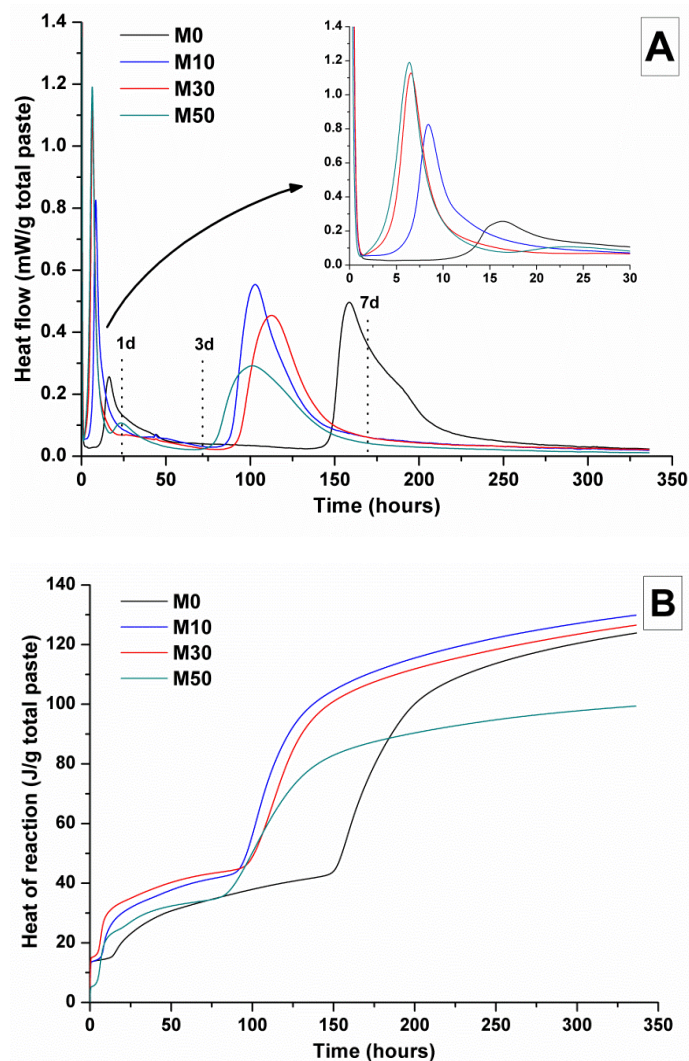


Figure 8.1. Normalised (to total weight) isothermal calorimetry curve (A) and cumulative heat of reaction (B) of sodium carbonate activated slag cements, as a function of the $\text{Mg}(\text{OH})_2$ content

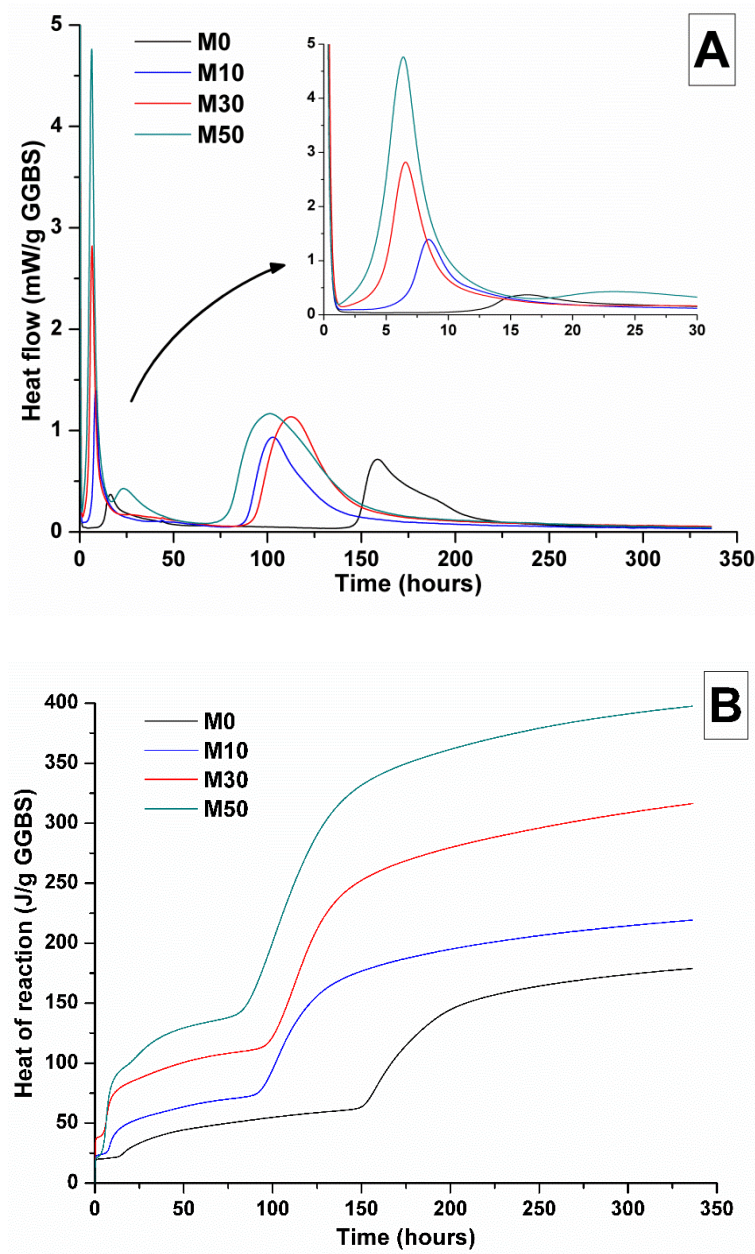
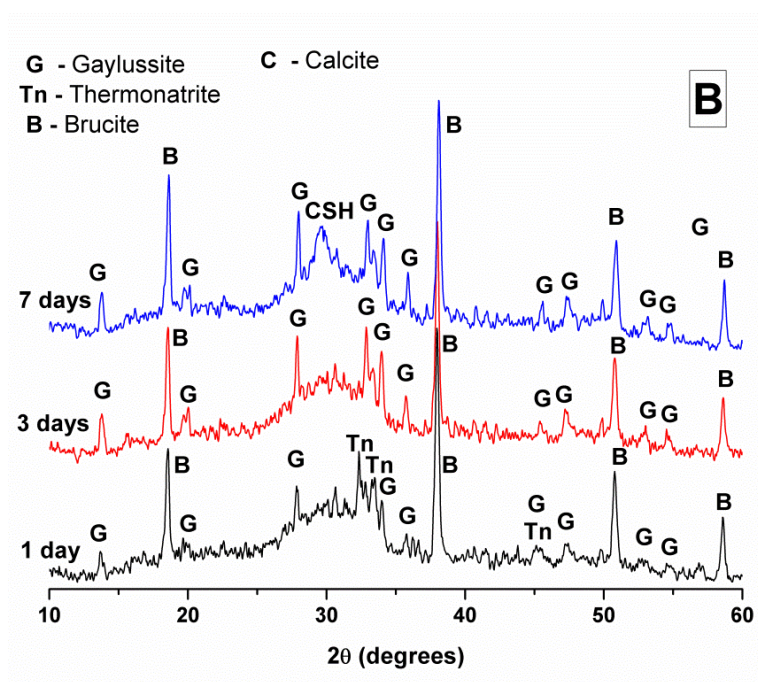
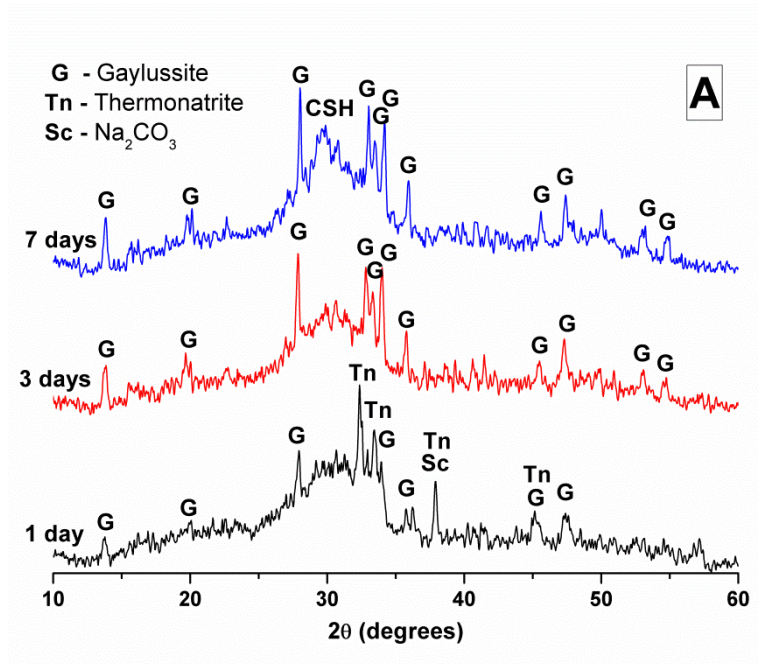


Figure 8.2. Normalised (to GGBS mass) isothermal calorimetry curve (A) and cumulative heat of reaction (B) of sodium carbonate activated slag cements, as a function of the $\text{Mg}(\text{OH})_2$ content



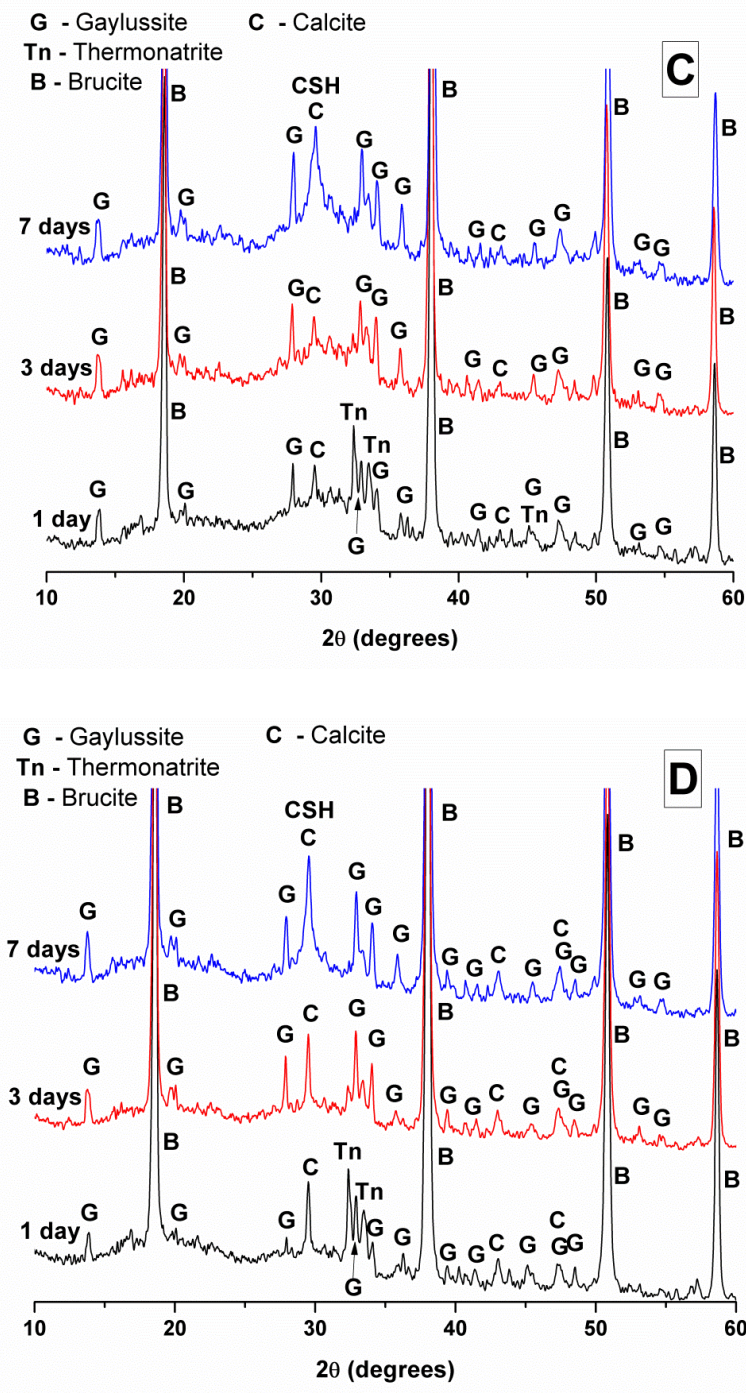


Figure 8.3. X-ray diffractograms of sodium carbonate activated slag cements after 1, 3 and 7 days curing, containing (A) 0 wt.%, (B) 10 wt.%, (C) 30 wt.% and (D) 50 wt.% $Mg(OH)_2$

Three main regions are identified from the calorimetric curves: <1 h, 5-24 h and 3-7 days, that each correspond to distinct exothermic processes. Within the first hour, initial particle wetting and dissolution, and disturbance from the insertion of vials into the calorimeter, dominate. Following this, each sample exhibited an exotherm

between 5-24 hrs, which can be attributed to formation of gaylussite ($\text{Na}_2\text{Ca}(\text{CO}_3)_2 \cdot 5\text{H}_2\text{O}$, powder diffraction file (PDF) # 074-1235) and thermonatrite ($\text{Na}_2\text{CO}_3 \cdot \text{H}_2\text{O}$, PDF #008-0448) as identified by XRD in all the samples after 1 day of curing (Figure. 8.3), independent of the content of $\text{Mg}(\text{OH})_2$ added. Additionally, calcite (CaCO_3 , PDF #005-0586) was identified in samples with higher content of $\text{Mg}(\text{OH})_2$ (Figure 8.3C and Figure 8.3D). Details of the mineral formulations are shown in Table 8.2 below. These results are consistent with what has been reported for sodium carbonate activated slag cements, where the Ca^{2+} released from the dissolved slag reacts with CO_3^{2-} from the activator to form carbonate salts such as calcite and gaylussite, to increase the pH through the release of hydroxide ions [644, 648].

The exothermic peak associated with the formation of carbonate phases was significantly delayed in cements without $\text{Mg}(\text{OH})_2$, appearing ~10 hours later than for samples with 30 wt.% and 50 wt.% $\text{Mg}(\text{OH})_2$. After this event, negligible heat evolution was observed for up to 3 days in all cases, although the XRD results (Figure 8.3) demonstrated that the formation of gaylussite continued over this time, whilst thermonatrite disappeared.

Table 8.2 Mineral phases identified within these GGBS- Na_2CO_3 cements

Mineral	Formulation
Brucite	$\text{Mg}(\text{OH})_2$
Gaylussite	$\text{Na}_2\text{Ca}(\text{CO}_3)_2 \cdot 5\text{H}_2\text{O}$
Calcite	CaCO_3
Thermonatrite	$\text{Na}_2\text{CO}_3 \cdot \text{H}_2\text{O}$
Hydrotalcite	$\text{Mg}_6\text{Al}_2(\text{CO}_3)(\text{OH})_{16} \cdot 4\text{H}_2\text{O}$
Monocarboaluminate ($\text{C}_4\text{A}\hat{\text{C}}\text{H}_{11}$)	$\text{Ca}_4\text{Al}_2(\text{OH})_{12}\text{CO}_3 \cdot 5\text{H}_2\text{O}$

Between 3 and 7 days of curing each sample exhibited a further large exotherm, consistent with an acceleration-deceleration period, distinctly associated with the nucleation, growth and precipitation of reaction products including a calcium silicate hydrate (C-S-H)-type gel, as evidenced by the appearance of diffuse scattering around $\sim 29^\circ 2\theta$ in the X-ray diffractograms (Figure 8.3) of all the cements assessed.

The formation of the C-S-H gel was significantly accelerated in each sample containing $\text{Mg}(\text{OH})_2$ replacement. The C-S-H type phase forming in these systems is the main reaction product formed in alkali-activated slag binders [647] and contributes substantially to the mechanical strength development of these materials.

The effect of $\text{Mg}(\text{OH})_2$ additions accelerating the precipitation of reaction products could be consequence of either a threshold effect of increasing Na_2O wt. % relative to the GGBS, or a filler effect from $\text{Mg}(\text{OH})_2$. As the ratio of $\text{Mg}(\text{OH})_2$ to GGBS is increased, the Na_2O dose relative to the mass of GGBS also increases (from 6.5 g to 14.6 g Na_2O / 100g GGBS in M0 and M50 respectively), as the Na_2CO_3 content is kept constant while the GGBS content is lowered. This higher proportion of activator might have exceeded a point at which formation of hydration products is accelerated. However, as the absolute quantity of Na_2CO_3 is kept constant, the acceleration of reaction product precipitation might also be due to a filler effect, around which reaction products can nucleate and precipitate [652-653]. $\text{Mg}(\text{OH})_2$ itself may act as a seed or a template for layered double hydroxide (LDH) formation, such as hydrotalcite-like products, which themselves have been identified as accelerating the kinetics of alkali carbonate activated systems [644]. Regardless of the method of action, this effect does appear to increase with further additions of $\text{Mg}(\text{OH})_2$, as acceleration does not increase beyond that observed when 10% $\text{Mg}(\text{OH})_2$ is added.

The overall heat output of cements with 10% and 30% additions of $\text{Mg}(\text{OH})_2$ (M10 & M30) in Figure 8.1B is similar to that observed without $\text{Mg}(\text{OH})_2$ (M0) addition. This demonstrates that $\text{Mg}(\text{OH})_2$ can be safely added to an alkali-carbonate activated slag matrix without prompting an increased exotherm, and is therefore safe to consider within the context of a nuclear wasteform cement. The heat release from the reaction is spread over a much wider timeframe than is typical in PC blends, which will ultimately lower the wasteform temperature and ensure safer processing. Further addition of $\text{Mg}(\text{OH})_2$ up to 50% (M50) lowers the overall heat of reaction, which is likely due to the reduced quantities of GGBS available to react, and the increased quantities of water within this sample diluting the heat output per gram (as Figure 8.1 is normalised to total weight inclusive of dry powders and water). Normalising the data to weight of dry GGBS (Figure 8.2) highlights a clear progression towards higher heat of reaction per gram of GGBS (Figure 8.2B) as $\text{Mg}(\text{OH})_2$ is increased up to 50%, which is indicative of either increased dissolution of the GGBS or a reaction

involving $\text{Mg}(\text{OH})_2$. Presentation of the heat flow data normalised in this way (Figure 8.2A) also shows the monotonic increase in the intensity of the acceleration-deceleration peak with $\text{Mg}(\text{OH})_2$ addition, particularly within the first 15 hours of reaction. Relative to the other samples, when normalised to GGBS content, the composition containing 50% $\text{Mg}(\text{OH})_2$ produces more heat during the C-S-H formation region (3-7 days), suggesting potentially more complete dissolution of the slag.

8.4.2 Long term structural evolution of a $\text{Mg}(\text{OH})_2$ modified sodium carbonate activated slag cement

8.4.2.1 X-ray diffraction

After 28 days of curing, X-ray diffraction patterns (Figure 8.4A) show the continued growth of a C-S-H type phase when compared with the 7-day data in Figure 8.3. Given the Al_2O_3 content of the slag, and the known hydration products of alkali activated slags, this is likely to be an aluminium substituted gel, C-A-S-H with a tobermorite-type structure, or potentially a further sodium modified C-(N-)A-S-H cross-linked gel [654-656]. High intensity reflections of the crystalline phases brucite ($\text{Mg}(\text{OH})_2$) and gaylussite were also identified. In all of the samples a reflection at $11.6^\circ 2\theta$ was identified, and assigned to the formation of a hydrotalcite-like phase, resembling $\text{Mg}_6\text{Al}_2(\text{CO}_3)(\text{OH})_{16}\cdot 4\text{H}_2\text{O}$ (PDF # 041-1428), but potentially with differences in Mg/Al ratio (see section 8.3.2.5), which was not observable after 7 days of curing (Figure 8.3). The main reflection assigned to this phase is especially prominent in samples with high contents of $\text{Mg}(\text{OH})_2$ (Figure 8.4A, M30 and M50). More intense reflections assigned to calcite and brucite were observed in the specimens containing 30 wt.% and 50 wt. % $\text{Mg}(\text{OH})_2$, however no crystalline peaks assignable to formation of magnesium/calcium carbonate phases were identified. The most intense reflection assigned to calcite overlaps with the C-S-H reflection at $29.4^\circ 2\theta$, however secondary reflections at 39.4° , 43.1° , 47.5° and $48.5^\circ 2\theta$ confirm the presence of large quantities of calcite in both of these samples.

Mg is known to become incorporated into calcite, forming magnesian calcites. This has been well studied within marine calcites, with Mg incorporation varying depending on $p\text{CO}_2$, temperature and pH [210, 215]. Formation of magnesian calcites would be difficult to determine from XRD, as although Mg incorporation affects the calcite lattice, resulting in a slight shift in the diffraction pattern, at low levels of incorporation [657-658], this is difficult to discern in complex samples such as these slag cements. In the literature higher Mg:Ca ratios are observed to affect CaCO_3 polymorph formations and stabilities; increasing Mg concentration in solution tends to stabilise aragonite and vaterite through retarding growth of calcite, while enhancing the formation of monohydrocalcite [210-212, 214]. None of these are identified within any of the samples analysed here, suggesting little reaction of $\text{Mg}(\text{OH})_2$, however it should be noted that established literature on magnesian calcite formation does not include information collected at high pH, and therefore the same conclusions may not be valid at the higher alkalinity of these sodium carbonate activated slag samples.

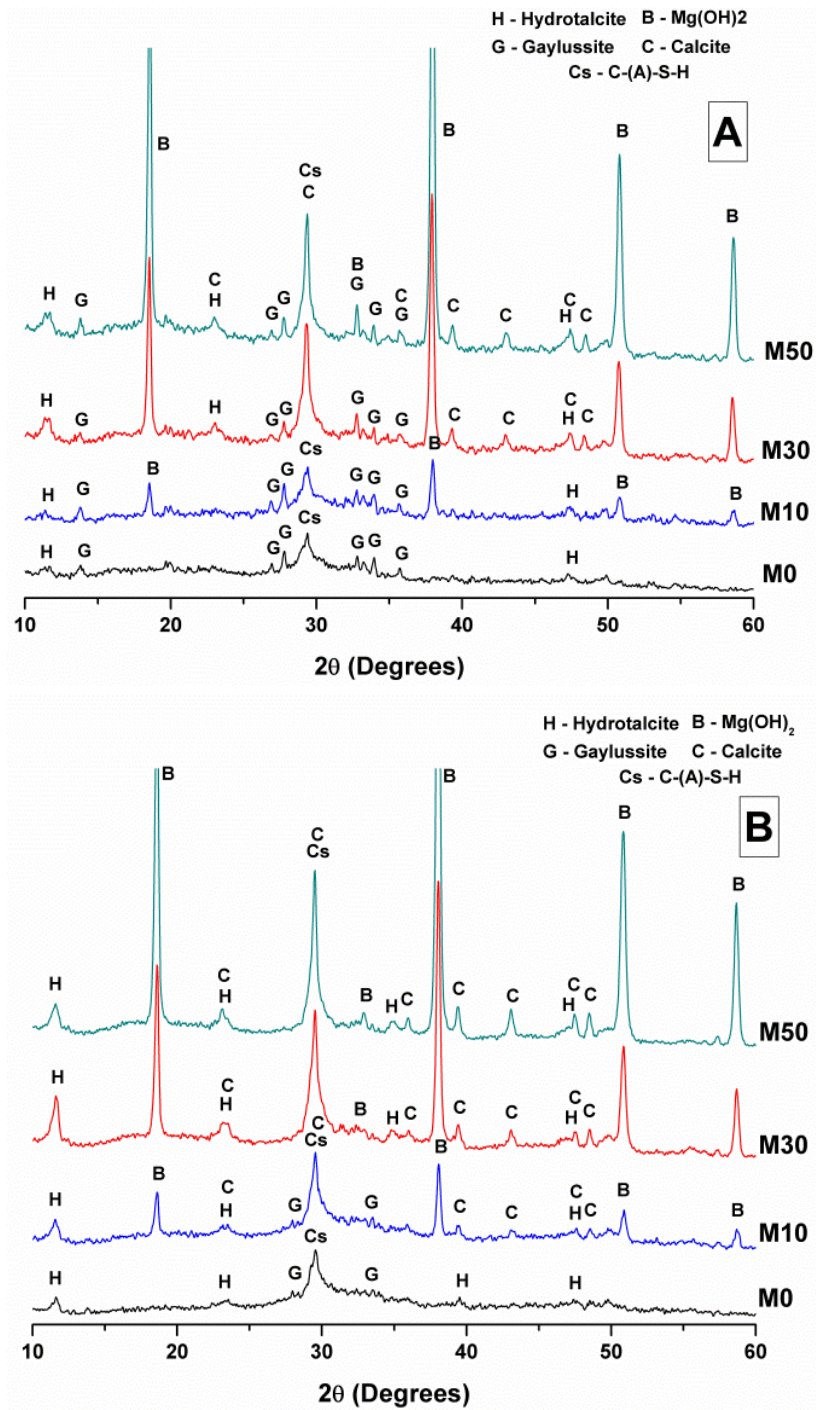


Figure 8.4. X-ray diffraction patterns of sodium carbonate activated slag binders after (A) 28 days, and (B) 18 months of curing

Although all samples form similar phases after 28 days of curing, their compressive strengths are notably varied (Table 8.3). The samples generally decrease in strength as more $Mg(OH)_2$ is included in the system, which also corresponds to an increasing water to solids ratio. This usually decreases the strength of cements, and is to be

expected [134]. Notably, however, the sample containing no $\text{Mg}(\text{OH})_2$ displays a lower strength than that with 10%. This is likely to be an artefact of sample preparation, as the $\text{Mg}(\text{OH})_2$ -free samples were slightly malleable when demoulded, whereas all the other samples were fully solid monoliths. Several of the cube edges were slightly squashed in the process, potentially leading to less than perfect samples for compressive strength testing.

Table 8.3 Compressive strengths of the sodium carbonate activated slag cements after 28 days of curing. Tests undertaken in triplicate on 50mm cubes.

	M0	M10	M30	M50
Mean strength (MPa)	49.8	55.6	40.8	20.8
Standard deviation	4.2	3.3	1.1	0.2

After 18 months of curing (Figure 8.4B) the phase assemblage of each binder continued to develop, with only minor gaylussite reflections identified in the samples. In its place, the continued formation of calcite was observed in all the samples, increasing in intensity with the replacement of the slag by $\text{Mg}(\text{OH})_2$. A high intensity reflection of the hydrotalcite-type phase was observed in all samples, displaying especially strong reflections in the sample with 30 wt.% $\text{Mg}(\text{OH})_2$ (Figure 8.4B, M30). The reflections assigned to $\text{Mg}(\text{OH})_2$ were strongly evident in all samples to which $\text{Mg}(\text{OH})_2$ was added, suggesting that any reaction between $\text{Mg}(\text{OH})_2$ and the bulk chemistry was far from complete. The increasing content of $\text{Mg}(\text{OH})_2$ did not appear to have an influence on the phase assemblage, other than increasing the intensity of the reflections assigned to calcite, C-A-S-H and hydrotalcite, which is commensurate with an increased degree of slag dissolution due to the increased content of activator added within the higher $\text{Mg}(\text{OH})_2$ content samples.

The overall phase evolution of these slag cements was similar to that previously identified in sodium carbonate activated slags [648, 659], although direct comparison

is difficult due to varying doses of Na₂O added to each of the systems and the differences in the chemistry of the slag used in this study compared to those described in the literature. The major difference between the results obtained here and the established literature is the presence of calcite, and the absence of CaCO₃ polymorphs aragonite and vaterite, which was contrary to the literature for aged samples [648, 659].

For a sodium carbonate activated slag (with a comparable composition, though with a reduced bulk MgO content), Myers et al. [656] predicted the formation of a C-(N)-A-S-H gel, calcite, natrolite (a zeolite; Na₂Al₂Si₃O₁₀·2H₂O), a magnesium-aluminium layered double hydroxide intercalated with OH⁻ groups (MA-OH-LDH) and a monocarboaluminate AFm phase (C₄A \hat{C} H₁₁). In this study, neither natrolite nor monocarboaluminates were detected, however the presence or absence of C₄A \hat{C} H₁₁ could not confidently be assigned as the diffraction patterns for this monocarboaluminate phase [660] (PDF #041-0219) present significant overlap with hydrotalcite-like phases, making elucidation difficult. The identification of the MA-OH-LDH phase is also challenging as this has a similar diffraction pattern to hydrotalcite-like phases containing CO₃²⁻ groups. Gaylussite is not predicted to be a stable phase within these cements, which is in line with the decreased reflections noted here after 18 months, which concurs with the results of other studies [648].

8.4.2.2 Fourier transform infrared (FTIR) spectroscopy

Figure 8.5 shows the infrared spectra of the samples at 28 days and 18 months. In both Figs. 8.5A (samples cured for 28 days) and 8.5B (samples cured for 180 days), the most notable difference among the samples was seen in the sharp peak at 3698 cm⁻¹, assigned to the OH stretching vibration mode of Mg(OH)₂. As expected, reduced contents of Mg(OH)₂ in the cement led to a lower intensity in the band assigned to the hydroxyl groups present in the brucite. Although significant quantities of Mg(OH)₂ remain in the samples after 18 months of curing, especially when adding high contents of Mg(OH)₂ (Figure 8.5B, M50), a slight reduction of the intensity of this band is observed when comparing pastes containing reduced

Mg(OH)₂ contents and cured for 28 days and 18 months, although this might be an artefact of sample preparation and analysis.

The broad band centred at 3455-8 cm⁻¹ corresponds to the H-OH stretching mode of bound water, while the resonance at 1644 cm⁻¹ is assigned to the bending mode of the H-OH bond [579-580]. These resonances are typical of bound and interlayer water within C-S-H/C-A-S-H gels [661-662] forming in cementitious systems, along with crystal water within hydrotalcite-type phases and gaylussite [580], consistent with the phases observed by X-ray diffraction (Figure 8.4).

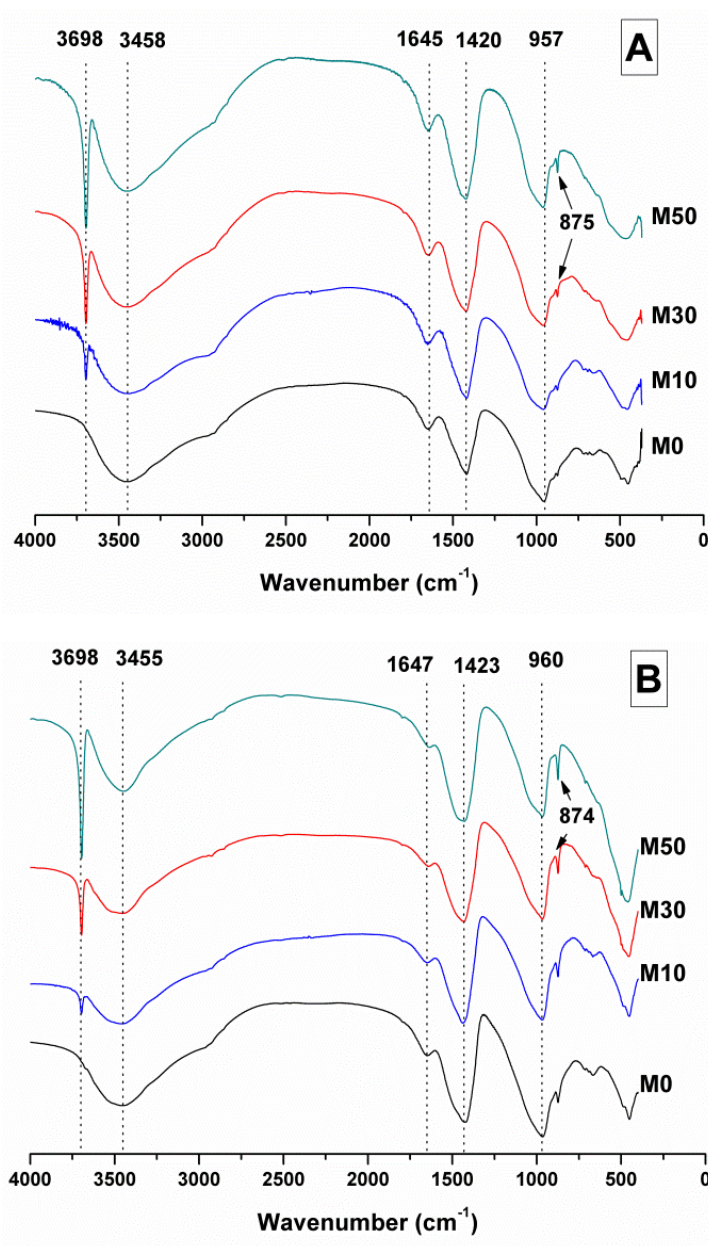


Figure 8.5. FTIR spectra of sodium carbonate activated slag binders after (A) 28 days, and (B) 18 months of curing

The Si-O-(Al,Si) stretching vibration mode was identified at $957\text{-}60\text{ cm}^{-1}$ and was assigned to the C-(A)-S-H gel, which would typically exhibit stretching bands $\geq 952\text{ cm}^{-1}$ [661], combined with contributions from residual slag. The position of this band was not affected by the addition of different contents of $\text{Mg}(\text{OH})_2$, which indicated that significant changes in either the degree of crosslinking or/and the chemical composition of the C-A-S-H phase did not occur, which is in agreement with NMR analysis to be presented in section 8.4.3.

The broad band at 1420 cm^{-1} was attributed to the ν_3 carbonate stretching typically present in carbonate phases, consistent with the identification of calcite, gaylussite and the hydrotalcite-like phase in the phase assemblages (Figure 8.3 and 8.4) of these samples, as the vibrations of all of these structures overlap in this region [580, 663]. Carbonate vibrations from calcite were more clearly evident in a sharp peak at $874\text{-}5\text{ cm}^{-1}$, which increased intensity in the samples with higher contents of $\text{Mg}(\text{OH})_2$ and also with curing age. This correlates well with the increasing intensity of the reflections assigned to calcite with $\text{Mg}(\text{OH})_2$ addition detected through XRD analysis at both curing ages (Figure 8.4).

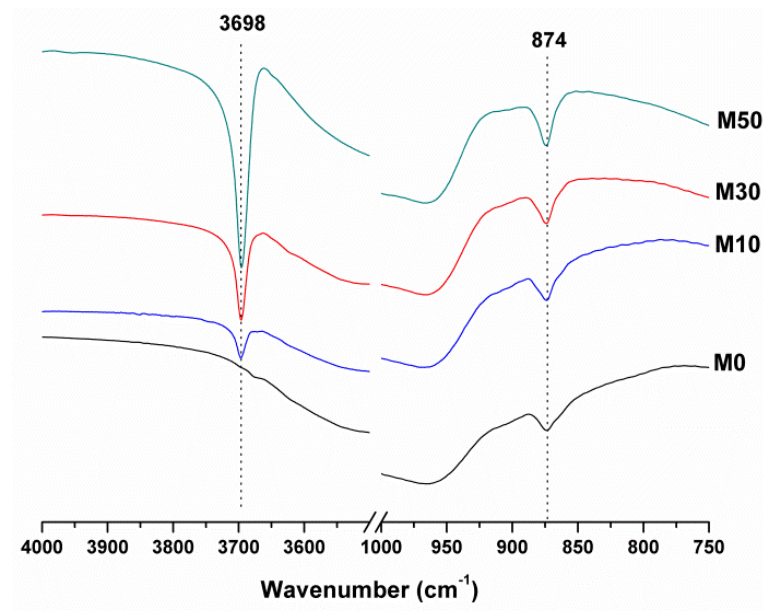


Figure 8.6. Expanded FTIR spectra of sodium carbonate activated slag binders after 18 months of curing

Both the OH stretching ($3800\text{-}3600\text{ cm}^{-1}$) and carbonate vibration ($900\text{-}850\text{ cm}^{-1}$) regions of the FTIR spectra of aged samples are shown in an expanded view in Figure 8.6, as these regions provide evidence for the formation (or absence) of other carbonate or hydroxy-carbonate phases. Due to the large quantity of $\text{Mg}(\text{OH})_2$ within these samples, there might exist opportunities for the formation of magnesium carbonate phases. Magnesite (MgCO_3) typically exhibits a sharp vibration at 885 cm^{-1} [580], while other hydrated magnesium carbonates display sharp vibrations in the region $3700\text{-}3500\text{ cm}^{-1}$ (nesquehonite ($\text{MgCO}_3\cdot 3\text{H}_2\text{O}$) at 3570 cm^{-1} [580], hydromagnesite ($\text{Mg}_5(\text{CO}_3)_4(\text{OH})_2\cdot 4\text{H}_2\text{O}$) at 3645 , 3505 and 3445 cm^{-1} [580], and dypingite ($\text{Mg}_5(\text{CO}_3)_4(\text{OH})_2\cdot 5\text{H}_2\text{O}$) at 3648 cm^{-1} [664]). The absence of these vibration modes, combined with evidence from XRD analysis as shown above, rules out the formation of pure magnesium carbonates other than the hydrotalcite-like phase. This analysis also rules out the formation of the CaCO_3 polymorphs aragonite and vaterite, as they display characteristic infrared vibrations in the region $900\text{-}850\text{ cm}^{-1}$ [580, 665].

Mg incorporation within Ca containing carbonate phases is slightly more difficult to determine within these samples. Huntite ($\text{CaMg}_3(\text{CO}_3)_4$) can be excluded, as this mineral exhibits strong vibrational modes ~ 892 and 869 cm^{-1} [580], which are not observed within these samples. Dolomite ($\text{CaMg}(\text{CO}_3)_2$) is known to have slow crystallisation kinetics [666] and typically displays a sharp vibration at 881 cm^{-1} , higher than observed here [667]. Incorporation of Mg into calcite to form a magnesian calcite is much more difficult to ascertain. FTIR analysis of calcites has shown an increase in the carbonate ν_2 vibrational mode wavenumber as the proportion of magnesium within the calcite structure increases, though this is typically only up to $\sim 876\text{-}7\text{ cm}^{-1}$ in naturally occurring magnesian calcites (e.g. $\text{Ca}_{0.84}\text{Mg}_{0.16}\text{CO}_3$ analysed in [668]). The principal vibration within these samples does not alter its position from 0 to 50% $\text{Mg}(\text{OH})_2$ suggesting little to no Mg incorporation within calcite, though some limited substitution cannot be ruled out.

8.4.2.3 Thermogravimetry analysis

Thermal analysis of the samples after 28 days (Figure 8.7A) and 18 months (Figs. 8.7B and 3.8) show a mass loss at temperatures below 200 °C which can be attributed to removal of free water in the samples, and the initial loss of the interlayer and structural water present in the C-S-H/C-A-S-H [669-670], identified as the main reaction product in these cements by XRD (Figure 8.4) and FTIR (Figs. 8.5 and 8.6). The sharp peak at 110 °C is assigned to gaylussite dehydration [548], in agreement with the XRD analysis, where noticeably reduced gaylussite intensities were observed after 18 months curing.

Dehydroxylation of $\text{Mg}(\text{OH})_2$ was prominent at ~400 °C, where mass loss increased commensurately with the addition of higher $\text{Mg}(\text{OH})_2$ contents in the sample. At ~630 °C, calcite decomposition was observed, followed by decarbonation from dehydrated gaylussite. In naturally formed samples of gaylussite, decarbonation can however begin at 620 °C [671]. The decomposition of the hydrotalcite-like phase was more difficult to determine as such phases typically exhibit several decomposition regions up to 400 °C, varying depending on the structure and interlayer anions within the phase [631, 635], and potentially overlapping with the mass loss corresponding with the $\text{Mg}(\text{OH})_2$ decomposition. This is highlighted within the differential thermogram of the 18 months cured sample without $\text{Mg}(\text{OH})_2$ addition (inset Figure 8.7B, M0), which shows a distinct shoulder at 200 °C and further mass loss at 350 °C. This is characteristic of a hydrotalcite-like phase [634-635] and can be noted in the other 18 month samples, where there is an apparent shift in the $\text{Mg}(\text{OH})_2$ decomposition peak from 380 °C towards a lower temperature associated with overlapping mass loss from this hydrotalcite-like phase at ~350 °C .

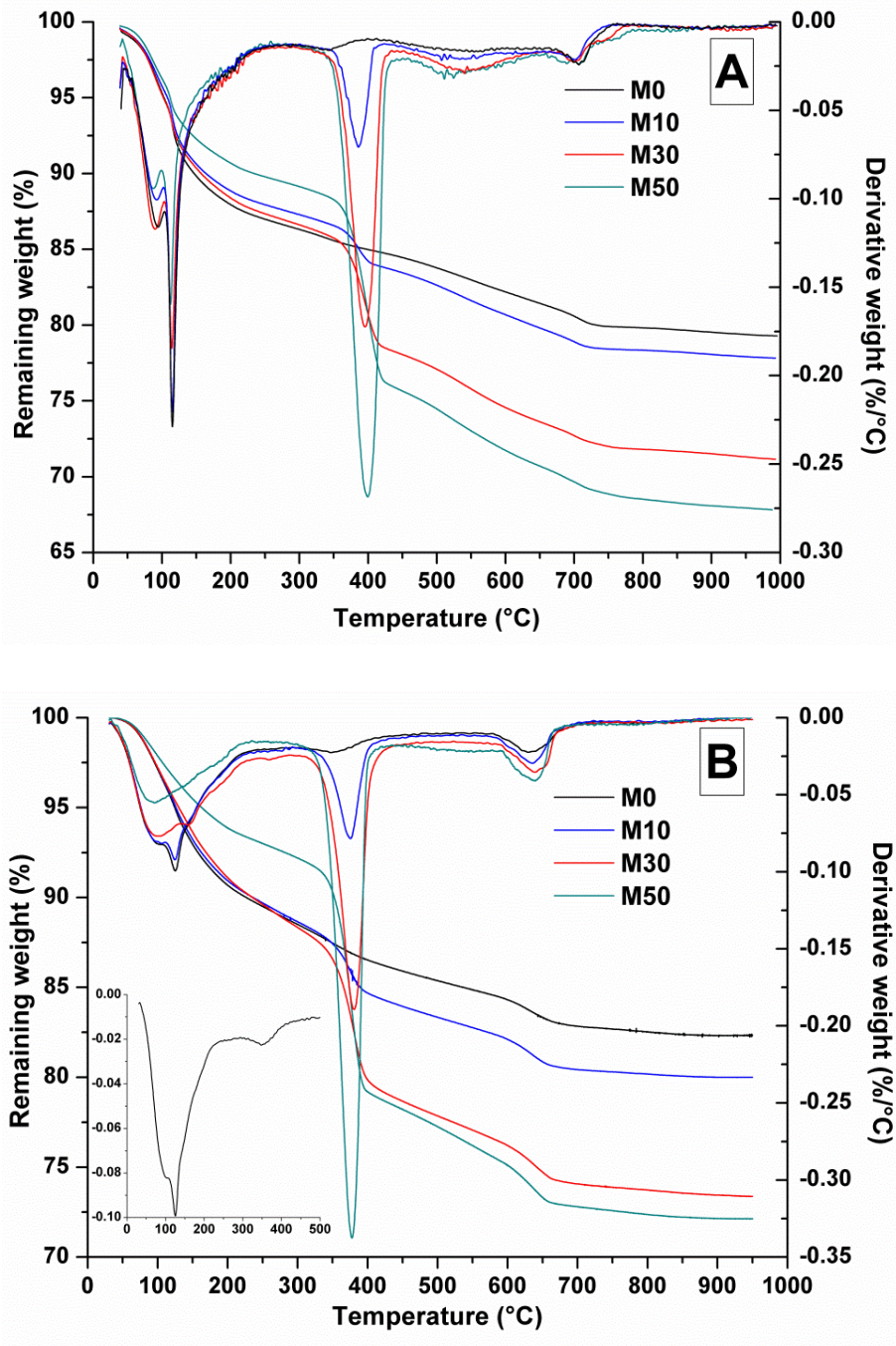


Figure 8.7. Thermogravimetric (TG) and differential thermogravimetric (DTG) analysis of samples after (A) 28 days curing and (B) 18 months curing, with M0 DTG data shown as an inset.

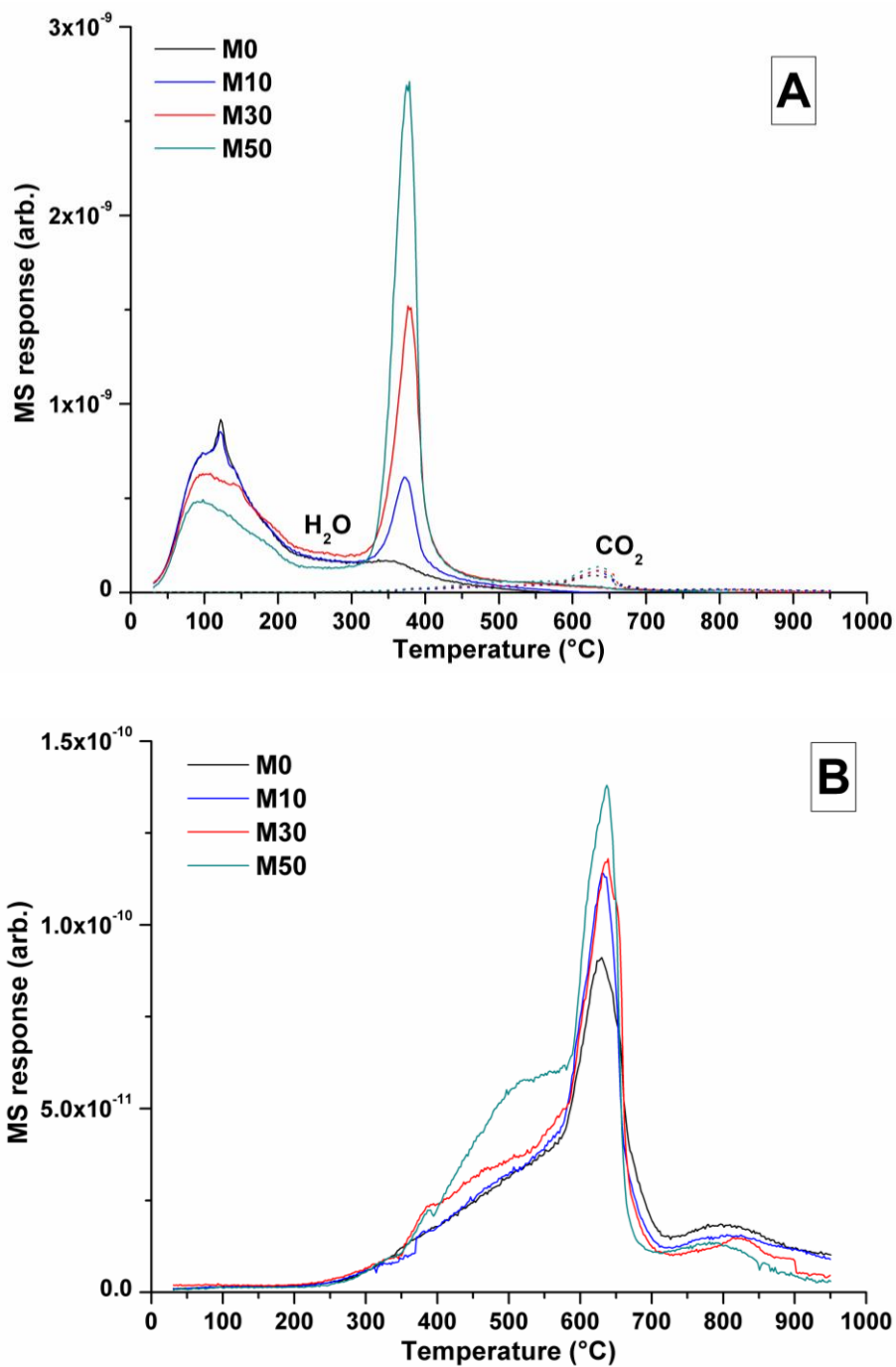


Figure 8.8. MS data for all samples after 18 months curing, (A) combined H₂O and CO₂, (B) CO₂ response

The TG-MS data (Figure 8.8) for samples with different contents of Mg(OH)₂ after 18 months provided an insight into the nature of this Mg-LDH phase. Within these samples the mass loss at ~350 °C only registered as H₂O, not as CO₂. Typically a carbonated hydroxalcite-like phase would evolve interlayer CO₂ within this region

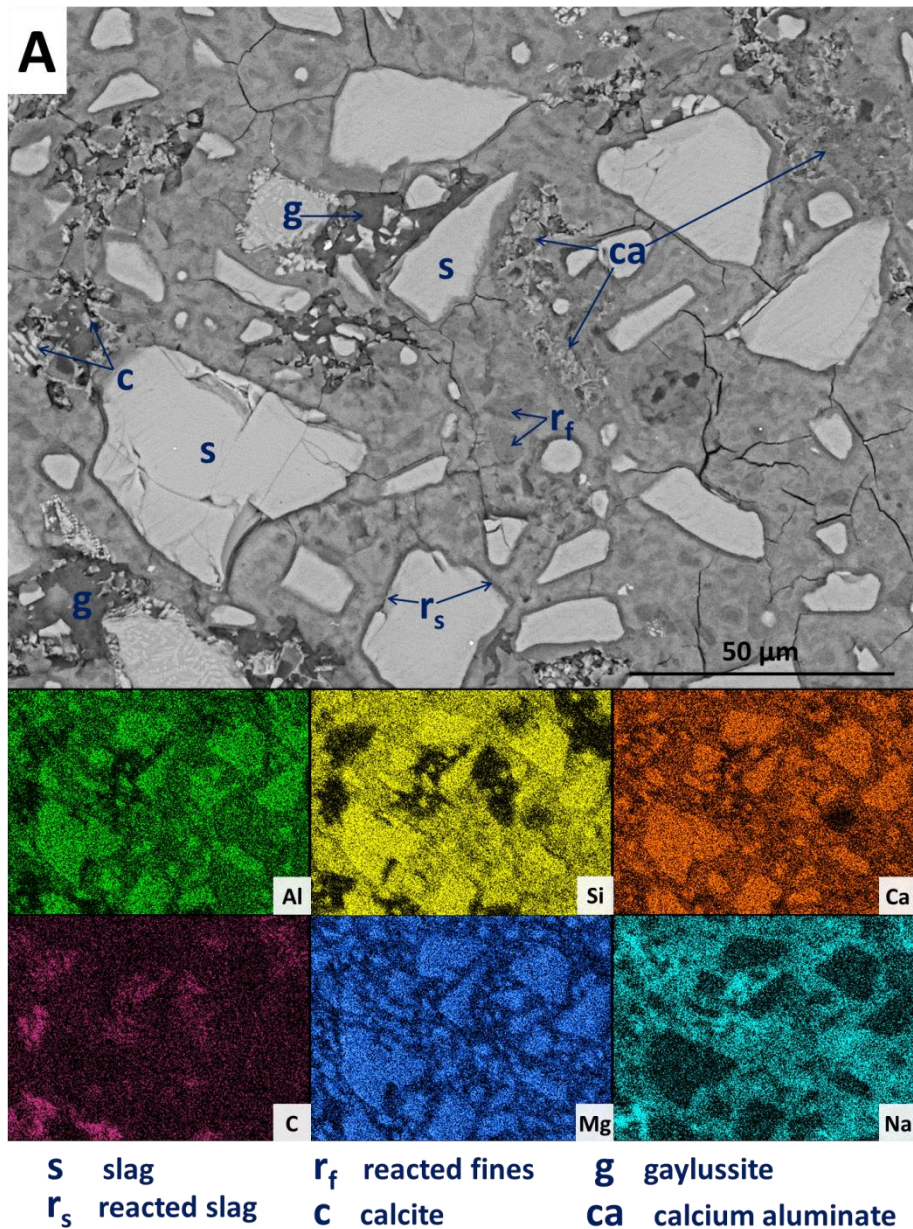
[635] however, CO₂ evolution was significantly lower than H₂O within this region (Figure 8.8A). Plotting CO₂ alone (Figure 8.8B) reveals slight evolution of CO₂ here, however this is part of a broader decarbonation culminating in calcite decomposition at 630 °C rather than a discrete event which could be attributed to a carbonate-containing LDH. This evidence supported the postulation by Myers *et al.* [656] that the hydrotalcite-group phase formed within these systems is in fact an MA-OH-LDH phase rather than a carbonate.

8.4.2.4 *Microstructural features of aged Mg(OH)₂-containing sodium carbonate activated cements*

Backscattered electron (BSE) micrographs for the Mg(OH)₂ free sample (M0) are displayed in Figure 8.9, along with the associated elemental maps (further supplementary images are reported in Appendix I). It was evident that the slag grains (labelled 's' in the micrographs) had undergone varying stages of dissolution, resulting in the formation of a dense matrix composed of a C-(N-)A-S-H type gel, as evidenced by the widespread distribution of Al, Si, Ca and Na, in which all the other features were embedded. The remaining slag particles were surrounded by thin darker reaction rims (labelled 'r_s' in the micrograph), clearly observed at a higher magnification (Figure 8.9B), particularly in the fully reacted slag fines, with a darker grey colour than the bulk matrix (labeled 'r_f' in the micrograph). This region was richer in Mg than the bulk matrix, indicating this might be enriched in a hydrotalcite-like phase consistent with that observed by other authors in sodium hydroxide and silicate activated slags [672-673], and in aged sodium carbonate activated slag cements [644].

Large darker regions (labelled as 'g' in the micrograph) are assigned to gaylussite, consistent with an enriched Na and C composition compared to the bulk matrix, along with absence of Al and Si. Similar features have been observed in sodium carbonate/silicate activated slag cements [648], where gaylussite is reported as a reaction product. Formation of calcite (labelled 'c' in the micrograph), corresponding to the regions observed in the EDX maps to be rich in Ca and C but lacking in Al and Si, was observed around gaylussite. It is also possible to observe the presence of

large darker patches (labelled 'ca' in the micrograph), which are particularly low in Si but still contain appreciable quantities of Ca, C and Al. This chemical composition suggest the formation of a calcium aluminate phase, potentially a monocarboaluminate $C_4A\hat{C}H_{11}$ type phase whose formation was predicted by Myers, *et al.* [656] via thermodynamic modelling, and recently identified by XRD and solid state NMR spectroscopy by Ke *et al.* [644] in aged sodium carbonate activated slag cements.



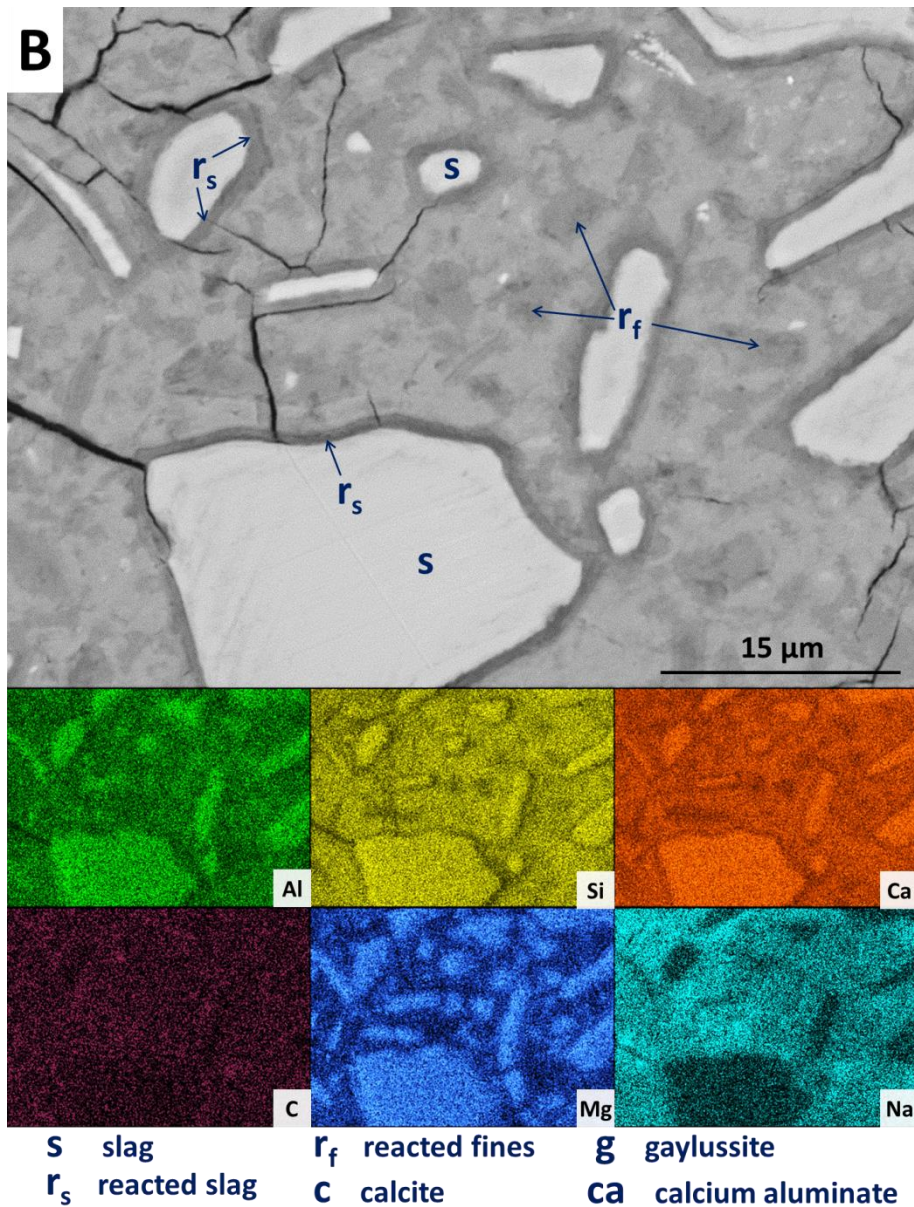


Figure 8.9. Backscattered electron micrograph and corresponding EDX maps of a sodium carbonate activated slag without $Mg(OH)_2$ addition (both A & B) after 18 months of curing

The presence of this hydrous calcium aluminate phase throughout the samples was evidenced when assessing the specimen at a lower magnification (Figure 8.10). The areas indicated by dashed lines indicated regions distinctly rich in Ca and Al but deficient in Si, relative to the bulk matrix. These large regions appeared to occur independently with no identifiable interaction with other phases, quite unlike the

formation of the MA-OH-LDH phase which was found to be spatially bound to slag particles.

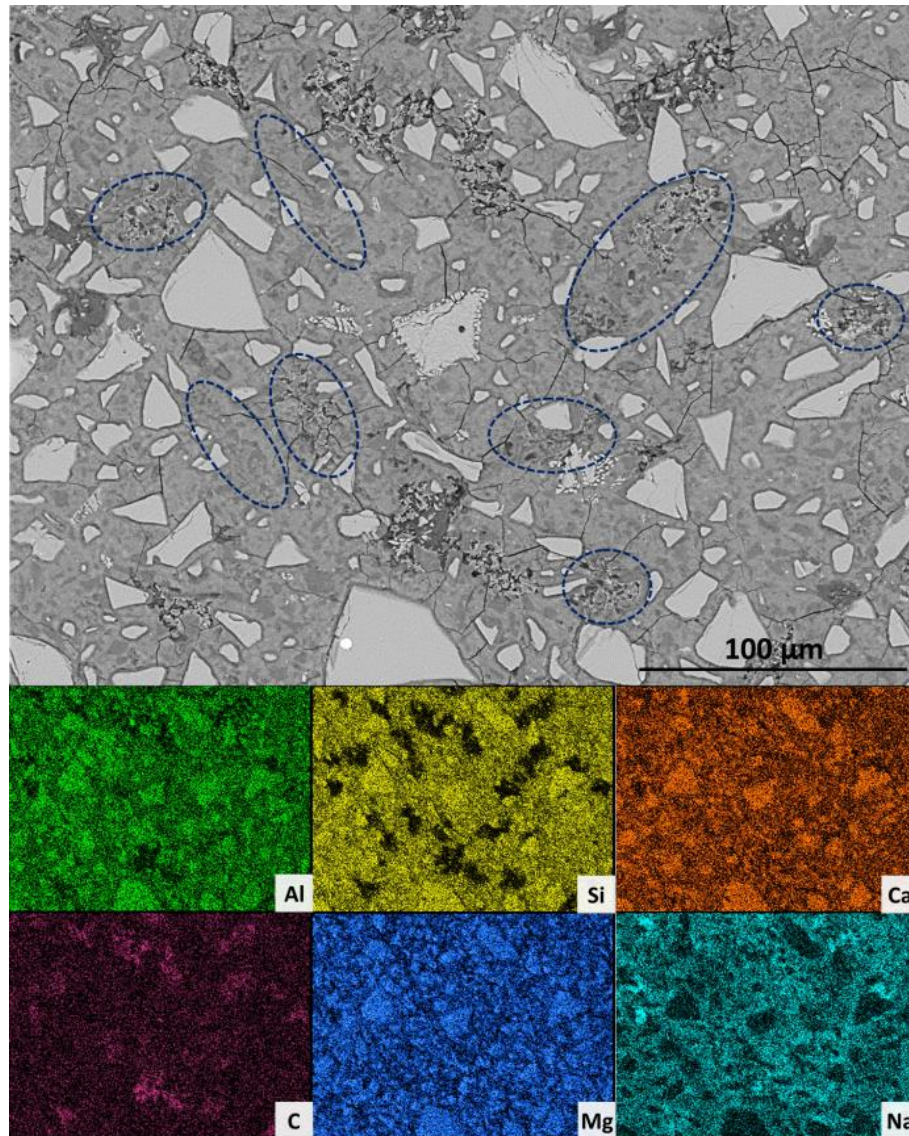
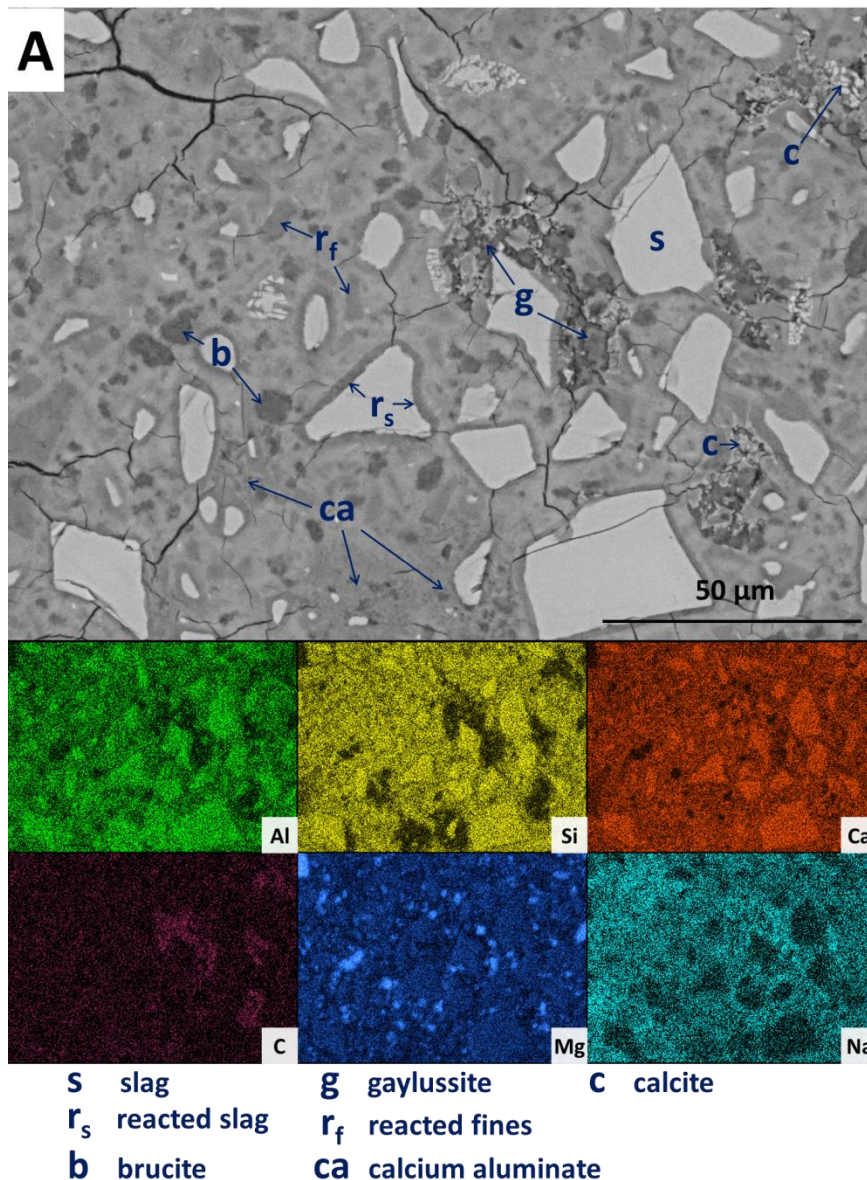


Figure 8.10. Backscattered electron micrograph and corresponding EDX maps of a sodium carbonate activated slag without $Mg(OH)_2$ addition after 18 months of curing, highlighted areas correspond to postulated $C_4A\hat{C}H_{11}$ phase

SEM results of specimens including 10 wt.% $Mg(OH)_2$ (sample M10) are shown in Figure 8.11, where it was observed that a significant quantity of unreacted slag (s) remained, around which reaction rims (r_s) have developed. As in Figure 8.9, remnant reaction rims from dissolution of slag fines (r_f) were observed, along with the presence of gaylussite (g) and with calcite (c) forming on the edges of gaylussite

patches. Small $\text{Mg}(\text{OH})_2$ particles (b) were observed throughout the sample, and do not appear to have undergone any reaction but instead remain embedded within the C-(N-)A-S-H rich bulk matrix. Figure 8.11B focuses at higher magnification on two large $\text{Mg}(\text{OH})_2$ particles, which are embedded in the bulk gel. The EDX maps do not reveal any reaction rim region surrounding the particles, nor is there evidence of decalcification or Al enrichment in the bulk surrounding these particles, which would indicate MA-OH-LDH formation around the $\text{Mg}(\text{OH})_2$ particles. This suggests that the $\text{Mg}(\text{OH})_2$ is not participating in any reaction with the slag chemistry, and is merely acting as a filler or site for nucleation for a C-(N-)A-S-H gel.



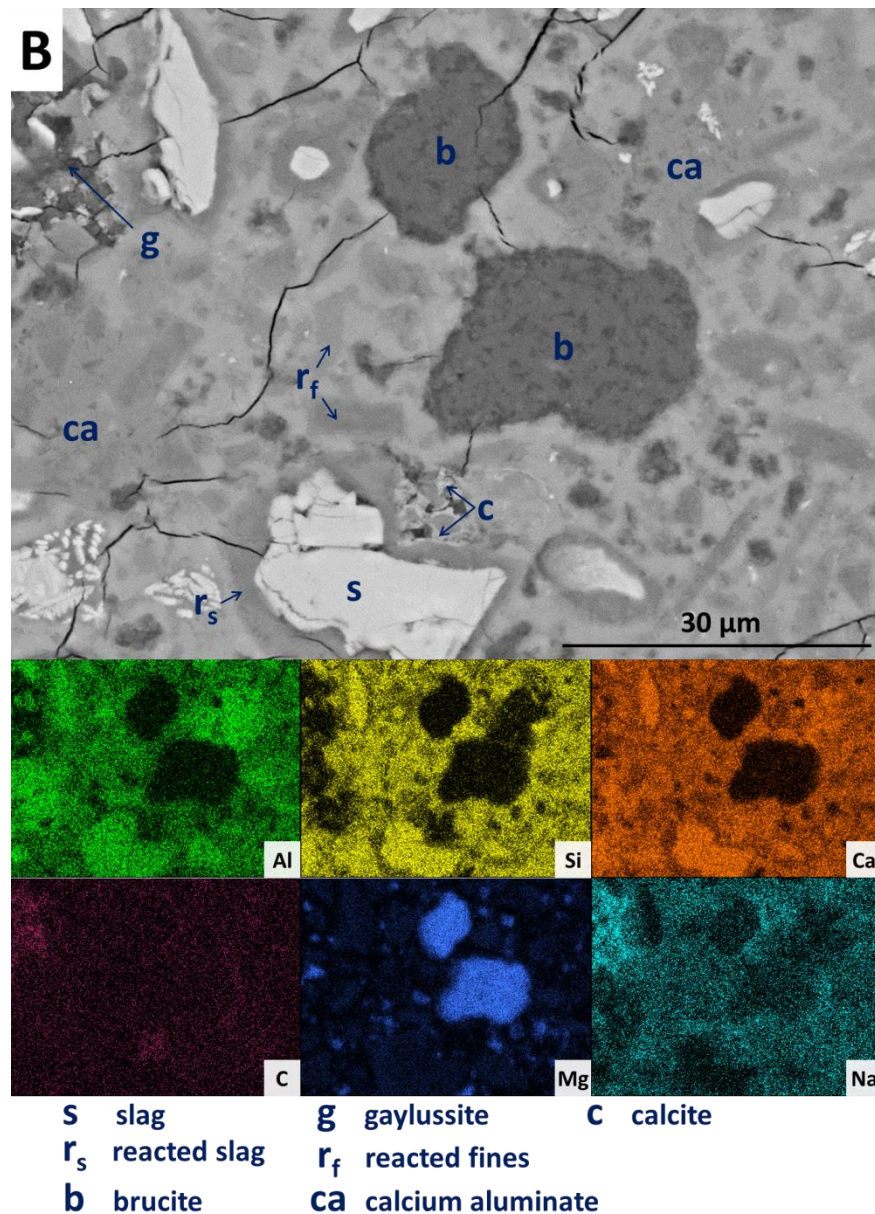
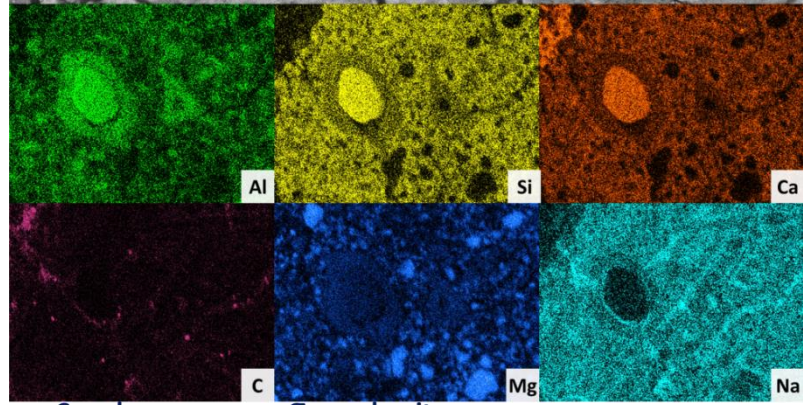
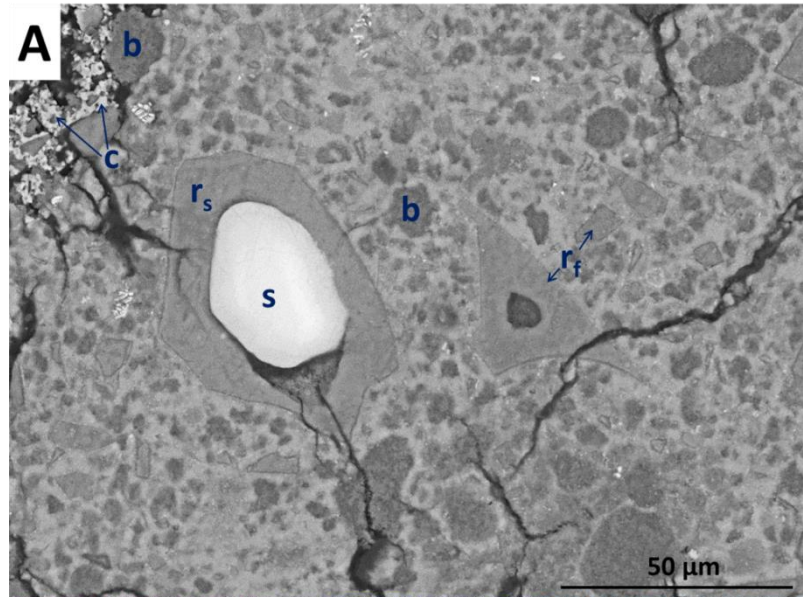


Figure 8.11. Backscattered electron micrograph and corresponding EDX maps of a sodium carbonate activated slag with 10 wt.% $\text{Mg}(\text{OH})_2$ addition (both A & B) after 18 months of curing

Increasing the level of replacement of GGBS with $\text{Mg}(\text{OH})_2$ further (30 wt.%, sample M30) resulted in a substantial change in the microstructure of the hardened cement paste, and an increased tendency to cracking and desiccation during sample preparation for electron microscopy. In M30 (Figure 8.12), little unreacted slag remained (s), and that which is left is surrounded by large reaction rims (r_s), which were higher in Mg and Al than the bulk matrix. Significant amounts of finely

dispersed $\text{Mg}(\text{OH})_2$ particles (b) are observed embedded throughout the matrix. As in Figure 8.11, these particles appear to be unreacted, with no transition region or visible reaction rims that could indicate dissolution. The XRD analysis (Figure 8.4B) suggested the presence of increased amounts of calcite in this mix compared with those with lower $\text{Mg}(\text{OH})_2$ contents. Consistent results are observed here, where large clusters of calcite (c) are identified, instead of the gaylussite, as previously observed in the specimens with reduced $\text{Mg}(\text{OH})_2$ contents. Interestingly, like the gaylussite, calcite is largely confined to large clusters rather than more uniformly distributed throughout the sample. It is, however, also present as minor clusters associated with the CO_2 -AFm phase, in Figure 8.12(B). This micrograph shows the extensive formation of CO_2 -AFm (highlighted by the dashed regions) in three locations. This is easily identifiable by a very strong content of Ca and Al within the EDX map for this region. Once again, this phase was clustered rather than diffuse throughout the sample.



s slag **g** gaylussite **c** calcite
r_s reacted slag **r_f** reacted fines
b brucite **ca** calcium aluminate

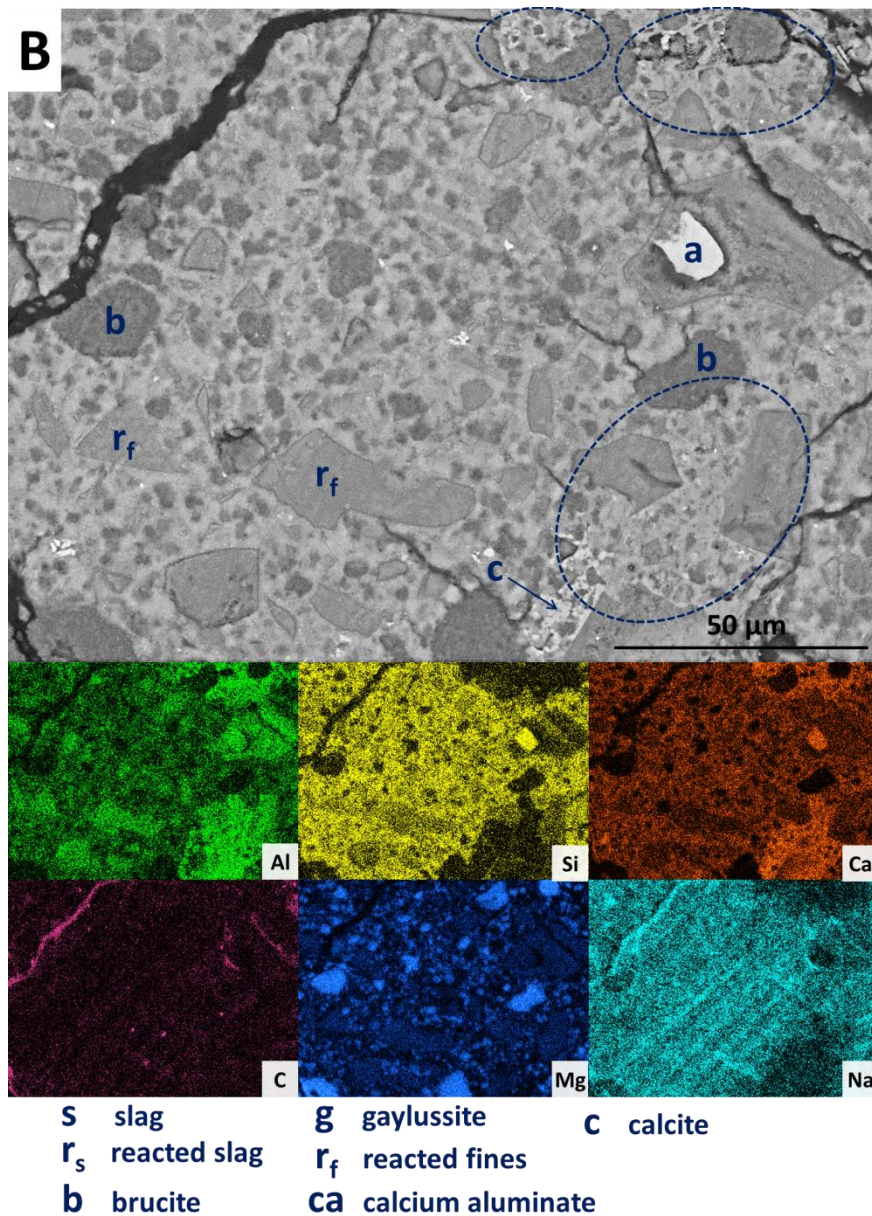
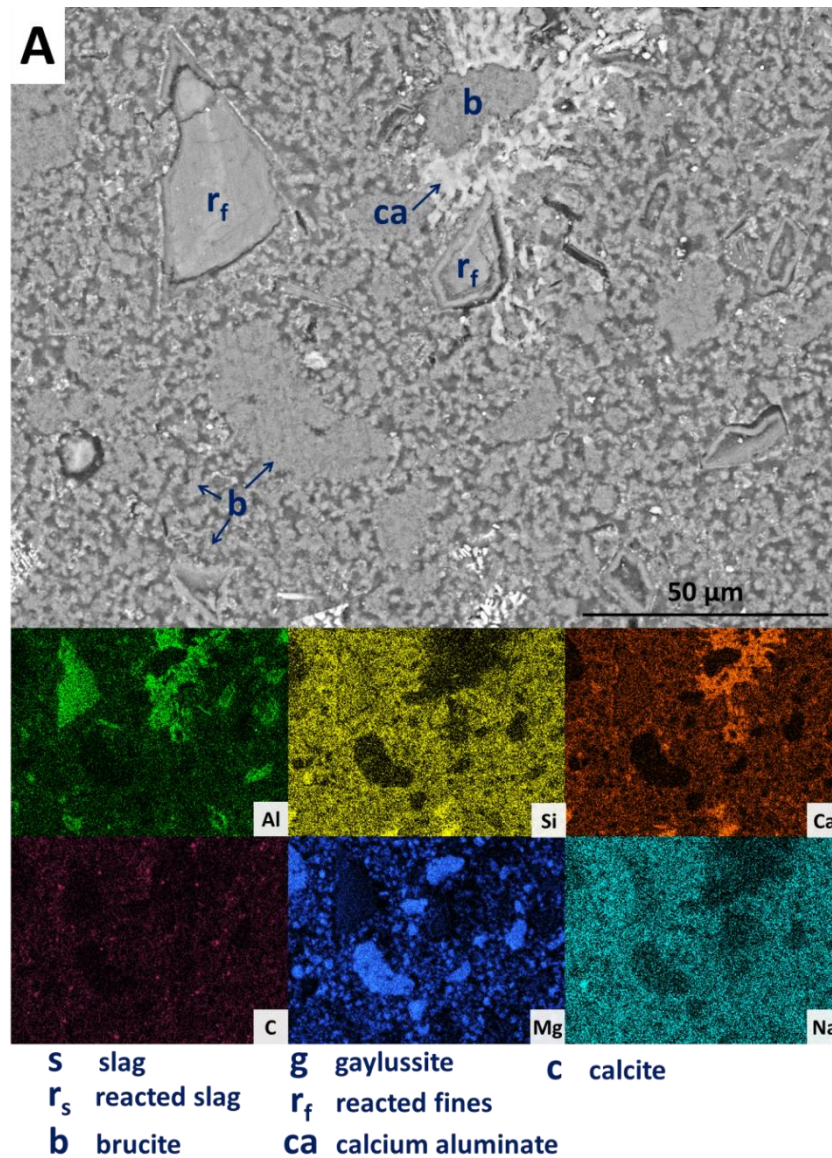


Figure 8.12. Backscattered electron micrograph and corresponding EDX maps of a sodium carbonate activated slag with 30 wt.% $\text{Mg}(\text{OH})_2$ addition (both A & B) after 18 months of curing

The replacement of 50% of the GGBS with $\text{Mg}(\text{OH})_2$ (M50) further changes the physical morphology of the sample. No slag grains were identified in Figs. 8.13A and B, having undergone full dissolution and leaving large reaction regions (r_f) that were enriched in Mg and Al. These appeared to have developed a secondary reaction rim, which was deficient in Si and Ca relative to both the bulk and interior of the reaction regions. This was further encircled by a thin layer of calcite (c) on some of

the reaction regions. $\text{Mg}(\text{OH})_2$ (b) was dispersed throughout the sample, both as large clumps and smaller particles, commensurate with such a large replacement level within this sample. A distinct MCA growth (ca) can be observed in Figure 8.13A, which appeared to be growing around one of the $\text{Mg}(\text{OH})_2$ particles, though no reaction region is identified. The MCA phase appeared brighter in greyscale value in this micrograph than in previous samples, but this was likely a contrast effect due to the high $\text{Mg}(\text{OH})_2$ content and lack of unreacted slag, which typically appeared lighter. Looking at a wider section of the sample in Figure 8.13B, the morphology was quite different from that of previous samples. Very large clusters of calcite (c) were present, along with fine speckles of calcite distributed throughout.



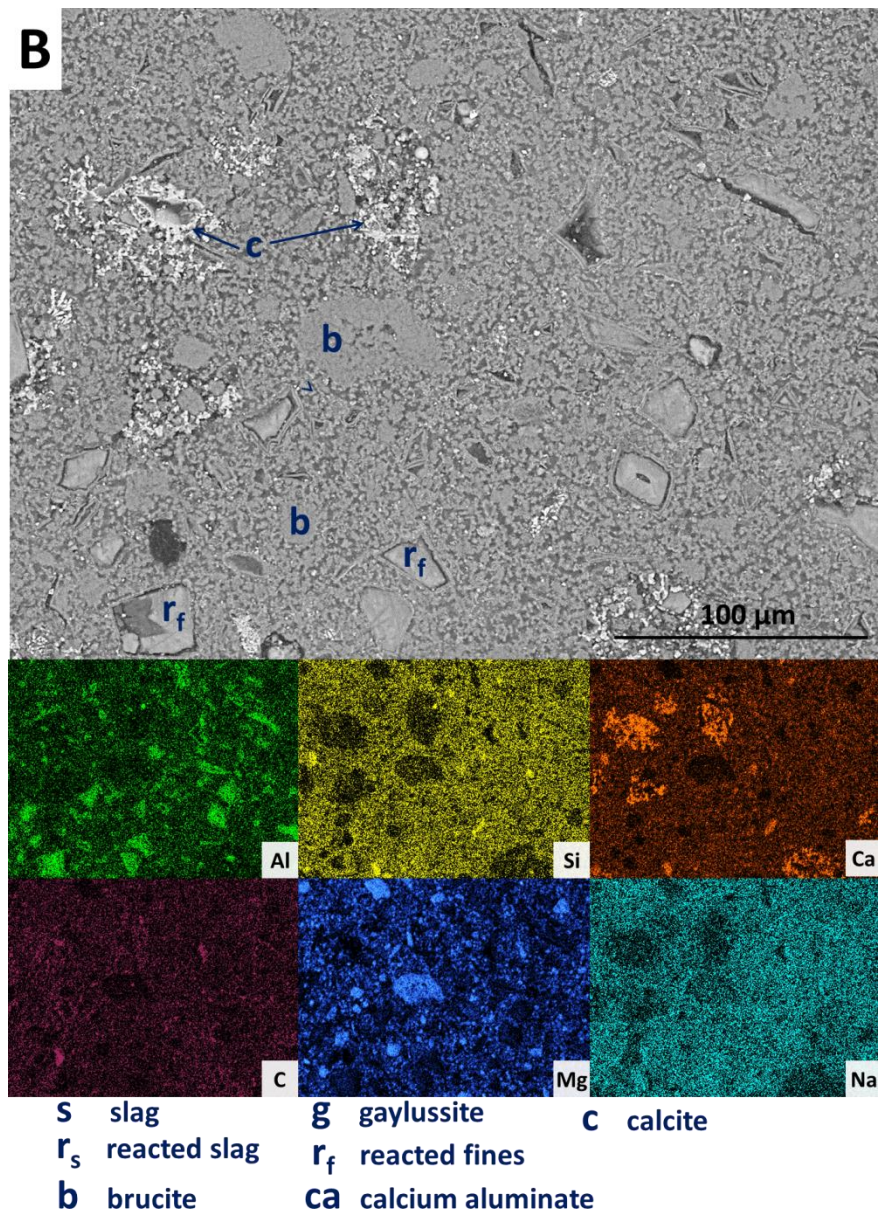


Figure 8.13. Backscattered electron micrograph and corresponding EDX maps of a sodium carbonate activated slag with 50 wt.% $\text{Mg}(\text{OH})_2$ addition after 18 months of curing

Looking more closely at one of the reacted slag particles, Figure 8.14, (r_f) distinct multiple reaction rims (r_o) were observed. The inner reaction rim (r_f) was similar in Si, Ca and Na contributions to the bulk matrix, although it appeared enriched in Mg and Al. This is likely indicating formation of a C-(N-)-A-S-H gel was intermixed with a MA-OH-LDH phase. The next reaction rim has a lower density darkened ring deficient in most elements, followed by another ring (r_o) enriched in only Al and Mg

alone, which is suggestive of the presence of the MA-OH-LDH phase only. This was also observed in several reacted slag regions throughout the sample. Both (r_o) sites highlighted also exhibit thin calcite (c) deposits around the outer rings, similar to those identified in existing literature on aged slag concrete [674].

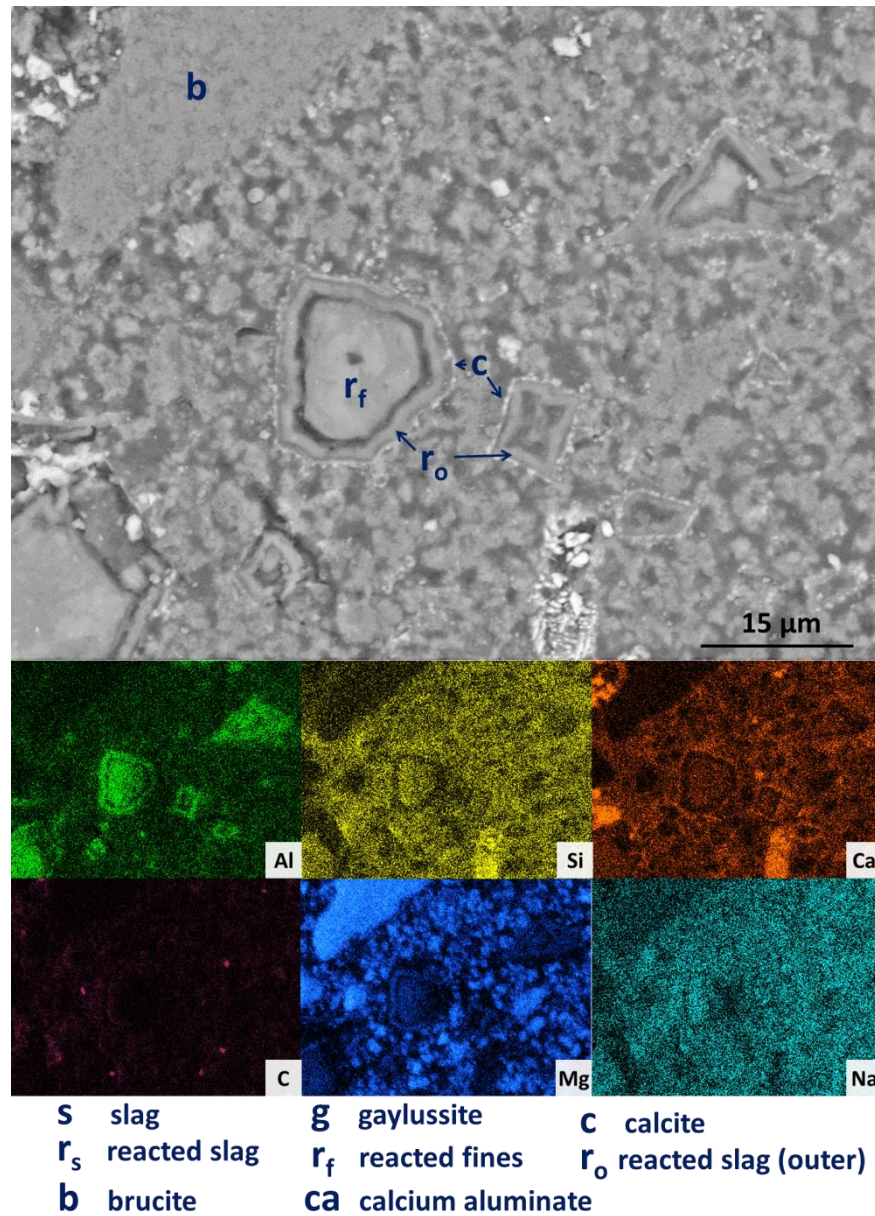


Figure 8.14. High magnification backscattered electron micrograph and corresponding EDX maps of a sodium carbonate activated slag with 50 wt.% Mg(OH)₂ addition after 18 months curing

A large $\text{Mg}(\text{OH})_2$ particle marked (b) in Figure 8.14 was singled out for observation, where the distributions of Ca, Si, Al and Na all reached up to the particle edge, indicative of this particle being embedded directly within a C-(N-)A-S-H gel. There was no preferential accumulation of Al along the particle edge, which would point towards the formation of a hydrotalcite-like phase. It was expected that any M-S-H formation would lead to Ca/Mg competition for the Si, leading to regions rich in Mg and Si only, to the exclusion of Ca. However, as no regions corresponding to this chemistry were identified along the edge of this $\text{Mg}(\text{OH})_2$ particle, it can therefore be concluded that the bulk $\text{Mg}(\text{OH})_2$ did not react to a significant extent within this system, and furthermore, the Mg source for the hydrotalcite-like phase identified *via* XRD analysis (Figure 8.3) was from within the slag (MgO content = 8.4 wt. % as determined by XRF analysis, Table 4.1).

8.4.2.5 Effect of $\text{Mg}(\text{OH})_2$ replacement on the chemical composition of the main reaction products forming in sodium carbonate activated slag cements

Spot EDX measurements were taken throughout the bulk matrix, reaction rims and the MCA phase to further understand the chemistries involved in these cements with different contents of $\text{Mg}(\text{OH})_2$.

Table 8.4 details the average atomic ratios for the spot EDX measurements conducted on these distinct features (rim, bulk, inner rim and outer rim) throughout all the samples after 18 months curing. The Ca/Si ratio of the bulk remained fairly similar between samples M0 – M50, ranging from 1.09 to 1.22, all within one standard deviation of one another. This is a typical Ca/Si ratio for sodium carbonate activated slags [648], though higher than typically identified in sodium silicate activated binders [675]. The same Ca/Si ratio was present in the reaction rim featured in all of the samples studied, lending credence to the identification of these as being intermixed MA-OH-LDH and C-(N-)A-S-H regions, while the bulk was largely a C-(N-)A-S-H gel, with some MA-OH-LDH present.

Table 8.4 Average EDX spot map atomic ratios after 18 months of curing

		Ca/Si	Mg/Si	Ca/Al	Mg/Al	Al/Si	Ca/Mg	Na/Si
M0	Rim	1.13	0.47	2.36	0.95	0.49	2.50	0.44
	SD	0.18	0.10	0.54	0.11	0.06	0.60	0.13
	Bulk	1.09	0.17	3.50	0.53	0.31	7.05	0.45
	SD	0.15	0.05	0.62	0.11	0.03	2.39	0.09
M10	Rim	1.10	0.82	1.82	1.33	0.61	1.37	0.50
	SD	0.19	0.13	0.33	0.10	0.07	0.27	0.14
	Bulk	1.11	0.28	3.60	0.89	0.31	4.31	0.45
	SD	0.18	0.09	0.69	0.24	0.03	1.24	0.08
M30	Rim	1.12	1.47	1.48	1.92	0.77	0.77	1.30
	SD	0.20	0.15	0.31	0.10	0.07	0.15	0.24
	Bulk	1.09	0.47	4.07	1.74	0.27	2.52	0.97
	SD	0.17	0.15	0.83	0.57	0.02	0.85	0.19
M50	Inner Rim (r_f)	1.16	2.45	1.15	2.41	1.02	0.48	1.35
	SD	0.17	0.20	0.20	0.18	0.09	0.07	0.23
	Outer Rim (r_o)	1.19	4.95	0.73	2.88	1.74	0.25	1.55
	SD	0.24	1.19	0.21	0.23	0.49	0.06	0.18
	Bulk	1.22	2.22	4.21	7.69	0.29	0.59	1.27
	SD	0.22	0.52	0.93	2.11	0.03	0.19	0.23

The Al/Si values of the rims were consistently higher than the bulk (up to 1.74 for sample M50), which also correlated with a higher Mg/Al ratio present in all of the reaction rims, with the exception of M50 where the Mg/Al ratio was 7.69. It is postulated that the bulk spot maps included Mg(OH)₂ particles due to their being finely dispersed throughout the microstructure in this sample. The higher Al/Si ratio confirms the preferential Mg-Al LDH formation within the slag reaction rims, as previously postulated in the EDX maps.

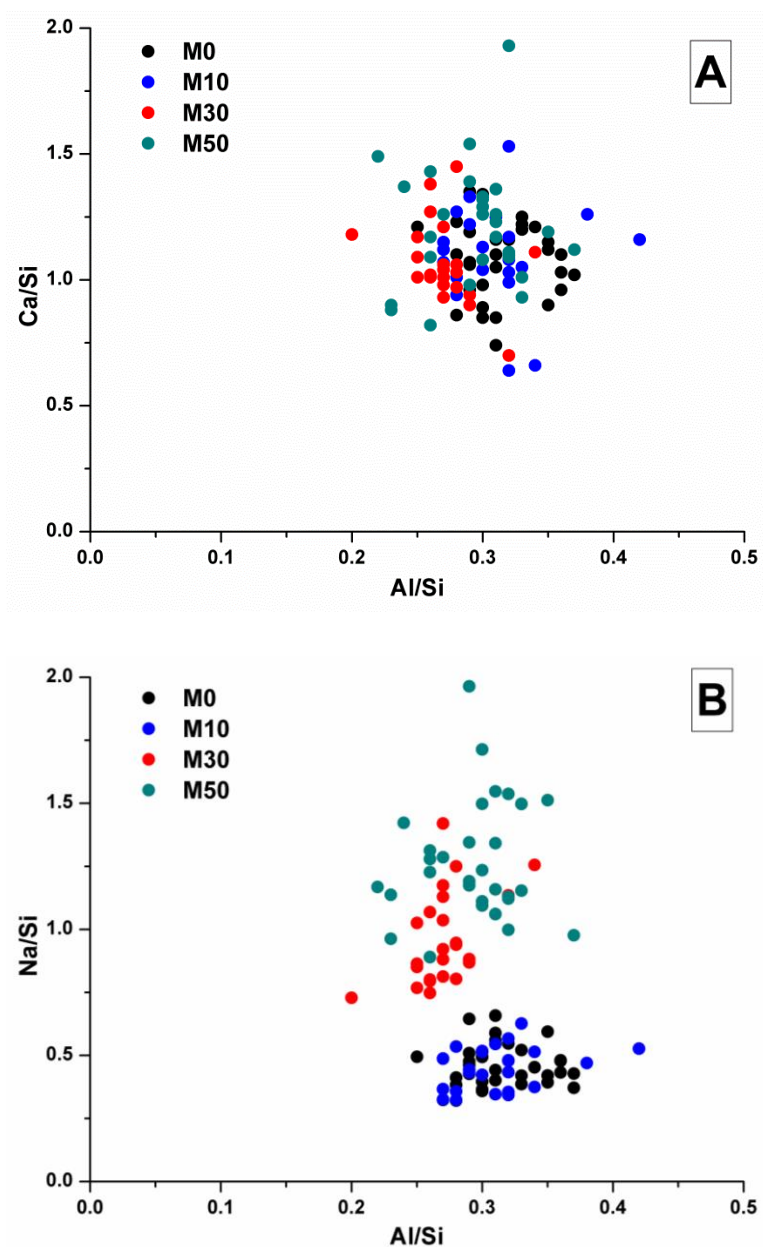


Figure 8.15. Plots of EDX spot map atomic ratios comparing (A) Ca/Si v Al/Si and (B) Na/Si v Al/Si in the bulk matrix

Figure 8.15A depicts the Ca/Si v Al/Si atomic ratios of the bulk in all the samples. There is considerable scatter between the individual points, however there is no discernible difference between any of the samples, suggesting that the overall bulk gel composition does not change significantly in terms of these elements as $\text{Mg}(\text{OH})_2$ is added into the system. This does not, however, mean that no changes are occurring. Figure 8.15B shows the Na/Si v Al/Si compositions for the bulk, noting a

distinct increase in Na/Si ratios when 30% and 50% Mg(OH)₂ is added into the samples. This raises the possibility of increased charge compensation by alkalis within a C-(N-)A-S-H gel, leading to structural changes, or the potential formation of a co-precipitated N-A-S-H gel. Neither of these would be easily determined *via* bulk EDX analysis, but might be elucidated *via* NMR analysis.

The Al/Si values of the bulk for samples M0 – M50 were very close, at 0.27-0.31. Though this is high for a C-(N-)A-S-H gel, the true Al/Si ratio of the C-A-S-H gel is likely to be 0.21 (as determined below, in Figure 8.16). It is postulated that the nature of this gel is likely to change as a result of the increased Na/Si ratio associated with the Mg(OH)₂ replacement level (and subsequently Na₂O eq. %) was increased. The average Na/Si ratio in the bulk for M0 and M10 was 0.45, and rose to 0.97-1.27 in the M30-M50 samples, respectively. Due to the significant quantity of Na₂CO₃ used relative to the GGBS in the higher Mg(OH)₂ formulations M30 and M50 (9.75 and 14.62 % Na₂O eq. respectively), and the relatively even distribution of Na throughout the bulk and reaction rims (as shown on the EDX maps), there is the potential for the additional formation of a N-A-S-H gel, although much of this is likely due to Na left behind through drying of pore solution.

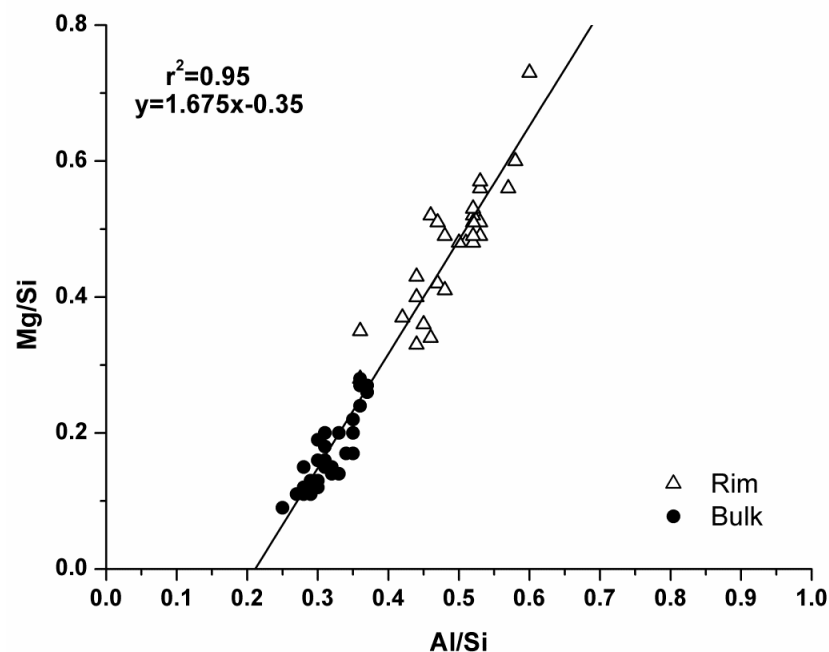


Figure 8.16. Plot of EDX spot map atomic ratios, correlating Mg/Si vs. Al/Si ratios of an 18 month cured sample with no added Mg(OH)₂ (M0)

The compositional change within the bulk is further complicated by the formation of the magnesium-rich layered double hydroxide-type phase within the samples. Although this has been noted to mainly precipitate in rims surrounding GGBS particles (or in the remnants of dissolved particles), analysis of the Mg/Si v Al/Si spot maps plotted in Figure 8.16 for M0 shows evidence of some formation within the bulk as well. This sample has no added Mg(OH)₂, with all Mg coming from the slag. There is a distinct positive correlation between Mg and Al, indicative of LDH formation in this sample, in both the bulk and the rim. Linear regression of these data leaves an Al/Si ratio in the C-(N-)A-S-H gel (the x-axis intercept) of 0.21, and a Mg/Al ratio within the MA-OH-LDH phase of 1.68. This is a lower Mg/Al ratio than typically found in activated GGBS pastes [649, 676], suggesting more Al might have formed a MA-OH-LDH phase, with less contributing to cross-linking C-S-H gels than is typical [672]. Performing the same calculations for samples with Mg(OH)₂ addition was not possible, as not all of the Mg detected could be assigned to a hydrotalcite-like phase due to fine dispersion of Mg(OH)₂ throughout the samples due to the high powder fineness.

Figure 8.17 shows the Mg/Si v Al/Si ratios for the bulk and rim EDX points in samples M0 – M50, along with the MCA data points for M0 as a comparison. Overall it was found that the Mg content of both the bulk and the reaction rim increased due to interference from Mg(OH)₂ particles present throughout the sample, which caused the bulk to appear rich in Mg, and also the reaction rim appear to have a higher Mg/Al ratio than was true. Interestingly, the outer rim within the M50 sample had a much higher Mg/Al ratio than the reacted slag rims in M50. This mirrors the observations in the EDX maps, which suggested this is almost completely an Mg-Al LDH phase, rather than a mix of C-(N-)A-S-H and MA-OH-LDH as was the case within the inner reaction rims, and the slag rims observed in the other samples.

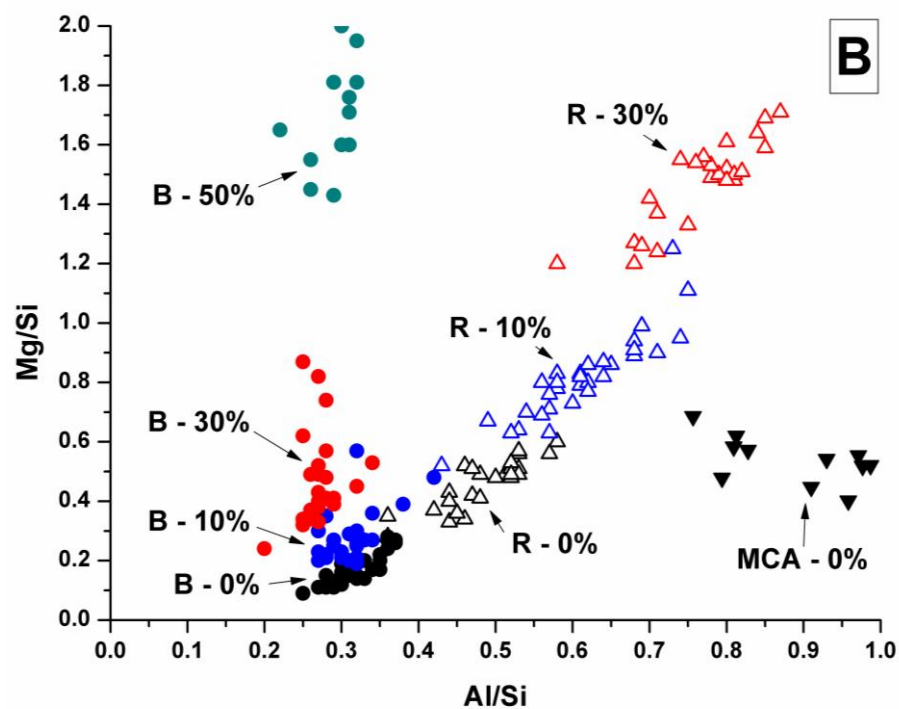
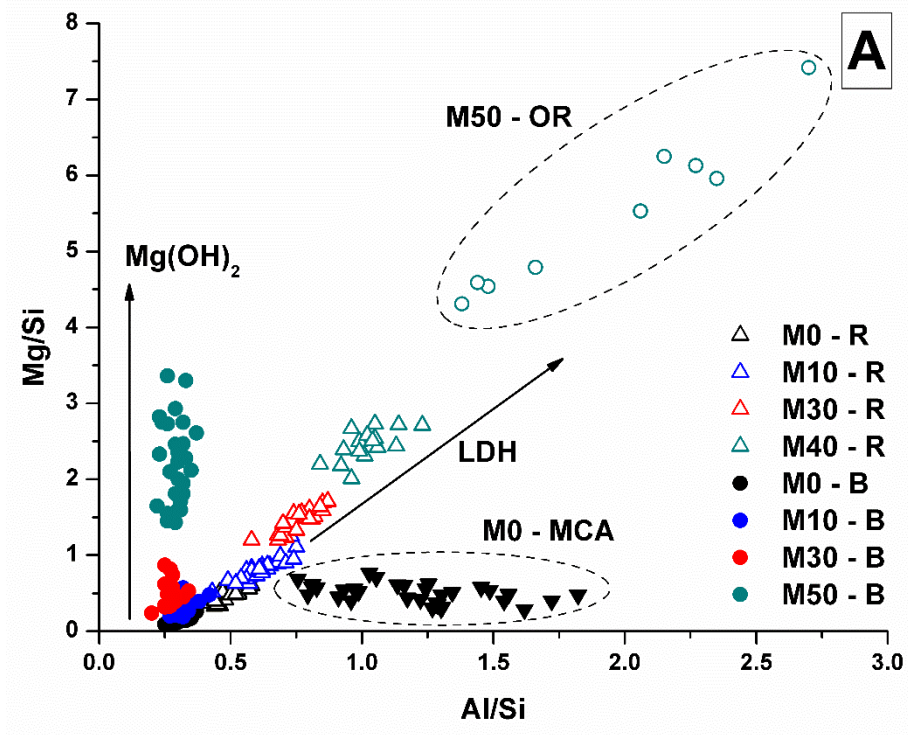


Figure 8.17. Plots of EDX spot map atomic ratios, comparing Mg/Si v Al/Si of 18 month samples with up to 50% Mg(OH)₂. (A) Full plot, (B) Enlarged region for clarity. Abbreviations used: *B* = Bulk, *R* = Rim, *OR* = Outer rim [*r*_o], *MCA* = Monocarboaluminate (CO₂-AFm), *LDH* = Layered double hydroxide

The formation of an additional AFm type phase, sometimes identified as C_4AH_{13} or C_2ASH_8 (strätlingite) has been observed in some other studies of alkali activated materials [672-673] as a platy-like material and was recently predicted by Myers, *et al.* [656] within sodium carbonate activated slag systems to exist as a monocarbonate $C_4\hat{A}CH_{11}$.

The atomic ratio correlations for Ca/Si vs Al/Si associated with the CO_2 -AFm regions identified in each sample (Figure 8.18), highlight the distinct correlation between Ca and Al across all of the samples. The mean Ca/Al ratio for M0 was 3.03, which decreased to 2.4-2.5 in the remaining samples. This overall Ca/Al ratio of M0 was higher than that required for the formation of $C_4\hat{A}CH_{11}$. This is highly likely the result of a higher intermixing with a C-(N-)A-S-H gel in M0, as evidenced by the lower Al/Si ratio (1.19) in M0 (Table 8.5), as there should be no Si within the CO_2 -AFm structure postulated here (although Si containing AFm phases do exist, such as C_2ASH_8).

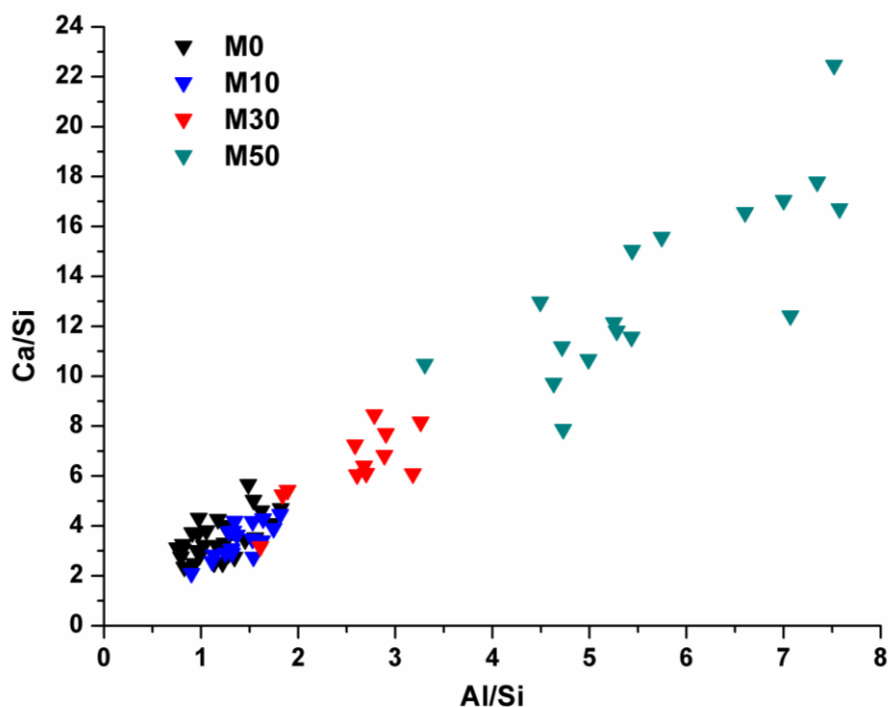


Figure 8.18. Plot of EDX spot map atomic ratios, comparing Ca/Si v Al/Si for CO_2 -AFm phases from each sample

Table 8.5 Average EDX spot map atomic ratios for CO₂-AFm in each sample

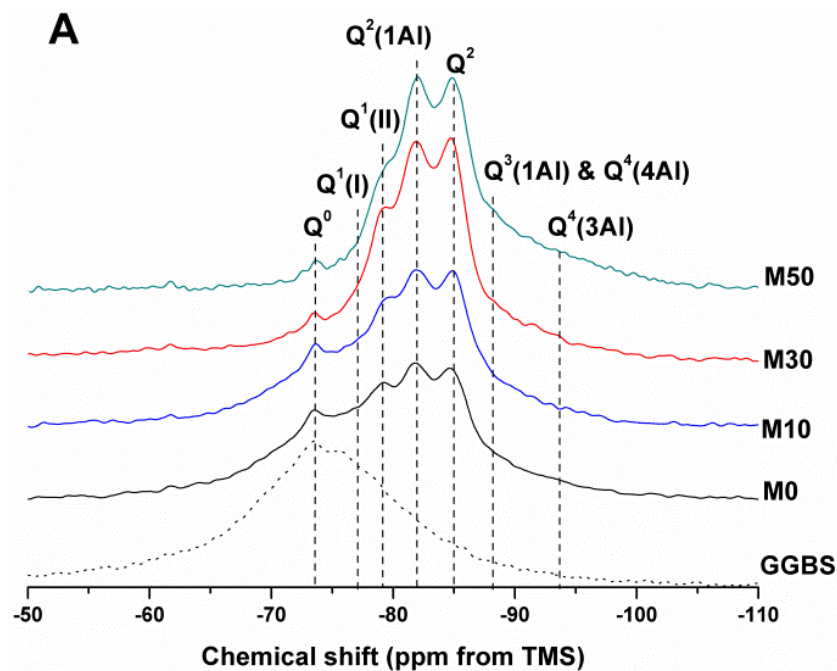
	Ca/Si	Ca/Al	Al/Si
M0	3.52	3.03	1.19
<i>SD</i>	<i>0.77</i>	<i>0.66</i>	<i>0.28</i>
M10	3.40	2.43	1.41
<i>SD</i>	<i>0.63</i>	<i>0.31</i>	<i>0.23</i>
M30	6.40	2.49	2.58
<i>SD</i>	<i>1.38</i>	<i>0.34</i>	<i>0.50</i>
M50	13.65	2.40	5.71
<i>SD</i>	<i>3.56</i>	<i>0.40</i>	<i>1.22</i>

8.4.2.6 Solid State Nuclear Magnetic Resonance spectroscopy

²⁹Si and ²⁷Al MAS NMR spectra (normalised to integrated area) of 18 months cured samples with different contents of Mg(OH)₂ are displayed in Figure 8.19, alongside with the spectrum of unreacted GGBS for reference. The potential incomplete dissolution of slag glass in sodium carbonate slag activated pastes hinders detailed deconvolution of the ²⁹Si MAS NMR spectra. However, no residual slag was detected in the SEM analysis for the M50 sample (Figs. 8.13 and 8.14), and as such this spectrum was deconvoluted (Figure 8.20) and the resultant peak positions were used as the basis for interpreting the remaining spectra.

The ²⁹Si MAS NMR spectrum for sample M50 (Figure 8.20) was deconvoluted following, where possible, the peak assignments previously determined by Myers, et al. [655] for alkali activated slag binders, interpreting this structure as mixed C-N-A-S-H/N-A-S-H type gels. The data presented show features typical of an alkali activated slag cement and strong similarities to those activated with both waterglass and sodium carbonate activators, although a higher degree of cross-linking was observed [644, 650, 677]. Four distinct peaks were readily identifiable within the ²⁹Si MAS NMR spectra (Figure 8.19A) assigned to Q⁰, Q¹(II), Q²(1Al) and Q² species, along with a broad resonance centred at -74ppm associated with residual slag. Other peaks and broad shoulders were inferred from the deconvolution in

Figure 8.20. The Q^1 region was split into two sites (-77.0 and -79.2 ppm), along the lines of Myers, *et al.* [655] who highlighted the potential existence of multiple Q^1 sites due to shielding by charge balancing Ca^{2+} , H^+ and Na^+ . In general, as GGBS is replaced by $Mg(OH)_2$, the broad resonance associated with the slag decreases in intensity. The proportion of $Q^2(1Al)$ to Q^2 sites appears to remain constant, though both sites increase in intensity. There is potentially a lower intensity of $Q^1(II)$ sites, though this overlaps with the broad slag region, making the absolute values difficult to determine. The continued development of the $Q^2(1Al)$ and Q^2 sites is commensurate with the formation of a cross-linked bulk gel and dissolution of the slag.



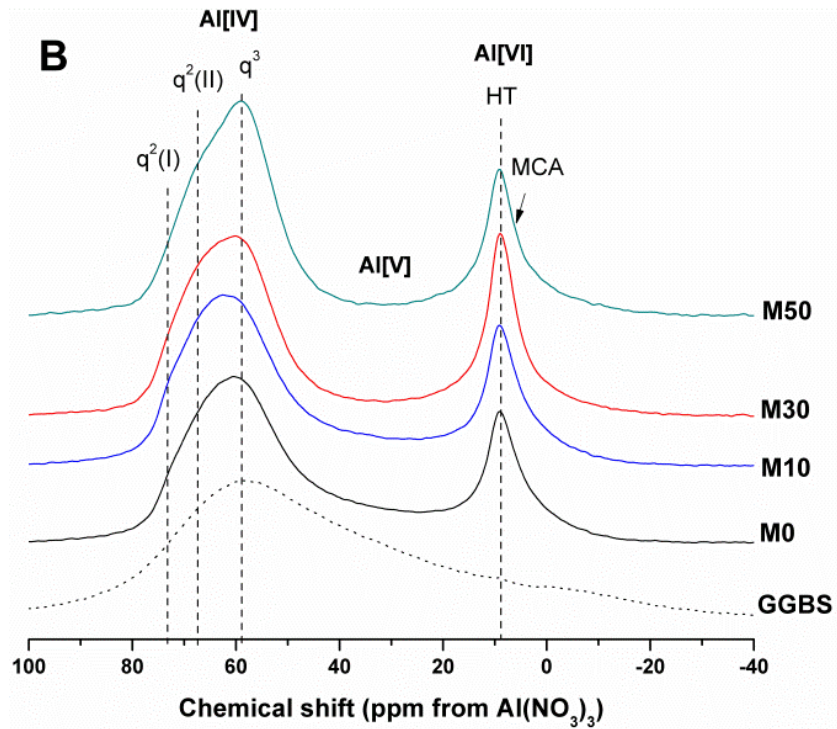


Figure 8.19. Solid state MAS NMR spectra of anhydrous GGBS and sodium carbonate activated slag binders after 18 months of curing, (A) ^{29}Si , (B) ^{27}Al

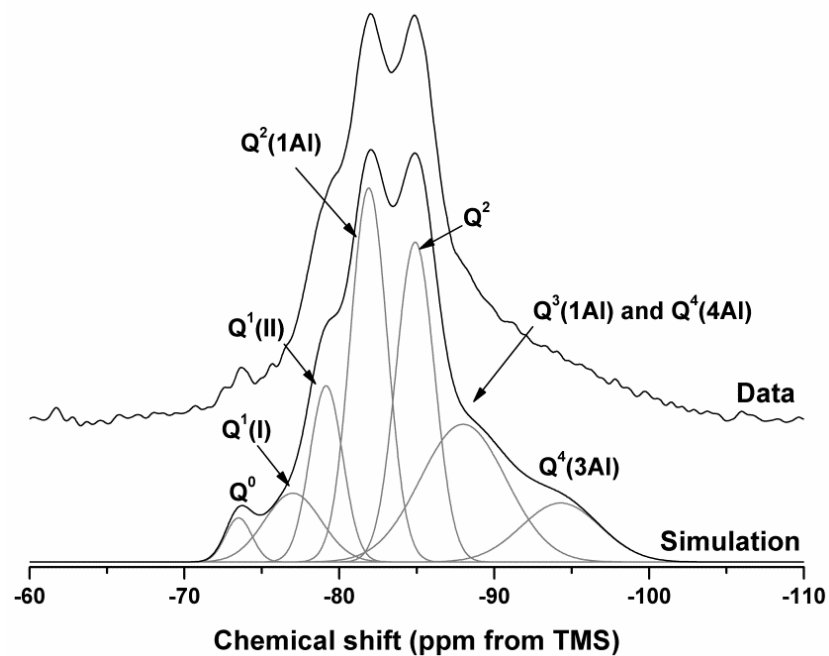


Figure 8.20. ^{29}Si MAS NMR spectrum for M50 after 18 months curing. Data are shown with simulation and constituent peaks underneath. Peak assignments detailed in Table 8.6.

The deconvoluted ^{29}Si MAS NMR spectrum for the paste with 50 wt.% $\text{Mg}(\text{OH})_2$ (Figure 8.20) had a lower proportion of $\text{Q}^1(\text{II})$ and $\text{Q}^2(1\text{Al})$, and larger Q^2 contribution than is typically identified for slag systems [650, 654, 677]. Although all the slag had reacted in sample M50, a minor Q^0 peak at -73.5 ppm remained, which was attributed to residual crystalline åkermanite [678] from the slag, which was also evident as a minor peak in all the other ^{29}Si MAS NMR spectra (Figure 8.19A). The $\text{Q}^2(1\text{Al})$ site was centred at -81.9 ppm, and the Q^2 site centred at -84.9 ppm. The reduced intensity for the $\text{Q}^2(1\text{Al})$ site indicated that the C-(N-)A-S-H gel contained a lower Al substitution than silicate-activated slag binders [650, 655]. This was consistent with the Al being incorporated into hydrotalcite-like and $\text{C}_4\text{A}\hat{\text{C}}\text{H}_{11}$ phases previously identified by XRD (Figure 8.4) and SEM analysis (Figure 8.13) respectively. The presence of an N-A-S-H-type gel is postulated due to the existence of sites upfield of the Q^2 site. The site at -88.0 ppm has been assigned to both $\text{Q}^3(1\text{Al})$ from cross linking within the C-(N-)A-S-H gel, and to a $\text{Q}^4(4\text{Al})$ site from a N-A-S-H type gel. This cannot arise from just a C-(N-)A-S-H gel alone, as the total contribution to the $\text{Q}^3(1\text{Al})$ site is much larger than is possible for a C-(N-)A-S-H gel (Table 8.5), which structurally can accommodate a maximum of 1 $\text{Q}^3(1\text{Al})$ per 4 $\text{Q}^2(0, 1\text{Al})$ sites [679]. Also due to the presence of a further site at -94.3 ppm, which is assigned to a $\text{Q}^4(3\text{Al})$ site, this provides strong evidence for there being a N-A-S-H gel contributing here to, as a $\text{Q}^4(4\text{Al})$ site.

Although this sample (M50) contained a substantial proportion of $\text{Mg}(\text{OH})_2$, there was no evidence of a $\text{Mg}(\text{OH})_2$ reaction to form additional magnesium phases, which is supported by the SEM analysis. One potential additional reaction which may be proposed to be taking place in this sample was the formation of an M-S-H type phase, with distinct resonances associated with M-S-H found between -86 and -89 ppm and between -93 and -98 ppm (depending on the M-S-H composition) [373, 393]. Although these are in the regions assigned to $\text{Q}^3(1\text{Al})/\text{Q}^4(4\text{Al})$ and $\text{Q}^4(3\text{Al})$, there was no evidence for the formation of these within X-ray diffraction analysis in Section 8.4.2.1, and as such have not been assigned here.

Table 8.6 Peak positions and widths (ppm) for deconvolution of ^{29}Si MAS NMR data (M50 – at 18 months) [Intensity as % area of integrated total fit]

	Q^0	$Q^1(\text{I})$	$Q^1(\text{II})$	$Q^2(1\text{Al})$	Q^2	$Q^3(1\text{Al}) / Q^4(4\text{Al})$	$Q^4(3\text{Al})$
Intensity (%)	2.2	7.3	10.9	25.9	22.9	22.1	8.7
Centre	-73.5	-77.0	-79.2	-81.9	-84.9	-88.0	-94.3
FWHM	2.0	4.3	2.5	2.8	2.9	6.5	6.0

The results from the ^{27}Al MAS NMR are split into Al[IV], Al[V] and Al[VI] regions, as noted in Figure 8.19B. The Al[IV] region contained Al resonances from the unreacted glassy slag, along with the cross linking Al sites within the C-(N-)A-S-H gel, which combined formed a broad region centred ~60 ppm. Within the Al[IV] region, the regions have been tentatively designated as distinct q sites, denoting connectivity much along the lines of Si. Considering the results of Myers, *et al.* [655] for sodium silicate activated slag cements, two q^2 sites have been observed, corresponding to Al sites in a C-(N-)A-S-H gel. The $q^2(\text{I})$ site ~74 ppm has been reported as being the Al in bridging positions linked to $Q^2(1\text{Al})$ silicon environments within a C-(N-)A-S-H gel, typically exhibiting a sharp peak [654], which is not clearly evident within these samples. This is concurrent with a reduced prominence of the $Q^2(1\text{Al})$ site within these samples compared to existing literature. The q^3 site (bridging crosslink site in C-A-S-H) is particularly prominent within these samples, also containing q^4 sites (in N-A-S-H) too. This fits with the identification of $Q^4(4\text{Al})$ and $Q^4(3\text{Al})$ sites within the ^{29}Si MAS NMR spectra.

The Al[V] region only consists of a minor Al environment within the region ~45-20 ppm, which resulted from within the glassy slag fraction, which correspondingly disappeared in samples with higher contents of $\text{Mg}(\text{OH})_2$ replacement (M30 and M50) as the slag underwent reaction.

The Al[VI] region is only represented by a single broad resonance at 8 and 9 ppm, whereas this resonance was likely associated with a combination of MA-OH-LDH hydrotalcite-like component and the hydrated calcium aluminate (postulated $\text{C}_4\text{A}\hat{\text{C}}\text{H}_{11}$) phase [680-681], which have similar chemical shifts. This made further

elucidation of this region difficult, but was supported by the identification of both phases in the XRD and SEM/EDX analysis.

The NMR analysis here demonstrates a highly cross-linked C-(N-)A-S-H gel, N-A-S-H gel and formation of MA-OH-LDH and CO₂-AFM phases. This is a complex system, with many phases formed which have the potential to immobilise or retain radionuclides of concern. None of these appear to have undergone any reaction or ionic substitution with Mg from Mg(OH)₂ which was added into this system. There is ultimately little evidence for the formation of a M-S-H or M-A-S-H gel from this NMR either, which combined with earlier XRD and SEM analysis, is highly suggesting of encapsulation of Mg(OH)₂ rather than reaction.

8.5 Conclusions

8.5.1 Scientific findings

This chapter has highlighted the hydration mechanisms of sodium carbonate activated slags, both with and without the addition of Mg(OH)₂. A C-(N-)A-S-H/N-A-S-H assemblage, a hydrotalcite-like compound and a calcium aluminate phase were the major hydration products identified in all samples, with calcite increasingly formed as the slag was replaced by Mg(OH)₂. The hydrotalcite-like compound was identified as a carbonate-free layered double hydroxide, postulated to contain OH⁻ interlayer anions. This is in contrast to that which may be intuitively expected for a sodium carbonate activated slag, but is in line with recent thermodynamic modelling for similar systems. Carbonate appears to be sequestered initially within gaylussite, which progressively dissolves and converts to calcite over time, which largely forms as clusters.

The added Mg(OH)₂ appeared only to act as a filler and nucleating medium, reducing the time taken for major strength forming phases to form, while undergoing little to no further reaction with any other components within the system. No magnesium bearing phases were identified around the Mg(OH)₂ particles, suggesting they acted as a nucleating feature primarily for C-(N-)A-S-H/N-A-S-H gels.

In addition to the phases already described, a calcium aluminate phase was prevalent throughout the samples, including that without any $\text{Mg}(\text{OH})_2$ addition. This was postulated to be $\text{C}_4\text{A}\hat{\text{C}}\text{H}_{11}$ from EDX measurements, and in line with recent thermodynamic modelling. The formation of this phase was difficult to elucidate *via* XRD or NMR analysis due to overlap with other phases. This highlights the importance of undertaking detailed EDX mapping of polished samples as part of a multi-instrumental phase identification process.

8.5.2 Industrial application

Overall, a sodium carbonate activated slag matrix would appear to be suitable for the encapsulation of Magnox sludge. Little if any reaction would occur between the $\text{Mg}(\text{OH})_2$ bearing waste material and the cementitious matrix. The release of the heat of reaction is accelerated when adding $\text{Mg}(\text{OH})_2$, though this does not increase the cumulative heat of reaction above that found in $\text{Mg}(\text{OH})_2$ -free samples. The slow hydration of these samples means they can be safely processed without risk of thermal runaway or heat of hydration induced cracking in larger samples. That these cements are not dependent on $\text{Mg}(\text{OH})_2$ reaction to form solid products means that Magnox sludge characterisation and reactivity control would not be as crucial as with M-S-H or mixed zeolite-hydrotalcite cements previously described. The samples also achieved a suitable strength, and remained stable over an 18 month period. These are likely to remain stable over longer timeframes, due to the cementitious phases formed in this system and in line with our knowledge of aged alkali activated cements.

9 Conclusions

Throughout this thesis the overarching aim has been the incorporation of $\text{Mg}(\text{OH})_2$ within a binding cementitious matrix, with the aim of utilising this as a raw material for binder formation, while forming a stable and solid wasteform. This work has focussed primarily on understanding the chemical interactions and incorporation using controlled laboratory grade materials, rather than utilising a more physically realistic simulant Magnox sludge material. As this material consists largely of $\text{Mg}(\text{OH})_2$ and does not undergo reaction with Portland cement blends, forming a cementitious matrix from this material led towards a magnesium based cement system.

Chapter 2 began with a review of nuclear power and the nuclear industry within the UK context. This had its origins in the development of nuclear weapons post WWII, before moving to a fully civilian nuclear programme, largely operating indigenous reactor designs. First generation of nuclear power reactors in the UK were metallic uranium fuelled, clad with a magnesium alloy. Due to this unique design coupled with the decision to reprocess spent nuclear fuel, there resulted in a build-up of magnesium cladding, some of which corroded within various facilities into a $\text{Mg}(\text{OH})_2$ rich sludge. This is highly radioactive, and is currently in the process of being removed from some of these facilities to enable decommissioning. These sludges are highly heterogeneous in nature, with varying levels of $\text{Mg}(\text{OH})_2$, organic material, fuel and other miscellaneous components. It is currently planned to encapsulate these sludges in conventional Portland-cement based blend, which have extensive usage in intermediate level waste immobilisation. Other encapsulation techniques have been suggested for Magnox sludges, including vitrification and hot isostatic pressing, however none of these have been developed beyond a prototype stage. Immobilised wasteforms in the UK (both vitrified high-level waste, and cemented intermediate-level waste) will eventually be located within an engineered geological repository, to be built in the future, which will house the majority of the UK's higher activity wastes.

To determine whether immobilisation of a $\text{Mg}(\text{OH})_2$ rich sludge within an alternative cementitious system was possible, an extensive literature review was undertaken on magnesium based cements over the past 150 years. This revealed an extensive

wealth of literature, both scientific and patent, stretching over magnesium oxysalt, phosphate, silicate and carbonate cements. Several of these, such as oxychloride and magnesium ammonium phosphate cements have found historical or niche uses, exploiting locally available materials or specific properties to produce useful products. Magnesium chloride cements have almost completely ceased to be used, however magnesium phosphate still find use as rapid setting patch repair cements for roads and runways, and more recently as alternative encapsulation matrixes for reactive metallic wastes in the nuclear industry. Although some niche uses for these still exist, magnesium carbonate cements are currently the most studied of the magnesium cements (especially as potential low-carbon cements), followed by magnesium silicates, which are still very underdeveloped and the principal binding phase of which is poorly understood. With regards to waste immobilisation, this study has revealed few suitable candidate cement systems for investigation. Magnesium oxysalt cements are prone to deterioration in water, magnesium phosphate cements would react too violently and rapidly with fine $\text{Mg}(\text{OH})_2$ bearing material, and magnesium carbonate cements would require extensive carbonation and to be formed as porous blocks. None of these were suitable candidates for a waste immobilisation matrix, leaving the choice as magnesium silicate cements.

A systematic study of the potential to use $\text{Mg}(\text{OH})_2$ as a raw material for a hydrated magnesium silicate (M-S-H) cement was undertaken, detailed in Chapter 5. Although weaker and slower to form than produced *via* MgO , it was possible to make stable cements from $\text{Mg}(\text{OH})_2$ and a source of reactive silica (silica fume), provided that the system could be fluidised with a polyphosphate based dispersant. The effect of this dispersant on the characteristics, behaviour and morphology of the M-S-H system was analysed, ultimately determining that the dispersant mildly hindered M-S-H formation, but greatly increased fluidity, enabling a reduction in water content. Higher curing temperatures were found to assist in M-S-H formation, with 40 °C chosen as a compromise temperature between quicker formation and risk of desiccation. Using solid state ^{29}Si & ^{25}Mg NMR techniques the structure of the M-S-H binder itself was studied in detail. M-S-H formed here more closely resembled that of a poorly crystalline lizardite structure, but appeared to retain some features of talc due to a higher than expected Mg/Si ratio (0.95).

The setting characteristics of this M-S-H binder were, however, potentially too long to be incorporated into current cement plant operations. In Chapters 6 and 7 attempts were made to improve this *via* the production of an aluminosilicate scaffold through addition of NaAlO_2 , around which an M-S-H gel could grow, giving early strength but also binding Mg within a matrix. These Mg(OH)_2 - NaAlO_2 - SiO_2 - H_2O systems hardened, producing solid binders, however there was overall little to no reaction of the Mg(OH)_2 with any siliceous components within the cements. A range of zeolites were formed (although these can be damaged and ion exchange capacity reduced by radiation [682-684]), which may hold benefit regarding ion exchange for certain radionuclides, the composition of which varied depending on the overall Al/Si ratios within the binding materials. Within the binders containing the highest Al/Si ratios some Mg(OH)_2 reacted to form a hydroxide intercalated hydrotalcite-like material. Up to the 2 years period the samples were studied, at no point was there formation of a M-S-H or aluminium substituted M-A-S-H identified with any analytical technique, including ^{25}Mg NMR.

Although this attempted M-A-S-H system produced solid samples, the heat of dissolution of the raw materials is likely to hinder larger scale industrial usage, and the longer-term stability of these systems can be questioned due to their continued evolution. Despite this, the formation of a hydrotalcite-like material demonstrates the feasibility of chemically immobilising Magnox sludges within an aluminosilicate binder, with the option of forming varied zeolites depending on the formulations.

Chapter 8 followed an alternative line of inquiry, studying the immobilisation of Mg(OH)_2 within an alkali carbonate activated blast furnace slag cement. This was chosen due to the relative stability of a calcium-aluminosilicate system, relative to the unknown long-term behaviour of the M-S-H or Mg(OH)_2 -zeolite systems formulated in previous chapters. The availability of MgO within slag cements was known to affect the phases formed and rate of hydration. Adding Mg(OH)_2 into these systems reduced the time required for the major strength forming phases to form, potentially active as a nucleating medium, however it but did not appear to have a major impact upon the composition or structure of the cementitious phases themselves. Alterations in the binding phases were largely due to increasing slag reaction, and a higher proportion of carbonates to slag. This formed extensively cross-linked C-(N-)A-S-H and N-A-S-H gels, along with calcite, a hydrotalcite-like

material and a carbonated AFm phase, postulated to be $C_4A\hat{C}H_{11}$. The hydrotalcite-like phase formed within this system was found to be due to vitreous MgO, and highly unlikely to be from reaction with any $Mg(OH)_2$. Ultimately this wasteform was the most stable of all tested, with slow heat evolution and the formation of relatively well characterised phases, however there was no observable reaction with $Mg(OH)_2$, resulting in encapsulation only. This cement binder benefits from easy to handle precursor powders, and does not rely on the reaction of $Mg(OH)_2$, which would require extensive characterisation and potential homogenisation of any Magnox sludges prior to encapsulation.

The data presented within this thesis detail the complex, and still poorly understood nature of several Mg-based cement binders. This has specifically contributed towards our understanding of the nature of the M-S-H phase, showing for the first time ^{25}Mg solid state NMR data for this in relation to other important magnesium silicate minerals. The formation of the M-S-H phase appears to be pH dependent, not forming within a highly alkaline system containing $NaAlO_2$. This precluded the formation of a M-A-S-H phase within the conditions tested.

The potential for industrial waste encapsulation using the cements demonstrated here is a mixed affair. This work has established the difficulties in producing a solid cementitious system from a $Mg(OH)_2$ bearing sludge, even under controlled laboratory conditions. An M-S-H based system is the most promising magnesium based binder, able to form a solid monolith from a range of Mg:Si ratios, however this is ultimately highly dependent on being able to fully characterise sludges prior to using these as a raw material. Ultimately a sodium carbonate activated slag binder is potentially the most suitable for integrating into current processing, curing at ambient temperature and with slow heat evolution. This would not be reliant on a reactive sludge, and could be incorporated within existing cementitious facilities with relative ease.

Although the work presented here has demonstrated the feasibility of using $Mg(OH)_2$ as a precursor material for cementitious binder production, in order to advance the development of these further it is suggested to:

- Assess the feasibility of producing a M-S-H matrix using Magnox sludge simulants of varying particle sizes, water contents and reactivity to more

accurately determine the Sludge composition envelopes which could be utilised.

- Determine other dispersant for use in M-S-H cements, potentially superplasticisers and other organics which may have a greater water reduction potential, enhancing waste loading or producing a less porous, more durable wasteform.
- Assess the long-term durability of M-S-H within a high calcium environment to determine if the matrix is compatible with a cementitious repository over a long timeframe.
- Optimisation the formulation of a sodium-carbonate slag blend, potentially using a lower concentration of activator to produce a 'just add water' cement for industry.
- Further understand the formation conditions of M-S-H gels, particularly with regards to the effect of pH. The inability to form M-S-H within a highly alkaline system suggests pH dependence. This is particularly important to understand the conditions of stability for M-S-H for long-term durability, and ties into the understanding of this gel within a highly alkaline $\text{Ca}(\text{OH})_2$ rich simulated repository environment.
- Investigate radionuclide retention within these cements, and how they compare to conventional Portland cement blends over extended times.
- Determine how these might fare under radiation damage, given the highly activate nature of Magnox sludges.

10 References

- (1) Bodansky, D. *Nuclear Energy: Principles, Practices and Prospects*, 2nd ed.; Springer-Verlag: New York, NY, 2004.
- (2) Choppin, G.; Liljenzin, J.-O.; Rydberg, J. *Radiochemistry and Nuclear Chemistry*, Butterworth-Heinemann: Woburn, MA, 2002.
- (3) Ojovan, M. I.; Lee, W. E. *An Introduction to Nuclear Waste Immobilisation*, Elsevier: Oxford, 2005.
- (4) Lilley, J. *Nuclear Physics - Principles and Applications*, John Wiley & Sons, Ltd.: Chichester, UK, 2001.
- (5) Audi, G.; Bersillon, O.; Blachot, J.; Wapstra, A. H. The NUBASE evaluation of nuclear and decay properties. *Nuclear Physics A* **1997**, *624*, 1-124.
- (6) Loveland, W.; Morrissey, D. J.; Seaborg, G. T. *Modern Nuclear Chemistry*, John Wiley & Sons: Hoboken, NJ, 2006.
- (7) International Atomic Energy Agency (IAEA). *Nuclear power reactors in the world; Reference data series no. 2*; IAEA: Vienna, 2015;
- (8) World Nuclear Association (WNA). Nuclear power in Japan. (accessed 09/01/2016), 2015).
- (9) IAEA. *Nuclear Power Reactors in the World*; IAEA 2011;
- (10) United Kingdom Atomic Energy Authority (UKAEA). *Harwell project profiles: GLEEP Graphite Low Energy Experimental Pile*; UKAEA: n/d;
- (11) Nuclear Decommissioning Authority (NDA). *Strategy*; 2011;
- (12) NDA; DEFRA. *The 2007 UK Radioactive Waste Inventory: A Review of the Processes Contributing to Radioactive Wastes in the UK*; 2008;
- (13) Department of Energy and Climate Change (DECC). *Digest of UK energy statistics*; DECC: 2014;
- (14) Department of Energy and Climate Change (DECC). *Digest of UK energy statistics: Long-term trends*; DECC: 2012;
- (15) Sherry, A.; Howarth, P.; Kearns, P.; Waterman, N. *A Review of the UK's Nuclear R&D Capability*; Dalton Nuclear Institute, NNL, Battelle n.d.;
- (16) Emoscopes. Magnox reactor schematic. https://commons.wikimedia.org/wiki/File:Magnox_reactor_schematic.svg, 2007).
- (17) Nuclear Decommissioning Authority (NDA). *Waste stream 9B21: FED Magnox*; NDA: 2014;
- (18) Greenfield, P. A comparison of Magnox A 12 and ZA alloys as canning materials for nuclear reactors. *Journal of Nuclear Materials* **1964**, *11*, 121-134.
- (19) Tipping, P. G. Introduction to Nuclear Energy, and Materials and Operation Aspects of Nuclear Power Plants. In *Understanding and mitigating ageing in nuclear power plants: Materials and operation aspects of plant life management (PLIM)*, Tipping, P. G., Ed.; Woodhead Publishing Limited: Cambridge, UK, 2010.
- (20) Health and Safety Executive: HM Nuclear Installations Inspectorate. *Report of HM Nuclear Installations Inspectorate on the results of Magnox Long Term Safety Reviews (LTSRs) and Periodic Safety Reviews (PSRs)*; HSE: 2000;
- (21) NDA; North, M.; South, M.; Sellafield. *The Magnox Operating Programme (MOP8)*; NDA 2010;
- (22) Magnox. Wylfa. <https://magnoxsites.com/site/wylfa> (accessed 09/01/2016), 2015).

- (23) World Nuclear Association (WNA). Country Profiles. <http://www.world-nuclear.org/info/Country-Profiles/> (accessed 15/01/2016), 2015).
- (24) International Atomic Energy Agency (IAEA). Power Reactor Information System (PRIS) - United Kingdom. <http://www.iaea.org/PRIS/CountryStatistics/CountryDetails.aspx?current=GB> (accessed 15/05/2015), 2015).
- (25) EDF Energy. Our energy. www.edfenergy.com/energy (accessed 15/05/2015), 2015).
- (26) Magnox Limited. Maximising generation: Wylfa. www.magnoxsites.co.uk/site/wylfa (accessed 15/05/2015), 2015).
- (27) World Nuclear News. EDF Energy extends lives of UK AGR plants. <http://www.world-nuclear-news.org/C-EDF-Energy-extends-lives-of-UK-AGR-plants-1602164.html> (accessed 03/06/2016), 2016).
- (28) International Atomic Energy Agency (IAEA). Research Reactors. <http://nucleus.iaea.org/RRDB/RR/ReactorSearch.aspx?filter=0> (accessed 15/05/2015), 2015).
- (29) International Atomic Energy Agency (IAEA). Glossary of terms in PRIS reports. <http://www.iaea.org/PRIS/Glossary.aspx> (accessed 15/05/2015), 2015).
- (30) Ministry of Defence (MOD). *Submarine dismantling project: Consultation document on the site for interim storage of intermediate level radioactive waste*; MOD: 2014;
- (31) Office for Nuclear Regulation (ONR). *Annual plan - 2015/16*; ONR: 2015;
- (32) Donald, I. *Waste Immobilization in Glass and Ceramic Based Hosts*, Wiley: Chichester, 2010.
- (33) Nuclear Decommissioning Authority (NDA). *Radioactive wastes in the UK: A summary of the 2013 inventory*; NDA: 2014;
- (34) NDA. *An Overview of NDA Higher Activity Waste*; NDA 2012;
- (35) Nuclear Decommissioning Authority (NDA). *2013 UK radioactive waste inventory: Radioactive waste composition*; NDA: 2014;
- (36) Nuclear Decommissioning Authority (NDA); Department of Energy and Climate Change (DECC). *Radioactive Wastes in the UK: The 2010 Estimate of Radioactive Waste for Geological Disposal*; NDA 2011;
- (37) Abraitis, P. K.; Davies, G. Disposability of the UK's Intermediate Level Wastes. *MRS Online Proceedings Library* **2008**, 1107.
- (38) Nuclear Decommissioning Authority (NDA); Department of Energy and Climate Change (DECC). *The 2010 UK Radioactive Waste Inventory*; NDA 2011;
- (39) LLWR. *Waste Acceptance Criteria - Overview*; LLWR 2011;
- (40) Nuclear Decommissioning Authority (NDA). *UK strategy for the management of solid low level radioactive waste from the nuclear industry*; NDA: 2010;
- (41) Nuclear Decommissioning Authority (NDA). *2013 UK radioactive waste inventory: Radioactivity content of wastes*; NDA: 2014;
- (42) Nuclear Decommissioning Authority (NDA). *2013 UK radioactive waste inventory: Waste quantities from all sources*; NDA: 2014;
- (43) Nuclear Decommissioning Authority (NDA). *2013 UK radioactive waste inventory: Scenario for future radioactive waste and material arisings*; NDA: 2014;
- (44) Nuclear Decommissioning Authority (NDA). *2013 UK radioactive waste inventory: Radioactive wastes and materials not reported in the 2013 UKRWI*; NDA: 2014;
- (45) Nuclear Decommissioning Authority (NDA). *Progress on approaches to the management of separated plutonium*; NDA: 2014;

- (46) NIREX. *Description of Long-term Management Options for Radioactive Waste Investigated Internationally*; NIREX 2002;
- (47) Rice, E. E.; Denning, R. S.; Friedlander, A. L. *Preliminary risk assessment for nuclear waste disposal in space: Vol II technical report*; National Aeronautics and Space Administration (NASA): 1982;
- (48) Beswick, A. J.; Gibb, F. G. F.; Travis, K. P. Deep borehole disposal of nuclear waste: engineering challenges. *Proceedings of the ICE - Energy* **2014**, *167*, 47-66.
- (49) Nuclear Decommissioning Authority (NDA). *Geological disposal: How the world is dealing with its radioactive waste*; NDA: 2013;
- (50) Nuclear Decommissioning Authority (NDA). *Geological Disposal: Generic disposal facility designs*; NDA 2010;
- (51) CoRWM. *Managing our Radioactive Waste Safely: CoRWM's recommendations to Government*; CoRWM 2006;
- (52) Committee on radioactive waste management (CoRWM). *Tenth annual report 2013-14*; CoRWM: 2014;
- (53) Nuclear Decommissioning Authority (NDA). *Geological Disposal: Package evolution status report*; NDA 2010;
- (54) Nuclear Decommissioning Authority (NDA). *Geological Disposal: Gas status report*; NDA 2010;
- (55) Nuclear Decommissioning Authority (NDA). *Geological Disposal: Near-field evolution status report*; NDA 2010;
- (56) Dauzeres, A.; Le Bescop, P.; Sardini, P.; Cau Dit Coumes, C. Physico-chemical investigation of clayey/cement-based materials interaction in the context of geological waste disposal: Experimental approach and results. *Cement and Concrete Research* **2010**, *40*, 1327-1340.
- (57) Gaucher, E. C.; Blanc, P. Cement/clay interactions – A review: Experiments, natural analogues, and modeling. *Waste Management* **2006**, *26*, 776-788.
- (58) Svensk Kärnbränslehantering AB. *Design and production of the KBS-3 repository*; TR-10-12; SKB: 2010;
- (59) Francis, A. J.; Cather, R.; Crossland, I. G. *Nirex safety assessment research programme: Development of the Nirex Reference Vault Backfill; report on current status in 1994*; NIREX: 1997;
- (60) Crossland, I. G.; Vines, S. P. *Why a cementitious repository?*; United Kingdom Nirex Limited: 2001;
- (61) Nuclear Decommissioning Authority (NDA). *Geological disposal: An introduction to the generic disposal system safety case*; NDA: 2010;
- (62) NDA; Sellafield; NMP. *Sellafield Plan*; 2011;
- (63) Sharp, J. H.; Hill, J.; Milestone, N. B.; Miller, E. W. Cementitious systems for encapsulation of intermediate level waste. *ASME Conference Proceedings* **2003**, *2003*, 1425-1433.
- (64) Fenton, A.; Holland, T. R. *The history and expected benefits of using cemented materials for the encapsulation of radioactive waste in the UK*; AEA Technology: 2001;
- (65) Collier, N. C.; Milestone, N. B. The encapsulation of Mg(OH)₂ sludge in composite cement. *Cement and Concrete Research* **2010**, *40*, 452-459.
- (66) Atkins, M.; Glasser, F. P. Application of portland cement-based materials to radioactive waste immobilization. *Waste Management* **1992**, *12*, 105-131.
- (67) Glasser, F. P. Progress in the immobilization of radioactive wastes in cement. *Cement and Concrete Research* **1992**, *22*, 201-216.

- (68) Angus, M. J.; Godfrey, I. H.; Hayes, M.; Foster, S. Managing change in the supply of cement powders for radioactive waste encapsulation - twenty years of operational experience. In *Waste management (WM) 2010 conference*, Phoenix, AZ, 2010.
- (69) Hayes, M.; Godfrey, I. Development of the use of alternative cements for the treatment of intermediate level waste. In *WM'07 Conference*, Tucson, AZ, 2007.
- (70) NDA. *WPS/300: Specification for 500 litre Drum Waste Package*; NDA 2008;
- (71) NDA. *WPS/500: Wasteform Specification for 500 litre Drum Waste Package*; NDA 2008;
- (72) NDA. *WPS/700: 500 litre drum waste package specifications: explanatory material and design guidelines*; NDA: 2008;
- (73) Nuclear Decommissioning Authority (NDA). *Geological disposal: generic post-closure safety assessment*; NDA: 2010;
- (74) Bennet, D. G.; Higgo, J. J. W.; Wickham, S. M. *Review of Waste Immobilisation Matrices*; Galson Sciences 2001;
- (75) NIREX. *WPS/904: Guidance on the Characteristics and Demonstration of Robust Formulation Envelopes for Cementitious Wasteforms*; NIREX 2007;
- (76) BNG. *Sellafield Integrated Waste Strategy*; BNG 2007;
- (77) Dounreay Site Restoration Ltd. Cementation plant. <http://www.dounreay.com/waste/radioactive-waste/higher-activity-waste/cementation-plant> (accessed 09/07/2015),
- (78) Nuclear Decommissioning Authority (NDA). *Geological Disposal: NDA RWMD interactions with waste packagers on plans for packaging radioactive wastes April 2009 - March 2010*; NDA 2010;
- (79) Nuclear Decommissioning Authority. *Plutonium: Credible options analysis*; NDA: 2010;
- (80) Cronin, J.; Collier, N. *Corrosion & Expansion of Grouted Magnox*; NDA 2011;
- (81) Collier, N. C.; Milestone, N. B.; Hill, J.; Godfrey, I. H. Immobilisation of Fe floc: Part 2, encapsulation of floc in composite cement. *Journal of Nuclear Materials* **2009**, 393, 92-101.
- (82) Hill, J.; Sharp, J. H. The hydration products of Portland cement in the presence of tin(II) chloride. *Cement and Concrete Research* **2003**, 33, 121-124.
- (83) Kinoshita, H.; Swift, P.; Utton, C.; Carro-Mateo, B.; Marchand, G.; Collier, N.; Milestone, N. Corrosion of aluminium metal in OPC- and CAC-based cement matrices. *Cement and Concrete Research* **2013**, 50, 11-18.
- (84) Gartner, E.; Young, J.; Damidot, D.; Jawed, I. Hydration of Portland cement. In *Structure and Performance of Cements*, 2nd ed.; Bensted, J., Barnes, P., Eds.; Spon Press: London, 2002; pp 57-113.
- (85) Commissariat à l'énergie atomique (CEA). *Nuclear waste conditioning*; 2009;
- (86) Hicks, T.; Baldwin, T.; Hooker, P.; Richardson, P.; Chapman, N.; McKinley, I.; Neall, F. *Concepts for the Geological Disposal of Intermediate-Level Radioactive Waste*; Galson Sciences 2008;
- (87) Mouazen, M.; Poulesquen, A.; Bart, F.; Vergnes, B. Effect of γ irradiation on nuclear bituminized waste products (BWP): X-ray microtomography and rheological characterization. *Journal of Nuclear Materials* **2011**, 419, 24-31.
- (88) NIREX. *WPS/901: Guidance Note on the Use of Organic Polymers for the Encapsulation of Intermediate Level Waste: Review of Candidate Materials*; NIREX 2005;

- (89) Serco. *Consideration of Polymer-Encapsulated ILW in a Geological Disposal Facility*; Serco 2010;
- (90) Sellafield. Novel Processes for the Treatment of ILW. www.rsc.org/images/MikeJames_tcm18-174205.pdf, 2010).
- (91) Covill, A.; Hyatt, N. C.; Hill, J.; Collier, N. C. Development of magnesium phosphate cements for encapsulation of radioactive waste. *Advances in Applied Ceramics* **2011**, *110*, 151-156.
- (92) Walker, B.; Langton, C.; Singh, D. Phosphate bonded solidification of radioactive incinerator wastes. In *Ceramic Transactions: Environmental Issues and Waste Management Technologies in the Ceramic and Nuclear Industries V*, Chandler, G., Feng, X., Eds.; American Ceramic Society: 2000; Vol. 107, pp 169-174.
- (93) Langton, C.; Singh, D.; Wagh, A. S.; Tlustochowicz, M.; Dwyer, K. Phosphate ceramic solidification and stabilization of cesium-containing crystalline silicotitanate resins. In *Ceramic Transactions: Environmental Issues and Waste Management Technologies in the Ceramic and Nuclear Industries V*, Chandler, G., Feng, X., Eds.; American Ceramic Society: 2000; Vol. 107, pp 175-187.
- (94) Jeong, S. Y.; Wagh, A. S.; Singh, D. Stabilization of lead-rich low-level mixed wastes in chemically bonded phosphate ceramics. In *Ceramic Transactions: Environmental Issues and Waste Management Technologies in the Ceramic and Nuclear Industries V*, Chandler, G., Feng, X., Eds.; American Ceramic Society: 2000; Vol. 107, pp 189-197.
- (95) Singh, D.; Mandalika, V. R.; Parulekar, S. J.; Wagh, A. S. Magnesium potassium phosphate ceramic for ^{99}Tc immobilization. *Journal of Nuclear Materials* **2006**, *348*, 272-282.
- (96) Wagh, A. S.; Strain, R.; Jeong, S. Y.; Reed, D.; Krause, T.; Singh, D. Stabilization of Rocky Flats Pu-contaminated ash within chemically bonded phosphate ceramics. *Journal of Nuclear Materials* **1999**, *265*, 295-307.
- (97) Xiaodong, S.; Sheng, Y.; Xuequan, W.; Mingshu, T.; Liji, Y. Immobilization of simulated high level wastes into AASC waste form. *Cement and Concrete Research* **1994**, *24*, 133-138.
- (98) Xuequan, W.; Sheng, Y.; Xiaodong, S.; Mingshu, T.; Liji, Y. Alkali-activated slag cement based radioactive waste forms. *Cement and Concrete Research* **1991**, *21*, 16-20.
- (99) Bai, Y.; Milestone, N. B.; Yang, C. Sodium sulphate activated GGBS/PFA and its potential as a nuclear waste immobilisation matrix. *MRS Online Proceedings Library* **2006**, *932*, 759-766.
- (100) Glasser, F. P. Application of inorganics cements to the conditioning and immobilisation of radioactive waste. In *Handbook of advanced radioactive waste conditioning technologies*, Ojovan, M. I., Ed.; Woodhead Publishing: Cambridge, 2011; pp 67-135.
- (101) Coumes, C. C. D.; Courtois, S.; Peysson, S.; Ambroise, J.; Pera, J. Calcium sulfoaluminate cement blended with OPC: A potential binder to encapsulate low-level radioactive slurries of complex chemistry. *Cement and Concrete Research* **2009**, *39*, 740-747.
- (102) Krivenko, P. V.; Skurchinskaya, J. V.; Lavrinenko, L. V.; Starkov, O. V.; Konovalov, E. E. Physico-chemical bases of radioactive wastes - Immobilisation in a mineral-like solidified stone, In *Proceedings of the First International Conference on Alkaline Cements and Concretes*; Krivenko, P. V., Ed. VIPOL Stock Company: Kiev, Ukraine, 1994; pp 1095-1106.

- (103) Vance, E. R.; Perera, D. S. Geopolymers for nuclear waste immobilisation. In *Geopolymers: Structures, Processing, Properties and Industrial Applications*, Provis, J. L., van Deventer, J. S. J., Eds.; Woodhead: Cambridge, UK, 2009; pp 403-422.
- (104) Khalil, M. Y.; Merz, E. Immobilization of intermediate-level wastes in geopolymers. *Journal of Nuclear Materials* **1994**, *211*, 141-148.
- (105) Davidovits, J.; Comrie, D. C. Long term durability of hazardous toxic and nuclear waste disposals, In *Proceedings of Geopolymer '88 - First European Conference on Soft Mineralurgy*; Davidovits, J., Orlinski, J., Eds. Universite de Technologie de Compeigne: Compeigne, France, 1988; pp 125-134.
- (106) Sellafield Ltd. *Sellafield 2015/2016 Procurement Plan: Procurement and Contracting Strategy*; NMP: 2014;
- (107) Nuclear Decommissioning Authority (NDA). *Waste stream 2D95.1: Magnox fuel storage pond sludge*; NDA: 2014;
- (108) Gregson, C. R.; Goddard, D. T.; Sarsfield, M. J.; Taylor, R. J. Combined electron microscopy and vibrational spectroscopy study of corroded Magnox sludge from a legacy spent nuclear fuel storage pond. *Journal of Nuclear Materials* **2011**, *412*, 145-156.
- (109) Parry, S.; Livens, F.; O'Brien, L. Corroded Magnox sludge and plutonium waste cementation. *Geochimica et Cosmochimica Acta* **2007**, *71*, A747-A815.
- (110) Nuclear Decommissioning Authority. *Waste stream 2D95.1 Magnox fuel storage pond sludge*; NDA: 2013;
- (111) Sellafield; NDA. *Technology Development and Delivery Summary: Review 2010-2011*; NDA 2010;
- (112) Sellafield Ltd. Magnox Swarf Storage Silos. <http://www.sellafieldsites.com/solution/risk-hazard-reduction/magnox-swarf-storage-silos/> (accessed 28/05/2016), n.d.).
- (113) Sellafield. *Performance Plan*; Sellafield Ltd: 2015;
- (114) World Nuclear News. Liquid waste removal progress at Sellafield silos. <http://www.world-nuclear-news.org/WR-Liquid-waste-removal-progress-at-Sellafield-silos-2002154.html> (accessed 28/05/2016), 2015).
- (115) Sellafield Ltd. Sellafield making strides in clean-up. <http://www.sellafieldsites.com/2015/07/sellafield-making-strides-in-clean-up/> (accessed 28/05/2016), 2015).
- (116) Nuclear Decommissioning Authority (NDA). *Waste stream 2D95.3: Sludge settling tank*; NDA: 2014;
- (117) Nuclear Decommissioning Authority (NDA). *Waste stream 2D95.4: Decanner settling tank sludge*; NDA: 2014;
- (118) Nuclear Decommissioning Authority (NDA). *Waste stream 2D95.2: Settling pond sludge*; NDA: 2014;
- (119) Nuclear Decommissioning Authority (NDA). *Waste stream 2D34: Sludge from sand filters and transfers*; NDA: 2014;
- (120) Nuclear Decommissioning Authority (NDA). *Waste stream 2D33: Fuel handling plant sludges*; NDA: 2014;
- (121) Hastings, J. J.; Rhodes, D.; Fellerman, A. S.; McKendrick, D.; Dixon, C. New approaches for sludge management in the nuclear industry. *Powder Technology* **2007**, *174*, 18-24.
- (122) Nuclear Decommissioning Authority (NDA). *Waste stream 2D35: Magnox cladding and miscellaneous solid waste*; NDA: 2014;

- (123) Nuclear Decommissioning Authority (NDA). *Waste stream 2D24: Magnox cladding and miscellaneous solid waste*; NDA: 2014;
- (124) Nuclear Decommissioning Authority (NDA). *Waste stream 2D22: Magnox cladding and miscellaneous solid waste*; NDA: 2014;
- (125) Nuclear Decommissioning Authority (NDA). *Waste stream 2D09: Magnox cladding and miscellaneous solid waste*; NDA: 2014;
- (126) Nuclear Decommissioning Authority (NDA). *Waste stream 2D08: Magnox cladding and miscellaneous solid waste*; NDA: 2014;
- (127) Sellafield. New plant ready to handle historic waste. <http://www.sellafieldsites.com/press/new-radioactive-sludge-plant-ready-to-go/>, 2014).
- (128) Sellafield. Major step forward for Sellafield clean-up. <http://www.nda.gov.uk/2015/03/major-step-forward-for-sellafield-clean-up/>, 2015).
- (129) Stewart, M. SYNROC - Demonstrated Capabilities, Project Status and Related Mo-99 Production Applicability. www.iaea.org/OurWork/NE/NEFW/RRS/documents/mo99/STEWARTmo99CM.pdf, 2010).
- (130) Campbell, P.; Deegan, D. Plasma solution to waste streams. *Nuclear Energy Review*, **2007**.
- (131) Deegan, D.; Chapman, C.; Ismail, S. Treatment of Nuclear Sludge. U.S. Patent 8404919, 2013.
- (132) Matlack, K.; Kot, W.; Gan, H.; Pegg, I.; Diener, G.; Bowan, B. Sellafield thermal treatment trials using advanced joule heated ceramic melter technology. In *WM2010 Conference*, Phoenix, AZ, 2010.
- (133) Mason, J.; Oliver, T. In-Container Mineralization. U.S. Patent 7476194, 2009.
- (134) Hough, T.; Palethorpe, S. Development of a direct encapsulation technique for the treatment of a mixed sludge / solid waste. In *WM'07 Conference*, Tucson, AZ, 2007.
- (135) Gougar, M. L. D.; Scheetz, B. E.; Roy, D. M. Ettringite and C-S-H Portland cement phases for waste ion immobilization: A review. *Waste Management* **1996**, *16*, 295-303.
- (136) Shrivastava, O. P.; Komarneni, S.; Breval, E. Mg²⁺ uptake by synthetic tobermorite and xonotlite. *Cement and Concrete Research* **1991**, *21*, 83-90.
- (137) Mostafa, N. Y.; Kishar, E. A.; Abo-El-Enein, S. A. FTIR study and cation exchange capacity of Fe³⁺ and Mg²⁺ substituted calcium silicate hydrates. *Journal of Alloys and Compounds* **2009**, *473*, 538-542.
- (138) Fernandez, L.; Alonso, C.; Andrade, C.; Hidalgo, A. The interaction of magnesium in hydration of C₃S and CSH formation using ²⁹Si MAS-NMR. *Journal of Materials Science* **2008**, *43*, 5772-5783.
- (139) Fernandez, L.; Alonso, C.; Hidalgo, A.; Andrade, C. The role of magnesium during the hydration of C₃S and C-S-H formation. Scanning electron microscopy and mid-infrared studies. *Advances in Cement Research* **2005**, *17*, 9-21.
- (140) Richardson, I. G.; Groves, G. W. The incorporation of minor and trace-elements into calcium silicate hydrate (C-S-H) gel in hardened cement pastes. *Cement and Concrete Research* **1993**, *23*, 131-138.
- (141) Rodger, S. A.; Groves, G. W. Electron microscopy study of ordinary Portland cement and ordinary Portland cement-pulverized fuel ash blended pastes. *Journal of the American Ceramic Society* **1989**, *72*, 1037-1039.

- (142) Mitsuda, T. Paragenesis of 11 Å tobermorite and poorly crystalline hydrated magnesium silicate. *Cement and Concrete Research* **1973**, *3*, 71-80.
- (143) Lothenbach, B.; Nied, D.; L'Hôpital, E.; Achiedo, G.; Dauzères, A. Magnesium and calcium silicate hydrates. *Cement and Concrete Research* **2015**, *77*, 60-68.
- (144) USGS. Cement. *Mineral commodity summaries 2015*; U.S. Geological Survey, Reston, VA, 2015; pp 38-39.
- (145) Eglinton, M. Resistance of concrete to destructive agencies. In *Lea's Chemistry of Cement and Concrete*, 4th ed.; Hewlett, P. C., Ed.; Butterworth Heinemann: Oxford, UK, 2003; pp 299-342.
- (146) Juenger, M. C. G.; Winnefeld, F.; Provis, J. L.; Ideker, J. Advances in alternative cementitious binders. *Cement and Concrete Research* **2011**, *41*, 1232-1243.
- (147) Olivier, J. G. J.; Janssens-Maenhout, G.; Peters, J. A. H. W. *Trends in global CO₂ emissions; 2012 Report*; PBL Netherlands Environmental Assessment Agency: The Hague, Netherlands, 2012; p40
- (148) European Commission. *Report on Critical Raw Materials for the EU: Report of the Ad Hoc Working Group on Defining Critical Raw Materials*; Brussels, Belgium, 2014; p41
- (149) USGS. Magnesium compounds. *Mineral commodity summaries 2015*; U.S. Geological Survey, Reston, VA, 2015; pp 96-97.
- (150) Jung, I.-H.; Decterov, S.; Pelton, A. Critical thermodynamic evaluation and optimization of the MgO-Al₂O₃, CaO-MgO-Al₂O₃, and MgO-Al₂O₃-SiO₂ Systems. *Journal of Phase Equilibria and Diffusion* **2004**, *25*, 329-345.
- (151) Gentile, A. L.; Foster, W. R. Calcium hexaluminate and its stability relations in the system CaO-Al₂O₃-SiO₂. *Journal of the American Ceramic Society* **1963**, *46*, 74-76.
- (152) European Commission. *Best available techniques (BAT) reference document for the production of cement, lime and magnesium oxide*; Joint Research Centre: Seville, Spain, 2013;
- (153) Canterford, J. H. Magnesia - an important industrial mineral: A review of processing options and uses. *Mineral Processing and Extractive Metallurgy Review* **1985**, *2*, 57-104.
- (154) Eubank, W. R. Calcination studies of magnesium oxides. *Journal of the American Ceramic Society* **1951**, *34*, 225-229.
- (155) Wright, J. M.; Colling, A. *Seawater: Its composition, properties and behaviour*, 2nd ed.; Elsevier Science: Oxford, UK, 1995.
- (156) Boyd, C. E. *Water quality: an introduction*, 2nd ed.; Springer International Publishing: Cham, Switzerland, 2005.
- (157) European Commission. *Reference document on the best available techniques for the manufacture of large volume inorganic chemicals - solids and others industry*; Seville, Spain, 2007;
- (158) Seeger, M.; Otto, W.; Flick, W.; Bickelhaupt, F.; Akkerman, O. S. Magnesium compounds. In *Ullmann's Encyclopedia of Industrial Chemistry*, Wiley-VCH Verlag GmbH & Co. KGaA: 2000.
- (159) Premier Periclase. Process. <http://www.premierpericlase.ie/process.html> (accessed 10 Nov 2015),
- (160) Shand, M. A. *The chemistry and technology of magnesia*, John Wiley & Sons: Hoboken, NJ, 2006.

- (161) USGS. *2013 Minerals Yearbook - Israel*; U.S. Geological Survey: Reston, VA, 2015;
- (162) Hirota, K.; Okabayashi, N.; Toyoda, K.; Yamaguchi, O. Characterization and sintering of reactive MgO. *Materials Research Bulletin* **1992**, *27*, 319-326.
- (163) Kotera, Y.; Saito, T.; Terada, M. Crystal growth of magnesium oxide prepared by the thermal decomposition of magnesium hydroxide. *Bulletin of the Chemical Society of Japan* **1963**, *36*, 195-199.
- (164) Strydom, C. A.; van der Merwe, E. M.; Aphane, M. E. The effect of calcining conditions on the rehydration of dead burnt magnesium oxide using magnesium acetate as a hydrating agent. *Journal of Thermal Analysis and Calorimetry* **2005**, *80*, 659-662.
- (165) Green, J. Calcination of precipitated Mg(OH)₂ to active MgO in the production of refractory and chemical grade MgO. *Journal of Materials Science* **1983**, *18*, 637-651.
- (166) Martin Marietta Magnesias Specialties. Light burned MgO. <http://magnesiasspecialties.com/light-burned-magnesium-oxide/> (accessed 12 Nov 2015),
- (167) Jin, F.; Al-Tabbaa, A. Characterisation of different commercial reactive magnesia. *Advances in Cement Research* **2014**, *26*, 101-113.
- (168) Zhu, J.; Ye, N.; Liu, J.; Yang, J. Evaluation on hydration reactivity of reactive magnesium oxide prepared by calcining magnesite at lower temperatures. *Industrial & Engineering Chemistry Research* **2013**, *52*, 6430-6437.
- (169) Chau, C. K.; Li, Z. Accelerated Reactivity Assessment of Light Burnt Magnesium Oxide. *Journal of the American Ceramic Society* **2008**, *91*, 1640-1645.
- (170) Liska, M.; Al-Tabbaa, A. Ultra-green construction: reactive magnesia masonry products. *Proceedings of the ICE - Waste and Resource Management* **2009**, *162*, 185-196.
- (171) Liska, M.; Al-Tabbaa, A.; Carter, K.; Fifield, J. Scaled-up commercial production of reactive magnesia cement pressed masonry units. Part II: Performance. *Proceedings of the ICE - Construction Materials* **2012**, *165*, 225-243.
- (172) Vlasopoulos, N.; Cheeseman, C. R. Binder composition. US Patent 8496751B2, 2013.
- (173) Jiang, F.; Speziale, S.; Duffy, T. S. Single-crystal elasticity of brucite, Mg(OH)₂, to 15 GPa by Brillouin scattering. *American Mineralogist* **2006**, *91*, 1893-1900.
- (174) Maslen, E. N.; Streltsov, V. A.; Streltsova, N. R. X-ray study of the electron density in magnesite, MgCO₃. *Acta Crystallographica Section B* **1993**, *49*, 980-984.
- (175) Giester, G.; Lengauer, C. L.; Rieck, B. The crystal structure of nesquehonite, MgCO₃·3H₂O, from Lavrion, Greece. *Mineralogy and Petrology* **2000**, *70*, 153-163.
- (176) Hill, R. J.; Canterford, J. H.; Moyle, F. J. New data for lansfordite. *Mineralogical Magazine* **1982**, *46*, 453-457.
- (177) Akao, M.; Iwai, S. The hydrogen bonding of artinite. *Acta Crystallographica Section B* **1977**, *33*, 3951-3953.
- (178) Akao, M.; Iwai, S. The hydrogen bonding of hydromagnesite. *Acta Crystallographica Section B* **1977**, *33*, 1273-1275.
- (179) Raade, G. Dypingite, a new hydrous basic carbonate of magnesium, from Norway. *American Mineralogist* **1970**, *55*, 1457-1465.
- (180) Faust, G. T. Huntite, Mg₃Ca(CO₃)₄, a new mineral. *American Mineralogist* **1953**, *38*, 4-24.

- (181) Du, C. A review of magnesium oxide in concrete. *Concrete International*, Dec, **2005**, 45-50.
- (182) Jin, F.; Zhang, G.; Luo, X.; Zhang, C. Modelling autogenous expansion for magnesia concrete in arch dams. *Frontiers of Architecture and Civil Engineering in China* **2008**, *2*, 211-218.
- (183) Neville, A. *Properties of Concrete*, 4th ed.; Pearson: Harlow, UK, 1995.
- (184) Bensted, J. Gypsum in cements. In *Structure and Performance of Cements*, 2nd ed.; Bensted, J., Barnes, P., Eds.; Spon Press: London, 2002; pp 253-264.
- (185) Taylor, H. F. W. *Cement Chemistry*, 2nd ed.; Thomas Telford Publishing: London, UK, 1997.
- (186) Nagataki, S.; Gomi, H. Expansive admixtures (mainly ettringite). *Cement and Concrete Composites* **1998**, *20*, 163-170.
- (187) Bullerjahn, F.; Schmitt, D.; Ben Haha, M. Effect of raw mix design and of clinkering process on the formation and mineralogical composition of (ternesite) belite calcium sulphoaluminate ferrite clinker. *Cement and Concrete Research* **2014**, *59*, 87-95.
- (188) Lothenbach, B.; Albert, B.; Morin, V.; Gartner, E. Hydration of belite-ye'elinite-ferrite cements: thermodynamic modeling, In *14th International Congress on the Chemistry of Cement (ICCC)*; Shi, C., Yao, Y., Eds. Beijing, China, 2015.
- (189) Chatterjee, A. K. Special cements. In *Structure and Performance of Cements*, 2nd ed.; Bensted, J., Barnes, P., Eds.; Spon Press: London, 2002; pp 186-236.
- (190) Chatterji, S. Mechanism of expansion of concrete due to the presence of dead-burnt CaO and MgO. *Cement and Concrete Research* **1995**, *25*, 51-56.
- (191) Odler, I. *Special inorganic cements*, E & FN Spon: London, UK, 2000.
- (192) Zheng, L.; Xuehua, C.; Mingshu, T. MgO-type delayed expansive cement. *Cement and Concrete Research* **1991**, *21*, 1049-1057.
- (193) Mo, L.; Deng, M.; Tang, M. Effects of calcination condition on expansion property of MgO-type expansive agent used in cement-based materials. *Cement and Concrete Research* **2010**, *40*, 437-446.
- (194) Lu, X.; Geng, F.; Zhang, H.; Chen, X. Influence of MgO-type expansive agent hydration behaviors on expansive properties of concrete. *Journal of Wuhan University of Technology-Mater. Sci. Ed.* **2011**, *26*, 344-346.
- (195) Mo, L.; Deng, M.; Tang, M.; Al-Tabbaa, A. MgO expansive cement and concrete in China: Past, present and future. *Cement and Concrete Research* **2014**, *57*, 1-12.
- (196) Harrison, A. J. W. Process for preparing reactive magnesium oxide cements. Eur. Patent 1254083B1, 2011.
- (197) Harrison, A. J. W. Reactive magnesium oxide cements. U.S. Patent 7347896, 2008.
- (198) Harrison, A. J. W. Reactive magnesium oxide cements. Can. Patent 2398793, 2005.
- (199) Harrison, A. J. W. Magnesium cements. Chinese Patent 1419523, 2010.
- (200) Pearce, F. Green foundations. *New Scientist*, **2002**, 39.
- (201) Harrison, A. J. W. TecEco. www.tececo.com (accessed July 17 2014),
- (202) Jackson, P. J. Portland cement: Classification and manufacture. In *Lea's Chemistry of Cement and Concrete*, Hewlett, P. C., Ed.; Butterworth Heinemann: Oxford, UK, 2003; pp 25-94.
- (203) Vandeperre, L. J.; Liska, M.; Al-Tabbaa, A. Microstructures of reactive magnesia cement blends. *Cement and Concrete Composites* **2008**, *30*, 706-714.

- (204) Vandeperre, L. J.; Liska, M.; Al-Tabbaa, A. Hydration and mechanical properties of magnesia, pulverised fuel ash, and portland cement blends. *Journal of Materials in Civil Engineering* **2008**, *20*, 375-383.
- (205) Cwirzen, A.; Habermehl-Cwirzen, K. Effects of reactive magnesia on microstructure and frost durability of Portland cement-based binders. *Journal of Materials in Civil Engineering* **2013**, *25*, 1941-1950.
- (206) Vandeperre, L. J.; Al-Tabbaa, A. Accelerated carbonation of reactive MgO cements. *Advances in Cement Research* **2007**, *19*, 67-79.
- (207) Mo, L.; Panesar, D. K. Effects of accelerated carbonation on the microstructure of Portland cement pastes containing reactive MgO. *Cement and Concrete Research* **2012**, *42*, 769-777.
- (208) Mo, L.; Panesar, D. K. Accelerated carbonation – A potential approach to sequester CO₂ in cement paste containing slag and reactive MgO. *Cement and Concrete Composites* **2013**, *43*, 69-77.
- (209) Panesar, D. K.; Mo, L. Properties of binary and ternary reactive MgO mortar blends subjected to CO₂ curing. *Cement and Concrete Composites* **2013**, *38*, 40-49.
- (210) Morse, J. W.; Wang, Q.; Tsio, M. Y. Influences of temperature and Mg:Ca ratio on CaCO₃ precipitates from seawater. *Geology* **1997**, *25*, 85-87.
- (211) Berner, R. A. The role of magnesium in the crystal growth of calcite and aragonite from sea water. *Geochimica et Cosmochimica Acta* **1975**, *39*, 489-504.
- (212) Loste, E.; Wilson, R. M.; Seshadri, R.; Meldrum, F. C. The role of magnesium in stabilising amorphous calcium carbonate and controlling calcite morphologies. *Journal of Crystal Growth* **2003**, *254*, 206-218.
- (213) Mucci, A.; Morse, J. W. The incorporation of Mg²⁺ and Sr²⁺ into calcite overgrowths: influences of growth rate and solution composition. *Geochimica et Cosmochimica Acta* **1983**, *47*, 217-233.
- (214) Kitamura, M. Crystallization and transformation mechanism of calcium carbonate polymorphs and the effect of magnesium ion. *Journal of Colloid and Interface Science* **2001**, *236*, 318-327.
- (215) Burton, E. A.; Walter, L. M. The effects of P_{CO2} and temperature on magnesium incorporation in calcite in seawater and MgCl₂-CaCl₂ solutions. *Geochimica et Cosmochimica Acta* **1991**, *55*, 777-785.
- (216) Katz, A. The interaction of magnesium with calcite during crystal growth at 25–90 °C and one atmosphere. *Geochimica et Cosmochimica Acta* **1973**, *37*, 1563-1586.
- (217) Mignardi, S.; De Vito, C.; Ferrini, V.; Martin, R. F. The efficiency of CO₂ sequestration via carbonate mineralization with simulated wastewaters of high salinity. *Journal of Hazardous Materials* **2011**, *191*, 49-55.
- (218) Harrison, A. L.; Power, I. M.; Dipple, G. M. Accelerated carbonation of brucite in mine tailings for carbon sequestration. *Environmental Science & Technology* **2013**, *47*, 126-134.
- (219) Todd Schaef, H.; McGrail, B. P.; Loring, J. L.; Bowden, M. E.; Arey, B. W.; Rosso, K. M. Forsterite [Mg₂SiO₄] carbonation in wet supercritical CO₂: An in situ high-pressure X-ray diffraction study. *Environmental Science & Technology* **2013**, *47*, 174-181.
- (220) Qafoku, O.; Dixon, D. A.; Rosso, K. M.; Schaef, H. T.; Bowden, M. E.; Arey, B. W.; Felmy, A. R. Dynamics of magnesite formation at low temperature and high pCO₂ in aqueous solution. *Environmental Science & Technology* **2015**, *49*, 10736-10744.

- (221) Béarat, H.; McKelvy, M. J.; Chizmeshya, A. V. G.; Gormley, D.; Nunez, R.; Carpenter, R. W.; Squires, K.; Wolf, G. H. Carbon sequestration via aqueous olivine mineral carbonation: role of passivating layer formation. *Environmental Science & Technology* **2006**, *40*, 4802-4808.
- (222) Hänchen, M.; Prigiobbe, V.; Baciocchi, R.; Mazzotti, M. Precipitation in the Mg-carbonate system—effects of temperature and CO₂ pressure. *Chemical Engineering Science* **2008**, *63*, 1012-1028.
- (223) Ballirano, P.; De Vito, C.; Ferrini, V.; Mignardi, S. The thermal behaviour and structural stability of nesquehonite, MgCO₃·3H₂O, evaluated by in situ laboratory parallel-beam X-ray powder diffraction: New constraints on CO₂ sequestration within minerals. *Journal of Hazardous Materials* **2010**, *178*, 522-528.
- (224) Ferrini, V.; De Vito, C.; Mignardi, S. Synthesis of nesquehonite by reaction of gaseous CO₂ with Mg chloride solution: Its potential role in the sequestration of carbon dioxide. *Journal of Hazardous Materials* **2009**, *168*, 832-837.
- (225) Swanson, E. J.; Fricker, K. J.; Sun, M.; Park, A.-H. A. Directed precipitation of hydrated and anhydrous magnesium carbonates for carbon storage. *Physical Chemistry Chemical Physics* **2014**, *16*, 23440-23450.
- (226) Jauffret, G.; Morrison, J.; Glasser, F. P. On the thermal decomposition of nesquehonite. *Journal of Thermal Analysis and Calorimetry* **2015**, *122*, 601-609.
- (227) Hales, M. C.; Frost, R. L.; Martens, W. N. Thermo-Raman spectroscopy of synthetic nesquehonite — implication for the geosequestration of greenhouse gases. *Journal of Raman Spectroscopy* **2008**, *39*, 1141-1149.
- (228) Dong, M.; Cheng, W.; Li, Z.; Demopoulos, G. P. Solubility and stability of nesquehonite (MgCO₃·3H₂O) in NaCl, KCl, MgCl₂, and NH₄Cl solutions. *Journal of Chemical & Engineering Data* **2008**, *53*, 2586-2593.
- (229) Hopkinson, L.; Rutt, K.; Gordon, C. The transformation of nesquehonite to hydromagnesite in the system CaO-MgO-H₂O-CO₂: An experimental spectroscopic study. *The Journal of Geology* **2008**, *116*, 387-400.
- (230) Davies, P. J.; Bubela, B. The transformation of nesquehonite into hydromagnesite. *Chemical Geology* **1973**, *12*, 289-300.
- (231) Robie, R. A.; Hemingway, B. S. The heat capacities at low-temperatures and entropies at 298.15 K of nesquehonite, MgCO₃·3H₂O, and hydromagnesite. *American Mineralogist* **1972**, *57*, 1768-1781.
- (232) Königsberger, E.; Königsberger, L.-C.; Gamsjäger, H. Low-temperature thermodynamic model for the system Na₂CO₃-MgCO₃-CaCO₃-H₂O. *Geochimica et Cosmochimica Acta* **1999**, *63*, 3105-3119.
- (233) Chaka, A. M.; Felmy, A. R. Ab initio thermodynamic model for magnesium carbonates and hydrates. *The Journal of Physical Chemistry A* **2014**, *118*, 7469-7488.
- (234) Walling, S.; Provis, J. A discussion of the papers “Impact of hydrated magnesium carbonate additives on the carbonation of reactive MgO cements” and “Enhancing the carbonation of MgO cement porous blocks through improved curing conditions”, by C. Unluer & A. Al-Tabbaa. *Cement and Concrete Research* **2016**, *76*, 424-426.
- (235) Dheilily, R. M.; Bouguerra, A.; Beaudoin, B.; Tudo, J.; Queneudec, M. Hydromagnesite development in magnesian lime mortars. *Materials Science and Engineering: A* **1999**, *268*, 127-131.
- (236) De Silva, P.; Bucea, L.; Sirivivatnanon, V. Chemical, microstructural and strength development of calcium and magnesium carbonate binders. *Cement and Concrete Research* **2009**, *39*, 460-465.

- (237) Liska, M.; Vandeperre, L. J.; Al-Tabbaa, A. Influence of carbonation on the properties of reactive magnesia cement-based pressed masonry units. *Advances in Cement Research* **2008**, *20*, 53-64.
- (238) Jha, A. Revealed: The cement that eats carbon dioxide. www.theguardian.com/environment/2008/dec/31/cement-carbon-emissions (accessed Aug 3 2014), 2008).
- (239) Vlasopoulos, N. Process for producing cement binder compositions containing magnesium. U.S. Patent Appl. 20130213273, 2013.
- (240) Unluer, C.; Al-Tabbaa, A. Impact of hydrated magnesium carbonate additives on the carbonation of reactive MgO cements. *Cement and Concrete Research* **2013**, *54*, 87-97.
- (241) Vlasopoulos, N.; Bernebeu, J. P. Production of magnesium carbonate. World Pat. Appl. 2014/009802 A2, 2014.
- (242) Loring, J. S.; Thompson, C. J.; Wang, Z.; Joly, A. G.; Sklarew, D. S.; Schaefer, H. T.; Ilton, E. S.; Rosso, K. M.; Felmy, A. R. In situ infrared spectroscopic study of forsterite carbonation in wet supercritical CO₂. *Environmental Science & Technology* **2011**, *45*, 6204-6210.
- (243) Matter, J. M.; Kelemen, P. B. Permanent storage of carbon dioxide in geological reservoirs by mineral carbonation. *Nature Geosci* **2009**, *2*, 837-841.
- (244) Gartner, E. M.; Macphee, D. E. A physico-chemical basis for novel cementitious binders. *Cement and Concrete Research* **2011**, *41*, 736-749.
- (245) Gartner, E.; Hirao, H. A review of alternative approaches to the reduction of CO₂ emissions associated with the manufacture of the binder phase in concrete. *Cement and Concrete Research* **2015**, *78*, Part A, 126-142.
- (246) Sichel, M. Method of producing dental cement. U.S. Patent 492056, 1893.
- (247) Wilson, A. D. The chemistry of dental cements. *Chemical Society Reviews* **1978**, *7*, 265-296.
- (248) Kingery, W. D. Phosphate Bonding in Refractories. D.Sc. Thesis, Massachusetts Institute of Technology, Cambridge, MA, 1950.
- (249) Kingery, W. D. Fundamental study of phosphate bonding in refractories: I, Literature review. *Journal of the American Ceramic Society* **1950**, *33*, 239-241.
- (250) Kingery, W. D. Fundamental study of phosphate bonding in refractories: II, Cold-setting properties. *Journal of the American Ceramic Society* **1950**, *33*, 242-246.
- (251) Wilson, A. D.; Paddon, J. M.; Crisp, S. The hydration of dental cements. *Journal of Dental Research* **1979**, *58*, 1065-1071.
- (252) Servais, G. E.; Cartz, L. Structure of zinc phosphate dental cement. *Journal of Dental Research* **1971**, *50*, 613-620.
- (253) Oilo, G. Luting cements: a review and comparison. *International Dental Journal* **1991**, *41*, 81-88.
- (254) Prosen, E. M. Refractory investment. U.S. Patent 2209035, 1940.
- (255) Finch, T.; Sharp, J. H. Chemical reactions between magnesia and aluminium orthophosphate to form magnesia-phosphate cements. *Journal of Materials Science* **1989**, *24*, 4379-4386.
- (256) Hipedinger, N. E.; Scian, A. N.; Aglietti, E. F. Magnesia-phosphate bond for cold-setting cordierite-based refractories. *Cement and Concrete Research* **2002**, *32*, 675-682.
- (257) Every, C. E. Improvements relating to mouldable compositions. Br. Patent 593172, 1947.
- (258) Greger, H. H. Phosphate cements. U.S. Patent 2450952, 1945.

- (259) Limes, R. W.; Ponzani, D. Basic refractory compositions for intermediate temperature zones. U.S. Patent 3285758, 1966.
- (260) Limes, R. W.; Russell, R. O. Production of fast-setting bonded aggregate structures. U.S. Patent 4059455, 1977.
- (261) Limes, R. W.; Russell, R. O. Process for preparing fast-setting aggregate compositions and products of low porosity produced therewith. U.S. Patent 3879209, 1975.
- (262) Schwartz, C. H. Patching method. U.S. Patent 3821006, 1974.
- (263) Stierli, R. F.; Tarver, C. C.; Gaidis, J. M. Magnesium phosphate concrete compositions. U.S. Patent 3960580, 1976.
- (264) Kruger, W. K.; Patterson, H. L. *Evaluation of six commercial fast-setting hydraulic patching mortars, a latex bonding agent, and an epoxy emulsion admixture*; Michigan State Highway Commission: Lansing, MI, 1973;
- (265) Brabston, W. N. *Bomb damage repair, precast slab design*; ESL-TR-84-21; Air force engineering and services center: Tyndall Air Force Base, FL, 1984;
- (266) Smith, K. G.; Fowler, D. W.; Meyer, A. H. *Laboratory and field evaluation of rapid setting materials used for repair of concrete pavements*; FHWA/TX-85/20+311-4; Texas State Department of Highways and Public Transportation: Austin, TX, 1984;
- (267) Sinclair, G. B.; Barton, F. G.; Kennedy, L. J. Military engineering in the Falkland Islands 1982-83. *Proceedings of the Institute of Civil Engineers* **1984**, *76*, 269-277.
- (268) Barde, A.; Parameswaran, S.; Chariton, T.; Weiss, J.; Cohen, M. D.; Newbolds, A. *Evaluation of rapid setting cement-based materials for patching and repair*; Purdue University: West Lafayette, IN, 2006;
- (269) Sugama, T.; Kukacka, L. E. Magnesium monophosphate cements derived from diammonium phosphate solutions. *Cement and Concrete Research* **1983**, *13*, 407-416.
- (270) Sugama, T.; Kukacka, L. E. Characteristics of magnesium polyphosphate cements derived from ammonium polyphosphate solutions. *Cement and Concrete Research* **1983**, *13*, 499-506.
- (271) Abdelrazig, B. E. I.; Sharp, J. H. A discussion of the papers on magnesia-phosphate cements by T. Sugama and L.E. Kukacka. *Cement and Concrete Research* **1985**, *15*, 921-922.
- (272) Popovics, S.; Rajendran, N.; Penko, M. Rapid hardening cements for repair of concrete. *Aci Materials Journal* **1987**, *84*, 64-73.
- (273) Abdelrazig, B. E. I.; Sharp, J. H.; El-Jazairi, B. The chemical composition of mortars made from magnesia-phosphate cement. *Cement and Concrete Research* **1988**, *18*, 415-425.
- (274) Hall, D. A.; Stevens, R.; Jazairi, B. E. Effect of water content on the structure and mechanical properties of magnesia-phosphate cement mortar. *Journal of the American Ceramic Society* **1998**, *81*, 1550-1556.
- (275) Sarkar, A. K. Hydration/dehydration characteristics of struvite and dittmarite pertaining to magnesium ammonium phosphate cement systems. *Journal of Materials Science* **1991**, *26*, 2514-2518.
- (276) Abdelrazig, B. E. I.; Sharp, J. H.; El-Jazairi, B. The microstructure and mechanical properties of mortars made from magnesia-phosphate cement. *Cement and Concrete Research* **1989**, *19*, 247-258.
- (277) Bensted, J. A discussion of the paper "Rapid setting magnesium phosphate cement for quick repair of concrete pavements-characterisation and durability

- aspects” by S.S. Seehra, S. Gupta and S. Kumar. *Cement and Concrete Research* **1994**, *24*, 595-596.
- (278) Yang, Q.; Wu, X. Factors influencing properties of phosphate cement-based binder for rapid repair of concrete. *Cement and Concrete Research* **1999**, *29*, 389-396.
- (279) Yang, Q.; Zhu, B.; Zhang, S.; Wu, X. Properties and applications of magnesia–phosphate cement mortar for rapid repair of concrete. *Cement and Concrete Research* **2000**, *30*, 1807-1813.
- (280) Wang, A.-j.; Yuan, Z.-l.; Zhang, J.; Liu, L.-t.; Li, J.-m.; Liu, Z. Effect of raw material ratios on the compressive strength of magnesium potassium phosphate chemically bonded ceramics. *Materials Science and Engineering: C* **2013**, *33*, 5058-5063.
- (281) Qiao, F.; Chau, C. K.; Li, Z. Property evaluation of magnesium phosphate cement mortar as patch repair material. *Construction and Building Materials* **2010**, *24*, 695-700.
- (282) Xing, F.; Ding, Z.; Li, Z.-J. Study of potassium-based magnesium phosphate cement. *Advances in Cement Research* **2011**, *23*, 81-87.
- (283) Mehta, P. K. History and status of performance tests for evaluation of soundness of cements. In *Cement standards - evolution and trends*, ASTM STP 663, Mehta, P. K., Ed.; American Society for Testing and Materials: Philadelphia, PA, 1978; pp 35-60.
- (284) Soudée, E.; Péra, J. Mechanism of setting reaction in magnesia-phosphate cements. *Cement and Concrete Research* **2000**, *30*, 315-321.
- (285) Teschemacher, E. F. An account of various substances found in the guano deposits and in their vicinity. *Memoirs and Proceedings of the Chemical Society* **1845**, *3*, 13-17.
- (286) Ulex, G. L. CLXIII. On struvite, a new mineral. *Memoirs and Proceedings of the Chemical Society* **1845**, *3*, 106-110.
- (287) Berzelius, J. J. Struvit. *Öfversigt af Kongliga Ventenskaps-Akademiens Förhandlingar* **1847**, *3*, 32-33.
- (288) Ulex, G. L. Über Struveit. *Neus Jahrbuch für Mineralogie, Geognosie, Geologie und Petrefakten-Kunde* **1851**, 51-59.
- (289) Ulrich, G. H. F. *Contributions to the mineralogy of Victoria*, John Ferres, Government printer: Melbourne, Australia, 1870.
- (290) vom Rath, M. G. Note sur deux nouveaux phosphate du guano. *Bulletin de al Société Minéralogique de France* **1879**, *20*, 79-82.
- (291) MacIvor, R. W. E. On Australian bat guano and some minerals occurring therein. *The Chemical News* **1887**, *55*, 215-216.
- (292) MacIvor, R. W. E. On minerals occurring in Australian bat guano. *The Chemical News* **1902**, *85*, 181-182.
- (293) Ferraris, G.; Fuess, H.; Joswig, W. Neutron diffraction study of $\text{MgNH}_4\text{PO}_4 \cdot 6\text{H}_2\text{O}$ (struvite) and survey of water molecules donating short hydrogen bonds. *Acta Crystallographica Section B* **1986**, *42*, 253-258.
- (294) Banks, E.; Chianelli, R.; Korenstein, R. Crystal chemistry of struvite analogues of the type $\text{MgMPO}_4 \cdot 6\text{H}_2\text{O}$ ($\text{M}^+ = \text{K}^+, \text{Rb}^+, \text{Cs}^+, \text{Tl}^+, \text{NH}_4^+$). *Inorganic Chemistry* **1975**, *14*, 1634-1639.
- (295) Ravikumar, R. V. S. S. N.; Rao, S. N.; Reddy, B. J.; Reddy, Y. P. Electronic spectra of hexa aqua coordinated transition metal doped zinc struvite. *Ferroelectrics* **1996**, *189*, 139-147.

- (296) Stefov, V.; Šoptrajanov, B.; Najdoski, M.; Engelen, B.; Lutz, H. D. Infrared and Raman spectra of magnesium ammonium phosphate hexahydrate (struvite) and its isomorphous analogues. V. Spectra of protiated and partially deuterated magnesium ammonium arsenate hexahydrate (arsenstruvite). *Journal of Molecular Structure* **2008**, *872*, 87-92.
- (297) Stefov, V.; Cahil, A.; Šoptrajanov, B.; Najdoski, M.; Spirovski, F.; Engelen, B.; Lutz, H. D.; Koleva, V. Infrared and Raman spectra of magnesium ammonium phosphate hexahydrate (struvite) and its isomorphous analogues. VII: Spectra of protiated and partially deuterated hexagonal magnesium caesium phosphate hexahydrate. *Journal of Molecular Structure* **2009**, *924–926*, 100-106.
- (298) Ravikumar, R. V. S. S. N.; Chandrasekhar, A. V.; Reddy, B. J.; Reddy, Y. P.; Ikeda, K. X-ray powder diffraction, DTA and vibrational studies of $\text{CdNH}_4\text{PO}_4 \cdot 6\text{H}_2\text{O}$ crystals. *Crystal Research and Technology* **2002**, *37*, 1127-1132.
- (299) Abdija, Z.; Najdoski, M.; Koleva, V.; Runčevski, T.; Dinnebier, R. E.; Šoptrajanov, B.; Stefov, V. Preparation, structural, thermogravimetric and spectroscopic study of magnesium potassium arsenate hexahydrate. *Zeitschrift für anorganische und allgemeine Chemie* **2014**, *640*, 3177-3183.
- (300) Ravikumar, R. V. S. S. N.; Chandrasekhar, A. V.; Rao, S. N.; Madhu, N.; Reddy, B. J.; Reddy, Y. P. Orthorhombic Site Symmetry of Cr^{3+} in $\text{ZnNH}_4\text{PO}_4 \cdot 6\text{H}_2\text{O}$ Crystals. *Crystal Research and Technology* **1999**, *34*, 911-914.
- (301) Chand, P.; Agarwal, O. P. Electron paramagnetic resonance study of doped synthetic crystals of struvite and its zinc analogue. *Spectrochimica Acta Part A: Molecular Spectroscopy* **1991**, *47*, 775-783.
- (302) Lin, J.; Chen, N.; Pan, Y. Arsenic incorporation in synthetic struvite ($\text{NH}_4\text{MgPO}_4 \cdot 6\text{H}_2\text{O}$): A synchrotron XAS and single-crystal EPR study. *Environmental Science & Technology* **2013**, *47*, 12728-12735.
- (303) Griffith, D. P. Struvite stones. *Kidney Int* **1978**, *13*, 372-382.
- (304) Borgerding, J. Phosphate deposits in digestion systems. *Journal (water pollution control federation)* **1972**, *44*, 813-819.
- (305) Stratful, I.; Scrimshaw, M. D.; Lester, J. N. Conditions influencing the precipitation of magnesium ammonium phosphate. *Water Research* **2001**, *35*, 4191-4199.
- (306) Liu, Y.; Kwag, J.-H.; Kim, J.-H.; Ra, C. Recovery of nitrogen and phosphorus by struvite crystallization from swine wastewater. *Desalination* **2011**, *277*, 364-369.
- (307) Rouff, A. A. Sorption of chromium with struvite during phosphorus recovery. *Environmental Science & Technology* **2012**, *46*, 12493-12501.
- (308) Ronteltap, M.; Maurer, M.; Gujer, W. The behaviour of pharmaceuticals and heavy metals during struvite precipitation in urine. *Water Research* **2007**, *41*, 1859-1868.
- (309) Le Corre, K. S.; Valsami-Jones, E.; Hobbs, P.; Parsons, S. A. Phosphorus recovery from wastewater by struvite crystallization: A review. *Critical Reviews in Environmental Science and Technology* **2009**, *39*, 433-477.
- (310) Ueno, Y.; Fujii, M. Three years experience of operating and selling recovered struvite from full-scale plant. *Environmental Technology* **2001**, *22*, 1373-1381.
- (311) Postl, W.; Walter, F.; Ettinger, K.; Bojar, H.-P. Erster Nachweis des Kalium-Analogons $\text{MgK}(\text{PO}_4) \cdot 6\text{H}_2\text{O}$ von Struvit, und der kristallinen Phase $\text{Mg}_2\text{KH}(\text{PO}_4)_2 \cdot 15\text{H}_2\text{O}$ aus dem ehemaligen Bleibergbau Rossblei, Eschachalm, Schladminger Tauern, Steiermark, Österreich. *Joannea Mineralogie* **2000**, *1*, 45-52.

- (312) Graeser, S.; Postl, W.; Bojar, H.-P.; Berlepsch, P.; Armbruster, T.; Raber, T.; Ettinger, K.; Walter, F. Struvite-(K), $\text{KMgPO}_4 \cdot 6\text{H}_2\text{O}$, the potassium equivalent of struvite – a new mineral. *European Journal of Mineralogy* **2008**, *20*, 629-633.
- (313) Wagh, A. S.; Singh, D.; Sarkar, A. K.; Mayberry, J. Stabilization of low-level mixed waste in chemically bonded phosphate ceramics, In *International Topical Meeting on Nuclear and Hazardous Waste Management (Spectrum '94)*; Atlanta, GA, 1994.
- (314) Singh, D.; Tlustochowicz, M.; Wagh, A. S. Development of zirconium/magnesium phosphate composites for immobilization of fission products. *Journal of the American Ceramic Society* **1999**, *82*, 43-49.
- (315) Wagh, A. S.; Singh, D.; Jeong, S. Y.; Strain, R. V. Ceramicrete stabilization of low-level mixed wastes - A complete story, In *18th U.S. DOE Low-Level Radioactive Waste Management Conference*; Salt Lake City, UT, 1997.
- (316) Fan, S.; Chen, B. Experimental study of phosphate salts influencing properties of magnesium phosphate cement. *Construction and Building Materials* **2014**, *65*, 480-486.
- (317) Lide, D. R. *CRC Handbook of Chemistry and Physics, 88th Edition*, CRC Press: Boca Raton, FA, 2007.
- (318) Wagh, A. S. *Chemically bonded phosphate ceramics: Twenty-first century materials with diverse applications*, Elsevier Ltd.: Oxford, UK, 2004.
- (319) Cantrell, K. J.; Westik, J. H. *Secondary waste form down selection data package - Ceramicrete*; PNNL-20681; Pacific Northwest National Laboratory, National Technical Information Service: Springfield, VA, 2011.
- (320) Wagh, A. S.; Singh, D.; Jeong, S. Y.; Graczyk, D.; TenKate, L. B. Demonstration of packaging of Fernald silo I waste in chemically bonded phosphate ceramic, In *WM'99 Conference*; Tucson, AZ, 1999.
- (321) Josephson, G. B.; Westik, J. H.; Pires, R. P.; Bickford, J. L.; Foote, M. W. *Engineering-scale demonstration of Duralith and Ceramicrete waste forms*; PNNL-20751; Pacific Northwest National Laboratory, National Technical Information Service: Alexandria, VA, 2011.
- (322) *CRADA Final Report: Ceramicrete stabilization of radioactive-salt-containing liquid waste and sludge water*; ANL/NE/C0300701; Argonne National Laboratory, 2010.
- (323) Wagh, A. S.; Singh, D.; Jeong, S. Y. Method of waste stabilization via chemically bonded phosphate ceramics. U.S. Patent 5830815, 1998.
- (324) Wagh, A. S.; Jeong, S. Y.; McDaniel, R. Chemically bonded phosphate ceramic sealant formulations for oil field applications. U.S. Patent 7438755, 2008.
- (325) Wagh, A. S.; Paul, J. W. Composition and application of novel sprayable phosphate cement (Grancrete) that bonds to styrofoam. U.S. Patent 7160383, 2007.
- (326) Setiadi, A.; Milestone, N. B.; Hill, J.; Hayes, M. Corrosion of aluminium and magnesium in BFS composite cements. *Advances in Applied Ceramics* **2006**, *105*, 191-196.
- (327) Vargel, C. *Corrosion of Aluminium*, Elsevier Ltd: Oxford, UK, 2004.
- (328) Hoch, A. R.; Smart, N. R.; Wilson, J. D.; Reddy, B. *A survey of reactive metal corrosion data for use in the SMOGG gas generation model*; SA/ENV-0895; Serco Ltd: Harwell, UK, 2010;
- (329) Stefanko, D. B.; Langton, C.; Singh, D. *Magnesium mono potassium phosphate grout for p-reactor vessel in-situ decommissioning (U)*; SRNL-STI-2010-00333; Savannah River National Laboratory: Aiken, SC, 2010;

- (330) Langton, C.; Stefanko, D. B.; Serranto, M. G.; Blankenship, J. K.; Griffin, W. B.; Waymer, J. T.; Matheny, D.; Singh, D. Use of cementitious materials for SRS reactor facility in-situ decommissioning. In *Waste Management Conference*, Phoenix, AZ, 2011.
- (331) Federal Highway Administration. Pioneering precast in Alaska. *Highways for Life*.
- (332) Hall, D. A.; Stevens, R.; El-Jazairi, B. The effect of retarders on the microstructure and mechanical properties of magnesia–phosphate cement mortar. *Cement and Concrete Research* **2001**, *31*, 455-465.
- (333) Winbow, H. D. The chemistry and properties of magnesia-phosphate cement systems. Ph.D. Thesis, University of Sheffield, 1988.
- (334) European Chemicals Agency (ECHA). *Candidate list of substances of very high concern for authorisation*. <http://echa.europa.eu/candidate-list-table> (accessed Jun 14 2015), 2015).
- (335) Seehra, S. S.; Gupta, S.; Kumar, S. Rapid setting magnesium phosphate cement for quick repair of concrete pavements — characterisation and durability aspects. *Cement and Concrete Research* **1993**, *23*, 254-266.
- (336) Arora, A. *Text book of inorganic chemistry*, Discovery publishing house: New Delhi, India, 2005.
- (337) Sen Gupta, P. K.; Swihart, G. H.; Dimitrijević, R.; Hossain, M. B. The crystal structure of lünbergite, $Mg_3(H_2O)_6[B_2(OH)_6(PO_4)_2]$. *American Mineralogist* **1991**, *76*, 1400-1407.
- (338) Wagh, A. S.; Jeong, S. Y. Chemically bonded phosphate ceramics: I, A dissolution model of formation. *Journal of the American Ceramic Society* **2003**, *86*, 1838-1844.
- (339) Yue, L.; Bing, C. Factors that affect the properties of magnesium phosphate cement. *Construction and Building Materials* **2013**, *47*, 977-983.
- (340) Singh, D.; Ganga, R.; Gaviria, J.; Yusufoglu, Y. *Secondary waste form testing: Ceramicrete phosphate bonded ceramics*; ANL-11/16; Argonne National Laboratory: Argonne, IL, 2011;
- (341) Gardner, L. J.; Bernal, S. A.; Walling, S. A.; Corkhill, C. L.; Provis, J. L.; Hyatt, N. C. Characterisation of magnesium potassium phosphate cements blended with fly ash and ground granulated blast furnace slag. *Cement and Concrete Research* **2015**, *74*, 78-87.
- (342) Gardner, L. J. Ph.D. thesis, University of Sheffield, 2016.
- (343) Cummings, U. Cement. U.S. Patent 402511, 1889.
- (344) Steiger, J. Manufacture of cement. U.S. Patent 627884, 1899.
- (345) Ulich, A. Process of manufacturing artificial stones. U.S. Patent 644953, 1900.
- (346) Merritt, H. W. Plastic compound for walls, &c. U.S. Patent 322307, 1885.
- (347) Pater, C. J. Fire and water proof composition. U.S. Patent 1067542, 1913.
- (348) Ashenhurst, H. S. Asbestos cement. U.S. Patent 1317853, 1919.
- (349) Mershon, S. L. Refractory article of manufacture. U.S. Patent 730834, 1903.
- (350) Michell, H. C. Manufacture of non-conducting covering, blocks, and slabs. U.S. Patent 774947, 1904.
- (351) Cole, W. F. A crystalline hydrated magnesium silicate formed in the breakdown of a concrete sea-wall. *Nature* **1953**, *171*, 354-355.
- (352) Bonen, D. Composition and appearance of magnesium silicate hydrate and its relation to deterioration of cement-based materials. *Journal of the American Ceramic Society* **1992**, *75*, 2904-2906.

- (353) Brew, D. R. M.; Glasser, E. P. Reactions of sulphate-resistant Portland cement and its blends with silica fume and aqueous magnesium sulphate. *Advances in Cement Research* **2002**, *14*, 101-111.
- (354) Santhanam, M.; Cohen, M. D.; Olek, J. Mechanism of sulfate attack: a fresh look: Part 2. Proposed mechanisms. *Cement and Concrete Research* **2003**, *33*, 341-346.
- (355) Gollop, R. S.; Taylor, H. F. W. Microstructural and microanalytical studies of sulfate attack. I. Ordinary Portland cement paste. *Cement and Concrete Research* **1992**, *22*, 1027-1038.
- (356) Kunther, W.; Lothenbach, B.; Scrivener, K. Deterioration of mortar bars immersed in magnesium containing sulfate solutions. *Materials and Structures* **2013**, *46*, 2003-2011.
- (357) Gollop, R. S.; Taylor, H. F. W. Microstructural and microanalytical studies of sulfate attack III. Sulfate-resisting Portland cement: Reactions with sodium and magnesium sulfate solutions. *Cement and Concrete Research* **1995**, *25*, 1581-1590.
- (358) Mather, B. Field and laboratory studies of the sulfate resistance of concrete. In *Performance of concrete*, Swenson, E. G., Ed.; University of Toronto Press: Toronto, Canada, 1968; pp 67-76.
- (359) Cohen, M. D.; Bentur, A. Durability of Portland Cement-Silica Fume Pastes in Magnesium Sulfate and Sodium Sulfate Solutions. *Aci Materials Journal* **1988**, *85*, 148-157.
- (360) Brew, D. R. M.; Glasser, F. P. The magnesia-silica gel phase in slag cements: alkali (K, Cs) sorption potential of synthetic gels. *Cement and Concrete Research* **2005**, *35*, 77-83.
- (361) Sandberg, B.; Mosberg, T. Use of Elkem Microsilica in binder systems for ultra-low cement castables and basic, "cement-free" castables. In *Ceramic Transactions: Advances in Refractories Technology*, Fisher, R. E., Ed.; American Ceramic Society: Westerville, OH, 1989; Vol. 4, pp 245-258.
- (362) Ødegård, C.; Feldborg, H.; Myhre, B. Magnesia-silica-hydrate bonded MgO castables, In *Proceedings of Unified International Technical Conference on Refractories (UNITECR'01)*; Nov 4-8; Cancun, Mexico, 2001.
- (363) Myhre, B.; Ødegård, C.; Feldborg, H. Periclase castables based on the bond MgO - SiO₂ - H₂O, In *IREFCON (5th India International Refractories Congress)*; Feb 7-8; Bhubaneswar, India, 2002.
- (364) Szczerba, J.; Prorok, R.; Śniezek, E.; Madej, D.; Maślona, K. Influence of time and temperature on ageing and phases synthesis in the MgO-SiO₂-H₂O system. *Thermochimica Acta* **2013**, *567*, 57-64.
- (365) Chen, Y.; Wei, J. Hydrated magnesium silica system gelling material coagulating and hardening at normal temperature and its preparation method. Chinese Patent 1267374 C, 2006.
- (366) Chen, Y.; Wei, J. Hydrated magnesium silica and synthesis method thereof. Chinese Patent 1315726 C, 2007.
- (367) Wei, J.; Chen, Y.; Li, Y. The reaction mechanism between MgO and microsilica at room temperature. *Journal of Wuhan University of Technology-Mater. Sci. Ed.* **2006**, *21*, 88-91.
- (368) Wei, J.; Yu, Q.; Zhang, W.; Zhang, H. Reaction products of MgO and microsilica cementitious materials at different temperatures. *Journal of Wuhan University of Technology-Mater. Sci. Ed.* **2011**, *26*, 745-748.

- (369) Zhang, T.; Cheeseman, C. R.; Vandeperre, L. J. Development of low pH cement systems forming magnesium silicate hydrate (M-S-H). *Cement and Concrete Research* **2011**, *41*, 439-442.
- (370) Zhang, T.; Cheeseman, C.; Vandeperre, L. J. Characterisation of corrosion of nuclear metal wastes encapsulated in magnesium silicate hydrate (MSH) cement. In *Ceramic Materials for Energy Applications II*, John Wiley & Sons, Inc.: 2012; pp 159-167.
- (371) Zhang, T.; Vandeperre, L. J.; Cheeseman, C. R. Magnesium-silicate-hydrate cements for encapsulating problematic aluminium containing wastes. *Journal of Sustainable Cement-Based Materials* **2012**, *1*, 34-45.
- (372) Zhang, T.; Vandeperre, L. J.; Cheeseman, C. Bottom-up design of a cement for nuclear waste encapsulation. In *Ceramic Materials for Energy Applications*, John Wiley & Sons, Inc.: 2011; pp 41-49.
- (373) Walling, S. A.; Kinoshita, H.; Bernal, S. A.; Collier, N. C.; Provis, J. L. Structure and properties of binder gels formed in the system $Mg(OH)_2-SiO_2-H_2O$ for immobilisation of Magnox sludge. *Dalton Transactions* **2015**, *44*, 8126-8137.
- (374) Berner, U.; Kulik, D. A.; Kosakowski, G. Geochemical impact of a low-pH cement liner on the near field of a repository for spent fuel and high-level radioactive waste. *Physics and Chemistry of the Earth, Parts A/B/C* **2013**, *64*, 46-56.
- (375) Posiva Oy. *Effects of cementitious leachates on the EBS*; Posiva 2013-04; Posiva: 2014;
- (376) Lothenbach, B.; Le Saout, G.; Ben Haha, M.; Figi, R.; Wieland, E. Hydration of a low-alkali CEM III/B-SiO₂ cement (LAC). *Cement and Concrete Research* **2012**, *42*, 410-423.
- (377) Pusch, R.; Zwahr, H.; Gerber, R.; Schomburg, J. Interaction of cement and smectitic clay—theory and practice. *Applied Clay Science* **2003**, *23*, 203-210.
- (378) Honty, M.; De Craen, M.; Wang, L.; Madejová, J.; Czímerová, A.; Pentrák, M.; Stríček, I.; Van Geet, M. The effect of high pH alkaline solutions on the mineral stability of the Boom Clay – Batch experiments at 60 °C. *Applied Geochemistry* **2010**, *25*, 825-840.
- (379) Savage, D.; Walker, C.; Arthur, R.; Rochelle, C.; Oda, C.; Takase, H. Alteration of bentonite by hyperalkaline fluids: A review of the role of secondary minerals. *Physics and Chemistry of the Earth, Parts A/B/C* **2007**, *32*, 287-297.
- (380) Kosakowski, G.; Berner, U. The evolution of clay rock/cement interfaces in a cementitious repository for low- and intermediate level radioactive waste. *Physics and Chemistry of the Earth, Parts A/B/C* **2013**, *64*, 65-86.
- (381) Codina, M.; Cau-dit-Coumes, C.; Le Bescop, P.; Verdier, J.; Ollivier, J. P. Design and characterization of low-heat and low-alkalinity cements. *Cement and Concrete Research* **2008**, *38*, 437-448.
- (382) García Calvo, J. L.; Hidalgo, A.; Alonso, C.; Fernández Luco, L. Development of low-pH cementitious materials for HLRW repositories: Resistance against ground waters aggression. *Cement and Concrete Research* **2010**, *40*, 1290-1297.
- (383) Cau Dit Coumes, C.; Courtois, S.; Nectoux, D.; Leclercq, S.; Bourbon, X. Formulating a low-alkalinity, high-resistance and low-heat concrete for radioactive waste repositories. *Cement and Concrete Research* **2006**, *36*, 2152-2163.
- (384) Lothenbach, B.; Rentsch, D.; Wieland, E. Hydration of a silica fume blended low-alkali shotcrete cement. *Physics and Chemistry of the Earth, Parts A/B/C* **2014**, *70-71*, 3-16.

- (385) Dauzeres, A.; Achiedo, G.; Nied, D.; Bernard, E.; Alahrache, S.; Lothenbach, B. Magnesium perturbation in low-pH concretes placed in clayey environment—solid characterizations and modeling. *Cement and Concrete Research* **2016**, *79*, 137-150.
- (386) Jenni, A.; Mäder, U.; Lerouge, C.; Gaboreau, S.; Schwyn, B. In situ interaction between different concretes and Opalinus Clay. *Physics and Chemistry of the Earth, Parts A/B/C* **2014**, *70–71*, 71-83.
- (387) Kalousek, G. L.; Mui, D. Studies on formation and recrystallization of intermediate reaction products in the system magnesia-silica-water. *Journal of the American Ceramic Society* **1954**, *37*, 38-42.
- (388) Yang, J. C.-S. The system magnesia-silica-water below 300°C.: I, Low-temperature phases from 100° to 300°C and their properties. *Journal of the American Ceramic Society* **1960**, *43*, 542-549.
- (389) Temuujin, J.; Okada, K.; MacKenzie, K. J. D. Formation of layered magnesium silicate during the aging of magnesium hydroxide–silica mixtures. *Journal of the American Ceramic Society* **1998**, *81*, 754-756.
- (390) Temuujin, J.; Okada, K.; MacKenzie, K. J. D. Role of water in the mechanochemical reactions of MgO-SiO₂ systems. *Journal of Solid State Chemistry* **1998**, *138*, 169-177.
- (391) Mitsuda, T.; Taguchi, H. Formation of magnesium silicate hydrate and its crystallization to talc. *Cement and Concrete Research* **1977**, *7*, 223-230.
- (392) Gunnarsson, I.; Arnórsson, S.; Jakobsson, S. Precipitation of poorly crystalline antigorite under hydrothermal conditions. *Geochimica et Cosmochimica Acta* **2005**, *69*, 2813-2828.
- (393) Brew, D. R. M.; Glasser, F. P. Synthesis and characterisation of magnesium silicate hydrate gels. *Cement and Concrete Research* **2005**, *35*, 85-98.
- (394) Capitani, G.; Mellini, M. The modulated crystal structure of antigorite: The m = 17 polysome. *American Mineralogist* **2004**, *89*, 147-158.
- (395) Mellini, M. The crystal structure of lizardite 1T: hydrogen bonds and polytypism. *American Mineralogist* **1982**, *67*, 587-598.
- (396) Perdikatsis, B.; Burzlaff, H. Strukturverfeinerung am Talk Mg₃[(OH)₂Si₄O₁₀]. *Zeitschrift für Kristallographie* **1981**, *156*, 177-186.
- (397) Liao, J.; Senna, M. Thermal behavior of mechanically amorphized talc. *Thermochimica Acta* **1992**, *197*, 295-306.
- (398) Suquet, H. Effects of dry grinding and leaching on the crystal structure of chrysotile. *Clays and Clay Minerals* **1989**, *37*, 439-445.
- (399) Aglietti, E. F. The effect of dry grinding on the structure of talc. *Applied Clay Science* **1994**, *9*, 139-147.
- (400) Drief, A.; Nieto, F. The effect of dry grinding on antigorite from Mulhacen, Spain. *Clays and Clay Minerals* **1999**, *47*, 417-424.
- (401) Roosz, C.; Grangeon, S.; Blanc, P.; Montouillout, V.; Lothenbach, B.; Henocq, P.; Giffaut, E.; Vieillard, P.; Gaboreau, S. Crystal structure of magnesium silicate hydrates (M-S-H): The relation with 2:1 Mg–Si phyllosilicates. *Cement and Concrete Research* **2015**, *73*, 228-237.
- (402) Sorel, S. Improved composition to be used as a cement and as a plastic material for molding various articles. U.S. Patent 53092, 1866.
- (403) Sorel, S. Sur un nouveau ciment magnésien. *Comptes Rendus Hebdomadaires Des Séances De L'Académie Des Sciences* **1867**, *65*, 102-104.
- (404) Shaw, J. B.; Bole, G. A. New developments in oxychloride stucco and flooring. *Journal of the American Ceramic Society* **1922**, *5*, 311-321.

- (405) Malkin, S.; Guo, C. *Grinding technology : theory and applications of machining with abrasives*, 2nd ed.; Industrial Press: New York, NY, 2008.
- (406) Skolnik, M. Burial vault and method of making same. U.S. Patent 2340209, 1944.
- (407) Paterson, J. H. Magnesium oxychloride cement. *Journal of the Society of Chemical Industry* **1924**, *43*, 215-218.
- (408) Greenleaf, E. F. Rubber deck covering used on ships. *Bureau of Ships Journal* **1952**, *1* (No.3), 26-29.
- (409) The "Olympic" and the "Titanic". *Scientific American Supplement*, Jun 17, **1911**, 380-383.
- (410) Harper, F. C. Effect of calcination temperature on the properties of magnesium oxides for use in magnesium oxychloride cements. *Journal of Applied Chemistry* **1967**, *17*, 5-10.
- (411) Matković, B.; Popović, S.; Rogić, V.; Žunić, T.; Young, J. F. Reaction products in magnesium oxychloride cement pastes. System MgO-MgCl₂-H₂O. *Journal of the American Ceramic Society* **1977**, *60*, 504-507.
- (412) Li, Z.; Chau, C. K. Influence of molar ratios on properties of magnesium oxychloride cement. *Cement and Concrete Research* **2007**, *37*, 866-870.
- (413) Dinnebier, R. E.; Oestreich, M.; Bette, S.; Freyer, D. 2Mg(OH)₂·MgCl₂·2H₂O and 2Mg(OH)₂·MgCl₂·4H₂O, two high temperature phases of the magnesia cement system. *Zeitschrift für anorganische und allgemeine Chemie* **2012**, *638*, 628-633.
- (414) Bianco, Y. Formation des chlorures basiques de magnésium de 50° à 175°, par voie aqueuse. *Comptes Rendus Hebdomadaires Des Séances De L'Académie Des Sciences* **1951**, *232*, 1108-1110.
- (415) Cole, W.; Demediuk, T. X-Ray, thermal, and dehydration studies on magnesium oxychlorides. *Australian Journal of Chemistry* **1955**, *8*, 234-251.
- (416) Kurdowski, W. The protective layer and decalcification of C-S-H in the mechanism of chloride corrosion of cement paste. *Cement and Concrete Research* **2004**, *34*, 1555-1559.
- (417) Peterson, K.; Julio-Betancourt, G.; Sutter, L.; Hooton, R. D.; Johnston, D. Observations of chloride ingress and calcium oxychloride formation in laboratory concrete and mortar at 5 °C. *Cement and Concrete Research* **2013**, *45*, 79-90.
- (418) Bender, C. Ueber die Hydrate des Magnesiumoxychlorids. *Justus Liebigs Annalen der Chemie* **1871**, *159*, 341-349.
- (419) Krause, O. Ueber Magnesiumoxychlorid. *Justus Liebigs Annalen der Chemie* **1873**, *165*, 38-44.
- (420) Robinson, W. O.; Waggaman, W. H. Basic magnesium chlorides. *Journal of Physical Chemistry* **1909**, *13*, 673-678.
- (421) Lukens, H. S. The composition of magnesium oxychloride. *Journal of the American Chemical Society* **1932**, *54*, 2372-2380.
- (422) Walter-Lévy, L. Chlorocarbonate basique de magnésium. *Comptes Rendus Hebdomadaires Des Séances De L'Académie Des Sciences* **1937**, *204*, 1943-1946.
- (423) Walter-Lévy, L.; de Wolff, P. M. Contribution à l'étude du ciment Sorel. *Comptes Rendus Hebdomadaires Des Séances De L'Académie Des Sciences* **1949**, *229*, 1077-1079.
- (424) Feitknecht, W. Über das Verhalten von schwer löslichen Metalloxyden in den Lösungen ihrer Salze. Zur Kenntnis der Magnesiumoxyd-Zemente I. *Helvetica Chimica Acta* **1926**, *9*, 1018-1049.

- (425) Feitknecht, W. Über das Verhalten von schwerlöslichen Metalloxyden in den Lösungen ihrer Salze. Zur Kenntnis der Magnesiumoxyd-Zemente II. *Helvetica Chimica Acta* **1927**, *10*, 140-167.
- (426) Feitknecht, W. Röntgenographische Untersuchungen der basischen Chloride des Magnesiums. Zur Kenntnis der Magnesiumoxyd-Zemente III. *Helvetica Chimica Acta* **1930**, *13*, 1380-1390.
- (427) Feitknecht, W.; Held, F. Über die Hydroxychloride des Magnesiums. *Helvetica Chimica Acta* **1944**, *27*, 1480-1495.
- (428) de Wolff, P. M.; Walter-Lévy, L. Structures et formules de quelques constituants du ciment Sorel. *Comptes Rendus Hebdomadaires Des Séances De L'Académie Des Sciences* **1949**, *229*, 1232-1234.
- (429) de Wolff, P. M.; Walter-Lévy, L. The crystal structure of $\text{Mg}_2(\text{OH})_3(\text{Cl},\text{Br})\cdot 4\text{H}_2\text{O}$. *Acta Crystallographica* **1953**, *6*, 40-44.
- (430) Sugimoto, K.; Dinnebier, R. E.; Schlecht, T. Structure determination of $\text{Mg}_3(\text{OH})_5\text{Cl}\cdot 4\text{H}_2\text{O}$ (F5 phase) from laboratory powder diffraction data and its impact on the analysis of problematic magnesia floors. *Acta Crystallographica Section B* **2007**, *63*, 805-811.
- (431) Sugimoto, K.; Dinnebier, R. E.; Schlecht, T. Chlorartinite, a volcanic exhalation product also found in industrial magnesia screed. *Journal of Applied Crystallography* **2006**, *39*, 739-744.
- (432) Walter-Lévy, L.; Bianco, Y. Action de la magnésie sur les solutions de chlorure de magnésium à 100°. *Comptes Rendus Hebdomadaires Des Séances De L'Académie Des Sciences* **1951**, *232*, 730-732.
- (433) Dinnebier, R. E.; Freyer, D.; Bette, S.; Oestreich, M. $9\text{Mg}(\text{OH})_2\cdot\text{MgCl}_2\cdot 4\text{H}_2\text{O}$, a high temperature phase of the magnesia binder system. *Inorganic Chemistry* **2010**, *49*, 9770-9776.
- (434) Newman, E. S.; Gilfrich, J. V.; Wells, L. S. Heat generation in the setting of magnesium oxychloride cements. *Journal of Research of the National Bureau of Standards* **1952**, *49*, 377-383.
- (435) Runčevski, T.; Dinnebier, R. E.; Freyer, D. Dehydration of the Sorel cement phase $3\text{Mg}(\text{OH})_2\cdot\text{MgCl}_2\cdot 8\text{H}_2\text{O}$ studied by in situ synchrotron X-ray powder diffraction and thermal analyses. *Zeitschrift für anorganische und allgemeine Chemie* **2014**, *640*, 100-105.
- (436) Altmaier, M.; Metz, V.; Neck, V.; Müller, R.; Fanghänel, T. Solid-liquid equilibria of $\text{Mg}(\text{OH})_2$ (cr) and $\text{Mg}_2(\text{OH})_3\text{Cl}\cdot 4\text{H}_2\text{O}$ (cr) in the system Mg-Na-H-OH-Cl-H₂O at 25 °C. *Geochimica et Cosmochimica Acta* **2003**, *67*, 3595-3601.
- (437) Xiong, Y.; Deng, H.; Nemer, M.; Johnsen, S. Experimental determination of the solubility constant for magnesium chloride hydroxide hydrate ($\text{Mg}_3\text{Cl}(\text{OH})_5\cdot 4\text{H}_2\text{O}$, phase 5) at room temperature, and its importance to nuclear waste isolation in geological repositories in salt formations. *Geochimica et Cosmochimica Acta* **2010**, *74*, 4605-4611.
- (438) Tooper, B.; Cartz, L. Structure and formation of magnesium oxychloride Sorel cements. *Nature* **1966**, *211*, 64-66.
- (439) Matkovic, B.; Young, J. F. Microstructure of magnesium oxychloride cements. *Nature physical science* **1973**, *246*, 79-80.
- (440) Sorrell, C. A.; Armstrong, C. R. Reactions and equilibria in magnesium oxychloride cements. *Journal of the American Ceramic Society* **1976**, *59*, 51-54.
- (441) Urwongse, L.; Sorrell, C. A. The system $\text{MgO}\text{-MgCl}_2\text{-H}_2\text{O}$ at 23°C. *Journal of the American Ceramic Society* **1980**, *63*, 501-504.

- (442) Chau, C. K.; Li, Z. Microstructures of magnesium oxychloride Sorel cement. *Advances in Cement Research* **2008**, *20*, 85-92.
- (443) Chau, C. K.; Li, Z. Microstructures of magnesium oxychloride. *Materials and Structures* **2008**, *41*, 853-862.
- (444) Macphee, D. E.; Lachowski, E. E. Cement components and their phase relations. In *Lea's Chemistry of Cement and Concrete*, 4th ed.; Hewlett, P. C., Ed.; Butterworth Heinemann: Oxford, UK, 2003; pp 95-129.
- (445) Papanikolaou, A. *The restoration of the Erechtheion (1979-1987) : Final report on the work; Reports on the Acropolis restoration works 1*; Hellenic Ministry of Education and Religious affairs, Culture and Sports: Athens, Greece, 2012;
- (446) Papakonstantinou, E.; Panou, A.; Franzikinaki, K.; Tsimereki, A.; Frantzi, G. The surface conservation project of the acropolis monuments: Studies and interventions, In *XXI International CIPA symposium*; Oct 1-6; Athens, Greece, 2007.
- (447) Maravelaki-Kalaitzaki, P.; Moraitou, G. Sorel's cement mortars decay susceptibility and effect on Pentelic marble. *Cement and Concrete Research* **1999**, *29*, 1929-1935.
- (448) Castellar, M. D.; Lorente, J. C.; Traveria, A.; Tura, J. M. Cracks in Sorel's cement polishing bricks as a result of magnesium oxychloride carbonation. *Cement and Concrete Research* **1996**, *26*, 1199-1202.
- (449) Bilinski, H.; Matković, B.; Mažuranić, C.; Žunić, T. The formation of magnesium oxychloride phases in the systems MgO-MgCl₂-H₂O and NaOH-MgCl₂-H₂O. *Journal of the American Ceramic Society* **1984**, *67*, 266-269.
- (450) Alegret, S.; Blanco, M.; Subirats, R. Potentiometric study of the reactivity of calcined magnesites for use in magnesium oxychloride cements. *Journal of the American Ceramic Society* **1984**, *67*, 579-582.
- (451) Bates, P. H.; Young, R. N. Plastic magnesia cements. *Journal of the American Ceramic Society* **1921**, *4*, 570-596.
- (452) Sorel, S. Improvement in the manufacture of cement for artificial stone. U.S. Patent 100944, 1870.
- (453) Alley, R. I.; Caine, G. E. Magnesium oxychloride cement compositions and methods for manufacture and use. U.S. Patent 5001505, 1991.
- (454) Caine, G. E.; Ellis, C. W. Magnesium oxychloride cement. U.S. Patent 7794688, 2010.
- (455) Yu, H.; Wen, J.; Dong, J.; Ying, L. Magnesium oxychloride cement mixed by water. Chinese Patent 102674725B, 2014.
- (456) Xia, S.; Xing, P.; Gao, S. Studies on the basic compounds of magnesia cement: the thermal behaviour of magnesium oxychlorides. *Thermochimica Acta* **1991**, *183*, 349-363.
- (457) Li, C.; Yu, H. Influence of fly ash and silica fume on water-resistant property of magnesium oxychloride cement. *Journal of Wuhan University of Technology-Mater. Sci. Ed.* **2010**, *25*, 721-724.
- (458) McCaughey, W. J. Oxychloride cement and process of making same. U.S. Patent 1634505, 1927.
- (459) Bole, G. A.; Shaw, J. B. The caustic calcination of dolomite and its use in Sorrel cements. *Journal of the American Ceramic Society* **1922**, *5*, 817-822.
- (460) Bidtel, E. Magnesia cement composition. U.S. Patent 757252, 1904.
- (461) Dudley, W. L. Magnesia-cement composition. U.S. Patent 839820, 1907.
- (462) MacKenzie, K. J. D.; Meinhold, R. H. Thermal decomposition of dolomite (calcium magnesium carbonate) studied by ²⁵Mg solid-state nuclear magnetic resonance. *Thermochimica Acta* **1993**, *230*, 331-337.

- (463) Haul, R. A. W.; Heystek, H. Differential thermal analysis of the dolomite decomposition. *American Mineralogist* **1952**, *37*, 166-179.
- (464) Sharp, J. H.; Wilburn, F. W.; McIntosh, R. M. The effect of procedural variables on TG, DTG and DTA curves of magnesite and dolomite. *Journal of Thermal Analysis* **1991**, *37*, 2021-2029.
- (465) McIntosh, R. M.; Sharp, J. H.; Wilburn, F. W. The thermal decomposition of dolomite. *Thermochimica Acta* **1990**, *165*, 281-296.
- (466) Kacker, K. P.; Mehrotra, G. S.; Rai, M. Petrographic and thermal evaluation of dolomites for the manufacture of magnesium oxychloride cement. *Journal of Applied Chemistry* **1970**, *20*, 189-193.
- (467) Shannon, R. Revised effective ionic radii and systematic studies of interatomic distances in halides and chalcogenides. *Acta Crystallographica Section A* **1976**, *32*, 751-767.
- (468) Elliott, J. S.; Wood, J. F. Improvement in the manufacture of imitation marble. U.S. Patent 124557, 1872.
- (469) Elliott, J. S.; Wood, J. F. Improvement in process of repairing millstones. U.S. Patent 124559, 1872.
- (470) Wood, J. F. Improvement in composition covers for coal-holes. U.S. Patent 133513, 1872.
- (471) Sorrell, C. A. Suggested chemistry of zinc oxychloride cements. *Journal of the American Ceramic Society* **1977**, *60*, 217-220.
- (472) Hubbell, D. S. A new inorganic cement and adhesive. *Industrial and Engineering Chemistry* **1937**, *29*, 123-132.
- (473) Hubbell, D. S. The formation of atacamite by the incorporation of copper powder in magnesium oxychloride compositions. *Journal of the American Chemical Society* **1937**, *59*, 215-216.
- (474) Hubbell, D. S. Cementitious material. U.S. Patent 2058984, 1936.
- (475) Hubbell, D. S. Cementitious material. U.S. Patent 2218679, 1940.
- (476) Hubbell, D. S. Sorel cement. U.S. Patent 2450513, 1948.
- (477) Whitehead, E. D. F. Oxychloride cementary material. U.S. Patent 2462030, 1949.
- (478) Farrell, M. A.; Wolff, R. T. Effect of cupric oxychloride cement on microorganisms. *Industrial and Engineering Chemistry* **1941**, *33*, 1185-1188.
- (479) Ryan, W. V. Cupric oxychloride cement foodservice flooring. U.S. Patent 6159280, 2000.
- (480) Zhou, Z.; Chen, H.; Li, Z.; Li, H. Simulation of the properties of MgO-Mg₂Cl₂-H₂O system by thermodynamic method. *Cement and Concrete Research* **2015**, *68*, 105-111.
- (481) Mielck, H. Magnesia-cement composition. U.S. Patent 764250, 1904.
- (482) Austin, L. W.; Rhodes, D. Stabilized Sorel cement and method of making. U.S. Patent 2466145, 1949.
- (483) Chau, C. K.; Chan, J.; Li, Z. Influences of fly ash on magnesium oxychloride mortar. *Cement and Concrete Composites* **2009**, *31*, 250-254.
- (484) Harrell, B. R.; Prindle, H. B.; Edwards, S. P. Addition of melamine-formaldehyde to magnesium oxycement to improve the resistance to the passage of water of said cement. U.S. Patent 3238155, 1966.
- (485) Wang, S.; Weng, R.; Zhu, Y.; Li, X.; Xi, Y. Effects of EVA latex on the properties of glass-fiber / magnesium-oxychloride cement composites. *Journal of Wuhan University of Technology-Mater. Sci. Ed.* **2006**, *21*, 139-142.

- (486) Li, J.; Li, G.; Yu, Y. The influence of compound additive on magnesium oxychloride cement/urban refuse floor tile. *Construction and Building Materials* **2008**, *22*, 521-525.
- (487) Stewart, L. C. Magnesia cement composition. U.S. Patent 1853522, 1932.
- (488) Deng, D. The mechanism for soluble phosphates to improve the water resistance of magnesium oxychloride cement. *Cement and Concrete Research* **2003**, *33*, 1311-1317.
- (489) Tan, Y.; Liu, Y.; Grover, L. Effect of phosphoric acid on the properties of magnesium oxychloride cement as a biomaterial. *Cement and Concrete Research* **2014**, *56*, 69-74.
- (490) Montle, J. F.; Mayhan, K. G. The role of magnesium oxychloride as a fire-resistive material. *Fire Technology* **1974**, *10*, 201-210.
- (491) Prymelski, F. Building materials in the form of woodstone panels or sheets and processes for their production. U.S. Patent 4150185, 1979.
- (492) Verth, J. Z.; Prymelski, F. Xyloolith building boards and sheets. U.S. Patent 3788870, 1974.
- (493) Feigin, M. E.; Choi, T. S. Magnesium oxide-based construction board. U.S. Patent 7998547, 2011.
- (494) MagBoard. MagBoard building systems. <http://www.mag-board.com/> (accessed Apr 8 2015),
- (495) Euroform Products. Magnaliner | Magnesium Oxide Board. <http://www.euroform.co.uk/Magnaliner-Magnesium-Oxide-Board.shtml> (accessed Apr 8 2015),
- (496) Lin, Q.-h. Process for producing gm-siding with wood grain. U.S. Patent 8025755, 2011.
- (497) Smith-Johannsen, R. Cement compositions. U.S. Patent 4209339, 1980.
- (498) Biefeld, L. P.; Armstrong, M. C.; Shannon, R. F. Bonded glass fiber product and method of making same. U.S. Patent 2717841, 1955.
- (499) King, B. J.; Totten, P. L. Well cementing method using acid removable low density well cement compositions. U.S. Patent 5213161, 1993.
- (500) Robertson, B.; Fowler, I. A. Rapid setting plugging compositions for sealing subterranean formations. U.S. Patent 7544641, 2009.
- (501) Reddy, B. R.; Lewis, S. J.; Santra, A. K.; Palmer, A. V. Wellbore sealant compositions containing cationic latexes. U.S. Patent. 7687440, 2010.
- (502) Bensted, J. Special cements. In *Lea's Chemistry of Cement and Concrete*, 4th ed.; Hewlett, P. C., Ed.; Butterworth Heinemann: Oxford, UK, 2003; pp 783-840.
- (503) Barthel, H. Composition and process for strengthening and sealing geological formations and strata in mining and deep drilling. U.S. Patent 3816148, 1974.
- (504) Freyer, D.; Gruner, M.; Priestel, U. Aushärtbare Baustoffmischung und deren Verwendungen. Ger. Patent 102010024974B4, 2012.
- (505) Brennecke, P. W. Radioactive waste disposal challenges in germany, In *WM2011 Conference*; Feb 27 - Mar 3; Phoenix, AZ, 2011.
- (506) Bundesamt für Strahlenschutz. *Endlager Asse II: Aktueller Stand der Arbeiten zur Stabilisierung und sicheren Schließung, September 2010*; Bundesamt für Strahlenschutz: Salzgitter, Germany, 2010;
- (507) Müller-Hoeppel, N.; Buhmann, D.; Czaikowski, O.; Engelhardt, H.-J.; Herbert, H.-J.; Lerch, C.; Linkamp, M.; Wiczorek, K.; Xie, M. *Integrität geotechnischer Barrieren: Teil 1 Vorbemessung - AP 9.2*; GRS - 287; Gesellschaft für Anlagen- und Reaktorsicherheit: Köln, Germany, 2012;

- (508) Krauke, W.; Fliß, T. *Konzeptplanung und Nachweisführung für ein Abdichtungsbauwerk im Hauptanhydrit aus Magnesiabiner; Planfeststellungsverfahren zur Stilllegung des Endlagers für radioaktive Abfälle Morsleben*; Bundesamt für Strahlenschutz: Salzgitter, Germany, 2008;
- (509) Enricht, L. Artificial stone or cement. U.S. Patent 448513, 1891.
- (510) Enricht, L. Manufacture of cement. U.S. Patent 486444, 1892.
- (511) Rueff, E. Magnesium cement and process of making the same. U.S. Patent 872375, 1907.
- (512) Jeroch, W. Magnesium cement and process of manufacturing same. U.S. Patent 833930, 1906.
- (513) Ryosaku Matsuura, S. Method of manufacturing a magnesia cement. U.S. Patent 1946327, 1934.
- (514) Thugutt, S. J. Mineralchemische Studien. *Zeitschrift für anorganische Chemie* **1892**, 2, 113-156.
- (515) Walter-Lévy, L. Contribution à l'étude des sulfates basiques de magnésium. *Comptes Rendus Hebdomadaires Des Séances De L'Académie Des Sciences* **1936**, 202, 1857-1859.
- (516) Walter-Lévy, L. Sulfatocarbonate basique de magnésium. *Comptes Rendus Hebdomadaires Des Séances De L'Académie Des Sciences* **1936**, 202, 1074-1076.
- (517) Dinnebier, R. E.; Pannach, M.; Freyer, D. $3\text{Mg}(\text{OH})_2 \cdot \text{MgSO}_4 \cdot 8\text{H}_2\text{O}$: A metastable phase in the system $\text{Mg}(\text{OH})_2$ - MgSO_4 - H_2O . *Zeitschrift für anorganische und allgemeine Chemie* **2013**, 639, 1827-1833.
- (518) Demediuk, T.; Cole, W. F. A study of magnesium oxysulfates. *Australian Journal of Chemistry* **1957**, 10, 287-294.
- (519) Runčevski, T.; Wu, C.; Yu, H.; Yang, B.; Dinnebier, R. E. Structural characterization of a new magnesium oxysulfate hydrate cement phase and its surface reactions with atmospheric carbon dioxide. *Journal of the American Ceramic Society* **2013**, 96, 3609-3616.
- (520) Urwongse, L.; Sorrell, C. A. Phase relations in magnesium oxysulfate cements. *Journal of the American Ceramic Society* **1980**, 63, 523-526.
- (521) Wu, C.; Yu, H.; Zhang, H.; Dong, J.; Wen, J.; Tan, Y. Effects of phosphoric acid and phosphates on magnesium oxysulfate cement. *Materials and Structures* **2013**, 48, 1-11.
- (522) Bischoff, J. L.; Seyfried, W. E. Hydrothermal chemistry of seawater from 25° to 350°C. *American Journal of Science* **1978**, 278, 838-860.
- (523) Keefer, K. D.; Hochella Jr, M. F.; Jong, B. The structure of magnesium hydroxide sulfate hydrate $\text{MgSO}_4 \cdot 1/3\text{Mg}(\text{OH})_2 \cdot 1/3\text{H}_2\text{O}$. *Acta Crystallographica Section B* **1981**, 37, 1003-1006.
- (524) Hamada, E.; Ishizawa, N.; Manumo, F.; Ohsumi, K.; Shimizugawa, Y.; Reizen, K.; Matsunami, T. Structure of $\text{Mg}_6\text{SO}_2(\text{OH})_{14}$ determined by micro-crystal X-ray diffraction. *Acta Crystallographica Section B* **1996**, 52, 266-269.
- (525) Fleet, M. E.; Knipe, S. W. Structure of magnesium hydroxide sulfate $[2\text{MgSO}_4 \cdot \text{Mg}(\text{OH})_2]$ and solid solution in magnesium hydroxide sulfate hydrate and caminite. *Acta Crystallographica Section B* **1997**, 53, 358-363.
- (526) Tao, Y.; Shiyang, G.; Lixia, Z.; Shuping, X.; Kaibei, Y. Crystal growth and crystal structure of magnesium oxysulfate $2\text{MgSO}_4 \cdot \text{Mg}(\text{OH})_2 \cdot 2\text{H}_2\text{O}$. *Journal of Molecular Structure* **2002**, 616, 247-252.
- (527) Haymon, R. M.; Kastner, M. Caminite: A new magnesium-hydroxide-sulfate-hydrate mineral found in a submarine hydrothermal deposit, East Pacific Rise, 21°N. *American Mineralogist* **1986**, 71, 819-825.

- (528) Gao, C.; Li, X.; Feng, L.; Xiang, Z.; Zhang, D. Preparation and thermal decomposition of $5\text{Mg}(\text{OH})_2 \cdot \text{MgSO}_4 \cdot 2\text{H}_2\text{O}$ nanowhiskers. *Chemical Engineering Journal* **2009**, *150*, 551-554.
- (529) Xiang, L.; Liu, F.; Li, J.; Jin, Y. Hydrothermal formation and characterization of magnesium oxysulfate whiskers. *Materials Chemistry and Physics* **2004**, *87*, 424-429.
- (530) Zhou, Z.; Deng, Y. Solution synthesis of magnesium hydroxide sulfate hydrate nanobelts using sparingly soluble carbonate salts as supersaturation control agents. *Journal of Colloid and Interface Science* **2007**, *316*, 183-188.
- (531) Zhou, Z.; Sun, Q.; Hu, Z.; Deng, Y. Nanobelt formation of magnesium hydroxide sulfate hydrate via a soft chemistry process. *The Journal of Physical Chemistry B* **2006**, *110*, 13387-13392.
- (532) Biefeld, L. P. Inorganic structural sheet material. U.S. Patent 2712512, 1955.
- (533) Popielinski, D. F.; Keller, J. A. Method of forming magnesium oxysulfate. U.S. Patent 3506465, 1970.
- (534) Cullity, B. D.; Stock, S. R. *Elements of X-Ray Diffraction*, Prentice Hall: Upper Saddle River, NJ, 2001.
- (535) Paulus, E. F.; Gieren, A. Structure analysis by diffraction. In *Ullmann's Encyclopedia of Industrial Chemistry*, Wiley-VCH Verlag GmbH & Co. KGaA: 2000.
- (536) Taylor, J. C.; Aldridge, L. P.; Matulis, C. E.; Hinczak, I. X-ray powder diffraction analysis of cements. In *Structure and performance of cements*, 2nd ed.; Bensted, J., Barnes, P., Eds.; Spon Press: London, 2002; pp 420-441.
- (537) STOE & Cie GmbH. *STOE Win XPOW*, 2.10; Darmstadt, Germany, 2004.
- (538) Stuart, B. H. *Infrared Spectroscopy: Fundamentals and Applications*, John Wiley & Sons: Hoboken, NJ, 2004.
- (539) Gremlich, H.-U. Infrared and raman spectroscopy. In *Ullmann's Encyclopedia of Industrial Chemistry*, Wiley-VCH Verlag GmbH & Co. KGaA: 2000.
- (540) Larkin, P. *Infrared and Raman Spectroscopy: Principles and Spectral Interpretation*, Elsevier: Oxford, UK, 2011.
- (541) Skibsted, J.; Hall, C.; Jakobsen, H. J. Nuclear magnetic resonance spectroscopy and magnetic resonance imaging of cements and cement-based materials. In *Structure and performance of cements*, 2nd ed.; Bensted, J., Barnes, P., Eds.; Spon Press: London, 2002; pp 457-476.
- (542) Meusinger, R.; Chippendale, A. M. Nuclear Magnetic Resonance Spectroscopy. In *Ullmann's Encyclopedia of Industrial Chemistry*, Wiley-VCH Verlag GmbH & Co. KGaA: 2000.
- (543) MacKenzie, K. J. D.; Smith, M. E. *Multinuclear Solid-State NMR of Inorganic Materials*, Pergamon: 2002; Vol. 6.
- (544) Apperley, D. C.; Harris, R. K.; Hodgkinson, P. *Solid-state NMR: Basic principles & practice*, Momentum Press: New York, NY, 2012.
- (545) Reed, S. J. B. *Electron microprobe analysis and scanning electron microscopy in geology*, 2nd ed.; Cambridge University Press: Cambridge, 2005.
- (546) Watt, I. M. *The principles and practice of electron microscopy*, 2nd ed.; Cambridge University Press: Cambridge, 1997.
- (547) Richardson, I. G. Electron microscopy of cements. In *Structure and performance of cements*, 2nd ed.; Bensted, J., Barnes, P., Eds.; Spon Press: London, 2002; pp 500-556.

- (548) Smykatz-Kloss, W.; Heide, K.; Klinke, W. Applications of thermal methods in the geosciences. In *Handbook of thermal analysis and calorimetry. Vol. 2.: Applicatons to inorganic and miscellaneous minerals*, Brown, M. E., Gallagher, P. K., Eds.; Elsevier: Amsterdam, 2003; Vol. 2, pp 451-593.
- (549) Ramachandran, V. S.; Paroli, R. M.; Beaudoin, J. J.; Delgado, A. H. *Handbook of Thermal Analysis of Construction Materials*, William Andrew Publishing: Norwich, NY, 2002.
- (550) Heal, G. R. Thermogravimetry and derivative thermogravimetry. In *Principles of Thermal Analysis and Calorimetry*, Haines, P., Ed.; The Royal Society of Chemistry: Cambridge, UK, 2002; pp 10-54.
- (551) Sparkman, D. O.; Penton, Z. E.; Kiston, F. G. *Gass Chromatrography and Mass Spectrometry: A Practical Guide*, 2nd ed.; Elsevier: Oxford, UK.
- (552) Johnstone, R. A. W.; Rose, M. E. *Mass Spectrometry for Chemistry and Biochemists*, 2nd ed.; Cambridge University Press: Cambridge, UK, 1996.
- (553) British Standards Institution. Part 1: Shape, dimensions and other requirements for specimens and moulds. In *Testing hardened concrete*, 2012; Vol. BS EN 12390-1:2012.
- (554) British Standards Institution. Part 3: Compressive strength of test specimens. In *Testing hardened concrete*, 2009; Vol. BS EN 12390-3:2009.
- (555) Kantro, D. L. Influence of water-reducing admixtures on properties of cement paste - a miniature slump test. *Cement, Concrete and Aggregates* **1980**, *2*, 95-102.
- (556) Rasband, W. S. *ImageJ*, 1.48; U. S. National Institutes of Health: Bethesda, Maryland, 2014.
- (557) Wadsö, L.; Arndt, M. An international round robin test on isothermal (conduction) calorimetry for measurement of three-day heat of hydration of cement. *Cement and Concrete Research* **2016**, *79*, 316-322.
- (558) Wadsö, L. Operational issues in isothermal calorimetry. *Cement and Concrete Research* **2010**, *40*, 1129-1137.
- (559) British Standards Institution. Part 6: Determination of fineness. In *Methods of testing cement*, 2010; Vol. BS EN 196-6:2010.
- (560) Malvern Instruments Ltd. Mastersizer 3000. <http://www.malvern.com/en/products/product-range/mastersizer-range/mastersizer-3000/default.aspx> (accessed 01/06/2016), 2016).
- (561) British Standards Institution. Part 3: Determination of setting times and sounness. In *Methods of testing cement*, 2009; Vol. BS EN 196-3:2005 + A1:2008.
- (562) Wang, S.-D.; Scrivener, K. L.; Pratt, P. L. Factors affecting the strength of alkali-activated slag. *Cement and Concrete Research* **1994**, *24*, 1033-1043.
- (563) Bernal, S. A.; Gutiérrez, R. M.; Provis, J. L.; Rose, V. Effect of silicate modulus and metakaolin incorporation on the carbonation of alkali silicate-activated slags. *Cement and Concrete Research* **2010**, *40*, 898-907.
- (564) Vance, E. R.; Moricca, S.; Begg, B. D.; Stewart, M.; Zhang, Y.; Carter, M. Advantages Hot Isostatically Pressed Ceramic and Glass-Ceramic Waste Forms Bring to the Immobilization of Challenging Intermediate-and High-Level Nuclear Wastes, In *Advances in Science and Technology*; Trans Tech Publ: 2011; pp 130-135.
- (565) Young, A. J.; Warwick, P.; Milodowski, A. E.; Read, D. Behaviour of radionuclides in the presence of superplasticiser. *Advances in Cement Research* **2013**, *25*, 32-43.

- (566) Serco. *Effect of ADVA cast 551 on the solubility of plutonium(IV) and uranium(VI)*; Serco 2011;
- (567) Otraj, S.; Bahrevar, M. A.; Mostarzadeh, F.; Nilforoshan, M. R. The effect of deflocculants on the self-flow characteristics of ultra low-cement castables in Al₂O₃–SiC–C system. *Ceramics International* **2005**, *31*, 647-653.
- (568) Andreola, F.; Castellini, E.; Lusvardi, G.; Menabue, L.; Romagnoli, M. Release of ions from kaolinite dispersed in deflocculant solutions. *Applied Clay Science* **2007**, *36*, 271-278.
- (569) Lawrence, C. D. Physicochemical and mechanical properties of Portland cements. In *Lea's Chemistry of Cement and Concrete*, Hewlett, P. C., Ed.; Butterworth Heinemann: Oxford, UK, 2003.
- (570) Farmer, V. C. *The Infrared Spectra of Minerals*, Mineralogical Society: London, 1974.
- (571) Piani, L.; Papo, A. Sodium Tripolyphosphate and Polyphosphate as Dispersing Agents for Alumina Suspensions: Rheological Characterization. *Journal of Engineering* **2013**, *2013*, 4.
- (572) Park, S.; Choi, G. R.; Kim, J. H.; Lee, J. C.; Kim, S.-J. Dispersion effect of sodium hexametaphosphate on the photocatalytic efficiency of a solution-combusted ZnO nanopowder. *Journal of the Korean Physical Society* **2012**, *61*, 1400-1403.
- (573) MacKenzie, K. J. D.; Meinhold, R. H. The thermal reactions of talc studied by ²⁹Si and ²⁵Mg MAS NMR. *Thermochimica Acta* **1994**, *244*, 195-203.
- (574) Takahashi, N.; Tanaka, M.; Satoh, T.; Endo, T. Study of synthetic clay minerals. III. synthesis and characterization of two dimensional talc. *Bulletin of the Chemical Society of Japan* **1994**, *67*, 2463-2467.
- (575) Smykatz-Kloss, W. *Differential thermal analysis. Application and results in mineralogy*, Springer-Verlag: Berlin, 1974.
- (576) Viti, C. Serpentine minerals discrimination by thermal analysis. *American Mineralogist* **2010**, *95*, 631-638.
- (577) Lippincott, E. R.; Valkenburg, A. V.; Weir, C. E.; Bunting, E. N. Infrared studies on polymorphs of silicon dioxide and germanium dioxide. *Journal of Research of the National Bureau of Standards* **1958**, *61*, 61-70.
- (578) Ocaña, M.; Fornés, V.; Serna, C. J. The variability of the infrared powder spectrum of amorphous SiO₂. *Journal of Non-Crystalline Solids* **1989**, *107*, 187-192.
- (579) Ryskin, Y. I. The vibrations of protons in minerals: hydroxyl, water and ammonium. In *The Infrared Spectra of Minerals*, Farmer, V. C., Ed.; Mineralogical Society: London, 1974; pp 137-182.
- (580) Chukanov, N. *Infrared spectra of mineral species*, Springer Netherlands: 2014; p 21-1701.
- (581) Farmer, V. C. The layer silicates. In *The infrared spectra of minerals*, Farmer, V. C., Ed.; Mineralogical Society: London, 1974; pp 331-364.
- (582) Russell, J. D.; Farmer, V. C.; Velde, B. Replacement of OH by OD in layer silicates, and identification of the vibrations of these groups in infra-red spectra. *Mineralogical Magazine* **1970**, *37*, 869-879.
- (583) d'Espinose de la Caillerie, J.-B.; Kermarec, M.; Clause, O. ²⁹Si NMR observation of an amorphous magnesium silicate formed during impregnation of silica with Mg(II) in aqueous solution. *The Journal of Physical Chemistry* **1995**, *99*, 17273-17281.
- (584) MacKenzie, K. J. D.; Meinhold, R. H. Thermal reactions of chrysotile revisited: A ²⁹Si and ²⁵Mg MAS NMR study. *American Mineralogist* **1994**, *79*, 43-50.

- (585) Kosuge, K.; Shimada, K.; Tsunashima, A. Micropore formation by acid treatment of antigorite. *Chemistry of Materials* **1995**, *7*, 2241-2246.
- (586) Nakata, S.; Asaoka, S.; Kondoh, T.; Takahashi, H. Characterization of natural zeolites and clay minerals by high-resolution solid-state NMR. *Nendo Kagaku* **1986**, *26*, 197-208.
- (587) Hilbig, H.; Köhler, F. H.; Schießl, P. Quantitative ^{29}Si MAS NMR spectroscopy of cement and silica fume containing paramagnetic impurities. *Cement and Concrete Research* **2006**, *36*, 326-329.
- (588) Trittschack, R.; Grobéty, B. Dehydroxylation kinetics of lizardite. *European Journal of Mineralogy* **2012**, *24*, 47-57.
- (589) Caruso, L. J.; Chernosky, J. V. The stability of lizardite. *The Canadian Mineralogist* **1979**, *17*, 757-769.
- (590) Pallister, P. J.; Moudrakovski, I. L.; Ripmeester, J. A. Mg-25 ultra-high field solid state NMR spectroscopy and first principles calculations of magnesium compounds. *Physical Chemistry Chemical Physics* **2009**, *11*, 11487-11500.
- (591) Cahill, L. S.; Hanna, J. V.; Wong, A.; Freitas, J. C. C.; Yates, J. R.; Harris, R. K.; Smith, M. E. Natural abundance ^{25}Mg solid-state NMR of Mg oxyanion systems: A combined experimental and computational study. *Chemistry – A European Journal* **2009**, *15*, 9785-9798.
- (592) Ashbrook, S. E.; Sneddon, S. New methods and applications in solid-state NMR spectroscopy of quadrupolar nuclei. *Journal of the American Chemical Society* **2014**, *136*, 15440-15456.
- (593) Laurencin, D.; Gervais, C.; Stork, H.; Krämer, S.; Massiot, D.; Fayon, F. ^{25}Mg solid-state NMR of magnesium phosphates: High magnetic field experiments and density functional theory calculations. *The Journal of Physical Chemistry C* **2012**, *116*, 19984-19995.
- (594) Freitas, J. C. C.; Smith, M. E. Recent advances in solid-state ^{25}Mg NMR spectroscopy. In *Annual Reports on NMR Spectroscopy*, Graham, A. W., Ed.; Academic Press: 2012; Vol. Volume 75, pp 25-114.
- (595) Slichter, C. P. *Principles of magnetic resonance*, 3rd ed.; Springer-Verlag: Berlin, 1996.
- (596) O'Hanley, D. S.; Wicks, F. J. Conditions of formation of lizardite, chrysotile and antigorite, Cassiar, British Columbia. *The Canadian Mineralogist* **1995**, *33*, 753-773.
- (597) Day, H. W.; Chernosky, J. V.; Kumin, H. J. Equilibria in the system $\text{MgO-SiO}_2\text{-H}_2\text{O}$: a thermodynamic analysis. *American Mineralogist* **1985**, *70*, 237-248.
- (598) Evans, B. W. The serpentinite multisystem revisited: chrysotile is metastable. *International Geology Review* **2004**, *46*, 479-506.
- (599) Peters, E. K. D- ^{18}O enriched waters of the Coast Range Mountains, northern California: Connate and ore-forming fluids. *Geochimica et Cosmochimica Acta* **1993**, *57*, 1093-1104.
- (600) Nesbitt, H. W.; Bricker, O. P. Low temperature alteration process affecting ultramafic bodies. *Geochimica et Cosmochimica Acta* **1978**, *42*, 403-409.
- (601) Hajimohammadi, A.; Provis, J.; van Deventer, J. One-part geopolymer mixes from geothermal silica and sodium aluminate. *Ind. Eng. Chem. Res.* **2008**, *47*, 9396-9405.
- (602) Brew, D. R. M.; MacKenzie, K. J. D. Geopolymer synthesis using silica fume and sodium aluminate. *J Mater Sci* **2007**, *42*, 3990-3993.

- (603) Criado, M.; Fernández-Jiménez, A.; de la Torre, A. G.; Aranda, M. A. G.; Palomo, A. An XRD study of the effect of the SiO₂/Na₂O ratio on the alkali activation of fly ash. *Cement and Concrete Research* **2007**, *37*, 671-679.
- (604) Palomo, Á.; Alonso, S.; Fernández-Jiménez, A.; Sobrados, I.; Sanz, J. Alkaline Activation of Fly Ashes: NMR Study of the Reaction Products. *Journal of the American Ceramic Society* **2004**, *87*, 1141-1145.
- (605) Aly, Z.; Vance, E. R.; Perera, D. S.; Hanna, J. V.; Griffith, C. S.; Davis, J.; Durce, D. Aqueous leachability of metakaolin-based geopolymers with molar ratios of Si/Al = 1.5 - 4. *Journal of Nuclear Materials* **2008**, *378*, 172-179.
- (606) Berger, S.; Frizon, F.; Jousset-Dubien, C. Formulation of caesium based and caesium containing geopolymers. *Advances in Applied Ceramics* **2009**, *108*, 412-417.
- (607) El-Kamash, A. M.; El-Dakroury, A. M.; Aly, H. F. Leaching kinetics of ¹³⁷Cs and ⁶⁰Co radionuclides fixed in cement and cement-based materials. *Cement and Concrete Research* **2002**, *32*, 1797-1803.
- (608) Brew, D.; Glasser, F. Synthesis and characterisation of magnesium silicate hydrate gels. *Cement and Concrete Research* **2005**, *35*, 85-98.
- (609) Iler, R. K. Effect of adsorbed alumina on the solubility of amorphous silica in water. *Journal of Colloid and Interface Science* **1973**, *43*, 399-408.
- (610) Chappex, T.; Scrivener, K. L. The effect of aluminum in solution on the dissolution of amorphous silica and its relation to cementitious systems. *Journal of the American Ceramic Society* **2013**, *96*, 592-597.
- (611) Shigemoto, N.; Sugiyama, S.; Hayashi, H.; Miyaura, K. Characterization of Na-X, Na-A, and coal fly ash zeolites and their amorphous precursors by IR, MAS NMR and XPS. *Journal of Materials Science* **1995**, *30*, 5777-5783.
- (612) Barrer, R. M. Zeolites and their synthesis. *Zeolites* **1981**, *1*, 130-140.
- (613) Subotić, B.; Škrtić, D.; Šmit, I.; Sekovanić, L. Transformation of zeolite A into hydroxysodalite: I. An approach to the mechanism of transformation and its experimental evaluation. *Journal of Crystal Growth* **1980**, *50*, 498-508.
- (614) Mon, J.; Deng, Y.; Flury, M.; Harsh, J. Cesium incorporation and diffusion in cancrinite, sodalite, zeolite and allophane. *Microporous and Mesoporous Materials* **2005**, *86*, 277-286.
- (615) Penilla, R. P.; Guerrero Bustos, A.; Goñi Elizalde, S. Immobilization of Cs, Cd, Pb and Cr by synthetic zeolites from Spanish low-calcium coal fly ash. *Fuel* **2006**, *85*, 823-832.
- (616) Stumpf, T.; Curtius, H.; Walther, C.; Dardenne, K.; Ufer, K.; Fanghänel, T. Incorporation of Eu(III) into hydrotalcite: a TRLFS and EXAFS study. *Environmental Science & Technology* **2007**, *41*, 3186-3191.
- (617) Aggarwal, S.; Angus, M. J.; Ketchen, J. *Sorption of radionuclides onto specific mineral phases present in repository cements*; AEA Technology: Windscale 2000;
- (618) Nuclear Decommissioning Authority. *Waste stream 2D16: Magnox fuel storage pond sludge*; NDA 2007;
- (619) Lee, W. K. W.; van Deventer, J. S. J. Use of infrared spectroscopy to study geopolymerization of heterogeneous amorphous aluminosilicates. *Langmuir* **2003**, *19*, 8726-8734.
- (620) Montanari, T.; Busca, G. On the mechanism of adsorption and separation of CO₂ on LTA zeolites: An IR investigation. *Vibrational Spectroscopy* **2008**, *46*, 45-51.

- (621) Flanigen, E. M. Structural analysis by infrared spectroscopy. In *Zeolite Chemistry and Catalysis, ACS Monograph Series 171*, Rabo, J. A., Ed.; American Chemical Society: Washington D.C., 1976; pp 80-117.
- (622) Wright, A. C.; Rupert, J. P.; Granquist, W. T. High- and low-silica faujasites: a substitutional series. *American Mineralogist* **1968**, *53*, 1293-1303.
- (623) Hajimohammadi, A.; Provis, J. L.; van Deventer, J. S. J. One-part geopolymer mixes from geothermal silica and sodium aluminate. *Industrial & Engineering Chemistry Research* **2008**, *47*, 9396-9405.
- (624) Walton, R. I.; Millange, F.; O'Hare, D.; Davies, A. T.; Sankar, G.; Catlow, C. R. A. An in situ energy-dispersive x-ray diffraction study of the hydrothermal crystallization of zeolite A. 1. Influence of reaction conditions and transformation into sodalite. *The Journal of Physical Chemistry B* **2001**, *105*, 83-90.
- (625) Greer, H.; Wheatley, P. S.; Ashbrook, S. E.; Morris, R. E.; Zhou, W. Early stage reversed crystal growth of zeolite A and its phase transformation to sodalite. *Journal of the American Chemical Society* **2009**, *131*, 17986-17992.
- (626) International Zeolite Association Structure Commission (IZA-SC). *Collection of simulated XRD powder patterns for zeolites*, 4th ed.; Amsterdam, Netherlands, 2001.
- (627) Subotić, B.; Šmit, I.; Madžija, O.; Sekovanić, L. Kinetic study of the transformation of zeolite A into zeolite P. *Zeolites* **1982**, *2*, 135-142.
- (628) Mills, S. J.; Christy, A. G.; Génin, J.-M. R.; Kameda, T.; Colombo, F. Nomenclature of the hydrotalcite supergroup: natural layered double hydroxides. *Mineralogical Magazine* **2012**, *76*, 1289-1336.
- (629) Allmann, R.; Jepsen, H. P. Die struktur des hydrotalkits. *Neues Jahrbuch für Mineralogie Monatshefte* **1969**, 544-551.
- (630) MacKenzie, K. J. D.; Meinhold, R. H. Thermal decomposition of brucite, Mg(OH)₂: a ²⁵Mg MAS NMR study. *Thermochimica Acta* **1993**, *230*, 339-343.
- (631) Valente, J. S.; Pfeiffer, H.; Lima, E.; Prince, J.; Flores, J. Cyanoethylation of alcohols by activated Mg–Al layered double hydroxides: Influence of rehydration conditions and Mg/Al molar ratio on Brønsted basicity. *Journal of Catalysis* **2011**, *279*, 196-204.
- (632) Felsche, J.; Luger, S. Phases and thermal decomposition characteristics of hydro-sodalites Na_{6+x}[AlSiO₄]₆(OH)_x·nH₂O. *Thermochimica Acta* **1987**, *118*, 35-55.
- (633) Joshi, U. D.; Joshi, P. N.; Tamhankar, S. S.; Joshi, V. P.; Idage, B. B.; Joshi, V. V.; Shiralkar, V. P. Influence of the size of extraframework monovalent cations in X-type zeolite on their thermal behavior. *Thermochimica Acta* **2002**, *387*, 121-130.
- (634) Constantino, V. R. L.; Pinnavaia, T. J. Basic properties of Mg^{2+1-x}Al^{3+x} layered double hydroxides intercalated by carbonate, hydroxide, chloride, and sulfate anions. *Inorganic Chemistry* **1995**, *34*, 883-892.
- (635) Klopogge, J. T.; Kristóf, J.; Frost, R. L. Thermogravimetric analysis-mass spectrometry (TGA-MS) of hydrotalcites containing CO₃²⁻, NO₃⁻, Cl⁻, SO₄²⁻ or ClO₄⁻. In *2001. A clay odyssey. Proceedings of the 12th international clay conference*, Bahía Blanca, Argentina, 2001.
- (636) Engelhardt, G. Chapter 9 Solid state NMR spectroscopy applied to zeolites. In *Studies in Surface Science and Catalysis*, van Bekkum, H., Flanigen, E. M., Jacobs, P. A., Jansen, J. C., Eds.; Elsevier: 2001; Vol. Volume 137, pp 387-418.
- (637) MacKenzie, K. J. D.; Meinhold, R. H.; Sherriff, B. L.; Xu, Z. ²⁷Al and ²⁵Mg solid-state magic-angle spinning nuclear magnetic resonance study of hydrotalcite

- and its thermal decomposition sequence. *Journal of Materials Chemistry* **1993**, *3*, 1263-1269.
- (638) Lippmaa, E.; Maegi, M.; Samoson, A.; Tarmak, M.; Engelhardt, G. Investigation of the structure of zeolites by solid-state high-resolution silicon-29 NMR spectroscopy. *Journal of the American Chemical Society* **1981**, *103*, 4992-4996.
- (639) Newsam, J. M. Silicon-29 chemical shifts in sodalite materials. *The Journal of Physical Chemistry* **1987**, *91*, 1259-1262.
- (640) Engelhardt, G.; Felsche, J.; Sieger, P. The hydrosodalite system $\text{Na}_{6+x}[\text{SiAlO}_4]_6(\text{OH})_x \cdot n\text{H}_2\text{O}$: formation, phase composition, and de- and rehydration studied by ^1H , ^{23}Na , and ^{29}Si MAS-NMR spectroscopy in tandem with thermal analysis, x-ray diffraction, and IR spectroscopy. *Journal of the American Chemical Society* **1992**, *114*, 1173-1182.
- (641) Zhuravlev, L. T. The surface chemistry of amorphous silica. Zhuravlev model. *Colloids and Surfaces A: Physicochemical and Engineering Aspects* **2000**, *173*, 1-38.
- (642) Bai, Y.; Collier, N. C.; Milestone, N. B.; Yang, C. H. The potential for using slags activated with near neutral salts as immobilisation matrices for nuclear wastes containing reactive metals. *Journal of Nuclear Materials* **2011**, *413*, 183-192.
- (643) Mobasher, N.; Bernal, S. A.; Hussain, O. H.; Apperley, D. C.; Kinoshita, H.; Provis, J. L. Characterisation of $\text{Ba}(\text{OH})_2\text{-Na}_2\text{SO}_4$ -blast furnace slag cement-like composites for the immobilisation of sulfate bearing nuclear wastes. *Cement and Concrete Research* **2014**, *66*, 64-74.
- (644) Ke, X.; Bernal, S. A.; Provis, J. Controlling the kinetics of reaction of sodium carbonate-activated slag cements using calcined layered double hydroxides. *Cement and Concrete Research* **2016**, *81*, 24-37.
- (645) Shi, C.; Krivenko, P. V.; Roy, D. *Alkali-Activated Cements and Concretes*, Taylor & Francis: Abingdon, UK, 2006.
- (646) Miyata, S. The syntheses of hydrotalcite-like compounds and their structures and physico-chemical properties - I: The systems $\text{Mg}^{2+}\text{-Al}^{3+}\text{-NO}_3^-$, $\text{Mg}^{2+}\text{-Al}^{3+}\text{-Cl}^-$, $\text{Mg}^{2+}\text{-Al}^{3+}\text{-ClO}_4^-$, $\text{Ni}^{2+}\text{-Al}^{3+}\text{-Cl}^-$ and $\text{Zn}^{2+}\text{-Al}^{3+}\text{-Cl}^-$. *Clays and Clay Minerals* **1975**, *23*, 369-375.
- (647) Provis, J. L.; Bernal, S. A. Geopolymers and related alkali-activated materials. *Annual Review of Materials Research* **2014**, *44*, 299-327.
- (648) Bernal, S. A.; Provis, J. L.; Myers, R. J.; San Nicolas, R.; van Deventer, J. S. J. Role of carbonates in the chemical evolution of sodium carbonate-activated slag binders. *Materials and Structures* **2015**, *48*, 517-529.
- (649) Ben Haha, M.; Lothenbach, B.; Le Saout, G.; Winnefeld, F. Influence of slag chemistry on the hydration of alkali-activated blast-furnace slag — Part I: Effect of MgO. *Cement and Concrete Research* **2011**, *41*, 955-963.
- (650) Bernal, S. A.; San Nicolas, R.; Myers, R. J.; Mejía de Gutiérrez, R.; Puertas, F.; van Deventer, J. S. J.; Provis, J. L. MgO content of slag controls phase evolution and structural changes induced by accelerated carbonation in alkali-activated binders. *Cement and Concrete Research* **2014**, *57*, 33-43.
- (651) Jin, F.; Gu, K.; Al-Tabbaa, A. Strength and drying shrinkage of reactive MgO modified alkali-activated slag paste. *Construction and Building Materials* **2014**, *51*, 395-404.
- (652) Berodier, E.; Scrivener, K. Understanding the filler effect on the nucleation and growth of C-S-H. *Journal of the American Ceramic Society* **2014**, *97*, 3764-3773.

- (653) Lothenbach, B.; Scrivener, K.; Hooton, R. D. Supplementary cementitious materials. *Cement and Concrete Research* **2011**, *41*, 1244-1256.
- (654) Bernal, S. A.; Provis, J. L.; Walkley, B.; San Nicolas, R.; Gehman, J. D.; Brice, D. G.; Kilcullen, A. R.; Duxson, P.; van Deventer, J. S. J. Gel nanostructure in alkali-activated binders based on slag and fly ash, and effects of accelerated carbonation. *Cement and Concrete Research* **2013**, *53*, 127-144.
- (655) Myers, R. J.; Bernal, S. A.; Gehman, J. D.; van Deventer, J. S. J.; Provis, J. L. The role of Al in cross-linking of alkali-activated slag cements. *Journal of the American Ceramic Society* **2015**, *98*, 996-1004.
- (656) Myers, R. J.; Lothenbach, B.; Bernal, S. A.; Provis, J. L. Thermodynamic modelling of alkali-activated slag cements. *Applied Geochemistry* **2015**, *61*, 233-247.
- (657) Althoff, P. L. Structural refinements of dolomite and a magnesian calcite and implications for dolomite formation in the marine environment. *American Mineralogist* **1977**, *62*, 772-783.
- (658) Falini, G.; Fermani, S.; Gazzano, M.; Ripamonti, A. Structure and morphology of synthetic magnesium calcite. *Journal of Materials Chemistry* **1998**, *8*, 1061-1065.
- (659) Sakulich, A. R.; Miller, S.; Barsoum, M. W. Chemical and microstructural characterization of 20-month-old alkali-activated slag cements. *Journal of the American Ceramic Society* **2010**, *93*, 1741-1748.
- (660) Fischer, R.; Kuzel, H. J. Reinvestigation of the system $C_4A.nH_2O - C_4A.CO_2.nH_2O$. *Cement and Concrete Research* **1982**, *12*, 517-526.
- (661) Garcia-Lodeiro, I.; Palomo, A.; Fernández-Jiménez, A.; Macphee, D. E. Compatibility studies between N-A-S-H and C-A-S-H gels. Study in the ternary diagram $Na_2O-CaO-Al_2O_3-SiO_2-H_2O$. *Cement and Concrete Research* **2011**, *41*.
- (662) García Lodeiro, I.; Macphee, D. E.; Palomo, A.; Fernández-Jiménez, A. Effect of alkalis on fresh C-S-H gels. FTIR analysis. *Cement and Concrete Research* **2009**, *39*, 147-153.
- (663) White, W. B. The carbonate minerals. In *The Infrared Spectra of Minerals*, Farmer, V. C., Ed.; Mineralogical Society: London, 1974; pp 227-284.
- (664) Frost, R. L.; Bahfenne, S.; Graham, J. Raman spectroscopic study of the magnesium-carbonate minerals—artinite and dypingite. *Journal of Raman Spectroscopy* **2009**, *40*, 855-860.
- (665) Andersen, F. A.; Brečević, L. Infrared spectra of amorphous and crystalline calcium carbonate. *Acta Chimica Scandinavica* **1991**, *45*, 1018-1024.
- (666) Land, L. S. Failure to precipitate dolomite at 25 °C from dilute solution despite 1000-fold oversaturation after 32 years. *Aquatic Geochemistry* **1998**, *4*, 361-368.
- (667) Huang, C. K.; Kerr, P. F. Infrared study of the carbonate minerals. *American Mineralogist* **1960**, *45*, 311-324.
- (668) Böttcher, M. E.; Gehlken, P.-L.; Steele, D. F. Characterization of inorganic and biogenic magnesia calcites by Fourier Transform infrared spectroscopy. *Solid State Ionics* **1997**, *101-103*, 1379-1385.
- (669) Ben Haha, M.; Lothenbach, B.; Le Saout, G.; Winnefeld, F. Influence of slag chemistry on the hydration of alkali-activated blast-furnace slag — Part II: Effect of Al_2O_3 . *Cement and Concrete Research* **2012**, *42*, 74-83.
- (670) Myers, R. J.; L'Hôpital, E.; Provis, J. L.; Lothenbach, B. Effect of temperature and aluminium on calcium (alumino)silicate hydrate chemistry under equilibrium conditions. *Cement and Concrete Research* **2015**, *68*, 83-93.

- (671) Johnson, D. R.; Robb, W. A. Gaylussite: Thermal properties by simultaneous thermal analysis. *American Mineralogist* **1973**, *58*, 778-784.
- (672) Wang, S.-D.; Scrivener, K. L. Hydration products of alkali activated slag cement. *Cement and Concrete Research* **1995**, *25*, 561-571.
- (673) Richardson, I. G.; Brough, A. R.; Groves, G. W.; Dobson, C. M. The characterization of hardened alkali-activated blast-furnace slag pastes and the nature of the calcium silicate hydrate (C-S-H) phase. *Cement and Concrete Research* **1994**, *24*, 813-829.
- (674) San Nicolas, R.; Bernal, S. A.; Mejía de Gutiérrez, R.; van Deventer, J. S. J.; Provis, J. L. Distinctive microstructural features of aged sodium silicate-activated slag concretes. *Cement and Concrete Research* **2014**, *65*, 41-51.
- (675) Ben Haha, M.; Le Saout, G.; Winnefeld, F.; Lothenbach, B. Influence of activator type on hydration kinetics, hydrate assemblage and microstructural development of alkali activated blast-furnace slags. *Cement and Concrete Research* **2011**, *41*, 301-310.
- (676) Richardson, I. G.; Skibsted, J.; Black, L.; Kirkpatrick, R. J. Characterisation of cement hydrate phases by TEM, NMR and Raman spectroscopy. *Advances in Cement Research* **2010**, *22*, 233-248.
- (677) Schneider, J.; Cincotto, M. A.; Panepucci, H. ^{29}Si and ^{27}Al high-resolution NMR characterization of calcium silicate hydrate phases in activated blast-furnace slag pastes. *Cement and Concrete Research* **2001**, *31*, 993-1001.
- (678) Merwin, L. H.; Sebal, A.; Seifert, F. The incommensurate-commensurate phase transition in akermanite, $\text{Ca}_2\text{MgSi}_2\text{O}_7$, observed by in-situ ^{29}Si MAS NMR spectroscopy. *Physics and Chemistry of Minerals* **1989**, *16*, 752-756.
- (679) Myers, R. J.; Bernal, S. A.; San Nicolas, R.; Provis, J. L. Generalized Structural Description of Calcium–Sodium Aluminosilicate Hydrate Gels: The Cross-Linked Substituted Tobermorite Model. *Langmuir* **2013**, *29*, 5294-5306.
- (680) Faucon, P.; Charpentier, T.; Bertrandie, D.; Nonat, A.; Virlet, J.; Petit, J. C. Characterization of calcium aluminate hydrates and related hydrates of cement pastes by ^{27}Al MQ-MAS NMR. *Inorganic Chemistry* **1998**, *37*, 3726-3733.
- (681) Le Saoût, G.; Ben Haha, M.; Winnefeld, F.; Lothenbach, B. Hydration degree of alkali-activated slags: A ^{29}Si NMR study. *Journal of the American Ceramic Society* **2011**, *94*, 4541-4547.
- (682) Gu, B. X.; Wang, L. M.; Ewing, R. C. The effect of amorphization on the Cs ion exchange and retention capacity of zeolite-NaY. *Journal of Nuclear Materials* **2000**, *278*, 64-72.
- (683) Gu, B.; Wang, L.; Ewing, R. C. The effects of radiation on the retention of strontium in zeolite-NaSrY. *Journal of Materials Chemistry* **2002**, *12*, 233-238.
- (684) Johnson, E.; Ferrer, J.; Chadderton, L. T. Radiolytic radiation damage of sodalite. *physica status solidi (a)* **1978**, *49*, 585-591.

11 Appendix I – Supplementary data

11.1 Magnesium silicate hydrate cementitious systems supplementary data

Below are supplementary data for variations in phosphate contents assessed up to 28 days. These follow similar hydration mechanisms as stated in Chapter 5, but with retardation when 5 wt. % phosphate is added.

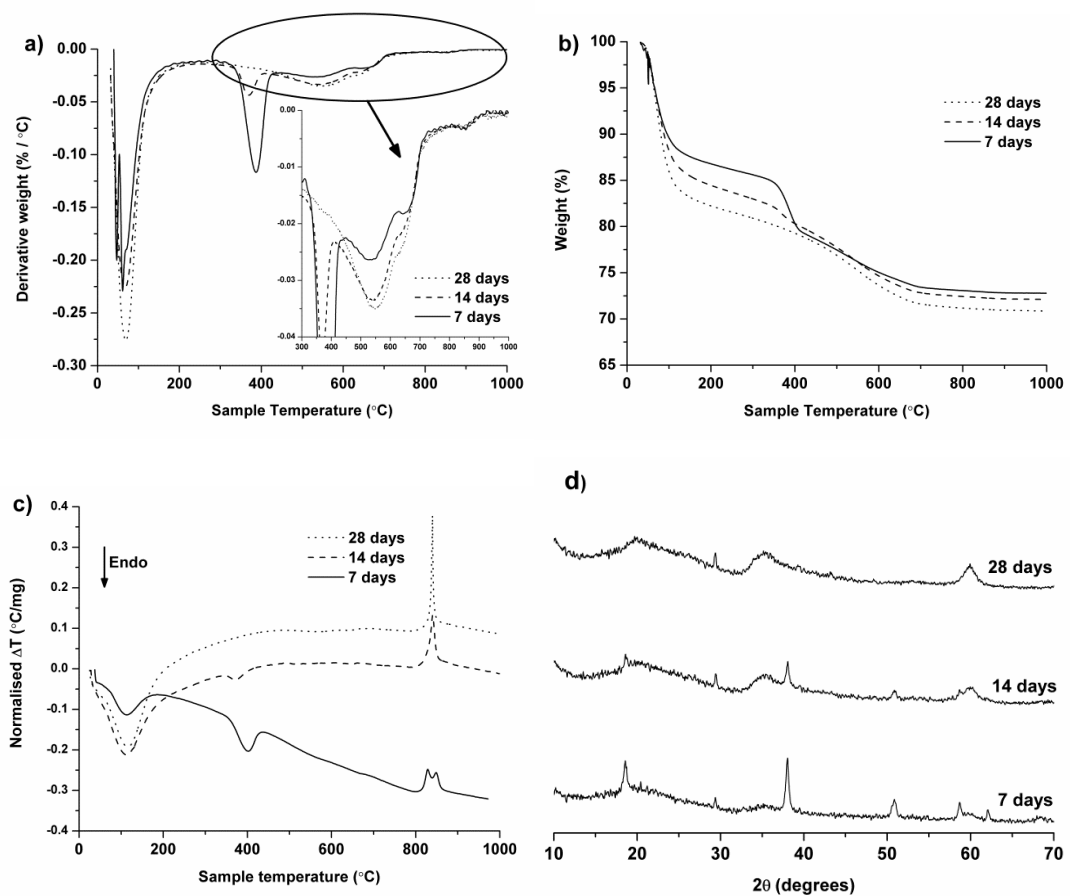


Figure 11.1 Properties of 1:1 Mg(OH)₂:SiO₂ (w/b = 1.0) binder with no phosphate addition, up to 28 days curing; a) DTG, b) TG, c) DTA, d) XRD

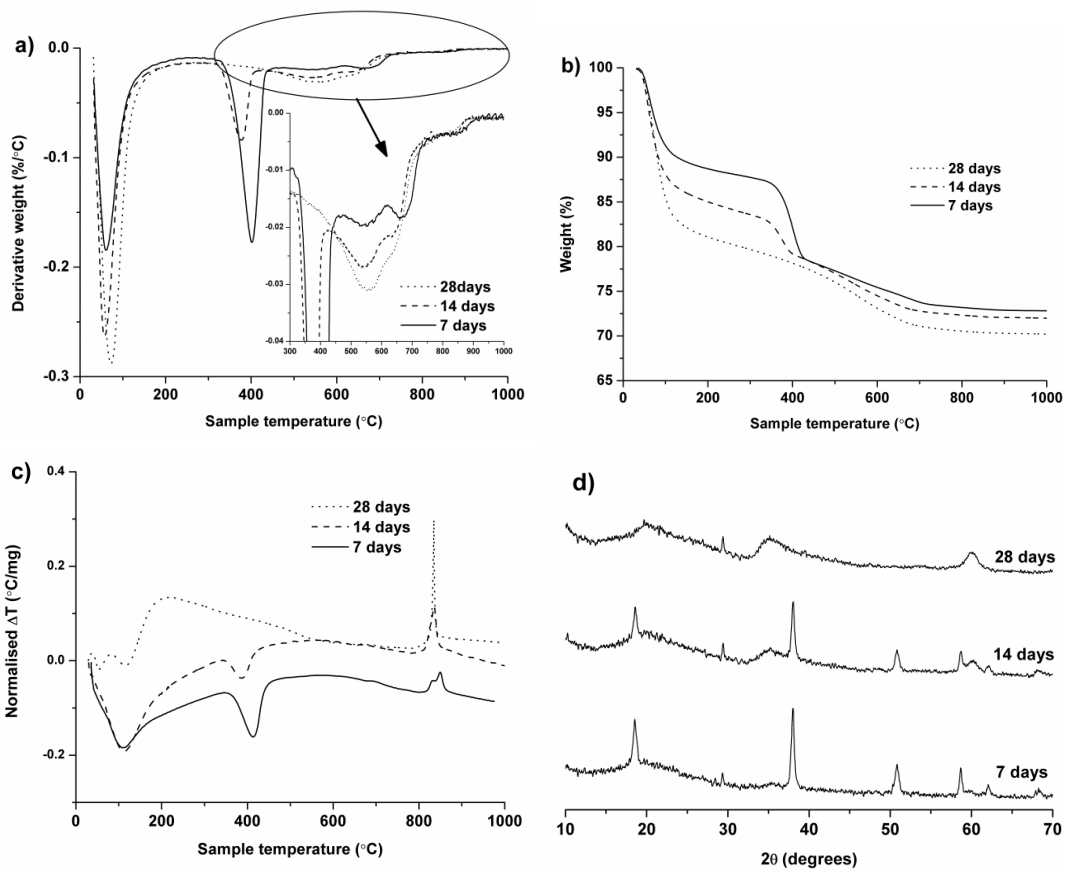


Figure 11.2 Properties of 1:1 Mg(OH)₂:SiO₂ (w/b = 1.0) binder with 1 wt. % (NaPO₃)₆ addition, up to 28 days curing; a) DTG, b) TG, c) DTA, d) XRD

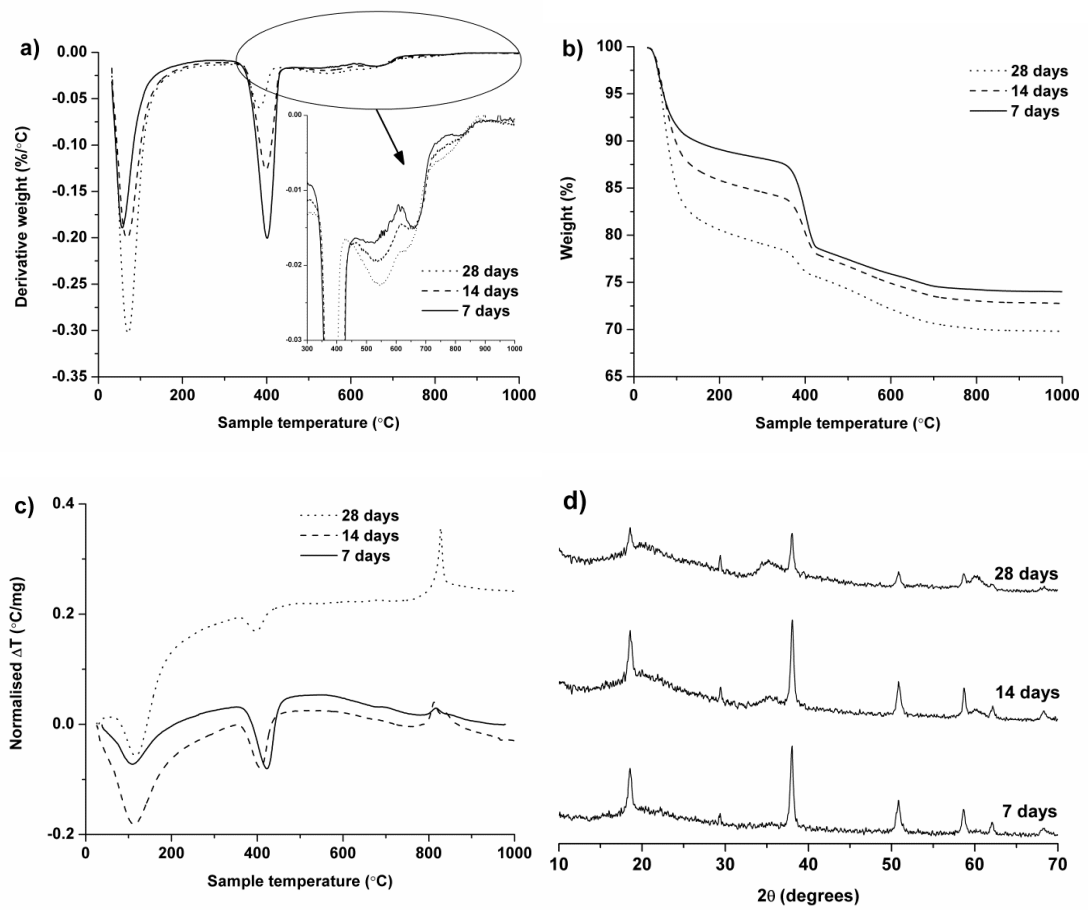


Figure 11.3 Properties of 1:1 Mg(OH)₂:SiO₂ (w/b = 1.0) binder with 5 wt. % (NaPO₃₆)₆ addition, up to 28 days curing; a) DTG, b) TG, c) DTA, d) XRD

11.2 Sodium carbonate activated slag – $\text{Mg}(\text{OH})_2$ binders supplementary SEM images and EDX maps

Below are listed supplementary SEM micrographs for 18 month cured sodium carbonate activated slag cements, as detailed in Chapter 8. These micrographs, although not discussed in the text, might be of interest to the reader as supporting information

11.2.1 $\text{Mg}(\text{OH})_2$ free binders

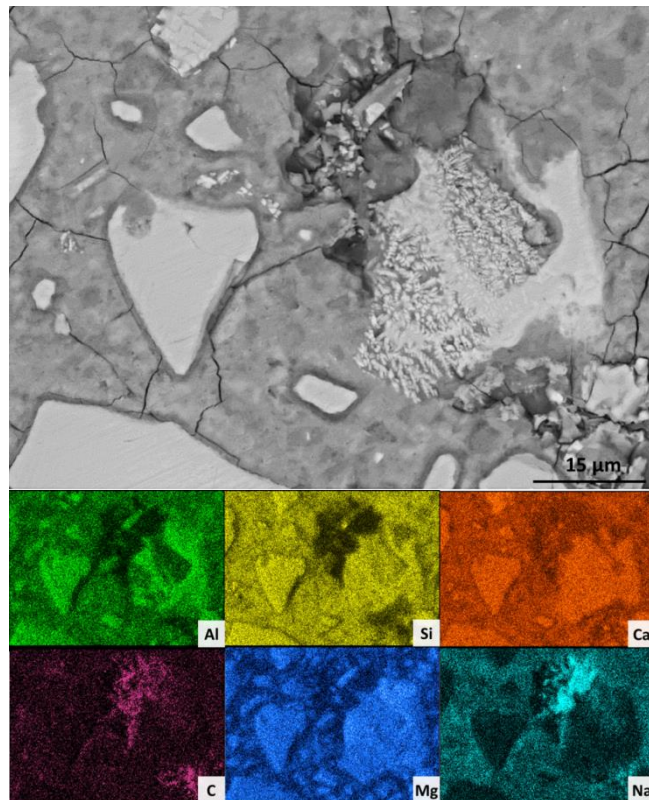


Figure 11.4 Backscattered electron micrograph and corresponding EDX maps of a sodium carbonate activated slag without $\text{Mg}(\text{OH})_2$ addition after 18 months of curing

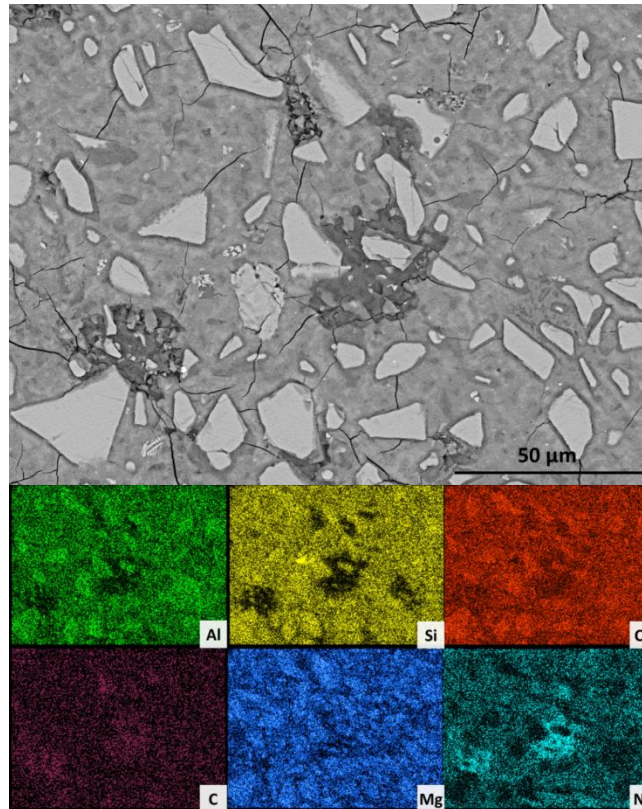


Figure 11.5 Backscattered electron micrograph and corresponding EDX maps of a sodium carbonate activated slag without $Mg(OH)_2$ addition after 18 months of curing

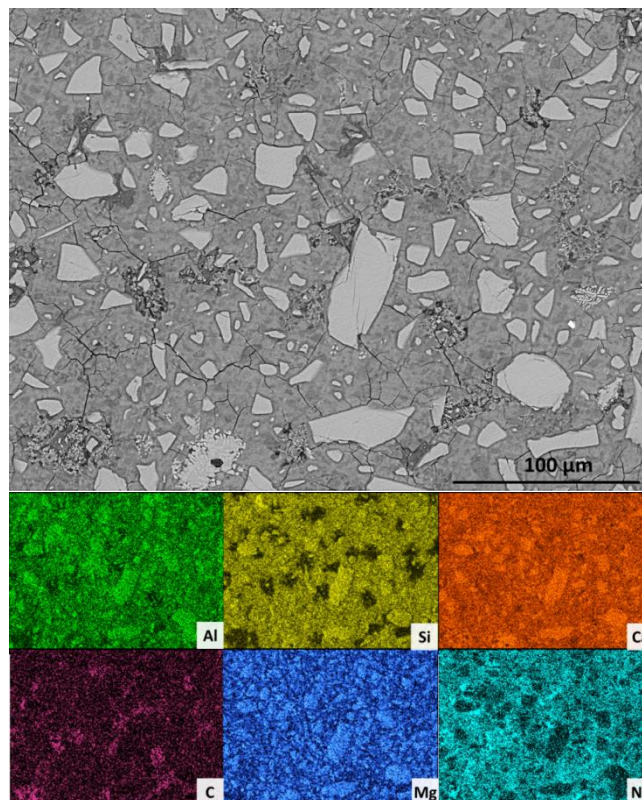


Figure 11.6 Backscattered electron micrograph and corresponding EDX maps of a sodium carbonate activated slag without $Mg(OH)_2$ addition after 18 months of curing

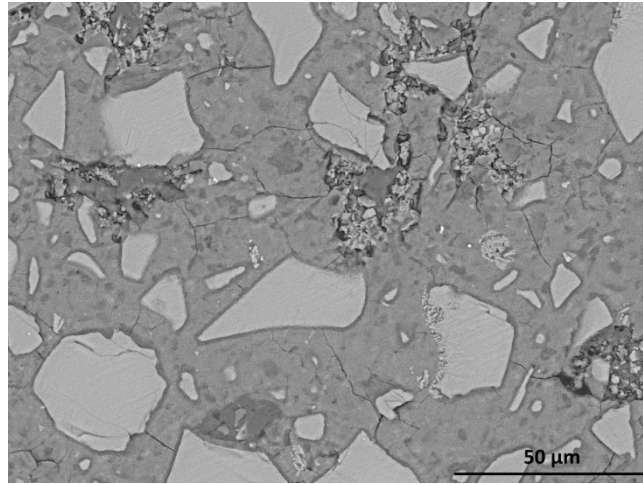


Figure 11.7 Backscattered electron micrograph and corresponding EDX maps of a sodium carbonate activated slag without $\text{Mg}(\text{OH})_2$ addition after 18 months of curing

11.2.2 10 % $\text{Mg}(\text{OH})_2$ binders

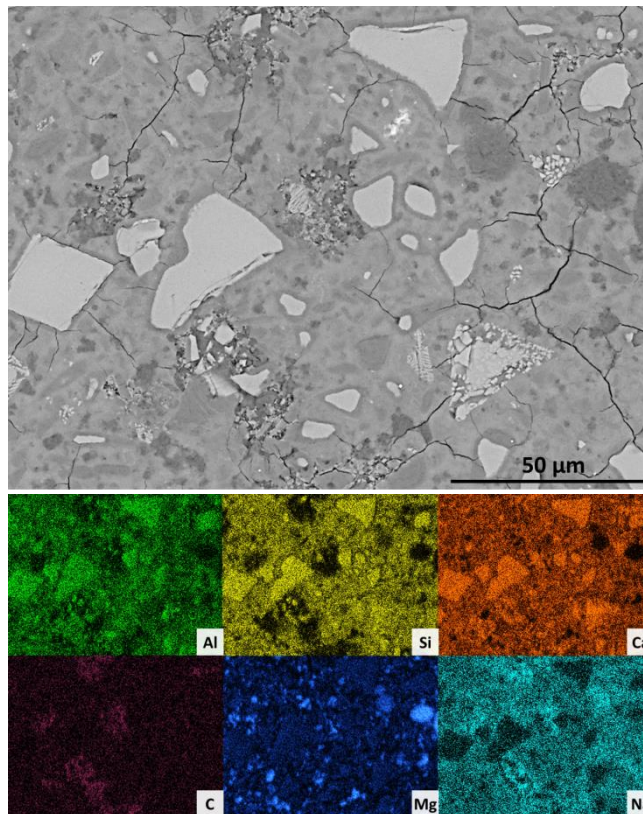


Figure 11.8 Backscattered electron micrograph and corresponding EDX maps of a sodium carbonate activated slag with 10 wt.% $\text{Mg}(\text{OH})_2$ addition after 18 months of curing

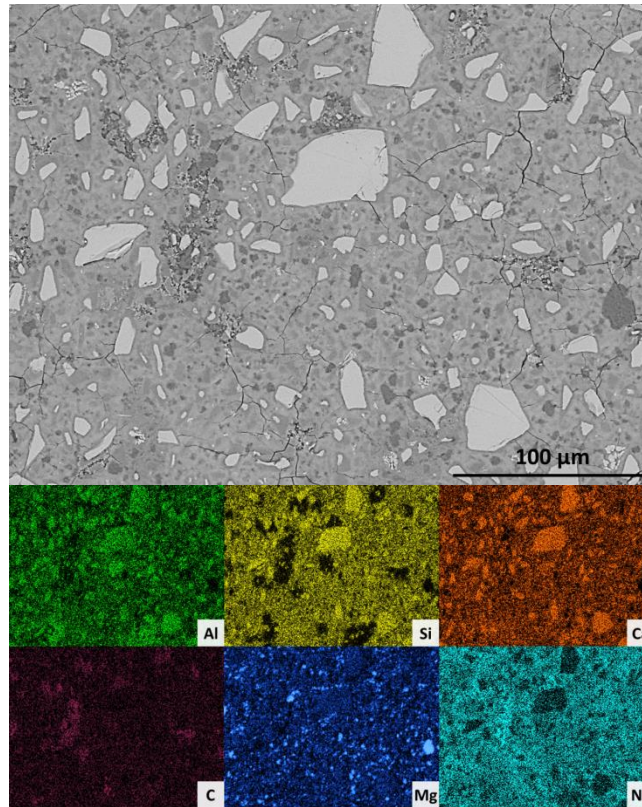


Figure 11.9 Backscattered electron micrograph and corresponding EDX maps of a sodium carbonate activated slag with 10 wt.% $Mg(OH)_2$ addition after 18 months of curing

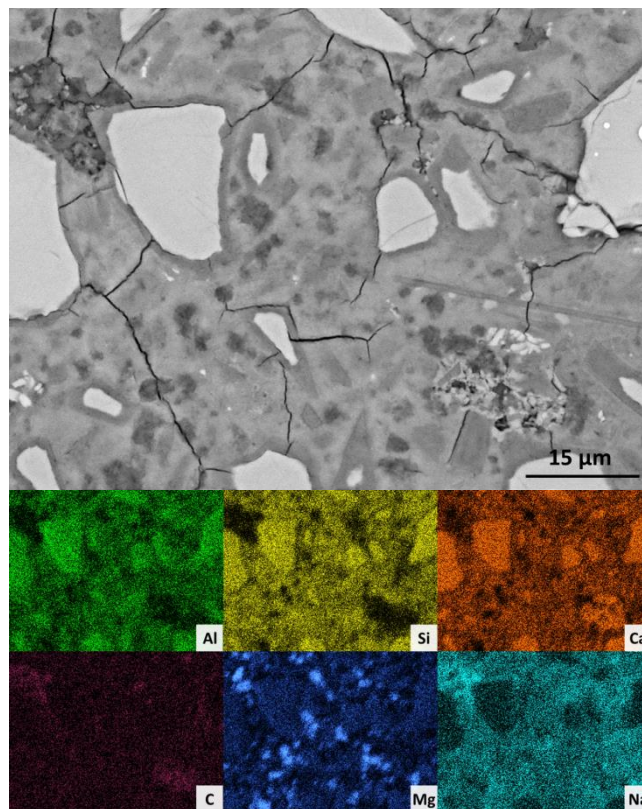


Figure 11.10 Backscattered electron micrograph and corresponding EDX maps of a sodium carbonate activated slag with 10 wt.% $Mg(OH)_2$ addition after 18 months of curing

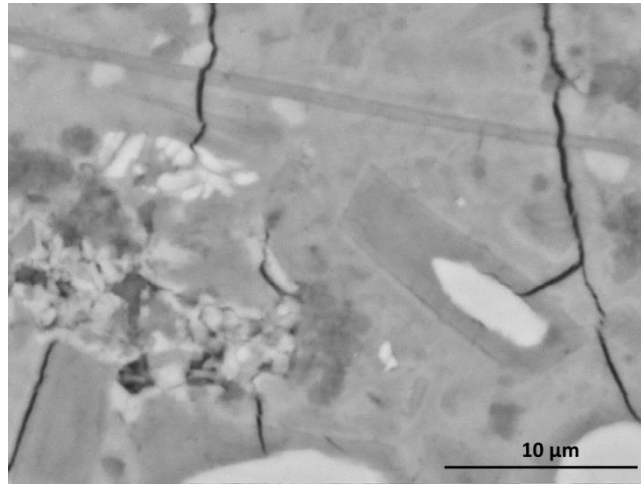


Figure 11.11 Backscattered electron micrograph and corresponding EDX maps of a sodium carbonate activated slag with 10 wt.% $\text{Mg}(\text{OH})_2$ addition after 18 months of curing

11.2.3 30 % $\text{Mg}(\text{OH})_2$ binders

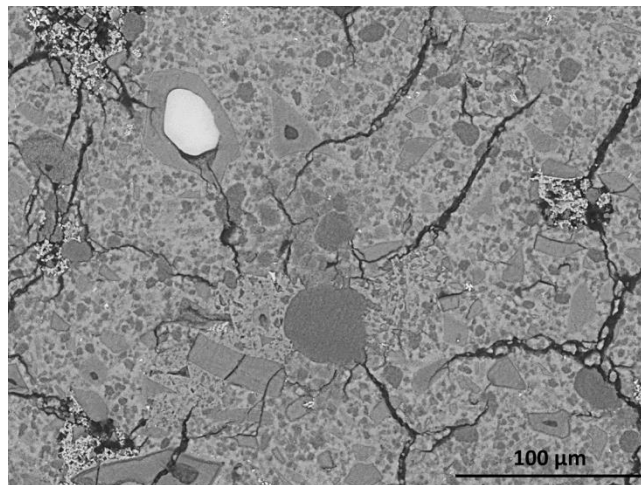


Figure 11.12 Backscattered electron micrograph and corresponding EDX maps of a sodium carbonate activated slag with 30 wt.% $\text{Mg}(\text{OH})_2$ addition after 18 months of curing

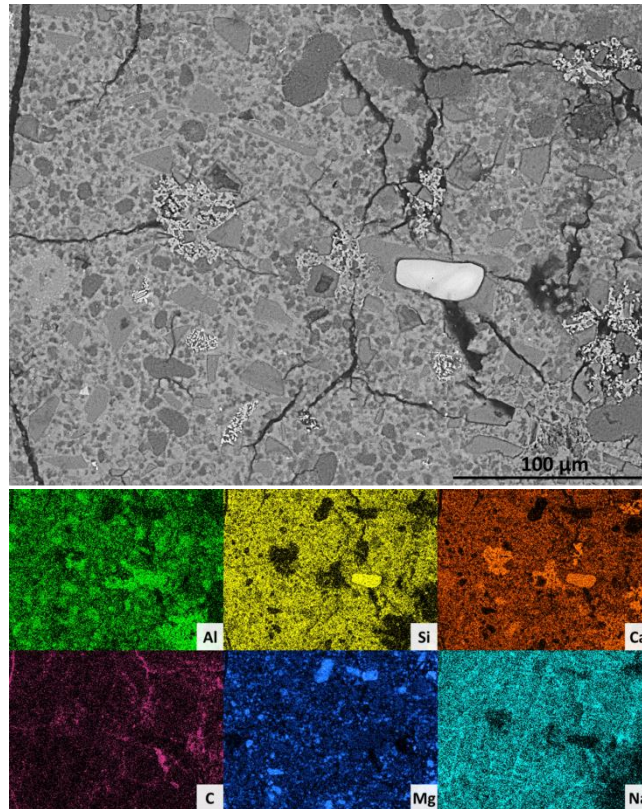


Figure 11.13 Backscattered electron micrograph and corresponding EDX maps of a sodium carbonate activated slag with 30 wt.% $\text{Mg}(\text{OH})_2$ addition after 18 months of curing

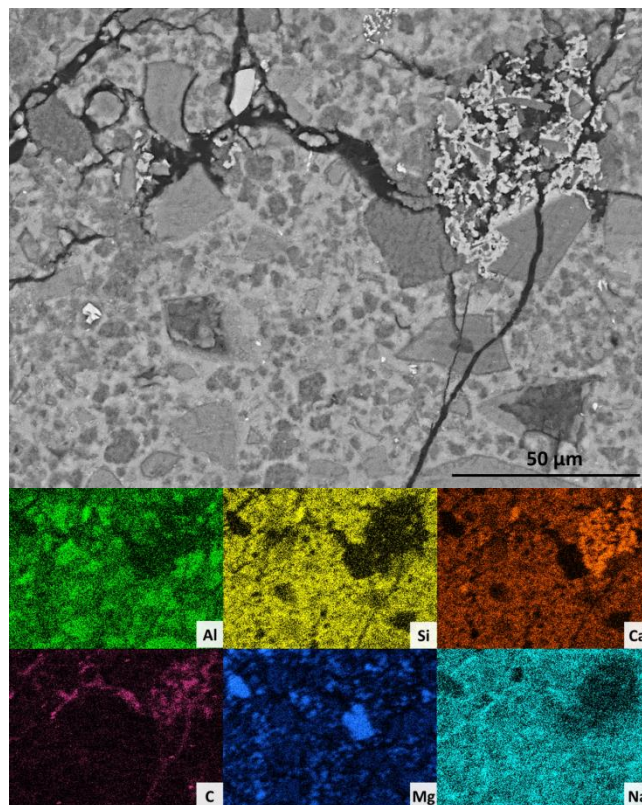


Figure 11.14 Backscattered electron micrograph and corresponding EDX maps of a sodium carbonate activated slag with 30 wt.% $\text{Mg}(\text{OH})_2$ addition after 18 months of curing

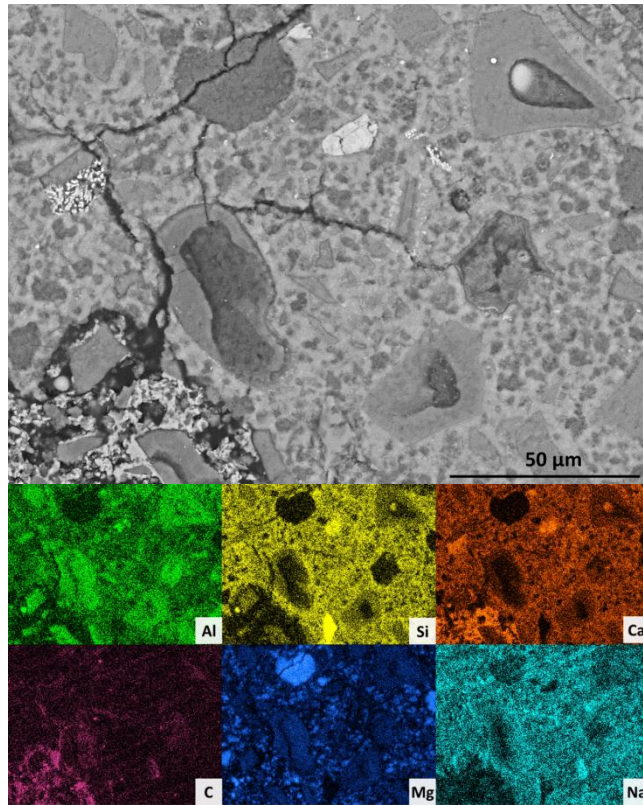


Figure 11.15 Backscattered electron micrograph and corresponding EDX maps of a sodium carbonate activated slag with 30 wt.% $\text{Mg}(\text{OH})_2$ addition after 18 months of curing

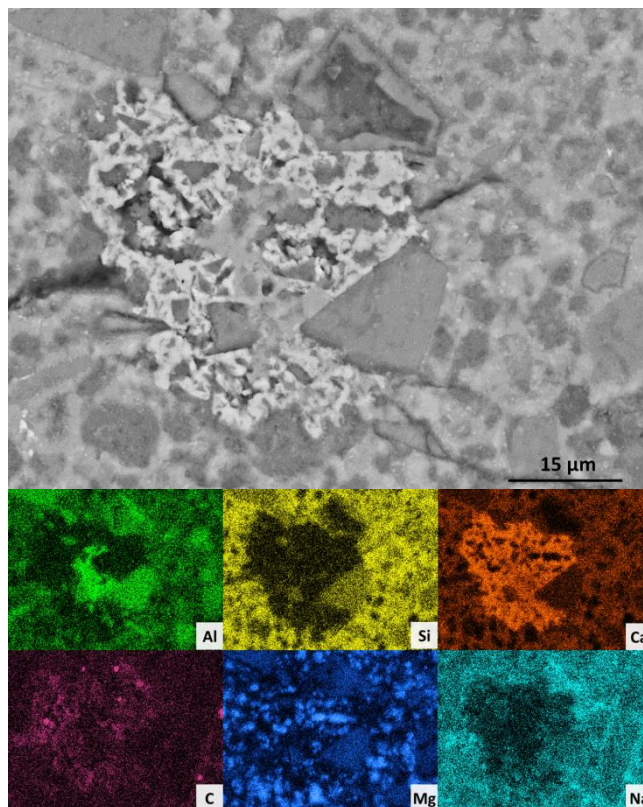


Figure 11.16 Backscattered electron micrograph and corresponding EDX maps of a sodium carbonate activated slag with 30 wt.% $\text{Mg}(\text{OH})_2$ addition after 18 months of curing

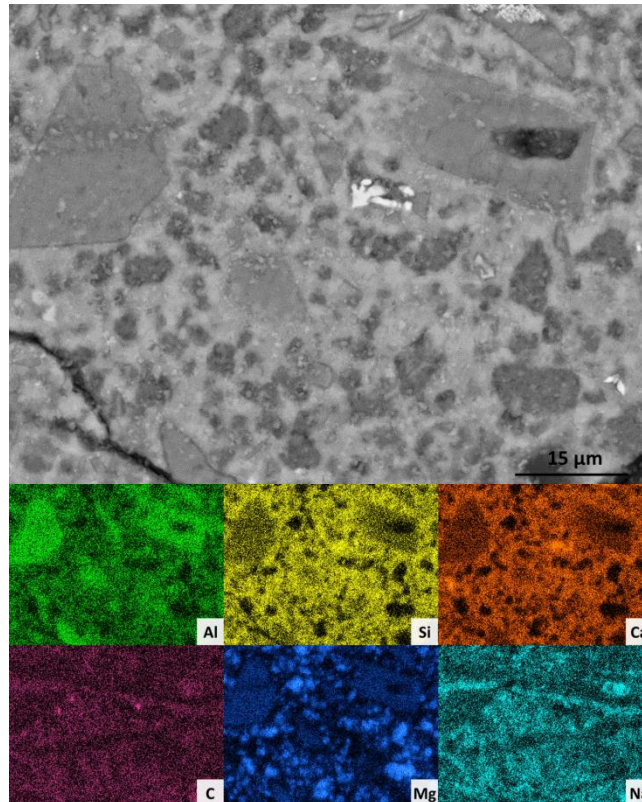


Figure 11.17 Backscattered electron micrograph and corresponding EDX maps of a sodium carbonate activated slag with 30 wt.% $\text{Mg}(\text{OH})_2$ addition after 18 months of curing

11.2.4 50 % $\text{Mg}(\text{OH})_2$ binders

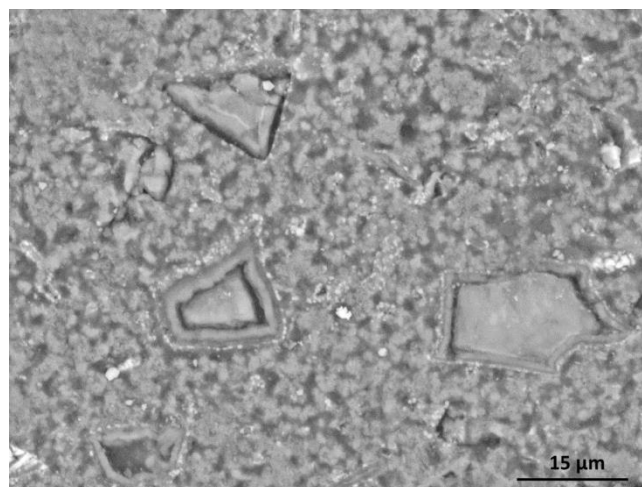


Figure 11.18 Backscattered electron micrograph and corresponding EDX maps of a sodium carbonate activated slag with 50 wt.% $\text{Mg}(\text{OH})_2$ addition after 18 months of curing

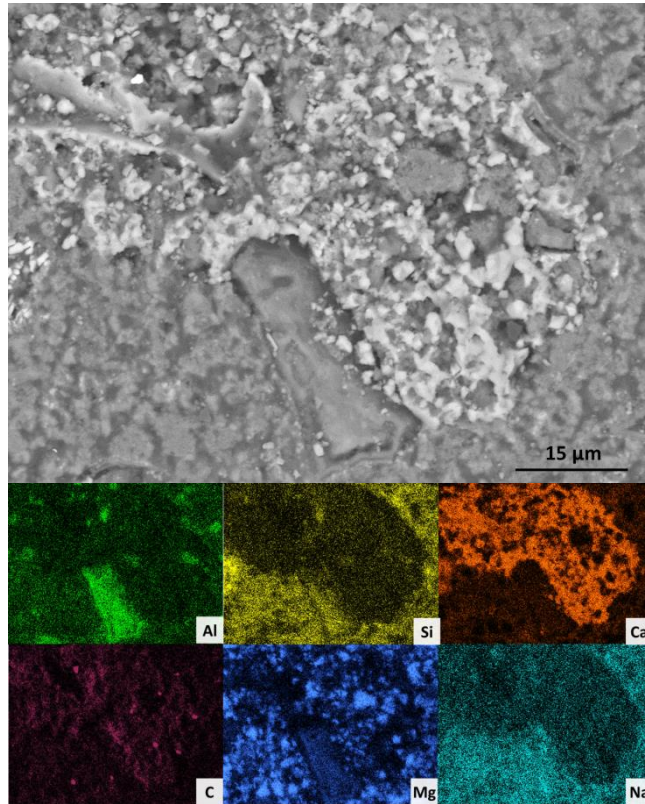


Figure 11.19 Backscattered electron micrograph and corresponding EDX maps of a sodium carbonate activated slag with 50 wt.% $\text{Mg}(\text{OH})_2$ addition after 18 months of curing

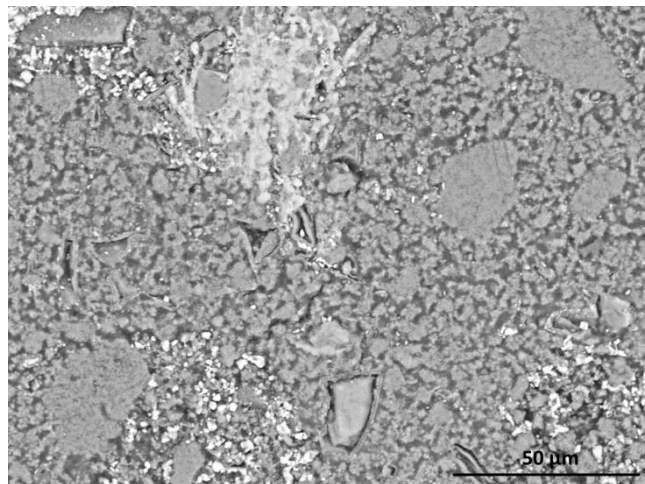


Figure 11.20 Backscattered electron micrograph and corresponding EDX maps of a sodium carbonate activated slag with 50 wt.% $\text{Mg}(\text{OH})_2$ addition after 18 months of curing

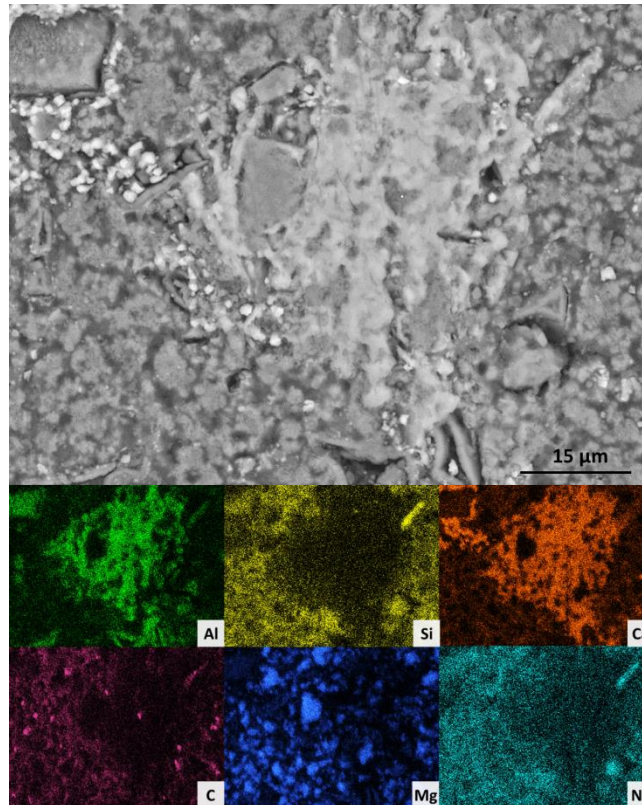


Figure 11.21 Backscattered electron micrograph and corresponding EDX maps of a sodium carbonate activated slag with 50 wt.% $Mg(OH)_2$ addition after 18 months of curing

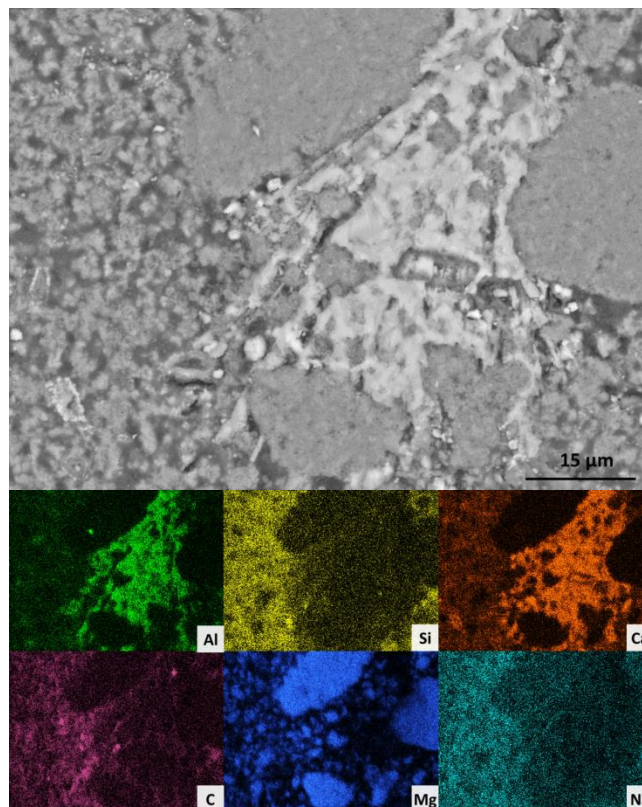


Figure 11.22 Backscattered electron micrograph and corresponding EDX maps of a sodium carbonate activated slag with 50 wt.% $Mg(OH)_2$ addition after 18 months of curing

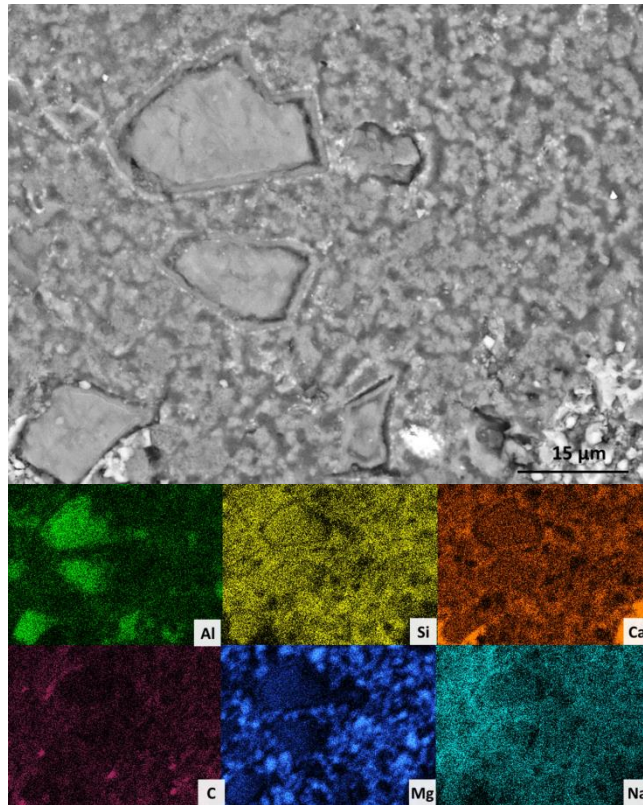


Figure 11.23 Backscattered electron micrograph and corresponding EDX maps of a sodium carbonate activated slag with 50 wt.% $Mg(OH)_2$ addition after 18 months of curing

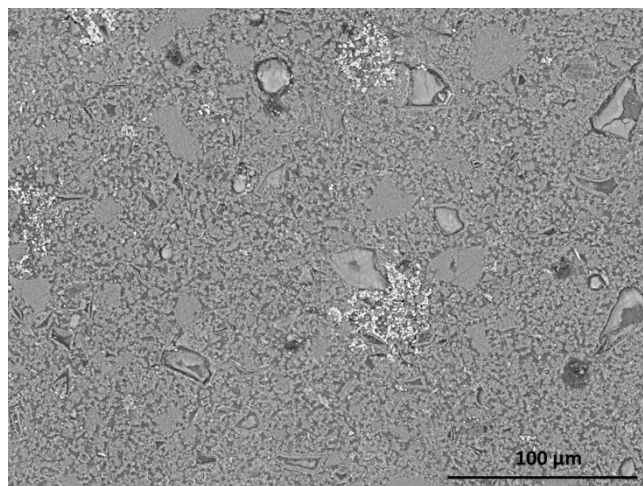


Figure 11.24 Backscattered electron micrograph and corresponding EDX maps of a sodium carbonate activated slag with 50 wt.% $Mg(OH)_2$ addition after 18 months of curing

12 Appendix II – CCR discussion publication

This appendix consists in its entirety the following manuscript, published in Cement and Concrete Research, 79 (2016) 424-426:

A discussion of the papers “*Impact of hydrated magnesium carbonate additives on the carbonation of reactive MgO cements*” and “*Enhancing the carbonation of MgO cement porous blocks through improved curing conditions*”, by C. Unluer & A. Al-Tabbaa

Sam A. Walling, John L. Provis*

Immobilisation Science Laboratory, Department of Materials Science & Engineering, University of Sheffield, Sheffield, S1 3JD, United Kingdom

**corresponding author: email: j.provis@sheffield.ac.uk, Tel: +44 114 222 5490*

Abstract

This paper is a discussion of two recent papers by Unluer & Al-Tabbaa [1, 2] which analysed accelerated carbonation of reactive MgO blocks. We suggest that the authors have incorrectly analysed key data, leading to overstated claims of MgO carbonation. Based on reassignment of their X-ray diffraction data, it is proposed that little MgO carbonation occurred in the samples discussed in those papers, with CaCO₃ instead forming during accelerated carbonation. We also draw attention to the thermodynamic instability of nesquehonite under ambient conditions, which calls into question the long-term stability of these binders.

Discussion

Cements containing reactive magnesia are of great interest as alternative binders, as they have been proclaimed to embody potentially lower CO₂ emissions during manufacture and service. Two recently published papers by Unluer and Al-Tabbaa [1, 2] have added to the body of literature on these cements, studying the effect of hydrated magnesium carbonate (HMC) addition and curing conditions, respectively, on the properties and structure of porous reactive MgO cement blocks exposed to

accelerated carbonation conditions. We will focus the discussion here on the first of these two papers, as the results presented in the second are largely an extension of the first, and contain similar points requiring re-analysis.

In these papers the authors claim to carbonate MgO to form a range of magnesium carbonates which constitute their binding phases; this is a key aspect of the ‘green’ credentials proposed for these alternative cements. Unfortunately, we are unable to reach the same conclusions made by the authors, based on our own analysis of the data presented in their papers. In our opinion, the scientific discussion in these two papers is based upon poorly-assigned X-ray diffraction patterns, which have led to incorrect interpretations of thermal analysis data, and consequently erroneous claims of high levels of carbonation.

In the paper “Impact of hydrated magnesium carbonate additives on the carbonation of reactive MgO cements” [1], the authors produce blocks containing natural aggregates, pulverised fuel ash (PFA) as filler, and MgO as the key anhydrous precursor, with hydrated magnesium carbonates (HMCs) added to some of the mixes. The combination of hydration and carbonation is proposed to lead to the formation of additional hydrated magnesium carbonates as binding phases, when cured under either natural or accelerated carbonation conditions. The authors achieved some interesting strength data, exceeding 20 MPa in compression in some instances, which shows that their methodology is of some interest.

However, there are several apparent discrepancies in the peak assignments in the two XRD patterns used by the authors to identify hydration products after accelerated carbonation (Figure 7 in [1]). This graphic is reproduced here as Figure 1, with our suggested peak assignments for their first set of XRD patterns overlaid on the original data. The authors of [1] mis-assign the major calcite peak at $29.4^\circ 2\theta$ (PDF # 005-0586), labelling it as nesquehonite and dypingite (both magnesium carbonate phases). Additional calcite reflections can be seen at 23° , 39.4° , and $48.5^\circ 2\theta$, confirming its presence in these samples. Nesquehonite (PDF # 020-0669) typically exhibits its highest intensity peak at $13.7^\circ 2\theta$, with a much lower intensity reflection at $29.5^\circ 2\theta$. Dypingite (PDF # 029-0857) has several reflections in the low-angle region, with strong reflections observed at 8.2° , 13.7° and $15^\circ 2\theta$ (elsewhere noted as 5.7° , 8.5° , 14° and $15.1^\circ 2\theta$ [3]). The absence of these reflections in the data leads us

to conclude that dypingite is not in fact present in these samples. The presence of only a small reflection for nesquehonite at 13.7° proves that the peak at 29.4° must be mostly due to calcite, with only a very small quantity of nesquehonite present.

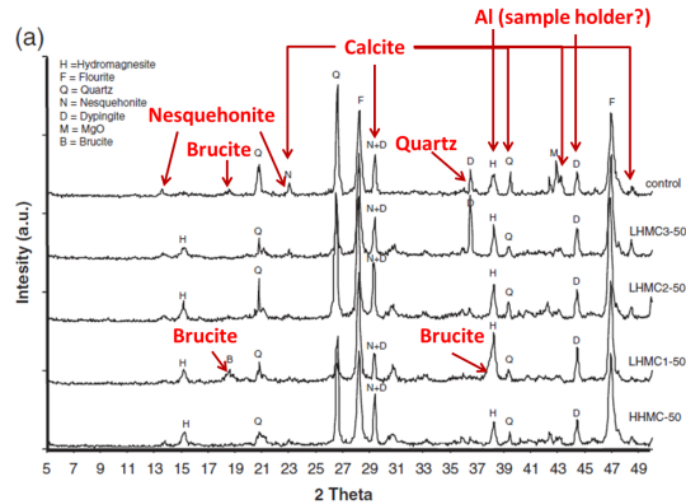


Figure 1. XRD patterns (Figure 7a of [1]), with our suggested peak assignments labelled with arrows above the authors' original assignments

The authors also mis-assign the reflection at $\sim 36.5^\circ$ 2θ to dypingite. There is a dypingite reflection listed in PDF card 029-0857 at this angle, but this is a minor reflection compared to many of the other dypingite reflections, which should be more intense, but are absent from the diffractograms. We tentatively assign this reflection to quartz (110), although this is also a relatively weak reflection of this phase. The other labelled quartz peaks at $\sim 21^\circ$ and $\sim 26.7^\circ$ 2θ vary greatly in intensity from sample to sample, possibly as a result of inclusion of differing amounts of the fine aggregates from the concrete specimens during the preparation of each sample for XRD analysis, which would be expected to be relatively coarse particles within the samples and thus potentially subject to preferred orientation issues. It is therefore unsurprising to find a quartz peak at $\sim 36^\circ$ 2θ in two of the samples, but not the others. The authors also label a peak at $\sim 44.5^\circ$ 2θ to dypingite. The PDF card for dypingite does show peaks around 44.6° 2θ , but due to the lack of other dypingite reflections in the diffractograms, this is most likely an aluminium (200) reflection from the XRD sample holder.

There is another peak at 38.3° 2θ which is labelled by the authors as hydromagnesite, and does correspond to the $(\bar{2}23)$ reflection of this phase, but this peak should only

be around $1/6^{\text{th}}$ of the intensity of the hydromagnesite (011) peak at $15.3^{\circ} 2\theta$. Major reflections for brucite (PDF # 044-1482) and aluminium (PDF # 004-0787, potentially from a sample holder as mentioned above) are located very close to this angle. The major reflections for hydromagnesite (PDF # 025-0513) are 15.3° and $30.8^{\circ} 2\theta$, which were observed in the four samples containing added HMCs (but not the control). Several minor reflections exist for this phase, including around $\sim 38^{\circ} 2\theta$, however all have significantly lower intensity than the two major reflections, so are unlikely to contribute to the peak observed here. This peak in the data set for the control sample was also incorrectly labelled as hydromagnesite, however this is more likely to be brucite (due to the absence of added HMCs in this sample) and potentially aluminium. This is also likely true of the HMC-containing samples.

This mistaken identification led the authors of [1] to infer that 100 % of the brucite has carbonated, when it is in fact much more difficult to determine how much has reacted, as will be discussed below in the context of the TGA data also presented in [1].

The authors of [1] then used the Reference Intensity Ratio method to quantify from the XRD patterns the degree of carbonation. However, as the reflection assignments were incorrect, with the diffractograms in fact potentially demonstrating very little carbonation of $\text{MgO}/\text{Mg}(\text{OH})_2$, the calculated figures cannot be considered reliable, particularly where 100% carbonation is claimed for samples with visible residual brucite peaks in the diffractograms. The authors of [1] also used an ‘acid digestion’ method to determine carbonation of MgO , but the results obtained by this technique must be considered questionable due to (a) unrecognised CaCO_3 formation within the samples, and (b) the inability of the reader to understand or reproduce the experimental protocol from the details provided.

The errors introduced in analysis of the XRD patterns were also carried over to the TG/DTA analysis (Figure 8 in [1]), where the decomposition of $\text{Mg}(\text{OH})_2$ at $\sim 400^{\circ}\text{C}$ and CaCO_3 decomposition at $\sim 780^{\circ}\text{C}$ were confused with the signals of magnesium carbonate decompositions. This confuses attempts to quantify the amount and type of magnesium carbonates formed, making this section of analysis unreliable. The strong endothermic peak and mass loss in the temperature range corresponding to

Mg(OH)₂ decomposition in all samples shown in Figure 8 of [1] must be related, at least in part, to the presence of this phase.

In our opinion, the authors have in fact largely carbonated the CaO impurities within the raw MgO (2 wt. % CaO from XRF analysis), or the CaO content of the PFA (6.8 wt.% CaO from XRF analysis) during accelerated carbonation, forming calcite (CaCO₃), rather than generating hydrous magnesium carbonates from the MgO. The mortars were made using 85 % aggregate, 5 % PFA, and 10 % magnesia-based cement (different blends of MgO and HMCs), which leaves ample ash available for carbonation, and it has previously been demonstrated that low calcium ashes can be induced to carbonate under elevated CO₂ conditions [4, 5]. We therefore believe that the accelerated used conditions in this paper (20 °C, 70-90% relative humidity, 20 % CO₂) could have caused carbonation of the PFA.

Due to these issues in the data analysis, the conclusions drawn in [1] regarding the use of HMC in reactive MgO blocks do not definitively demonstrate the full or effective carbonation of MgO in these specimens. The subsequent publication, [2], essentially follows the same route in data analysis, and suffers from the same inconsistencies in peak assignments and phase analysis. We will not recapitulate our arguments in detail regarding this specific paper, other than to say that the discussion presented above is also relevant to the conclusions presented in [2] regarding phase analysis by X-ray diffraction and thermal analysis.

As a side note, we are also concerned that the authors claim to be producing stable and durable construction materials involving nesquehonite as a key binding phase, when this phase is known to be thermodynamically unstable with respect to hydromagnesite under normal environmental conditions [6, 7], decomposing by release of water and CO₂ at room temperature and normal ambient humidities over a period of several years. This does not appear to have been considered, and could have significant consequences in terms of the longer-term behaviour of the materials produced by this method.

A recent thermodynamic study [8] of magnesium carbonates has determined that nesquehonite has a narrow range of stability. Although relatively easily formed under laboratory conditions using elevated CO₂ concentrations, it is actually

thermodynamically unstable with regard to both hydromagnesite and magnesite at ambient temperature, relative humidity and partial pressure of CO₂. The free energy diagram in Figure 2 is adapted from reference [8], and beneath this is shown the unit cell volume per mole of Mg atoms for the relevant phases. Conversion from nesquehonite to magnesite would entail a >60% reduction in density per mole of Mg, though slow growth kinetics of magnesite are likely to inhibit this process during the service life of a porous block. Conversion directly to hydromagnesite is, however, more kinetically favourable, and yields a reduction in density of more than 40% per mole of Mg. Such a change in density, with expulsion of water, is liable to destabilise a binder relying on nesquehonite for its strength. We feel that significant caution is required when relying on a binder that is so unstable under normal temperature variations.

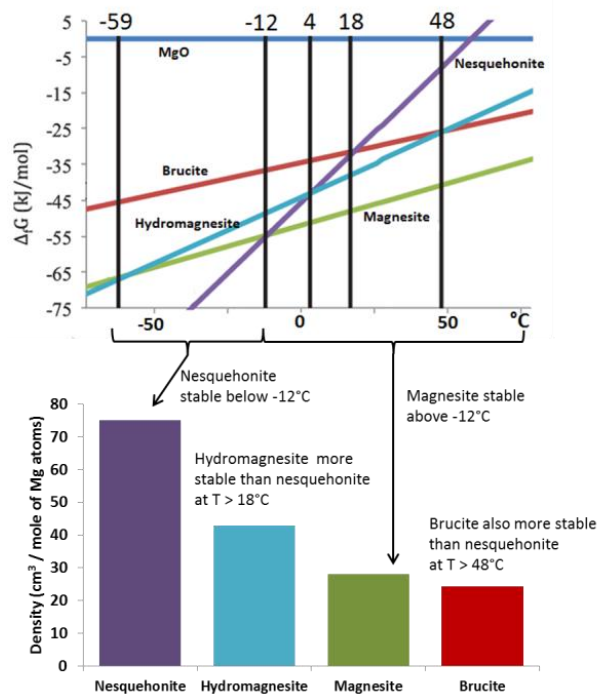


Figure 2. Free energy phase diagram for hydrous magnesium carbonates calculated by Chaka and Felmy [8], under conditions of $p\text{CO}_2 = 400$ ppm and $p\text{H}_2\text{O} = 32$ mbar (saturation vapour pressure at 298 K), along with the density per mole of Mg atoms of stable magnesium phases (data from Webmineral.com)

Acknowledgements

The doctoral project of S.A.W. is funded by the Nuclear Decommissioning Authority (UK), and by the Engineering and Physical Sciences Research Council through the Doctoral Training Centre 'Nuclear FiRST'.

References

- [1] C. Unluer, A. Al-Tabbaa, Impact of hydrated magnesium carbonate additives on the carbonation of reactive MgO cements, *Cem. Concr. Res.*, 54 (2013) 87-97.
- [2] C. Unluer, A. Al-Tabbaa, Enhancing the carbonation of MgO cement porous blocks through improved curing conditions, *Cem. Concr. Res.*, 59 (2014) 55-65.
- [3] J.H. Canterford, G. Tsambourakis, B. Lambert, Some observations on the properties of dypingite, $Mg_5(CO_3)_4(OH)_2 \cdot 5H_2O$, and related minerals, *Miner. Mag.*, 48 (1984) 437-442.
- [4] H.Y. Jo, J.-H. Ahn, H. Jo, Evaluation of the CO₂ sequestration capacity for coal fly ash using a flow-through column reactor under ambient conditions, *J. Hazard. Mater.*, 241–242 (2012) 127-136.
- [5] G. Montes-Hernandez, R. Pérez-López, F. Renard, J.M. Nieto, L. Charlet, Mineral sequestration of CO₂ by aqueous carbonation of coal combustion fly-ash, *J. Hazard. Mater.*, 161 (2009) 1347-1354.
- [6] R.A. Robie, B.S. Hemingway, The heat capacities at low-temperatures and entropies at 298.15 K of nesquehonite, $MgCO_3 \cdot 3H_2O$, and hydromagnesite, *American Mineralogist*, 57 (1972) 1768-1781.
- [7] Y. Xiong, A.S. Lord, Experimental investigations of the reaction path in the MgO–CO₂–H₂O system in solutions with various ionic strengths, and their applications to nuclear waste isolation, *Appl. Geochem.*, 23 (2008) 1634-1659.
- [8] A.M. Chaka, A.R. Felmy, Ab initio thermodynamic model for magnesium carbonates and hydrates, *J. Phys. Chem. A.*, 118 (2014) 7469-7488.
- [9] L.J. Vandeperre, A. Al-Tabbaa, Accelerated carbonation of reactive MgO cements, *Adv. Cem. Res.*, 19 (2007) 67-79.